OXFORD BROOKES UNIVERSITY

Taking a closer look:
Exploring the functional roles of P10 in baculovirus-infected cells

Leo Peter Graves

A thesis submitted in partial fulfilment of the requirements of Oxford Brookes University for the award of Doctor of Philosophy

September 2016

Abstract

P10 is a small, highly expressed baculovirus protein whose function continues to be a mystery. Believed to be non-essential during virus infection, P10 is associated with a number of intracellular structures with suggested roles in polyhedron formation, nuclear stability and lysis. The work presented here aimed to elucidate the functional role of this protein during virus infection of cell cultures. To investigate the role of P10 during infection, a variety of Autographa californica nucleopolyhedrovirus (AcMNPV) mutants were constructed by a process of co-transfection and plaque-purification.

These recombinant viruses included; a *p10* deletion and associated rescue virus that confirmed that P10 is essential for nuclear lysis and the formation of an intact polyhedral envelope. Additional virus recombinants to investigate the host-cell specificity of P10 were explored with the replacement of the AcMNPV P10 coding region with that from Spodoptera frugiperda (Sf) NPV (Ac_sf*p10*). The resulting low expression of SfMNPV P10 resulted in the absence of a P10 perinuclear cage, nuclear lysis and induced cytoxic effects. To determine whether reduced P10 synthesis was a factor in P10 function, a set of nine AcMNPV promoter deletions, made upstream from the ATG translation site of the *p10* coding region, were constructed. Analysis of these viruses showed that a decrease in P10 expression correlated with a reduction in promoter length and a concomitant decrease of nuclear lysis with reduced P10 expression.

This thesis describes the first use of serial block-face scanning electron microscopy (SBF-SEM) for the study of P10 structure formation in AcMNPV-infected TN-368 cells, identifying the independent formation of cytoplasmic and nuclear P10 fibrous bodies. The use of 3D modelling of P10 highlighted an expanding nuclear “worm-like” feature and dynamic cytoplasmic structures. The cytoplasmic structures developed from thin angular fibrils that condensed to thicker fibrous structures, forming a peri-nuclear cage that remodelled over time to form a large polarised mass. The high-resolution 3D characterisation of P10 structures using SBF-SEM provided previously unparalleled data on P10 and suggests a possible mechanism in nuclear stability and then lysis.

During these studies an intimate association was found between P10, electron dense spacers (EDS) and occlusion bodies. To determine whether P10 was essential for EDS formation and calyx formation, recombinant viruses absent of the *p10* gene were observed using electron microscopy. These viruses confirmed EDS continues to form in the absence of P10, however, EDSs fail to associate with occlusion bodies, which result in a fragmented calyx. This indicates EDS may require the presence of P10 to associate with

polyhedra and the production of an intact polyhedral envelope. This was supported from SBF-SEM of AcMNPV-infected cells that showed EDS completely encased the occlusion bodies, providing a mechanism for the role of EDS in calyx formation.

This study provides new insights in to the structural features of P10 and its association with other virus structures, and establishes the functional requirement for *p10* to be expressed to high levels. These results will contribute to the long running quest to understand this multifunctional protein.

Poster and oral Presentations

Talk

Leo Graves, Louise Hughes, Sarah L. Irons, Robert D Possee & Linda A King (2016). 3-dimensional ultrastructural modelling of Autographa californica multicapsid nucleopolyhedrovirus infection in insect cells to help determine the role of P10 during baculovirus infection. 2016 annual meeting of Society for Invertebrate Pathology, Tours, France. **Honorary mention for best oral presentation.**

Leo Graves, Sarah L. Irons, Robert D Possee & Linda A King (2014). The role of P10 and its functional domains during baculovirus infection. Oxford Brookes University 2014 postgraduate research student symposium, Oxford, UK. **Winner of best oral presentation**.

Poster

Leo Graves, Louise Hughes, Sarah L. Irons, Robert D Possee & Linda A King (2015). Baculovirus P10 structure and function. 2015 Annual meeting of Society for Invertebrate Pathology, Vancouver, Canada. **Third place for best poster presentation.**

Leo Graves, Sarah L. Irons, Robert D Possee & Linda A King (2015). Determining the role of P10 during baculovirus infection through the development of novel mutants in Autographa californica multicapsid nucleopolyhedrovirus. Oxford Brookes University 2015 postgraduate research student symposium, Oxford, UK.

Leo Graves, Farheen Raza, Sarah L. Irons, Robert D Possee & Linda A King (2014). Determining the role of P10 during baculovirus infection through the development of novel mutants in Autographa californica multicapsid nucleopolyhedrovirus. 2014 Annual meeting of Society for Invertebrate Pathology, Mainz, Germany.

Leo Graves, Sarah L. Irons, Robert D Possee & Linda A King (2014). The role and function of P10 during baculovirus infection. Oxford Brookes University 2014 Graduate online conference, Oxford, UK.

Leo Graves, Sarah L. Irons, Robert D Possee & Linda A King (2013). Determining the role of P10 during baculovirus infection. Oxford Brookes University 2013 Graduate online conference, Oxford, UK. **Winner of best online presentation**.

Acknowledgements

I am not too sure where to start with acknowledgements, as trying to complete a PhD is not a simple task and requires the help of lots of people.

I think it's best to start with my supervisors, Linda King, Robert Possee and Sarah Irons. It has been with their extensive help and support that I have been able to write this thesis. They have provided me with mentoring and guidance throughout my time here and been understanding of my epilepsy, which has made this PhD all the more challenging for myself.

Another important mention is to Louise Hughes, who has helped and inspired my new found interest in microscopy. She has helped provide advice on many technical aspects during my four years and enabled me to obtain such amazing data.

Another great thank you also goes to members working at the Insect Virus Research Group and Oxford Expression Technologies, who have had to put up with my humming and complaints. They offered help when required, especially on walks to buy coffee with coffee buddy, Adam Chambers. I have also had the pleasure of meeting many friends during my studies, which provided me with food (thanks Turk), beer and a good game of darts (thanks Nathan) or coffee (everyone else!)

My family have also provided me with a lot of support and love during my time at Oxford Brookes University and I take great pride that they take such interest in what I do, with questions such as "what is a P10?" and "Does it do anything?" My parents and brothers have always been willing to listen as I waffled on, even providing support with my models with the help of Lotus and Mercedes Formula 1.

I also want to say special thanks to my lovely girlfriend Marloes Franssen, who has been with me most of this journey. She has always provided moral support when required and helped me stay strong with my many faltering conditions; I look forward to many more years with you.

In closing this opportunity would not be possible without the financial support and help of Oxford Brookes University, so a massive thank you to the University for allowing me to have so many exciting experiences on this tough, yet exciting journey. I hope I have not caused too much trouble.

To all that sailed on this P10 ship of excitement, THANK YOU!

Contents Page

Figures

Tables

Abbreviations

3D:	Three-Dimensional
β-galactosidase gene	*lacZ*
aa:	Amino acid
ATP	Adenosine triphosphate
BEVs:	Baculovirus expression vectors
bp:	Base pairs
BSA:	Bovine serum albumin
Bt:	*Bacillus thuringiensis*
BV:	Budded virions
C-terminal:	Carboxy-terminal
DAPI:	4',6-diamidino-2-phenylindole
DMF:	Dimethylformimide
DMSO:	Dimethylsulphoxide
DNA:	Deoxyribonucleic acid
dNTP:	Deoxynucleotide triphosphate
dpi:	Days post infection
dsDNA:	Double stranded deoxyribonucleic acid
egt:	Ecdysteroid-UDP-glycosyl transferase (gene)
EDS:	Electron dense spacer
EM:	Electron microscopy
GV:	Granulovirus
HFW:	Horizontal field width
hpi:	Hours post infection
Hi5:	BTI-Tn-5B1-4 (High Five™)
ICTV:	International Committee on the Taxonomy of Viruses
kV:	KiloVolts
MAP:	Microtubule associated protein
MNPV:	Mulit-capsid nucleopolyhedrovirus
MOI:	Multiplicity of infection
MSA:	Multiple Sequence Alignment
MT:	Microtubule
NCBI:	National Centre for Biotechnology Information
NPV:	Nucleopolyhedrovirus
nt:	Nucleotides
ODV:	Occlusion derived virions
orf:	Open reading frame
P10:	The baculovirus 10 kDa protein
p10:	The baculovirus 10 kDa protein gene
Pa:	Pascal
PBS:	Phosphate buffered saline
PCR:	Polymerase chain reaction
PE:	Polyhedral envelope
PEP:	Polyhedral envelope protein
pfu:	Plaque forming units
PIF:	*Per os* infectivity factor
PM:	Peritrophic membrane
RE:	Restriction enzyme
RNA:	Ribonucleic acid
rpm:	Rotations per minute
SBF-SEM:	Serial block-face Scanning electron microscopy
SDS:	Sodium dodecyl sulfate
SDS-PAGE:	Sodium dodecyl sulfate polyacrylamide gel electrophoresis
SEM:	Scanning electron microscopy

Sf:	*Spodoptera frugiperda*
Sf21:	IPLB-SF-21 cell line
SNPV:	Single-capsid nucleopolyhedrovirus
T.ni:	*Trichoplusi ni*
TEM:	Transmission electron microscopy
TN-368:	Mulit-capsid nucleopolyhedrovirus
WT:	Wild type
X-gal:	5-Bromo-4-chloro-3-indolyl β-D-galactopyranoside

Baculoviridae

Alphabaculovirus

Autographa californica nucleopolyhedrovirus	(AcMNPV)
Antheraea pernyi nucleopolyhedrovirus	(ApNPV)
Anticarsia gemmatalis nucleopolyhedrovirus	(AgNPV)
Bombyx mandarina nucleopolyhedrovirus	(BmNPV)
Bombyx mori NPV	(BmNPV)
Choristoneura fumiferana DEF MNPV	(CfMNPV_Def)
Choristoneura fumiferana MNPV	(CfMNPV)
Choristoneura murinana nucleopolyhedrovirus	(ChmuNPV)
Choristoneura occidentalis nucleopolyhedrovirus	(CoNPV)
Choristoneura rosaceana nucleopolyhedrovirus	(CrNPV)
Condylorrhiza vestigialis nucleopolyhedrovirus	(CoVeNPV)
Epiphyas postvittana nucleopolyhedrovirus	(EpNPV)
Hyphantria cunea nucleopolyhedrovirus	(HyCuNPV)
Maruca vitrata nucleopolyhedrovirus	(MvNPV)
Orgyia pseudotsugata MNPV	(OpMNPV)
Plutella xylostella nucleopolyhedrovirus	(PlxyMNPV)
Rachiplusia ou nucleopolyhedrovirus	(RaouMNPV)
Thysanoplusia orichalcea nucleopolyhedrovirus	(ThorNPV)
Adoxophyes honmai nucleopolyhedrovirus	(AdhoNPV)
Adoxophyes orana nucleopolyhedrovirus	(AdorNPV)
Agrotis ipsilon nucleopolyhedrovirus	(AgipMNP)
Agrotis segetum nucleopolyhedrovirus	(AgseNPV_A)
Agrotis segetum nucleopolyhedrovirus B	(AgseNPV_B)
Apocheima cinerarium nucleopolyhedrovirus	(ApciNPV)
Buzura suppressaria nucleopolyhedrovirus	(BusuNPV)
Chrysodeixis chalcites nucleopolyhedrovirus	(CcNPV)
Clanis bilineata nucleopolyhedrovirus	(CbNPV)
Ecotropis obliqua nucleopolyhedrovirus	(EoNPV)
Euproctis pseudoconspersa nucleopolyhedrovirus	(EupsNPV)
Helicoverpa armigera nucleopolyhedrovirus	(HearMNPV)
Helicoverpa armigera nucleopolyhedrovirus	(HearNPV)
Helicoverpa armigera nucleopolyhedrovirus	(HearNPV_NNg1)
Helicoverpa armigera nucleopolyhedrovirus G4	(HearNPV_G4)
Helicoverpa zea nucleopolyhedrovirus	(HzSNPV)
Hemileuca sp. nucleopolyhedrovirus	(HespNPV)
Leucania separata nucleopolyhedrovirus	(LsNPV)
Lymantria dispar nucleopolyhedrovirus	(LdMNPV)
Lymantria xylina nucleopolyhedrovirus	(LyxyMNPV)
Mamestra brassicae nucleopolyhedrovirus	(MabrMNPV)
Mamestra configurata nucleopolyhedrovirus	(McNPV_A)
Mamestra configurata nucleopolyhedrovirus	(McNPV_B)

Orgyia leucostigma nucleopolyhedrovirus	(OlNPV)
Pseudoplusia includens nucleopolyhedrovirus	(PsinSNPV)
Spodoptera exigua nucleopolyhedrovirus	(SpexMNPV)
Spodoptera frugiperda nucleopolyhedrovirus	(SfMNPV)
Spodoptera litura nucleopolyhedrovirus	(SpliNPV)
Spodoptera litura nucleopolyhedrovirus II	(SpliNPV_II)
Trichoplusia ni nucleopolyhedrovirus	(TniSNPV)

Betabaculovirus

Adoxophyes orana granulovirus	(AdorGV)
Choristoneura occidentalis granulovirus	(ChocGV)
Clostera anachoreta granulovirus	(CaGV)
Clostera anastomosis granulovirus	(ClanGV)
Helicoverpa armigera granulovirus	(HearGV)
Pieris rapae granulovirus	(PrGV)
Plutella xylostella granulovirus	(PlxyGV)
Pseudaletia unipuncta granulovirus	(PsunGV)
Spodoptera litura granulovirus	(SpliGV)
Xestia c-nigrum granulovirus	(XecnGV)

Chapter One:

Introduction

1.1 Baculovirus history

Baculoviruses do not cause human disease, however, their existence has been known for many years, with the earliest written accounts found in ancient Chinese literature. This made reference to a baculovirus-like disease in cultured silkworms (reviewed by Miller, 1997). The first mention of baculoviruses in western literature was made as early as 1527, in a poem called “De bombyce” by Marco Girolamo Vida, in which the demise of the silkworm was described. Vida wrote on an apparent ‘jaundice’ disease that caused larvae to swell, eventually rupturing and releasing a purulent liquid (reviewed by Benz, 1986).

It was not until the late 19th century, with the introduction of more powerful microscopes, that more detailed scientific descriptions of the ‘jaundice’ disease were published by Maestri and Cornalia in 1856 (reviewed by Benz, 1986). The authors commented on the peculiar presence of strongly refractive crystals or corpuscles in the blood and tissue of the infected silkworms. These refractive crystals, later termed ‘polyhedral granules’, were shown by Bolle in 1894 (reviewed by Benz, 1986) to be the causative agent of the insect disease.

In the early 20th Century, von Prowazek in 1907, (reviewed by Benz, 1986) demonstrated that the absence of polyhedra still resulted in the infection of silkworms, thus indicating that polyhedra were not the carrier of the virus and an alternative system resulted in the infection of the insect. This proposal was confirmed by the work of Acqua (1918-1919; reviewed by Benz, 1986), who convincingly confirmed that a filterable virus, invisible with microscopes at the time, caused the infection in silkworms. A few years later, work demonstrated by Komarek and Breindl in 1924 (reviewed by Benz, 1986) provided conclusive evidence that the infectious agent of silkworms existed both within the polyhedra (as suggested by Bolle in 1894), and within the filtrate (as presented by von Prowazek in 1907).

This early pioneering work was facilitated by the development of the electron microscope (EM) in 1933, allowing baculovirus research to progress from the isolation and definition of these insect viruses, to more detailed characterisation of the viral structures. The increased resolution of the EM enabled the identification of the filterable infectious agent as large rod-shaped capsids. Investigators were surprised to find the presence of bundles of membrane-bound particles encased in a polyhedral protein crystal (Bergold, 1947; Bergold, 1950; Hughes, 1950; Benz, 1986). These structures became recognised as occlusion derived viruses (ODV) and non-occluded viruses, also known as budded virus (BV) (Henderson *et al.*, 1974; Volkman *et al.*, 1976)

1.1.1 Baculovirus taxonomy

As a result of the continued identification of new baculoviruses, several attempts were made to implement a classification scheme that was largely based on a Linnean system (Steinhaus, 1949; Bergold, 1953). Classification and identification of baculoviruses later utilised morphological differences between the granulovirus (GV), nucleopolyhedrovirus (NPV) (multiple (M) or single (S) nucleocapsids) and non-occluded viruses (Harrap and Payne, 1979; Bilimoria, 1986) and was made official since the publication of the 6th report of the international committee on the taxonomy of viruses (Murphy *et al.*, 1995).

The advances in genome sequencing over the last decade resulted in a new classification system that was based on phylogenetic evidence, genome composition and morphological traits (Jehle *et al.*, 2006; Carstens and Ball, 2009; Miele *et al.*, 2011; Rohrmann, 2013). This led to a revision of the classification and nomenclature of baculoviruses into four main genera: alphabaculovirus (lepidopteran NPV), betabaculovirus (Lepidopteran GV), gammabaculovirus (Hymenopteran NPV) and deltabaculovirus (Dipteran) (Jehle *et al.*, 2006). Phylogenetic studies on alphabaculovirus proposed a subdivision into alphabaculovirus type I and type II, dependent on gene content: notably the presence of GP64 (Type I) or F protein (Type II) as reviewed by Miele *et al*. (2011).

Comparative analysis between baculoviruses have reported 37 core genes, with the possible addition of AC83 (p95) (unpublished work presented by Javed at SIP 2016), which are commonly conserved in all baculovirus genomes (Garavaglia *et al.*, 2012; Rohrmann, 2013). Another subset of genes have been categorised as essential and desirable. The essential gene is characterised from gene deletions that result in the baculovirus unable to produce infectious virus. The nonessential, yet desirable genes will provide a beneficial trait to the virus (Rohrmann, 2013).

1.1.2 Application of baculoviruses against pest insects

Research during the first half of the 20th century (reviewed by Benz, 1986) identified that the narrow host range of baculoviruses and general features of the insect virus (discussed in Section 1.2) provided a natural pathogen of insects. It was only in the second half of the 20th century with the detailed work by Steinhaus from 1950 until 1975 (reviewed in Miller, 1997) that the first baculovirus bio-pesticide control agent was registered and sold in the United States. This was Elcar® in 1975 used to control many species belonging to the genera *Helicoverpa* and *Heliothis*

Bio-pesticides have primarily been employed for the treatment of crops such as corn, rice, cereals, soybean, fruit, vegetables and cotton with their use in forestry remaining small. The forestry market has historically been dominated by the inclusion of *Bacillus thuringiensis* for the control of lepidopteran pests (Dent, 1993), however, other bio-pesticides include: baculovirus (Table 1.1), fungi, protozoa and nematodes (Fuxa, 1982; Hunter-Fujita *et al.*, 1998).

The use of baculovirus as an active ingredient in bio-pesticide has not always been well received and initially lacked commercial interest. This was likely due to limited cross reactivity of the narrow host range of baculoviruses and prolonged speed of kill, often taking up to 25 days. Therefore providing a longer period for crop damage to occur (Hunter-Fujita et al., 1998). The continued advances in baculovirus research helped the development of new baculovirus-based products (as reviewed by Miller, 1997); however, strong competition with chemical pesticides hindered its growth. For example, baculovirus-based bio-pesticides made up only a small proportion (1%) of the estimated $380 million bio-pesticide market in 1995 (reviewed by Hunter-Fujita *et al.* 1998). Additional reports on the world pesticide usage in 1994, as reviewed by Miller (1997), highlighted the small market share for the use of bio-pesticides, making up only 1.5% of the total pesticide industry. Pharmaceutical companies were often reluctant to invest in this particularly small baculovirus market (Hunter-Fujita *et al.*, 1998).

The last two decades have seen an increased demand for alternatives to chemical pesticides to minimise the potentially harmful and toxic chemicals used for cultivation of crops (Gerhardson, 2002). This demand has resulted in the development of over 175 registered active-ingredients for 700 bio-pesticide products (Dutta, 2010). This increased demand has seen the global market for bio-pesticides increase to $2.1 billion by 2012 and this rise is predicted to continue (Dutta, 2010; Koivunen *et al.*, 2013). This expansion has largely been due to new regulations requiring farmers to reduce broad spectrum chemical pesticides, therefore making the use of bio-pesticides a more favourable system (Lacey *et al.*, 2015). A recent estimation for baculovirus based bio-pesticide sales from the 2010 worldwide bio-pesticide market summary (reviewed in Lacey, 2015), showed baculoviruses had increased from 1% in 1995 to 12% in 2010 for the total bio-pesticide market (Table 1.1).

Table 1.1: Review of recent baculoviruses based bio-pesticides[1].

Product	Active ingredient
Abietiv	Neodiprion abietis nucleopolyhedrovirus
Capex	Adoxophyes orana (summer fruit) granulosis virus
Carpostop	Cydia pomonella granulosis virus
Carpovirusine	Cydia pomonella granulosis virus
Cryptex	Cryptophlebia leucotreta granulovirus
CYD-X	Cydia pomonella granulosis virus
Exilon	Agrotis ipsilon nuclear polyhedrosis virus
Gemstar	Occulusion bodies of the nuclear of Helicoverpa zea
Granupom	Cydia pomonella granulosis virus
Gypchek	Lymantria dispar nucleopolyhedrovirus
Helicovex	Helicoverpa armigera nucleopolyhedrovirus
Littovir	Spodoptera littoralis nucleopolyhedrovirus
loopex	Autographa californica nucleopolyhedrovirus
Madex	Cydia pomonella granulosis virus
Pavois	Cydia pomonella granulosis virus
Pomonellix	Cydia pomonella granulosis virus
Spexit	Spodoptera exigua nucleopolyhedrovirus
Spod-X	Spodoptera exigua nucleopolyhedrovirus
TM Biocontrol-1	Orgyia pseudotsugata nucleopolyhedrovirus
Virex	Cydia pomonella granulosis virus
Virgo	Cydia pomonella granulosis virus
Virosoft	Cydia pomonella granulosis virus
Virtuss	Orgyia pseudotsugata nucleopolyhedrovirus

[1] Data acquired from the Biopesticide database (Agriculture and Agri-Food Canada, 2013) and Andermatt Biocontrol AG (Jäggin, 2016) with permission.

The potential strength of the baculoviruses is conductive to larger scale and long term control due to the mechanism of baculovirus infection. One early example of biological control of large pest populations was an outbreak of *Gilpinia hercyniae* in North America 1938. With little assistance from humans this NPV spread over 12,000 square miles and by 1940 ceased to be a pest. The absence of further outbreaks is attributed to the continued survival of the baculovirus and thus suppression of the pest (reviewed by Hunter-Fujita *et al.* 1998).

1.1.3 Baculovirus expression technology

An alternative and lucrative system for the use of baculoviruses, was the development of an protein expression system. The most important discovery was found in the early

1980s, which identified polyhedrin and P10 accumulate to very high levels late in infection (Adang and Miller, 1982; Smith *et al.*, 1982; Smith *et al.*, 1983c). It demonstrated that these proteins, encoded by polyhedrin and *p10* genes, were not essential for the propagation of the virus in cell culture (Smith *et al.*, 1983a; Smith *et al.*, 1983b; Miller *et al.*, 1986; Vlak *et al.*, 1988). This allowed for the deletion of the open reading frame (ORF) and the replacement with foreign genes that allowed high quantities of almost any protein to be produced under the very late promoters of *p10* and polyhedrin (reviewed by Cox, 2012). This became what is now known as the baculovirus expression vector system (BEVS). Due to the baculovirus genome being too large to insert foreign genes directly, the adaption of a system that used an additional step was developed. This used a transfer vector containing flanking sequences to the promoters. Then the foreign gene is inserted into the virus genome using insect cell homologous recombination, which resulted in recombinant virus (Possee, 1997; Kelly *et al.*, 2007; van Oers *et al.*, 2015).

During the thirty years since the first paper was published by Smith *et al*. (1983b), major improvements have been made in the industrial production of recombinant proteins and These advances have made the BEVS a more attractive system for protein production. Improvements to BEVS included a BacPAK6 system that replaces polyhedrin with *lacZ*. Digestion with Bsu361 removes lacZ and a fragment of the essential gene, *orf1629*, required for replication in insect cells. Co-transfection with relevant transfer vector restores infectivity as well as inserting foreign gene. The system provided an increased recovery of recombinant virus, however it still required purification by plaque assay (Kitts and Possee, 1993). This additional purification step was later addressed with the development of the The flashBAC™ system by Oxford Brookes University and NERC CEH oxford and sold by Oxford Expression Technologies (Possee *et al.*, 2008). flashBAC™ is an AcMNPV genome that lacks an essential gene, *orf1629* and contains a bacterial artificial chromosome, which replaces the polyhedrin coding region. Unlike BacPAK6, the flashBAC™ does not require linearisation prior to use. A process of Co-transfection into insect cells with a transfer vector restores the function of ORF1629. As parental DNA, flashBAC™, is unable to replicate no plaque purification is required (Possee *et al.*, 2008). Further developments including flashBACGOLD™ (Hitchman *et al.*, 2010b) and FlashBACULTRA™ has resulted in increased protein yields (Hitchman *et al.*, 2010a).

An additional important milestone in the development of the BEVS has been the delivery and expression of heterologous genes in mammalian cells as reviewed by van Oers *et al*. (2015), along with the manufacturing of virus-like particles (VLPs) (Pidre *et al.*, 2013).

The first VLP to be produced by baculovirus was in the early 1990s using human immunodeficiency virus (HIV) group specific antigen protein (gag) by Morikawa in 1991 as reviewed by Possee *et al.* (2010). It was observed forming retroviral core like particles within the cytoplasm of baculovirus-infected cells. Since then VLPs from other viruses such as papillomavirus virus L1 protein (Suzich *et al.*, 1995) and rotavirus, influenza, orbivirus, Norwalk virus and others, have been used (reviewed by Possee *et al.*, 2010). The current use of the BEVS for the production of recombinant vaccines is shown in Table 1.2 (Senger *et al.*, 2009; Medema *et al.*, 2011; Cox, 2012), with a number of future vaccine candidates; influenza, diabetes, hepatitis E, parovirusB-19 and norovirus currently in clinical development (Cox, 2012).

Table 1.2: Currently approved vaccines and therapies based on baculovirus expression technology[1]

Name	Company	Expressed product	Use	Release year
Porcilis Pesti	MSD Animal Health	E2 glycoprotein	Pigs	1998
Circumvent PCV	MSD Animal Health	Porcine circovirus ORF2	Pigs	2005
Cervarix	GlaxoSmithKline	Human papillomavirus L1 protein	Girls	2007
CircoFLEX	Ingelvac	Porcine circovirus ORF2	Pigs	2008
Porcilis PCV	MSD Animal Health	Porcine circovirus ORF2	Pigs	2009
Provenge (sipuleucel-T)	Dendreon	PAP-GM-CSF[2]	Men	2010
Glybera	UniQure	AAV vector with lipoprotein lipase transgene	Humans	2012
Flublok	Protein Sciences	Influenza HA	Humans	2012

[1] Adapted from Van Oers *et al*. (2015) with permission.
[2]Prostatic acid phosphatase coupled to granulocyte macrophage colony-stimulating factor

1.1 The Baculoviridae

The *Baculoviridae,* is a large family of arthropod-specific, double-stranded DNA (dsDNA) viruses (Miller, 1997; Rohrmann, 2011). To date existing literature contains descriptions of baculoviruses from over 500 different species, primarily in insect orders, Lepidoptera (604 species in butterflies and moths), Hymenoptera (30 species ranging from sawflies, wasps, bees and ants) and Diptera (27 species of fly) (Miller, 1997; Rohrmann, 2011). Other baculoviruses have been reported Trichopetera (caddisfly), Coleoptera (beetle) and Neuropteran (net-winged insects) as reviewed by Rohrmann (2013), however many of these yet remain to be characterised at a molecular level.

1.2.1 Baculovirus Structures

The baculovirus is characterised by rod shaped virions, which contain apical and basal ends (Figure 1.1). The nucleocapsids contain capsids, mainly composed of VP39, which contain highly condensed, circular, supercoiled dsDNA genomes ranging from 80 to 180 kilobase pairs (kbp) (Pearson *et al.*, 1988; Thiem and Miller, 1989). These virions measure between 250-400 nm in length and 30-70 nm in diameter (Boucias and Pendland, 1998; Jehle *et al.*, 2006) depending on the viral genome size (Slack and Arif, 2006).

The baculovirus has a bi-phasic replication cycle that produces two distinct virion forms that encapsulate nucleocapsids: ODV and BV. The BV (Figure 1.1) comprises a single nucleocapsid encased in a virion envelope that is acquired from the plasma membrane on egress from the infected cell, as discussed in detail in Section 1.3 (Blissard and Rohrmann, 1990; Riegel and Slavicek, 1997). Recent evidence suggests that the BV exhibits a more 'ovoid' shape with electron-lucent pockets either side of the nucleocapsid (Wang *et al.*, 2016). This updated structural model for BV highlights dispersal of envelope proteins at each polar end (Figure 1.1), which had previously only been identified at the apical cap (Wang *et al.*, 2016).

The ODV comprises of a single or multiple nucleocapsids contained within a lipid bi-layer envelope (Figure 1.1; reviewed by Slack *et al.,* 2006). The most recent studies highlighting the formation of ODV, suggest that the nucleocapsids, which get retained in the nucleus during the later phases of infection and get bundled together.

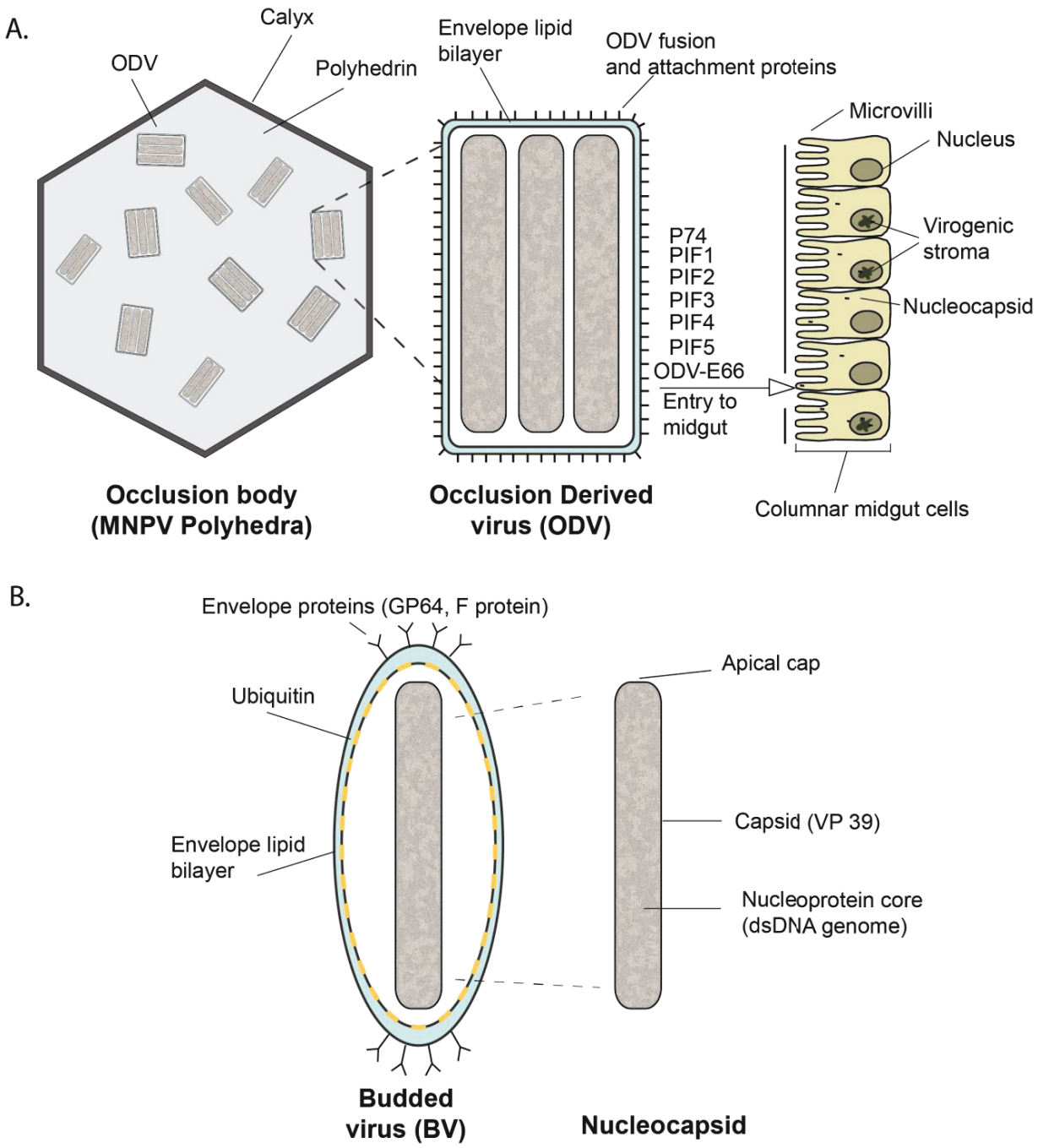

Figure 1.1 Structures formed from alphabaculovirus multiple nucleopolyhedrovirus (MNPV)-infected insect cells. A) Schematic of MNPV occlusion body (OB) containing multiple occlusion derived virus (ODV). Upon digestion by the host, the strong alkaline conditions of the midgut release the ODV. The ODV then penetrate the peritrophic membrane and enter the microvilli of the columnar midgut cells mediated by *per os* infectivity factors (PIF). The nucleocapsids (NC) are released into the cytoplasm. B) Indicates new proposed model for the MNPV budded virus (BV) and distribution of envelope proteins. The BV contains a single NC that is enveloped in a lipid bilayer.

The nucleocapsids then adhere to large microvesicles, which are formed from the fusion of smaller vesicles or a complicated process where the invaginated intranuclear membrane forms either large or small vesicles (Shi *et al.*, 2015). The introduction of more nucleocapsids forces the microvesical to deform and rupture into an arch-shape membrane. The nucleocapsids along the membrane eventually become encapsulated, resulting from the continued fusion of small microvesicals to the membrane. The nucleocapsids then bundle in parallel to each other and the membrane invaginates to form separate bundles of new ODVs (Shi *et al.*, 2015). This envelopment process occurs prior to embedding of the ODV in the occlusion bodies (OB) (Figure 1.1).

Occlusion bodies consist of a crystalline matrix that comprises polyhedrin in NPVs (Figure 1.1) and granulin in GVs. The NPV polyhedra range between 0.6μm and 2μm and granules range from 0.2μm and 0.4μm in diameter (Ackermann and Smirnoff, 1983). One major difference between NPV and GV is that polyhedra of the NPV virus normally contain many ODVs comprising either single or multiple nucleocapsids (Figure 1.1, Summers and Arnott, 1969), whereas the majority of granules from the GV carry only a single ODV consisting of one nucleocapsid (Arnott and Smith, 1967).

The ODVs become integrated into OBs and finally a polyhedral envelope (PE)/calyx forms around the OB (Minion *et al.*, 1979), as shown in Figure 1.1. This calyx consists largely of a polyhedral envelope protein (PEP), shown to be PP34 in Autographa californica MNPV (AcMNPV) (van Lent *et al.*, 1990; Lee *et al.*, 1996) and PP32 in Orgyia psuedotsugata MNPV (OpMNPV) (Russell *et al.*, 1991; Gross *et al.*, 1994) and carbohydrate matrix. This forms an electron dense membrane with a thickness of 5nm to 8nm. The development of PE has shown to provide protection from environmental hazards, such as UV light, and resistance to viral and other enzymes. In the absence of the PE the OBs surface look fragmented with a pitted surface, characteristic of ODVs falling out of the polyhedra (Russell and Rohrmann, 1990; Russell *et al.*, 1991).

The process for PE formation is still the subject of speculation, however, both P10 and electron dense spacers (EDS) appear to play an intimate role in OB formation (Summers and Arnott, 1969; Williams *et al.*, 1989; Gross *et al.*, 1994) and will be discussed in detail later (Section 1.4.4).

1.3 Replication cycle of baculovirus

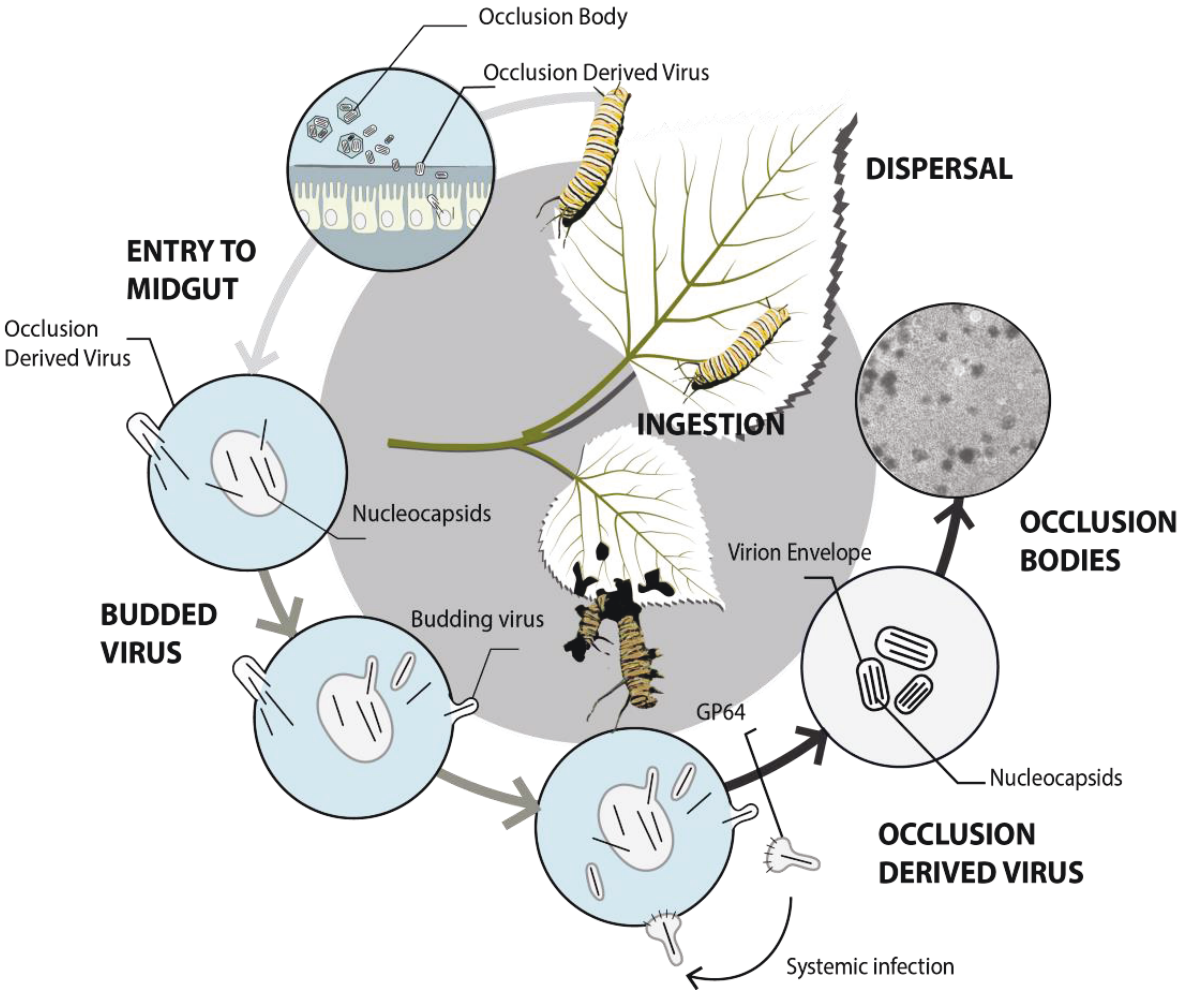

Figure 1.2 The replication cycle of the baculovirus during infection of a host insect. The image displays the cycle from the consumption of polyhedra, leading on to the formation of the two virus forms of the bi-phasic replication, budded virus and occlusion derived virus. The final stages result in the production of the polyhedra prior to liquefaction of the host.

1.3.1 Primary phase of baculovirus infection

The replication of the baculovirus during infection of the host has been highlighted in Figure 1.2, with the important phases of infection explored below.

Infection of the host is initiated when the insect larvae inadvertently consumes OB-contaminated food. After consumption of the OBs, the structures naturally travel to the midgut, where the strong alkaline conditions (pH 10-11) and host proteases trigger dissolution of the proteinaceous polyhedrin matrix and calyx (Harrap, 1972; Pritchett *et al.*, 1984) to release embedded ODVs (Bergold, 1947; Granados and Lawler, 1981; Blissard and Rohrmann, 1990; Slack and Arif, 2006; Chiu *et al.*, 2012).

Upon release from the polyhedra, the ODVs gain passage to the host cell. Before the ODV reaches the cell, it first travels through the peritrophic membrane (PM) by chance encounters with lesions or from the dissolution of the mucin-like protein that bridges the chitin strands in the PM (Wang *et al.*, 1994; Wang and Granados, 1997; Rohrmann, 2011). On entry through the PM, the ODVs proceed to infect the midgut epithelial cells (Figure 1.1). The ODVs contain more than ten different envelope proteins (Braunagel and Summers, 2007) of which five are highly conserved (PIF1, PIF2, PIF3, PIF4 and P74) and known as *per os* infectivity factors (PIFs) that are essential for oral infectivity (Peng *et al.*, 2010). It has been suggested AcMNPV encodes 10 PIF genes, with PIF1-PIF3 found to form a stable complex with P74 to mediate binding of the ODV to the microvilli of the columnar midgut cells. This fusion with the host cell enables the release of the nucleocapsids into the cytosol (Horton and Burand, 1993; Haas-Stapleton *et al.*, 2004; Slack and Arif, 2006; Braunagel and Summers, 2007).

1.3.2 Transport into the nucleus

On entry into the midgut cells, the nucleocapsids are transported to the nucleus using actin filaments in conjunction with myosin (Figure 1.3). In AcMNPV-infected cells, nucleocapsid motility was shown to be driven by the association of capsid proteins VP78/83 with the host Arp2/3 complex for actin polymerisation (Ohkawa *et al.*, 2010; Au *et al.*, 2013). Nucleocapsids have also been shown to acquire an actin comet tail, which was suggested by the authors to play a role in propulsion (Mueller *et al.*, 2014), however, this was speculative and would warrant further research.

Evidence suggests that for entry to the nucleus, both alphabaculoviruses and betabaculoviruses have evolved different methods of entry. Alphabaculovirus nucleocapsids appear to enter through the remodelling of the nuclear pore complex (NPC) using nuclear localisation signals and import receptors (importin-β) (Ohkawa *et al.*, 2010; Au *et al.*, 2013). This mechanism has evolved to deliver intact nucleocapsids into the nucleus as reviewed by Au *et al*. (2013). In contrast, the nuclear import for betabaculovirus has evolved to eject the genome through the NPC leaving an empty capsid at the cytoplasmic face of the NPC (reviewed by Au *et al*., 2013).

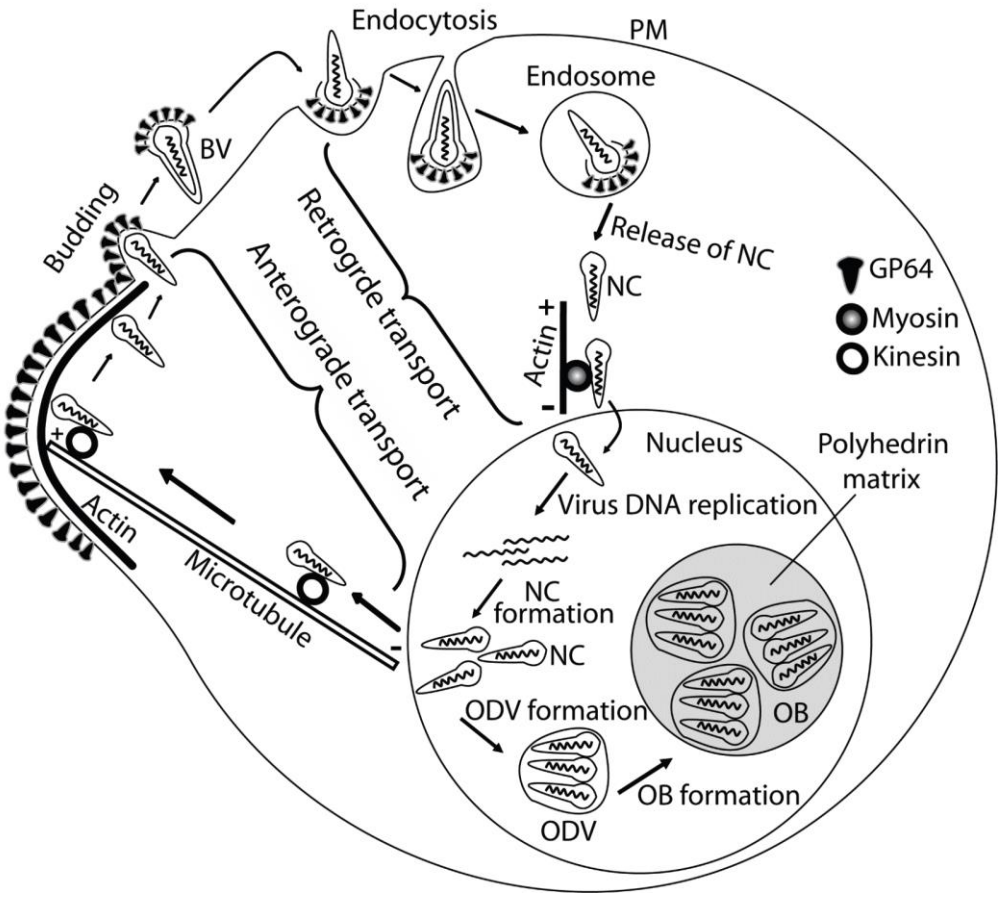

Figure 1.3 Life cycle of Baculovirus Autographa californica multiple nucleopolyhedrovirus (AcMNPV). The AcMNPV produces two virus forms, occlusion body (OB) and occlusion derived virus (ODV). The BV enters the cell following interaction between the BV surface glycoprotein (GP64) and cell surface receptor allowing clathrin-mediated endocytosis. The BV-containing endosome releases the nucleocapsid (NC) into the cytoplasm, which is then transported using actin filaments in conjunction with myosin. Following virus DNA replication in the nucleus, newly formed NC move from the nucleus the cytoplasm and transported using microtubules to the cell surface. The NC bud from the cell gaining an envelope enriched with GP64. During the later phases of infection, NCs retain in the nucleus and are enveloped to form ODV, which are embedded in the forming occlusion bodies (OB). The final stage of the life-cycle involves the release and spread of the OB for new insect hosts. From Possee *et al*. (2010) with permission.

Inside the nucleus the virus genome un-coats (Figure 1.3) and initiates a cascade of virus gene expression, DNA replication and eventual assembly of a new progeny viruses (Granados, 1978; Slack and Arif, 2006). These genes are classified as immediate-early (3 hours post infection (hpi)), delayed early (3 to 6 hpi), late (6-24 hpi) and very late genes (18 to 72 hpi) as reviewed in Miller (1997).

1.3.3 Formation of budded virus for systemic infection of the host

At approximately 12 hpi, there is a concomitant appearance of an electron-translucent ring zone around the virogenic stroma and the presence of newly assembled nucleocapsids (Xeros, 1956). The nucleocapsids form within the cavities of the intrastromal space of the virogenic stroma (Harrap, 1972; Young *et al.*, 1993) and trafficked from the nucleus through the cytoplasm to the cell membrane using the microtubules as shown in Figure 1.3 (Fang *et al.*, 2009; Danquah *et al.*, 2012). The nucleocapsids are transported to the host cell membrane at regions of highly concentrated viral envelope fusion proteins, notably GP64 or F-proteins (Monsma *et al.*, 1996; Westenberg *et al.*, 2004; Slack and Arif, 2006), from which nucleocapsids 'bud out' (Figure 1.1 and 1.3). During the budding process the nucleocapsid acquires a new envelope enriched with fusion proteins (Figure 1.1 and 1.3), allowing for the systematic infection and propagation of the virus (reviewed by Miller, 1997).

The envelope fusion proteins on the BV surface trigger a clathrin-mediated endocytosis, allowing for entry of BV to new cells (Figure 1.3). After uptake into the endosome, acidification of its contents triggers GP64-mediated fusion of the viral and endosomal membrane (Volkman and Goldsmith, 1985; Blissard and Wenz, 1992; Plonsky *et al.*, 1999; Possee *et al.*, 2010). This breakdown of the endosome membrane by fusion with BV envelope releases the nucleocapsids into the cytoplasm for transport to the nucleus (Monsma *et al.*, 1996; Long *et al.*, 2006). The same mechanism for transport, replication and exit of the nucleocapsids from the host is as described earlier for ODV.

1.3.4 The final stages of baculovirus infection: Polyhedra formation

During the final stages of infection, from 16 to 24 hpi the nucleocapsids are retained in the nucleus (Granados and Lawler, 1981), where they become encapsulated by microvesicles to form ODV as described in Section 1.2.1 (Figure 1.1). Within this time frame, post 18 hpi, the very-late expressing protein, polyhedrin, becomes hyper-expressed. As described above, the polyhedrin forms a matrix that crystallizes around the ODV, to form OBs prior to lysis (Figure 1.1 and 1.2).

1.3.5 The final stages of baculovirus infection: host liquefaction and occlusion body dispersal

The final stage of baculovirus infection, after maturation of the polyhedra, is complete liquefaction of the host for the dispersal of polyhedra (Figure 1.1). Prior to this final stage, an interesting event occurs. The extended phenotype of the baculovirus has been shown

to cause hyperactivity and Wipfelkrankheit, translated as “tree-top” disease. This has resulted in the hyperactivity of the virus-infected lepidoptera and their intrinsic movement to the plant top prior to death (Hoover *et al.*, 2011). Specific genes, protein tyrosine phosphatase (ptp) (van Houte *et al.*, 2014a) and ecdysteroid UDP glucosyltransferase (egt) (Hoover *et al.*, 2011) have been attributed to this interesting behaviour. Additionally, studies identified that phototaxis and/or light perception had a direct influence on Spodoptera exigua (Se) MNPV infected-larvae. The infected-larvae were observed prior to liquefaction to be attracted to the position of the light source. The uninfected control larvae were not affected by the light (van Houte *et al.*, 2014b).

1.3.6 Lysis and the role of the auxiliary proteins chitinase, cathepsin and P10

Key auxiliary proteins chitinase, cathepsin and P10 act together to facilitate lysis and the release of OBs from the host (Hawtin *et al.*, 1997; Thomas *et al.*, 1998; Hom and Volkman, 2000).

AcMNPV chitinase, a 58 kDa protein that is detected from 12 hpi and degrades chitin, the main constituent of arthropod exoskeletons (Reviewed in Merzendorfer and Zimoch, 2003). Chitinase catalyses the hydrolysis of β-(1-4)-glycosidic bonds to release glucosamine and *N*-acetylglucosamine for the degradation of chitin (Merzendorfer and Zimoch, 2003). Chitinase and Cathepsin (V-CATH) a viral homolog of lysosomal cysteine protease, cathepsin L have been shown to induce a characteristic liquefaction of baculovirus infected larvae (Slack *et al.*, 1995; Hom and Volkman, 2000). An important stage in the baculovirus lifecycle for the release of the polyhedra from the host. Cadavers from Chitinase and Cathepsin deletion mutants remained ‘intact’ after death suggesting they might work in conjunction with each other (Slack *et al.*, 1995). It is proposed the inactive form of V-CATH accumulates as a proenzyme (proV-CATH), which becomes activated by chitinase to mature V-CATH. The formation of V-CATH thus enables the degradation of the proteinaceous constituents of the larvae (Hom and Volkman, 2000; Daimon *et al.*, 2007).

The functional role of P10 has been of some speculation for many years, but as discussed in Section 1.4.2 has an important role in nuclear lysis in cell culture (Williams *et al.*, 1989; van Oers *et al.*, 1993). The role *in vivo is* less dramatic, with similar *p10*-deletion mutants only delaying the demise and liquefaction by 24 hours (Thomas *et al.*, 1998; Bianchi *et al.*, 2000). It is still of speculation to why the virus would continue to highly express P10, even though it has limited benefit to the virus. However, the continued conservation of this gene

indicates an important role (Reviewed in Carpentier *et al.*, 2008). The role for P10 in this process is discussed in detail in Section 1.4.2.

1.4 The P10 baculovirus protein

1.4.1 A brief history of P10

Early observations of baculovirus-infected cells by transmission EM noted the formation of large fibrous structures in the nucleus and cytoplasm of the host cell during the later phase of infection (Summers and Arnott, 1969; MacKinnon *et al.*, 1974; Knudson and Harrap, 1976; Chung *et al.*, 1980). It was proposed by the authors that these fibrous structures represented the polyhedral protein in its physical state prior to formation of OBs due to the close association with developing polyhedra. It was not until later, with the characterisation of two abundant very-late expressing AcMNPV genes, polyhedrin and a 10-kDa protein, referred to as P10 (Adang and Miller, 1982; Smith *et al.*, 1982; Rohel *et al.*, 1983; Smith *et al.*, 1983c; Kuzio *et al.*, 1984) that these fibrous structures were identified as separate to polyhedral bodies (van der Wilk *et al.*, 1987). This was confirmed by immunogold protein A-gold labelling of P10 and polyhedrin by Van Der Wilk *et al.* (1987), with polyhedrin locating to the OBs and P10 to the fibrous structures.

Following sequencing of the *p10* gene (Kuzio *et al.*, 1984), work characterising the effect of deleting *p10* on infected host cells soon followed (Croizier *et al.*, 1987; Vlak *et al.*, 1988; Williams *et al.*, 1989; van Oers *et al.*, 1993). These mutants resulted in cells that were lacking fibrous structures, failed to lyse and often produced polyhedra containing a fragmented calyx (Vlak *et al.*, 1988; Williams *et al.*, 1989; van Oers *et al.*, 1993).

Further examination of the P10 structures was made possible with immunolabelling and fluorescence microscopy. Using a polyclonal anti-P10 antibody, a complex network of filaments was observed (Quant-Russell *et al.*, 1987; Volkman and Zaal, 1990; Alaoui-Ismaili and Richardson, 1998; Patmanidi *et al.*, 2003; Carpentier *et al.*, 2008). From observing P10 structures at different time points, it was noted P10 formed both thin cytoskeletal-like filamentous structures in the cytoplasm from 24-48 hpi and thicker perinuclear structures during the later phases of infection (Patmanidi *et al.*, 2003; Carpentier *et al.*, 2008) as shown in Figure 1.4, A. Nuclear P10 was further seen to localise to the nucleus forming a worm like feature (Figure 1.4, B).

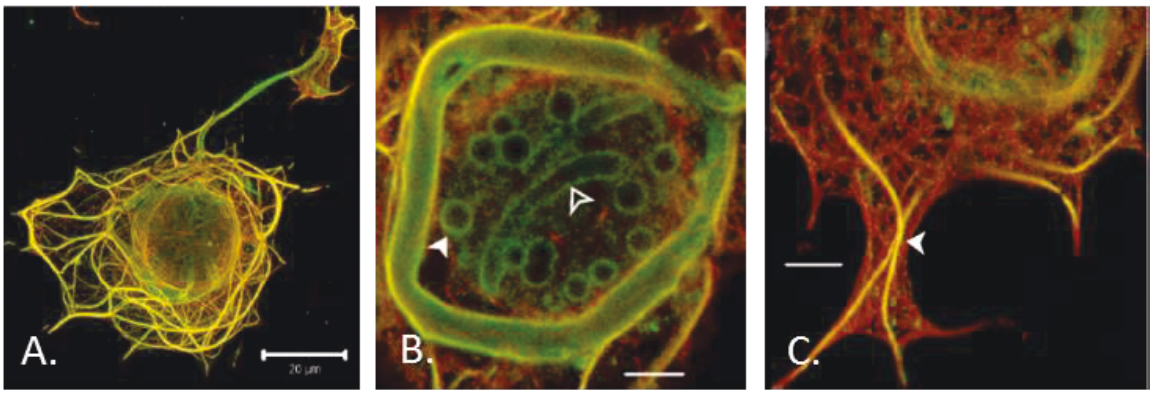

Figure 1.4 Immuno-fluorescent labelling of P10 and microtubule structures in Autographa californica multiple nucleopolyhedrosis virus-infected TN-368 cells. The two structural features of the P10 (A) shows the filamentous and tubular structures. (B) Image of the perinuclear P10 tubular structure, whilst also displaying (arrow) other P10 associated structures. The filled arrow points to circular bodies that are seen to encapsulating the polyhedra (when visualised by light microscopy) and the open arrows highlight tubular P10. (C) Represents a colocalisation between P10 filaments and thickened microtubules. Images with permission from Carpentier *et al*. (2008). Scale bars for A is 20 µm and B & C is 5 µm.

1.4.2 Multifunctional roles of P10

Even though it has become widely accepted that P10 contributes to polyhedra formation, nuclear stability and lysis (van der Wilk *et al.*, 1987; Vlak *et al.*, 1988; Williams *et al.*, 1989; Russell *et al.*, 1991; van Oers *et al.*, 1993; Gross *et al.*, 1994; van Oers and Vlak, 1997; Patmanidi *et al.*, 2003; Carpentier *et al.*, 2008; Carpentier and King, 2009), the mechanisms underlying these roles have remained a mystery.

1.4.3 The role of P10 in lysis

As briefly described earlier, host liquefaction is a common feature during the final stages of the baculovirus life cycle and a number of early papers have suggested that P10 plays a functional role in this process (Williams *et al.*, 1989; van Oers *et al.*, 1993; van Oers *et al.*, 1994; van Oers *et al.*, 1998). This was confirmed in early studies characterising P10, where recombinant AcMNPV-infected Sf21 cells containing a truncated *p10* mutant (Ac231), failed to lyse (Williams *et al*., 1989). It was observed from TEM images of Ac231-infected cells that associated P10 structures also failed to form. It was proposed that a stepwise exhaustion of the nuclear membrane by P10 structures could lead to rupturing of the nucleus, escalated by increased internal pressure from the accumulation of polyhedra and P10 fibrous structures (Williams *et al.*, 1989).

Similar to observations made by Williams *et al*. (1989), later studies by van Oers *et al*. (1993) also confirmed a role for P10 in nuclear lysis. This study characterised P10 by using a variety of *p10* deletions; a *p10* deletion vector 'pAcAS3' (Vlak *et al.*, 1990) that contained complete deletion of *p10* coding sequence and a set of truncated *p10* recombinant viruses. These truncations contained deletions made to the carboxy-terminal (8, 15 and 42 aa) (van Oers *et al.*, 1993). It was shown with deletions of more than 42 aa that P10 failed to facilitate nuclear lysis and polyhedra retained inside the cell nucleus (van Oers *et al.*, 1993). However, contradictory to Williams *et al*. (1989), the theory for the role of P10 structures in lysis was not supported. It was observed with a 15 aa truncated P10, nuclear lysis was present, even though P10 failed to assemble into fibrillar bodies (van Oers *et al.*, 1993; van Oers and Vlak, 1997). This suggests that the aggregation of P10 into cytoplasmic and nuclear P10 fibrous bodies do not play a role in lysis.

Interestingly, a more recent study by Dong *et al*. (2005; 2007) with similar deletions to the C-terminus to van Oers *et al*. (1993) showed that P10 continued to form fibrous like structures (Figure 1.4), as confirmed by confocal analysis and TEM. It is thus apparent that the range of characterisation work on P10 and different approaches to creating deletion viruses has yielded conflicting results.

1.4.4 Functional role in Polyhedra maturation

It has often been reported that P10 fibrous structures share a close association between EDS and polyhedra (Hess and Falcon, 1978; Russell and Rohrmann, 1990; Lee *et al.*, 1996). TEM images of baculovirus infected cells (Figure 1.5) have shown in the presence of nuclear P10 fibrous bodies, EDS are seen to protrude off P10 and often wrap/form around polyhedra (Summers and Arnott, 1969; MacKinnon *et al.*, 1974; Chung *et al.*, 1980).

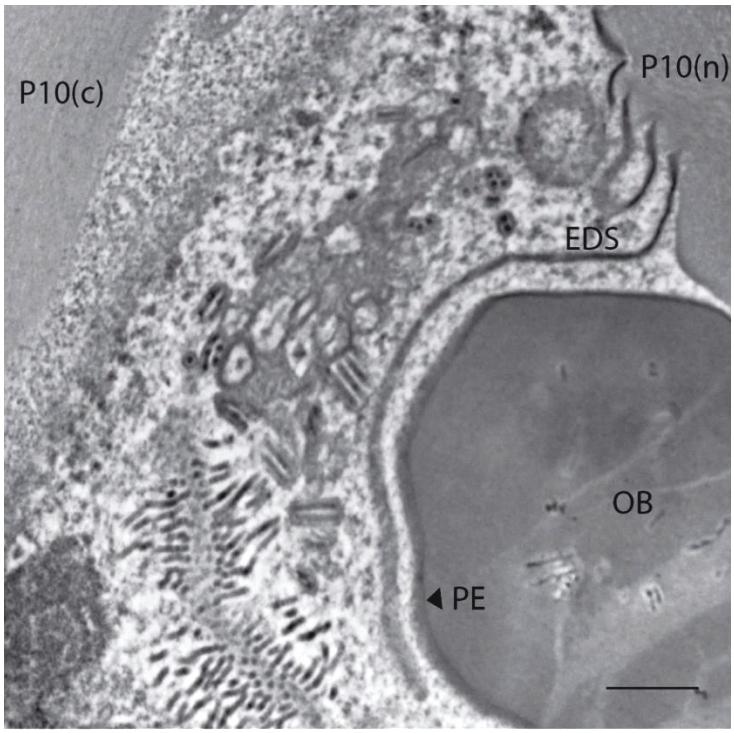

Figure 1.5 Transmission electron microscopy of EDS forming around polyhedra at 72 hpi. Electron micrograph of Autographa californica multiple nucleopolyhedrosis virus-infected TN-368 cells harvested at 72 hpi. The electron dense spacers (EDS) are seen in close association with nuclear (n) P10 and occlusion body (OB) and show a similar composition to the polyhedral envelope (PE) indicated by the arrow. The EDS was not seen in association with cytoplasmic (c) P10. Scale bar, 500nm.

This close association was first discussed in some detail by Summers *et al*. (1969), who observed thin dark dense lines presenting around P10 structures and polyhedra as shown in Figure 1.5, labelling them 'membrane like' profiles. It has since been recorded as 'cisternae' or 'condensed fibrous sheets; but recent terminology favours calling them EDS (Summers and Arnott, 1969; MacKinnon *et al.*, 1974; Knudson and Harrap, 1976; Hess and Falcon, 1978; Chung *et al.*, 1980).

It was speculated that the EDS play a functional role in polyhedra maturation and are a precursor to polyhedra maturation, which was noted due to the close association of the EDS and polyhedra (Summers and Arnott, 1969). Later TEM observations of polyhedra also commented on the similarities between the EDS and calyx, going on to suggest the spacers were closely involved in the formation of the PE (MacKinnon *et al.*, 1974; Hess and Falcon, 1978; Minion *et al.*, 1979; Chung *et al.*, 1980). It was first suggested by Summers *et al*. (1969) and Mackinnon *et al*. (1974) that the PE was a result of the EDS directly associating with the polyhedra. However, a later paper by Hess *et al*. (1978) disputed this theory, noting a consistent gap always remained between the EDS and the polyhedra. The authors suggested the formation of the calyx resulted from the condensing and compression of EDS around the polyhedra (Hess and Falcon, 1978).

Immunoelectron microscopy studies of the PE (van Lent *et al.*, 1990; Russell *et al.*, 1991; Lee *et al.*, 1996) found a progressive continuity between P10 fibrous structures, EDS and the developing PE. These structures were observed to bind to *p10* and calyx antibodies, suggesting a similar composition and function (Gross *et al.*, 1994). Further studies characterising the relationship between P10, EDS and polyhedra, found *p10* gene deletion mutants retained the ability to form EDS (Croizier *et al.*, 1987; Vlak *et al.*, 1988; Williams *et al.*, 1989; van Oers *et al.*, 1993). The absence of P10 resulted in a fragmented or an absent PE structure (Vlak *et al.*, 1988; van Lent *et al.*, 1990). The polyhedra were often recorded with irregular shapes (Williams *et al.*, 1989) and a rough pitted surface (Figure 1.6) (Gross *et al.*, 1994; van Oers and Vlak, 1997). It should be noted that imaged polyhedra from all variations of *p10* deletions in the study by van Oers *et al*. (1993) and reviewed by van Oers and Vlak (1997) formed a complete PE, however it is unclear if detailed SEM observations were used to confirm the presence of the calyx .

As P10 has been shown to play an intimate role in calyx formation (Vlak *et al.*, 1988; Gross *et al.*, 1994), it was proposed that P10 contains a binding site for EDS and its association with polyhedra, to facilitate maturation of the calyx (van Oers and Vlak, 1997). Further evidence of this association was provided from TEM images of P10 minus viruses, where EDS were observed, but were shown to wrap onto themselves rather than around polyhedral bodies (Williams *et al.*, 1989; van Oers *et al.*, 1993). This is similar to results observed with a AcMNPV-polyhedrin deletion mutant, which in the absence of polyhedra, displayed unassociated EDS wrapped onto itself (Lee *et al.*, 1996).

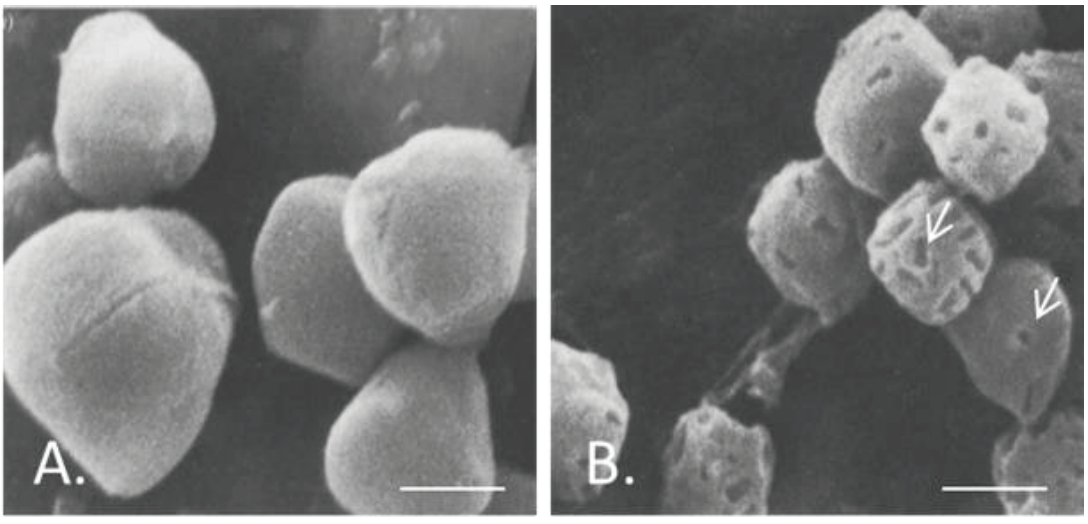

Figure 1.6 SEM of polyhedra from wild-type and mutant *p10*-deletion virus. A) Polyhedra extracted by sonication from Orgyia pseudotsugata multiple nuclepolyhedrovirus (OpMNPV) exhibited a smooth surface. B) Polyhedra extracted from OpMNPV mutant that lacks *p10,* displays a fragmented and incomplete polyhedral envelope. Arrows show pitted surface on polyhedra that appear to result from loss of virion bundles. Scale bar represents 1µm. Images from Gross *et al*. (1994) with permission.

1.4.5 The role of P10 in nuclear stability

Early immuno-fluorescence studies on the P10 homologue of OpMNPV, a virus closely related to AcMNPV, demonstrated that by 36 hpi, P10 formed cytoplasmic filaments that matured into a continuous network of thick rod-shaped structures (Quant-Russell *et al.*, 1987). Later studies on AcMNPV, using an anti-tubulin and *p10* antibody, found P10 structures might facilitate crosslinking with microtubules for reorganisation of the cytoskeleton for increased stability (Patmanidi *et al.*, 2003; Carpentier *et al.*, 2008), with P10 associated filaments causing a distinct thickening effect (Volkman and Zaal, 1990). Supporting evidence for this association was provided by both antibody pulldown and yeast two-hybrid experiment showing an interaction between P10 with host-cell tubulin (Patmanidi *et al.*, 2003). More recent studies by Carpentier *et al.* (2008) highlighted that P10 forms as two distinct cytoskeletal structures, with early structures forming filaments that link with the cytoskeleton. Depolymerisation of the microtubule network with colchicine prevented the formation of P10 filaments, however it was noted that the later thick-tubules continued to form (Volkman and Zaal, 1990; Carpentier *et al.*, 2008).

The thicker cytoplasmic P10 tubules found from 48 hpi did not colocalise with tubulin, or show reorganisation of the microtubules (Carpentier *et al.*, 2008). Instead, the tubular structures form a perinuclear cage that encapsulates the nucleus during infection. This close association of P10 around the nucleus is attributed to stabilising the nucleus, preventing nuclear disruption and early release of the polyhedra, thus allowing maturation of the polyhedra (Carpentier *et al.*, 2008).

1.4.6 The structural domains of P10

The functional roles described above have often been associated with the structural domains of P10, which through multiple sequence alignment, proteomic prediction and previous P10 deletion work, revealed three distinct regions. This includes an amino-terminal coiled-coil domain and variable domain (Figure 1.7) that consists of a proline rich and carboxyl terminal positive basic region, as reviewed in van Oers *et al*. (1997) and Carpentier and King (2009).

The P10 coiled-coil region (Figure 1.7), recognisable from the α-helical protein chains (Crick, 1952; Crick, 1953) and improved predictions from protein sequences, identifies that the more highly conserved P10 amino-terminal region forms a helical structure (Wilson *et al.*, 1995; Carpentier *et al.*, 2008). This is achieved by a group of seven aa's containing small hydrophobic residues (leucine, isoleucine and valine and to a lesser

extent methionine and alanine) at the first and fourth aa position (Lupas *et al.*, 1991; Cohen and Parry, 1994; Carpentier and King, 2009) as highlighted in Figure 1.7. Characterisation of this domain highlighted seven heptad repeat motifs for alphabaculovirus type one (Figure 1.7, coiled-coil domain) and eight to eleven heptad repeat motifs for alphabaculovirus type two (Wilson *et al.*, 1995; Carpentier *et al.*, 2008).

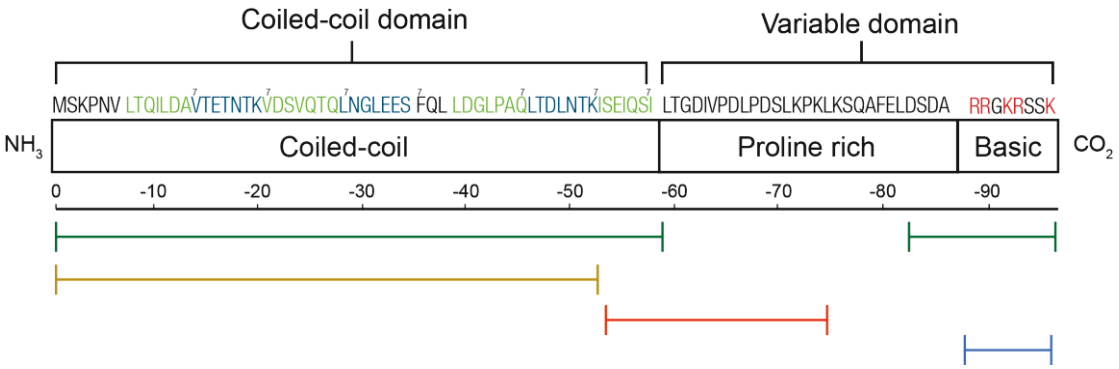

Figure 1.7 Schematic representation of P10 domains for the Autographa californica multiple nucleopolyhedrosis virus amino acid sequence. P10 is separated into three groups: coiled-coil, proline-rich and basic, which forms two domains. These domains have been separated based on the characteristic features of the P10 sequence. The amino acid sequence for P10 is represented, with heptad repeats (1-7) represented by amino acid residues highlighted with alternating green and blue colours. The red residues, R: Arginine and K:Lysine, represent the positive charged basic region. The coloured bars represent a specific function for the representative amino acid sequence. Green: aggregation and formation of P10 filament, Yellow: nuclear localisation, Red: disintegration of the nuclei lysis, Blue: microtubule binding domain.

1.4.7 The coiled-coil and variable domain

Coiled-coil

The coiled-coil domain has shown to be necessary for the aggregation and formation of the P10 fibrous bodies in both *Helicoverpa armigera* (Hear) NPV (Dong *et al.*, 2005) and AcMNPV (Dong *et al.*, 2007). Deletions made in the coiled-coil sequence, HearNPV (pN60-GFP) or AcMNPV (pAcP10$_{\Delta 52\text{-}94}$), observed that P10 failed to assemble into the characteristic filamentous P10 structures (Figure 1.4), giving evidence for the coiled-coil domain in filament formation (Figure 1.7, Green).

Earlier studies by van Oers *et al.* (1993) further indicated the coiled-coil domain was important for P10 formation, with deletions made to the P10 amino-terminus absent of a detectable P10 by immunogold-labelled sections. It was further proposed this domain was important for the supramolecular organisation of P10 molecules.

Another possible function attributed to the coiled-coil domain is a site for nuclear localisation (Figure 1.7: Yellow). In a study by Vlak *et al*. (1988), partial P10 deletions

fused with *lacZ*, caused intranuclear accumulation of large *lacZ* granular structures at sites corresponding to P10 fibrillar bodies of wildtype (WT) infections (Vlak *et al.*, 1988).

Variable domain

Studies by van Oers *et al.* (1993) identified that deletions made to the variable domain, also failed to assemble into fibrous bodies, suggesting that the variable domain might also be important in P10 filament formation (Figure 1.7, Green). This was in contrast to Dong *et al*. (2004; 2007), with similar P10 deletion mutants (pN66-GFP and pAcP10$_{\Delta 65\text{-}94}$) still shown to assemble into P10 structures (Figure 1.7). However, it should be noted that Van Oers *et al*. (2003) used recombinant viruses in their studies, rather than plasmid transfections used in the Dong *et al*. (2004; 2007) studies. Therefore, the authors could not rule out the possibility that the results might be different with viral infection and proposed that additional viral proteins might bind to the C-terminal for P10 filament formation (Dong *et al.*, 2007).

Bioinformatic analyses of P10 homologues (Figure 4.1) have also identified that the P10 variable domain contains a common positively-charged basic domain (Figure 1.7) that is recognised as a microtubule binding domain (van Oers and Vlak, 1997; Patmanidi *et al.*, 2003; Carpentier and King, 2009). The positively-charged basic domain resembles a microtubule interacting region of other microtubule associated proteins (MAP) and has been closely compared to MAP2 and MAP4 and Tau and (Cheley *et al.*, 1992; Carpentier and King, 2009) (Figure 1.7: Blue). A definitive site for microtubule binding has yet to be confirmed.

Even though a specific role for the proline rich region has not been determined, it has been linked to nuclear lysis (van Oers *et al.*, 1993). It was shown that *p10* deletion recombinant viruses, lacking up to 15 aa from the carboxy-terminal, continued to lyse, whereas deletions of more than 52 aa failed to lyse (Figure 1.7, Red). This led the authors to propose that the sequence between 52 and 79 aa was involved in the disintegration of the nuclei (van Oers *et al.*, 1993; van Oers and Vlak, 1997).

1.5 Addressing current research

P10 is a multi-functional protein with various roles during infection. Previous research on P10 often used mutants in which P10 was not at its natural locus, contained an incomplete *p10* deletion sequence or contained additional gene deletions as discussed in detail in Chapter Three. The limitation of these approaches has been that any observed

differences to the WT virus could not unambiguously be attributed to P10. Thus to truly uncover the functional roles for P10 these problems need to be addressed.

1.6 Aims of project

This work aimed to address contrasting reports on P10 function. By re-examining historical approaches with recent advances in biochemical, sequencing and microscopy techniques, a greater understanding of P10 will be possible.

My project was primarily based on using an AcMNPV novel mutant in which *p10* was deleted from the virus genome and variants of *p10* were introduced into the virus genome at the natural locus, in what is otherwise a 'wild-type' virus genome. This ensured any observed effects could be directly attributed to the *p10* deletion or *p10* variant.

The aims presented below were established to develop our current understanding of P10 and its role in baculovirus infection with the hope of discovering the mysterious nature of this unique and small protein.

1) **To study the functional role of P10 during baculovirus infection of an insect cell**

- Study the impact of a P10-minus virus
- Is *p10* functional role species-specific?

2) **To better understand the P10 promoter**

- Why is P10 modulated by such a strong promoter?
- Is function related to expression levels?

3) **To better understand the formation of P10 and other AcMNPV viral structures**

- Can 3-Dimensional AcMNPV structures be studied using serial block facing scanning electron microscopy?
- How do P10 structures develop during the later phases of AcMNPV-infected cells?
- Can these structures provide an insight into their functional role during infection?

Chapter Two:
Materials and Methods

2.1 Bioinformatics

2.1.1 Baculovirus sequences

The protein sequences used in the bioinformatics study were obtained from a protein BLAST search of the National Centre for Biotechnology Information (NCBI) for gene homologues encoding the target protein P10.

2.1.2 Multiple sequence alignments, protein pattern and phylogenetic studies

Amino acid sequences were aligned using either the T-Coffee multiple sequence alignment program or Clustal Omega software hosted by the European Bioinformatics Institute, which is part of the European Molecular Biology Laboratory. T-Coffee used a neighbour-joining tree with default parameters with an aligned order. Additional phylogenetic tree reconstructions used T-rex. This software used a neighbour-joining method with a bootstrap value of 1000.

More detailed analysis on protein sequences used the software PredictProtein from Biosof LLC and COILS (Lupas *et al.*, 1991) as hosted by export protein analysis system (ExPASy) bioinformatics resource portal. A protein search for phylogenetic tree reconstructions was chosen as it provided a more sensitive and reliable search than using DNA alignments. DNA searches have also shown to have a 5-10 fold shorter evolutionary look-back time (Pearson, 2013).

2.2 Materials

2.2.1 Chemicals

General reagents and chemicals were purchased from the following companies unless stated otherwise: BDH Chemicals Ltd, Fisher Scientific, Sigma-Aldrich, Invitrogen, New England Biolabs, Fermentas or Promega. Sterilisation was performed by autoclaving at 15 pounds per square inch (p.s.i.) or by filtration through 0.45 or 0.2 μm filters. Milli-Q ultrapure (>18 mega ohms) water was used.

2.3 Cells, plasmids and viruses

2.3.1 Cultured cell lines

The experiments described in this thesis utilised cell lines derived from *Spodoptera frugiperda* (Sf): Sf9 (reviewed in Wickham *et al.*, 1992) and Sf21 (Vaughn *et al.*, 1977) and *Trichoplusia ni* (T.ni): High Five™ (Wickham *et al.*, 1992) and TN-368 (Hink, 1970). The cell cultures were all maintained at 28ºC in cell-line specific medium (Table 2.1). Sf21, Sf9 and High Five™ cells were sub-cultured in suspension cultures and TN-368 was maintained as adherent cultures. Cells were monitored regularly and every 2-4 days a small sample was taking for counting to determine cell viability. Cells were passaged to maintain them in a log-phase and prevent them reaching the stationary phase. The cells were passaged by seeding fresh media with an appropriate number of cells (Table 2.1).

Table 2.1 Insect cell culture

Cell line	Type	Medium	(Max Density) Seeding density	Source
Sf21	Spinner culture (80-90 rpm)	TC-100 insect medium (with 10% (v/v) fetal calf serum (Gibco))	(1-2x10^6 cells/ml) 2-3x10^5 cells/ml	R.D. Possee (OET Ltd.)
Sf9	Shake culture (135 rpm)	Insectagro Sf9 (Corning®) or ESF 921 Serum-free media (Expression Systems™)	(3-8x10^6cells/ml) 4-5x10^5 cells/ml	Invitrogen™
High Five™	Shake culture (135 rpm)	EX-CELL® 405 Serum-free media (Sigma-Aldrich®) or ESF 921® Serum-free media (Expression Systems™)	(3-6x10^6cells/ml) 2-3x10^5 cells/ml	Invitrogen™
TN-368	Adherent	TC-100 insect medium with 10% (v/v) fetal calf serum (Gibco)	(At confluence) 1:10 ratio	R.D. Possee (OET Ltd.)

2.3.2 Plasmids and viruses

All the viruses and plasmids stocks used or generated in this study are presented in Table 2.2. Viruses and plasmids have been categorised dependant on modifications at the *p10* locus. For storage of these stocks, plasmids were kept at -20ºC and viruses, containing 5% v/v FCS (foetal calf serum) at 4ºC. For long term storage, viruses containing 5% v/v FCS were kept at -80ºC.

Table 2.2 Plasmids and viruses used in this thesis

Plasmid	Virus	Modification at *p10* locus	Notes
pAcUW1	N/A	Partial deletion	Supplied by R.D. Possee (OET Ltd.) for construction of plasmids
pCH110	N/A	N/A	Supplied by R.D. Possee (OET Ltd.) for excision of *lacZ*
AcMNPV Controls (Chapter Three – Chapter Six)			
N/A	AcMNPV(WT)	Wildtype ACMNPV	Wild-type virus used as a positive control
pAcLG1_P10	Ac_P10^{Rescue}	Complete *p10* coding region	Rescue mutant to ensure reintroduction of *p10* restores phenotype
***p10* deletions (Chapter Three – Chapter Five)**			
pAcLG1_*lacZ*	Ac∆*p10_lacZ*	Replace *p10* with *lacZ* cassette	To introduce selectable marker in core virus to create other variants
pAcLG1	Ac∆*p10*	*p10* deletion	Complete *p10* deletion mutant with no other variants as *lacZ* has shown to cause additional effects during infection.
SfMNPV viruses (Chapter Four)			
N/A	SfMNPV	Wildtype SfMNPV	Wild-type virus used as a positive control
pAc_Sf*p10*	Ac_Sf*p10*	Addition of SfMNPV *p10*	Examine an alternative Alphabaculovirus P10 protein in AcMNPV backbone
***p10* promoter truncations (Chapter Five)**			
pAc_P10^{Control}	Ac∆P10_P10^{control}	Promoter rescue control	Promoter Control plasmid
pAc_P10^{Prl-4}	Ac∆P10_P10^{Prl-4}	4 bp promoter deletion	Test effect of promoter truncation on P10 expression
pAc_P10^{Prl-8}	Ac∆P10_P10^{Prl-8}	8 bp promoter deletion	Test effect of promoter truncation on P10 expression
pAc_P10^{Prl-12}	Ac∆P10_P10^{Prl-12}	12 bp promoter deletion	Test effect of promoter truncation on P10 expression
pAc_P10^{Prl-16}	Ac∆P10_P10^{Prl-16}	16 bp promoter deletion	Test effect of promoter truncation on P10 expression
pAc_P10^{Prl-20}	Ac∆P10_P10^{Prl-20}	20 bp promoter deletion	Test effect of promoter truncation on P10 expression
pAc_P10^{Prl-30}	Ac∆P10_P10^{Prl-30}	30 bp promoter deletion	Test effect of promoter truncation on P10 expression
pAc_P10^{Prl-40}	Ac∆P10_P10^{Prl-40}	40 bp promoter deletion	Test effect of promoter truncation on P10 expression
pAc_P10^{Prl-50}	Ac∆P10_P10^{Prl-50}	50 bp promoter deletion	Test effect of promoter truncation on P10 expression
pAc_P10^{Prl-60}	Ac∆P10_P10^{Prl-60}	60 bp promoter deletion	Test effect of promoter truncation on P10 expression

2.3.3 Virus amplification

Virus stocks were amplified in Sf9 cells using the method described by King and Possee (1992). Sf9 cells were seeded at a density of 1.5 – 2 x10^6 cells/ml in a shake culture. The cells were infected with the virus at a multiplicity of infection (MOI) of 0.1 pfu/cell and incubated for 4-5 days at 28°C on a shaking platform. A small aliquot was taken to check all cells displayed cytopathic effects before harvesting the cell suspension. Following centrifugation at 4000rpm for 15 minutes at 4°C (TY-JS 4.2 rotor, J6-MI Beckman centrifuge) to remove cells, the clarified culture medium containing budded virus was stored in aliquots at 4°C. The viruses were stored at 4°C in the dark in the presence of 2-5% v/v FCS. For longer-term storage small aliquots in the presence of 5% v/v FCS were stored at -80ºC.

2.3.3a Small scale infection of cultured cells

Sf21, Sf9, *T.ni* Hi5 or TN-368 cells were seeded at relevant dilution (stated in text) for 6- and 12-well dishes and left 1-2 hours for cells to adhere to the surface. The virus inoculum was diluted in relevant media to the appropriate MOI (pfu/cell). The cell medium was removed and replaced with 100µl of relevant virus dilution. The inoculated cells were left on a rocker for one hour at room temperature (RT). After the incubation, the virus overlay was removed and replaced with either 1ml (12-well dish) or 2ml (35mm/6-well dish) of cell culture media. The cells were incubated at 28°C for the desired time until harvest or imaging.

2.3.4 Co-transfection of insect cells to derive recombinant viruses

2.3.4a Lipofectin reagent

Insect cells were transfected with DNA using a liposome-mediated transfection reagent, Lipofectin® (Invitrogen) to generate recombinant viruses. Sf9 cells were seeded at 1x10^6 cells/35mm dish and incubated at 28°C for 2 hours. During incubation, a transfection master mix was made in two separate 7ml bijoux tubes each containing 0.5ml of serum-free TC100 media. In one bijoux, 5µl of lipofectin® was added and incubated for five minutes at RT. In the other bijoux, 100ng of linearised virus DNA and 500ng of transfer plasmid DNA as quantified by NanoVue™ spectrophotometer (GE Healthcare), was added. After incubation, the contents of the two bijoux were combined and incubated for a further 20 minutes at RT, allowing liposome complexes to form. The cell culture media was then removed and the DNA/liposome complex was immediately added to the dish,

and incubated for either five hours or overnight at 28°C. An additional 1ml of appropriate growth media, containing penicillin-streptomycin (Penstrep) mixture (200U/ml, Gibco®), was added to the cells and then incubated for a further four days at 28°C. After 5 days incubation, the cell media containing budded viruses was harvested and stored at 4°C.

2.3.4b TransIT-LT1 transfection reagent

An alternative method for transfection, using TransIT®-LT1 (Mirus®) transfection reagent followed the manufacturer's instructions. Sf9 cells were seeded at $1x10^6$ cells/35mm dish and incubated at 28°C for 2 hours. During the cell incubation, a transfection mix was prepared containing 100 ng of linearised virus DNA and 500ng of plasmid diluted with 100µl of serum-free media. Then, 1µl of TransIT® transfection reagent was added to the media, gently mixed, and incubated for 15-20 minutes at RT to enable DNA complexes to form. Prior to addition of the transfection mixture, 1ml of media was removed from the dishes of cells then the total mixture was added to the cells. The final incubation and harvest of budded virus is as described in Section 2.3.4a.

2.3.5 Titration of virus stocks

Virus stocks were titrated using either a standard plaque-assay, $TCID_{50}$ or a qPCR-based titration system, *baculo*QUANT™ (Oxford Expression Technologies Ltd, (Hitchman *et al.*, 2007)).

2.3.5a Plaque-assay titration

Baculoviruses stocks were titrated as described by King and Possee (1992). Sf21 cells were seeded in six-well or twelve-well dishes at $1.4x10^6$ cells/well or $0.5x10^6$ cells/well, respectively. The virus to be titrated was diluted in TC100 containing 10% v/v FCS in ten-fold dilution with media. The cell medium was removed and replaced with 100µl of relevant virus dilution. The inoculated cells were left on a rocker for one hour at RT. After the incubation, the virus overlay was removed and replaced with either 1ml (12-well dish) or 2ml (35mm/6-well dish) of 1% w/v low-gelling temperature agarose (LGT, Lonza) (1:1 of 2% w/v LGT and TC100 10% v/v FCS). Once solidified, an additional 1ml liquid overlay of TC100 10% v/v FCS was added and the cells incubated at 28°C.

After 3 - 5 dpi, the cells were stained with 1ml of neutral red for 4–18 hours to visualise plaques. The neutral red working solution was made by diluting the stock solution (0.5% w/v) 1:20 with phosphate buffered saline solution (PBS, 0.14 M NaCl, 0.01 M PO_4 Buffer, 0.003 M KCl). After incubation, the neutral red solution was removed, and the cells were stored at RT until plaques were identifiable for counting.

2.3.5b BaculoQUANT™ qPCR

BaculoQUANT™ titration by qPCR was carried out on an Applied Bio systems 7500 Real-Time PCR following the supplier's instructions. In a sterile environment, a serial log (1 in 10) dilution of a known virus standard (~$1x10^8$ pfu/ml) was created in RNase-free water. Aliquots of 90µl water were pipetted into PCR tubes with 10µl of the virus standard to the first PCR tube ($1x10^7$ pfu/ml) and vortexed. After mixing 10µl was then taken from the diluted virus and placed into the next PCR tube to make ($1x10^6$ pfu/ml) and vortexed. The virus standard was diluted down to ($1x10^3$ pfu/ml). After completion of the dilution series, 80µl of each dilution was aliquoted into a fresh PCR tube. An additional aliquot of 80µl was taken from all virus inoculum to be tested and pipetted into separate PCR tubes. The PCR tubes were centrifuged for five minutes at 13,000 rpm to pellet the budded virus. The pellet was re-suspended in 20µl of DLS6 lysis buffer and placed into a SureCycler 8800 thermal cycler and a pre-set lysis program was run (Table 2.3). After incubation in the lysis buffer, the sample was stored overnight at -20°C or directly used for qPCR titration.

Table 2.3 Thermal cycler conditions for virus lysis

Step	Temperature	Duration (minutes)
1	65°C	15
2	96°C	2
3	65°C	4
4	96°C	1
5	65°C	1
6	96°C	0.5
7	20°C	Hold

For the qPCR, an initial master mix was made of 23µl per sample; this included qPCR Low ROX mix (12.5µl), RNase free water (7.5µl), SensiFAST™ lo-ROX probe (Bioline) and a forward and reverse primer (1µl each), as supplied in baculoQUANT™ virus titration kit (OET Ltd). A total of 23µl master mix was aliquoted into wells of a 96-well PCR plate with either 2µl of control or sample viral DNA added to triplicate wells containing master mix. A negative control of water, instead of viral DNA was used. The plate was then sealed and briefly centrifuged. Samples were then run on the Applied Bio-systems 7500

Real-Time PCR machine following supplier's instructions for fluorescent dyes (6FAM and TAMRA) and cycling conditions (Table 2.4).

Table 2.4 Applied Bio-systems 7500 Real-Time PCR cycling conditions

Step	Temperature	Duration	Cycles
Enzyme activation	95°C	10 Minutes	1
Denaturation	95°C	15 Seconds	40
Annealing	60°C	60 Seconds	40

2.3.6 Purification of recombinant viruses by plaque assay

Purification of recombinant viruses by plaque-assay was performed as described by King and Possee (1992). The virus was titrated in 6- or 12-well dishes as described for plaque titration (Method 2.3.5a) with dilutions plated from neat to 10^{-6}. After 3 - 5 dpi, 15µl/ml of 4% w/v X-gal (5-Bromo-4-chloro-3-indolyl β-D-galactopyranoside) in dimethylformamide (DMF) was added to 1:20 PBS diluted neutral red from 0.5% w/v stock solution. This mix was added to each well and incubated for 4–18 hours for the development of plaques. After incubation, the liquid was removed and the plaques left at RT. After incubation, the plaques were either clear or blue due to β-galactosidase expression from *lacZ*. Agar plugs were then selected according to presence or absence of colour as necessary, using sterilised glass Pasteur pipettes. The budded virus within the agar plugs was dispersed in 200-300µl TC100/10% v/v FCS media and used to re-plaque purify the virus until all plaques were either clear (absence of *lacZ*) or all blue (presence of *lacZ)*. Budded virus within the final plaque-pick was amplified by infecting Sf9 cells at $1x10^6$ cells per dish in a 35 mm dish. This virus stock (PO) was harvested and used to generate subsequent viral stocks (P1 and P2) as described in section 2.3.3.

2.3.7 Purification of Baculovirus DNA via caesium chloride density gradients

Purification of large quantities of baculovirus DNA was achieved by using caesium chloride density gradients as described in King and Possee (1992). A 400 ml culture of Sf9 cells seeded at a density of $2x10^6$ cells/ml was infected with virus at an MOI of 0.1 pfu/cell. After 4-6 days, when all cells expressed a cytopathic effect, the cell culture was centrifuged at 4,000 rpm for 15 minutes at 4ºC (TY-JS 4.2 rotor, J6-MI Beckman centrifuge) to remove cell debris. The clarified culture medium was centrifuged at 24,000 rpm for 1 hour (Ti-70 4.2 fixed angle rotor, Optima LE-80K Beckman Ultracentrifuge) to

pellet the BV. The pellet was incubated overnight at 4ºC with the addition of 2ml of 1X TE buffer (10mM Tris.Cl, pH 8.0, 1 mM EDTA) to aid resuspension of the BV.

The BV was gently resuspended and the 2 ml was loaded onto a 10%-50% (w/v) discontinuous sucrose gradient, with a liquid paraffin overlay. After centrifugation at 24,000 rpm for 1 hour at 4ºC, the BV-containing band was retrieved and diluted with 10 volumes of 1X TE buffer. This was then centrifuged at 24,000 rpm for 1 hour at 4ºC to pellet the purified BV, which was re-suspended in 1ml 1X TE buffer.

The purified BV were lysed with the addition of sarkosyl (final concentration of 4% w/v) with a 30 minute incubation at 60ºC. The sample was layered onto 5ml of 50% w/w caesium chloride in TE buffer, containing 0.5 µg/ml ethidium bromide. An overlay of liquid paraffin was added to seal the tube. The samples were centrifuged at 35,000 rpm for 1 hour at 20ºC and the viral genomic DNA band was harvested. Ethidium bromide was removed by addition of water-saturated butanol and the upper phase was removed. The virus DNA was dialysed in a 2 litre beaker against 500ml TE, stirring constantly at 4ºC in the dark for 2-4 days, replacing the TE every 24 hours. The resulting DNA was stored at 4ºC protected from the light. The quality and concentration of DNA was determined by restriction enzyme analysis and spectrophotometric measurements on a NanoVue™.

2.3.8 Purification of baculovirus DNA via column extraction

Where less pure DNA was required, virus DNA was extracted from 35mm dishes of infected cells using a DNeasy® spin column, as described by the manufacture (Qiagen®)

2.4 Bacterial Methods

2.4.1 Competent cells

Bacterial cell lines used for the amplification and production of plasmid DNA are referred to in Table 2.5.

Table 2.5 Competent cell lines for transformation

Bacteria name	Strain
DH5α	F- endA1 glnV44 thi-1 recA1 relA1 gyrA96 deoR nupG Φ80d*lacZ*ΔM15Δ(*lacZYA-argF*)U169, hsdR17(rK- mK+), λ–, (Invitrogen)
XL10-Gold	TetrD(mcrA)183 D (mcrCB-hsdSMR-mrr)173 endA1 supE44 thi-1 recA1 gyrA96 relA1 lac Hte [F´ proAB lacIqZDM15 Tn10 (Tetr) Amy Camr]. 200314-(Agilent technologies)

2.4.2 Preparation of competent *E. coli* cells – Inoue method

The production of ultra-competent *E.coli* cells were made using the Inoue method (Sambrook and Russell, 2006) to give a high transformation efficiency. A 5 ml LB culture was set up by picking a single colony (2-3mm in diameter) from a plate of *E. coli* cells and transferred to 25ml of fresh SOB medium (20g tryptone, 5g yeast extract and 0.5g NaCl in 1 litre of deionised water after pH adjusted to 7.0, sterilised by autoclaving). This was incubated for 6-8 hours at 37^{o}C with shaking (200 rpm). Varying volumes of 2ml, 4ml or 10ml of this culture was then used to inoculate three flasks containing 250ml of SOB media. These starter cultures were then grown overnight at 18^{o}C-22 ^{o}C with shaking. When the cultures had reached a cell density of 0.55 at OD_{600} they were chilled on ice for 30 minutes. The cells were harvested by centrifugation in a pre-chilled rotor at 2500g for 10 minutes (TY-JS 4.2 rotor, J6-MI Beckman centrifuge). The cell pellet was then resuspended in 80ml ice-cold Inoue buffer (55mM $MnCl_2$, 15mM $CaCl_2$, 250mM KCl, 10mM PIPES, pH 6.7) and re-pelleted by centrifugation. The final pellet was re-suspended in 10ml Inoue buffer and 750µl DMSO and quickly aliquoted into 1.5ml micro-centrifuge tubes. The tubes were flash frozen in liquid nitrogen and stored at -80^{o}C until needed.

2.4.3 Transformation of competent *E.coli* cells with plasmid DNA

For transformation, competent cells were thawed on ice and 50µl aliquoted into a 1.5ml Eppendorf tube. Plasmid DNA (~1ng) or ligated DNA (25ng) was added to the cells, incubated on ice for 20-30 minutes and then heat-shocked for 90 seconds at 42 ^{o}C. The cells were incubated on ice for 2 minutes to allow the cells recover. Following recovery, 800-1000µl of SOC (SOB containing 20mM glucose) was added to the cells, which were then incubated at 37^{o}C for 1 hour with shaking at 180 rpm. After incubation, 100µl of transformed bacterial cells were plated on LB plates (containing 50µg/ml ampicillin) and incubated overnight at 37^{o}C. After 18 hours, the plates were removed and stored at 4^{o}C to prevent further growth and the formation of satellite colonies (a result of degraded ampicillin) prior to use for liquid culture.

2.4.4 Plasmid DNA purification from *E. coli* cells

Individual colonies were picked from agar plates using a sterile pipette tip and placed in 30ml universals, containing 3-5mls of LB media with ampicillin, and were shaken

overnight at 37°C at 180 rpm overnight. The cell suspension was centrifuged at 4000 rpm for 5 minutes to pellet cells for plasmid DNA purification.

Plasmid DNA was purified using a QIAprep Spin Miniprep Kit (Qiagen®) for small-scale purification of 3-5ml overnight culture as described by the manufacture (Qiagen®). The plasmids were eluted in water at a final volume of 30-50µl dH_2O. A restriction enzyme digest was performed to confirm the correct construction of the plasmid (Method 2.6.1).

2.5 Protein Analysis

2.5.1 Antibodies

Primary and secondary antibodies used for immunostaining are shown in Table 2.6. Primary and secondary antibodies were stored at -20ºC and 4ºC, respectively, and diluted to the desired concentration when required.

Table 2.6 Primary antibodies used for immunofluorescence and western blot analysis

Antibody	Type	source	Dilution
Anti-acP10	Guinea pig polyclonal	IVRG	1:500 - 1:750
Anti-acP10	Rabbit polyconal	IVRG	1:450 - 1:750
Anti-Tubulin	Mouse monoclonal (IgG1, clone DM1A)	SIGMA-ALDRICH	1:750
Anti-V-Cath	Rabbit polyconal	IVRG	1:500
Anti-sfP10	Rabbit polyconal	IVRG	1:125-1:250

Table 2.7 Secondary antibodies used for immunofluorescence and western blot analysis

Antibody	Source	Dilution
Alexa Fluor® 488 Goat anti-guinea pig IgG	Molecular probes, Invitrogen	1:400
Alexa Fluor® 568 Goat anti-rabbit IgG	Molecular probes, Invitrogen	1:400
Alexa Fluor® 568 Goat anti-mouse IgG	Molecular probes, Invitrogen	1:400
Goat anti-guinea pig IgG alkaline phosphatase conjugated	SIGMA-ALDRICH	1:10,000
Goat anti-rabbit IgG alkaline phosphatase conjugated	SIGMA-ALDRICH	1:30,000
anti-mouse IgG alkaline phosphatase conjugated	SIGMA-ALDRICH	1:50,000
Goat anti-rabbit IgG horseradish peroxidase	SIGMA-ALDRICH	1:50,000

2.5.2 Electrophoresis of protein samples

Protein samples were analysed by sodium dodecyl sulphate polyacrylamide gel electrophoresis (SDS-PAGE) as described in Sambrook and Russell (2001). The samples were prepared from baculovirus-infected cells that were lysed with Cytobuster™ protein extraction reagent (Novagen), as directed by the supplier. An additional 1/5th volume of 6XLaemmli SDS-PAGE loading buffer (250mM Tris-HCl pH 6.8, 10% w/v SDS, 50% v/v glycerol, 0.05-0.5% w/v bromophenol blue and 25% v/v β-mercaptoethanol) was added to the sample. This mix was boiled for ~4 minutes in a water bath. Protein separation was performed on Tris-glycine SDS-polyacrylamide gels (at either 12%, for standard protein analysis, or 15% gel for smaller proteins) using the Mini-PROTEAN Tetra handcast system (BioRad). After separation of proteins, they were visualised through Coomassie Brilliant Blue staining or western blotting.

2.5.2a Coomassie staining

For visualisation of total proteins Coomassie staining was used. Samples were soaked in 0.25% (w/v) Coomassie Brilliant Blue R-250 dissolved in 50% v/v methanol, 10% v/v glacial acetic acid until bands were visible. Excess stain was removed with distilled water and the gels were de-stained in 30% v/v methanol, 10% v/v glacial acetic acid for ~4 hours. Images were acquired on a ChemiDoc™MP imaging system (BioRad).

2.5.2b Western blotting

Following SDS-PAGE, proteins were transferred to Amersham Protran nitrocellulose or PVDF using the TransBlot® Turbo Transfer system (BioRad) following the manufacturer's instructions. After blotting, the membranes were incubated in blocking buffer (PBS with 0.1% v/v Tween-20 (PBS-T) with 5% w/v skimmed milk powder (Marvel) for 1 hour at RT on an orbital shaker. The membranes were probed with a primary antibody (Table 2.6) diluted in (PBS-T) with 5% w/v skimmed milk powder and incubated for 1 hour at RT or at 4^{o}C overnight on a tube roller. A series of 4 X 10 minute washes with PBS-T were performed on the membrane. A secondary antibody (Table 2.7) diluted in PBS-T with 5% w/v skimmed milk powder was added for an hour, followed by a final series of 4 X 10 minute washes with PBS-T. For development with the alkaline phosphatase conjugated antibody, 10ml of alkaline phosphatase buffer (100mM Tris-HCl pH 9.5, 100mM NaCl, 5mM $MgCl_2$) containing 66µl Nitro blue tetrazolium (stock concentration at 50mg/ml in 70% v/v DMF) and 33µl 5-Bromo-4-chloro-3-indolyl phosphate p-toluidine salt (stock concentration at 50mg/ml in dH_2O) were added to the membrane. The membrane was

developed in the dark (checking at regular intervals) to monitor colour development. To stop the reaction, the membrane was washed with distilled water. For enhanced chemi-luminesence (ECL), which uses horseradish peroxidase-conjugated secondary antibodies (Table 2.7), the Clarity™ western ECL substrate was used. This combined 1.5ml of each solution (peroxide and luminol/enhancer solution) and developed for 5 minutes in the dark prior to imaging. A colorimetric or chemi-luminesence image was taken using a ChemiDoc™MP imaging system (BioRad).

2.6 Molecular biology methods

2.6.1 Restriction digest enzymes

All restriction endonucleases were purchased from New England Biolabs (NEB) and reactions carried out according to manufacturer's recommendations. Enzyme activity was normally stopped after one hour by either heat-inactivation or spin column purification and samples were stored at -20^{o}C.

2.6.2 Dephosphorylation of DNA

Dephosphorylation of DNA 5' phosphate ends, was performed using shrimp alkaline phosphatase (Promega). This was performed to prevent re-ligation of restriction digested ends. Manufacturer's guidelines were followed.

2.6.3 Ligation of DNA

The ligation reaction allows for two of more DNA fragments to be ligated at their complementary ends. The ligation was performed using a T4 DNA Ligase (Promega) with 50ng of linearised plasmid DNA with a pre-calculated volume of insert that depends on both length and concentration. Reactions were normally overnight at 4ºC and then were used for transformation (Section 2.4.3).

2.6.4 Agarose gel electrophoresis and purification of DNA

Agarose gel electrophoresis was performed using agarose (Fisher) at 0.6% to 2% w/v for the separation of DNA. Prior to running of the samples, they were mixed with an appropriate volume of 6x loading buffer (30% v/v glycerol, 0.25% w/v bromophenol blue dye, 0.25% w/v xylene cyanol), and then the desired amount was loaded into pre-set

wells. The DNA was electrophoresed at 25-100 volts in 1X TAE buffer diluted from a 50X stock solution (Tris 40mM, acetate 20mM, EDTA 1 mM) containing 0.5µg/ml ethidium bromide or post-stained with 1X SYBR® gold nucleic acid (LifeTechnologies) for gel purification. Gel images were acquired on a ChemiDoc™MP imaging system using an ultraviolet (UV) trans-illuminator.

For the purification of DNA fragments, the required band was viewed on a UV box and excised using a scalpel. DNA within the gel fragment was purified using the QIAquick gel extraction kit (Qiagen®) following the supplier's instructions. The DNA was eluted in water at a final volume of 30-50µl dH_2O and was analysed using gel electrophoresis.

2.6.5 Polymerase chain reaction (PCR)

Fragments of DNA for either analytical or cloning purposes were amplified by PCR. Reactions were carried out using *Taq* DNA polymerases (NEB) for analytical PCR or proof-reading Herculase II fusion DNA polymerase (Agilent) for cloning. Reactions were carried out in a total volume of 50µl in thin walled PCR tubes. The PCR master mix consisted of 1-10ng template DNA, 250µM deoxynucleotide triphosphate mix (dNTP), 0.25µM DNA primers and 1X supplied buffer at final concentration. 1-4 units of DNA polymerase were used for each reaction. MilliQ dH_2O was used to give a total volume of 50µl. PCR reactions were carried out using a SureCycler 8800 thermal cycler (Agilent Genomics) PCR machine (Table 2.8).

Table 2.8 PCR reaction conditions

Step	Temperature	Duration	cycles
1	Denaturing 95°C	2[1] or 5[2] minutes	1
2	Denaturing 95°C Annealing 45 -68 °C Extension 68-72[2] °C	20 seconds 20 seconds 30[1]secs or 60[2]secs per/kb	26-30
3	Extension 68[2]-72[1] °C	3[1] - 5[2] minues	1

[1]Herculase II optimised parameters
[2]Taq advised optimised parameters

2.6.6 Primers

Oligonucleotide primers were synthesised by Eurofins MWG Operon (Germany). Primers were resuspended, from a lyophilised sample in ultrapure dH_2O to a stock solution of 100pmol/ml and stored at -20ºC (Refer to Table 2.9).

Table 2.9 Oligonucleotide primer sequences used in thesis

	PRIMER NAME	SEQUENCE 5'-3'
1	pAcLG1 1	CGGGACCTTTAATTCAACCCAC
2	pAcLG1 2	GTGGCAACATGGAAATCGCTGA
3	pAcLG1 3	GTGCTGATTACGACCGCTCA
4	pAcLG1 4	GTGGCGTTTACAGCATTTGT
5	pAcLG1 5	GACGTCTCGTTGCTGCATAA
6	pAcLG1 6	CCACGCGATGGGTAACAGTC
7	pAcLG1 7	GGTTACAAATAAAGCAATAGCATC
8	pAcLG1 8	GCCGACAATGGAGCTGGCTT
9	pAcLG1 9	GGTTGCGCGAGATTATAGAG
10	lpgP10f1	CTGAGATCTATGAATCGTTTTTAAAATAACAAATC
11	lpgP10r1	CTCAGATCTGATTGTAAATAAAATGTAATTTACAG
12	pAcLGP10_For	GTGCTAAGTAAATGAATCGTTTTTAAAATA
13	PACLGP10_R ev	TATTTTAAAAACGATTCATTTACTTAGCAC
14	pAcLG1 12	CTGTCAACCTTTGTGTTAGTTTCCG
15	pAcLG1 13	GTTGGATAATTCTGTGGTGTCGGGG
16	iLOVLGF 1	CAGGGGATCCATGATAGAGAAGAATTTCGTCATC
17	iLOVLGR 2	GCCAGGATCCTTACTTGGAACTGCGTTTACCAC
18	iLOVLGF 3	CTCGATGGAAGTGATCATGTAGGCATACGTTAGATGTCAAAGCCTAAC GTTTTG
19	iLOVLGR 4	CAAAACGTTAGGCTTTGACATCTAACGTATGCCTACATGATCACTTCCA TCGAG
20	pAcLGPhos93For	CGT CGT GGT AAA CGC AGT GCC AAG TAA ATG AAT CG
21	pAcLGPhos93Rev	CGA TTC ATT TAC TTG GCA CTG CGT TTA CCA CGA CG
22	PrimeLGR -20bp	TTACAGTATAGTATTTTAATTAATA
23	PrimeLGF -30bp	GTATTTTAATTAATATACAAATGAT
24	PrimeLGF -40bp	TAATATACAAATGATTTGATAATAA
25	PrimeLGF -50bp	ATGATTTGATAATAATTCTTATTTA
26	PrimeLGF -60bp	AATAATTCTTATTTAACTATAATAT
27	PrimeLGR -20bp_ACL1	GTCAACGTTAGGCTTTGACATTTACAGTATAGTATTTTA
28	PrimeLGF -30bp_ACL1	GCTAACGTTAGGCTTTGACATGTATTTTAATTAATATAC
29	PrimeLGF -40bp_ACL1	GCTAACGTTAGGCTTTGACATTAATATACAAATGATTTG
30	PrimeLGF -50bp_ACL1	GCTAACGTTAGGCTTTGACATATGATTTGATAATAATTC
31	PrimeLGF -60bp_ACL1	GTCAACGTTAGGCTTTGACATAATAATTCTTATTTAACT
32	PrimeLG_ECOR1_F	CTTGGAATTCGAGAGGCGTCC
33	KOZAK_1_A-T_FOR	GTAAATTACATTTTATTTACATTCATGTCAAAGCCTAACGTTTTG
34	KOZAK_2_A-T_REV	CAAAACGTTAGGCTTTGACATGAATGTAAATAAAATGTAATTTAC
35	pAcLG1 4b	GTGGCGTTTACAGCATTTGTTATAC
36	PRIMELG-Control	GATTGTAAATAAAATGTAATTTACAG
37	PrimeLG-4	GTAAATAAAATGTAATTTACAGTATAG
38	PRIMELG-8	ATAAAATGTAATTTACAGTATAGTA
39	PRIMELG-12	AATGTAATTTACAGTATAGTATTTTAATTAATATAC
40	PRIMELG-16	TAATTTACAGTATAGTATTTTAATTAATATAC
41	PRIMELG_CON_ACL	GTCAACGTTAGGCTTTGACATGATTGTAAATAAAATGTAATTTAC
42	PrimeLG-4_ACL	GCTAACGTTAGGCTTTGACATGTAAATAAAATGTAATTTACAG
43	PRIMELG-8_ACL	GCTAACGTTAGGCTTTGACATATAAAATGTAATTTACAGTATAG
44	PRIMELG-12_ACL	GCTAACGTTAGGCTTTGACATAATGTAATTTACAGTATAGTATTTTAA TTAATATAC
45	PRIMELG-16_ACL	GCTAACGTTAGGCTTTGACATTAATTTACAGTATAGTATTTTAATTAATA TAC
46	P10_nHIS_FOR	CGCGGATCCATGCATCACCATCACCATCACTCAAAGCCTAACGTTT

Table 2.9 (Continued)

47	P10_nHIS_TEV_For	CGCGGATCCATGCATCACCATCACCATCACGAAAACCTGTATTTTC
48	T7 SFP10 For	TAATACGACTCACTATAGGGATGAAGAAAAATAAGTTTATTCC
49	T7 SFP10 Rev	TAATACGACTCACTATAGGGTTACTTTTTAGTGGTAGTAGTGG
50	pAcLG_Sf10 Rev	GTTGGATAATTCTGTGGTGTCGGGG
51	RDP923_Sf	ACGAAGCTTTTACTTTTTAGTGGTAGTAGTGG
52	RDP924Sf_for	ATTAATTAAAATACTATACTGTAAATTACATTTTATTTACAATCATGAAGAAAAATAAGTTTATTCCTC

2.6.7 Site-directed mutagenesis

Site-specific mutation of a plasmid DNA (Vandeyar *et al.*, 1988) was performed using a QuickChange® II site-directed mutagenesis kit using instructions from Agilent Technologies. Briefly, this method required three steps; (1) the desired plasmid DNA was subjected to PCR, with forward (pAcLGPhos93F) and reverse (pAcLGPhos93R) primers containing complementary mutagenic sites; (2) the PCR product containing the parental methylated DNA was digested with *DpnI* for 1 hour and then heat-inactivated at 80ºC for 20 minutes; and (3), competent cells were transformed with an aliquot of PCR-formed plasmid (see Section 2.4.3).

2.6.8 DNA sequencing

All sequencing was performed by Source Bioscience (Oxford, UK). Sequencing data was analysed using SnapGene® software.

2.7 Microscopy methods

2.7.1a Fixation and immunostaining

For confocal microscopy, TN-368 cells were seeded onto sterile cover slips placed in 35mm dishes at $0.2x10^6$ cells/dish. Cells were left to adhere overnight at 28°C prior to infection with virus at 5 MOI in a final volume of 200µl/well. Samples were incubated for 1 hour on a rocking table. After the incubation period, the virus inoculum was removed and 2mls of medium was added and samples incubate at 28°C for the desired time. The

medium was discarded and the cells were carefully washed with 2ml PBS prior to fixation. For chemical fixation, 1ml 4% v/v formaldehyde in PBS was added to each well and incubated at RT for 1 hour. The formaldehyde was removed and cells washed with PBS before temporary storage at 4^{o}C or immediate processing by immunofluorescence staining.

For staining, the fixed cells were permeabilised by a 10 minute treatment with 1ml of PBS-BSA (PBS containing 1% w/v bovine serum albumin) containing 0.1% v/v Triton X-100. The cells were then washed twice with 2ml PBS, followed by 2 washes with PBS-BSA blocking solution. Following washing, the cells were probed with 200µl of primary antibody (Table 2.7) and incubated at RT for 45-50 minutes. Unbound antibody was removed with three washes of 2ml PBS-BSA. After washing, the cells were probed with 200µl of fluorophore-conjugated secondary antibody (Table 2.7) and incubated for 45 minutes at RT. A final set of three PBS washes was performed before mounting the coverslips onto slides. The coverslips were mounted onto microscope slides with Vecta-shield mounting media (Vector Laboratories) and sealed with clear nail varnish, to stop samples drying out. The slides were stored at 4^{o}C protected from light and imaged within one week. For imaging of P10 protein structures by confocal microscopy, a primary anti-P10 antibody was used with the corresponding Alexa-fluor 488® secondary antibody.

2.7.1b Confocal microscopy

The fixed cells were imaged using a Zeiss LSM 510 meta laser scanning microscope using the 488nm excitation line of the argon laser, with fluorescence detected using a 488/543 nm dichroic beam splitter and a 505-530nm band pass filter for Alexa-Fluor 488®. Images were acquired using an oil immersion objective; Plan-Apochromat 63X (1.4 numerical aperture). Post-acquisition image processing and Z-stack image projections were processed using LSM 5 image Browser (Zeiss).

2.7.2 Transmission electron microscopy (TEM)

2.7.2a Sample preparation and fixation

For TEM, baculovirus-infected TN-368 cells were seeded into a T75 flask at 5 x 10^6 cells per flask. After one hour, the media was removed and the cell monolayer was infected with 1ml of inoculum at 5-10 MOI and incubated at 28ºC for the desired time. The infected cells were either tapped or scraped off and pelleted at 800rpm for 5 minutes in a 1.5ml

Eppendorf. The pellet was washed twice with PBS and fixed in 0.5ml of primary fixative (2% w/v paraformaldehyde and 2.5% v/v glutaraldehyde in 0.2M w/v sodium cacodylate buffer (pH 7.4), 0.1% w/v tannic acid). The fixative was allowed to infiltrate using a series of microwave fixation steps: six 5 second bursts on full power (900-watts). Samples were incubated on a rocker for 15 minutes. The pellet was washed four times for 5 minutes with 0.1M sodium cacodylate buffer (pH 7.4) (mixed 1:1 with dH_20) and centrifuged at full speed if required (unspecified rpm). A secondary fixation was performed with 1% v/v osmium tetroxide in 0.2 M sodium cacodylate buffer (1:1 mix), and infiltrated using a series of microwave fixation steps: six 5 seconds blasts on full power, followed by a 1 hour incubation on rocking table. The cell pellet was then rinsed with dH_20 five times and centrifuged to prevent sample loss, if required (*for SBF-SEM sample preparation, see Section 2.7.3).

A sequence of dehydration steps was then performed on the pellet, with the sequential addition of 500µl of 10%, 30%, 50% v/v ethanol (diluted in dH_2O) for 10 minute soaks each time. After each period, ethanol was removed and the sample centrifuged. After the removal of the 50% ethanol, 70% ethanol containing 2% v/v uranyl acetate was added (500µl) via a 0.2 µm filter and incubated overnight at 4^{o}C. The ethanol mix was removed and replaced twice with 70% ethanol with 10 minute incubation each time. Next, one 90% and three 100% ethanol additions with 10 minute incubations were performed. Finally, 500µl of 100% dried ethanol was added for 10 minutes then removed.

For infiltration, 500µl of Epon 812 epoxy resin was used at ratios of 1:3, 1:1 and 3:1 v/v with 100% dried ethanol for 15 minutes each. Three final changes of 100% Epon 812 resin were performed on the sample with 30 minutes incubations. Between each change, the tube was centrifuged at full speed for 3-5 minutes to aid infiltration of resin, and then removed prior to addition of fresh resin. On the final change, the sample was polymerised overnight at 70^{o}C and stored at RT for sectioning.

2.7.2b Sectioning and post-staining

For imaging samples by TEM, the resin was first shaped into an isosceles trapezoid. Using the PT-PC PowerTome Ultramicrotome (RMC™) ultra-thin 80-100nm sections were obtained from the resin using a diamond knife with water-filled trough. The sections were then gathered onto formvar coated grids. These were allowed to air dry and stored at RT prior to post-staining.

For increased staining of lipid membranes, post-staining was performed on the sections. The grids were washed (face-down) in dH_2O then stained in filtered 2% w/v aqueous

uranyl acetate for 10-20 minutes. An additional 3X dH_2O washes were performed, then grids were placed on 10% w/v lead citrate (1.33g $Pb(NO_3)_2$, 1.76g Na_3 ($C_6H_5O_7$), ~42ml dH_2O, 8ml 1N $NaOH_2$) in a Petri dish, surrounded by sodium hydroxide pellets to reduce precipitation. The grids were rinsed in 1N sodium hydroxide followed by a further three dH_2O washes. A final 8 minutes uranyl acetate stain was performed followed by three washes with dH_2O. Samples were allowed to dry before grids were visualised using the Hitachi H7650 electron microscope. Images were collected at 100kV with varying magnifications.

2.7.3 Serial-block face scanning electron microscopy (SBF-SEM)

The SBF-SEM is an automated system that allows for the acquisition of multiple sections from a single block face over one or two days. This technique was used to allow the three-dimensional architecture of an AcMNPV-infected cell to be modelled (Chapter Six).

Sample preparation and fixation were prepared as described in 2.7.2a with an addition of 2% v/v osmium tetroxide included to increase visualisation of infected cell cultures (see * in 2.7.2a). After the cell pellet was then rinsed with dH_20 five times, an additional 2% v/v osmium tetroxide was added to cell pellets and then incubated on rocker for 40 minutes at RT. The pellet was then subjected to five washes with dH_20 prior to dehydration. See Chapter six for more information on protocol. Samples were captured with technical help from Dr Louise Hughes.

2.7.4 Scanning electron microscopy

2.7.4a Polyhedra extraction

Scanning electron microscopy (SEM) was performed on polyhedra extracted from baculovirus-infected cell cultures. For SEM, TN-368 cells were seeded in T75 flasks at 5 x 10^6 cells per flask at 5 MOI. After five days the infected cells and culture medium were harvested and pelleted at 800g for 10 minutes and washed in 1X TE buffer. The cells were then lysed in 0.5% w/v SDS in dH_2O and incubated for 10 minutes at RT. The polyhedra were pelleted at 800 rpm and the media removed and the pellet was washed in 1X TE buffer.

2.7.4b Polyhedra fixation

For fixation, the polyhedra were washed with gentle resuspension in PIPES buffer (0.1M PIPES pH7.2, 5mM EGTA, 2mM $MgCl_2$, 10mM KCl, from Williams *et al.,* 1989) and pelleted at 800g for 5 minutes. The polyhedra were fixed in 4% formaldehyde in PIPES buffer for 1h, and then washed once in PIPES buffer. The polyhedra were then dehydrated in an ethanol series of 30%, 50%, 70% v/v and 100% at two washes each for 10 min. The dehydrated polyhedra were densely seeded onto glass coverslips (10-20µl).

2.7.4c SEM imaging

Once air dried, the coverslips containing sample were mounted on to stubs and sputter-coated with gold using the Agar auto sputter coater with thickness monitor control. The samples were then imaged using a Hitachi S3400N or Zeiss Merlin compact field emission gun SEM. Samples were captured with technical help from Dr Louise Hughes.

2.7.8 Enumerating OBs from insect cells

A diluted sub-sample of extracted polyhedra suspension (2.7.4a) was placed into the wells of a C-chip haemocytometer (Labtech) and allowed to settle for 10 minutes. The polyhedra were counted in triplicate under a light microscope phase-contrast objective at X400 magnification and the concentration of polyhedra calculated.

2.7.9 Statistical analysis of data

Data was analysed using software package Microsoft Office Excel 2010 and GraphPad Prism 7, which were used to compare the enumerated polyhedra and their size. Graphs were developed using GraphPad Prism 7. Statistical comparisons were made using t-test (α=0.05) when comparing two population means or a ANOVA test (α=0.05) when comparing differences amongst group means.

Chapter Three:

Construction of a recombinant AcMNPV with a complete deletion of the P10 gene

3.1 Introduction

P10 is a small protein that is hyper-expressed in the very late phase of the baculovirus replication cycle. Electron microscopy has shown P10 structures to be formed of fibrous-like structures in both the cytoplasm and the nucleus. Over 40 years of research has led to suggestions that P10 is likely to play a role in nuclear stability, polyhedra formation and, in the terminal phase of replication, nuclear lysis to release polyhedra. However to date, the mechanisms by which P10 fulfils these roles remain elusive.

The starting point for most studies on P10 function has involved construction of a virus in which P10 production is inhibited, so that comparisons can be made in the presence and absence of the protein. The construction of such viruses has been approached in three main ways: insertional inactivation of, partial deletion or complete removal of *p10*.

Insertional inactivation interrupts the *p10* coding sequence with another foreign gene. The first studies using this method, successfully inactivated *p10* by insertion of a phosphotransferase gene (Croizier *et al.*, 1987). Later studies used *E. coli lacZ,* which produced beta-galactosidase under *p10* promoter control. Hydrolysis of X-gal produced a strong blue colour in virus-infected cells, providing a useful selection marker (Vlak *et al.*, 1988; Williams *et al.*, 1989). In comparison with wild-type infections, cells infected with viruses containing an inactivated *p10* demonstrated: absence of nuclear lysis; absence of characteristic fibrous structures; and lack of association of EDS with the polyhedron envelope (Vlak *et al.*, 1988; Williams *et al.*, 1989). These results suggested a role for P10 in nuclear lysis and maturation of polyhedra; however, there were concerns that accumulation of high levels of β-galactosidase interfered with normal baculovirus replication (increased virulence and polyhedra production) that may have accounted for some of the observations made (Vlak *et al.*, 1988; Williams *et al.*, 1989).

Therefore, other studies used partial deletion of *p10* to disrupt function, without the need for insertion of marker genes. The first to use this approach to study the role of P10 was Williams *et al*. (1989), who produced a virus containing a truncated *p10* in which the N-terminal 29 aa were deleted. In another study, an in-depth analysis of recombinant viruses containing partial deletions at the carboxy-terminal of P10 (8, 15 and 42 aa) was performed by van Oers *et al*. (1993). Deletion of the entire *p10* was also used for comparison. Viruses containing either the 8 or 15 aa deletion, expressed an identifiable P10 protein, however, in cells infected with virus containing the 42 aa deletion, no P10-related protein was detected (van Oers *et al.*, 1993). The virus-infected cell phenotype produced by the 42 aa deletion was similar to that of the full *p10* deletion; neither nuclear lysis nor P10 structures were detected. P10 molecules lacking either 8 or 15 aa residues

also failed to assemble into P10 fibril structures in the nucleus and cytoplasm however, nuclear lysis with the liberation of polyhedra from cells was retained. This suggested that expression of a partial *p10* with a C-terminal truncation can still produce a functional protein (van Oers *et al.*, 1993).

The construction of viruses containing the complete removal of *p10* are likely to provide a better platform to characterise the role that P10 plays during infection, as it eliminates the possibility that expression of a partial gene could affect the virus-infected cell phenotype (Vlak *et al.*, 1988; Williams *et al.*, 1989; van Oers *et al.*, 1993). However, many of these complete *p10* deletions have used transfer vectors and construction designs that have introduced other gene deletions, mutations or insertions into the virus genome. Often inserted genes acted as selection markers, for example, insertion of *lacZ* under the control of the *hsp70* promoter or as transcription termination signals e.g., SV40 sequences (Vlak *et al.*, 1990; Weyer *et al.*, 1990; van Oers *et al.*, 1993; Wang *et al.*, 2009).

To address possible problems that could arise from using these historic approaches, this chapter describes the production of an AcMNPV mutant in which the entire *p10* coding region was deleted from the virus genome but without any other gene deletion or insertion (Figure 3.1), thus ensuring any functional changes observed could be directly attributed to the loss of *p10*. The system was also used for the construction of a rescue virus, with *p10* restored to the virus genome to act as an additional control for any unintentional mutations introduced during construction. The *p10* deletion virus was also used as the base vector to introduce modified *p10* sequences into the virus genome at the natural *p10* locus, as described in Chapters Four and Five.

3.2 Construction of an intermediate virus Ac∆*p10_lacZ* that replaces the *p10* coding region with *lacZ*

For the construction of Ac∆*p10_lacZ,* a series of plasmid constructs were made that would enable the construction of a mutant AcMNPV lacking *p10*. The first step was to remove the *p10* coding region and replace it with *lacZ* sequences that acted as a selectable marker. The modifications were prepared in a transfer plasmid (Figure 3.1 A) and the construct was transferred into the AcMNPV genome by co-transfection of insect cells (Sf9) with the plasmid and virus DNA (Figure 3.1 B). The natural process of homologous recombination replaced the native virus gene with the modified version (Method 2.3.4). The recombinant virus was isolated by selecting blue plaques in the presence of X-gal (Method 2.3.5). DNA from the *lacZ*-positive virus, Ac∆*p10_lacZ*, was used for the

production of further recombinant viruses using reverse selection of colourless plaques in the presence of X-gal.

3.2.1 Construction of plasmid pAc∆*p10_lacZ*

The transfer plasmid used to replace the *p10* coding region with those from *lacZ* was based on pAcUW1 (Weyer *et al.*, 1990), which contains virus sequences flanking a partial deletion of *p10*. pAcUW1 was digested with *Bgl*II and *Bcl*I to remove the remaining *p10* coding sequence, which was replaced with *lacZ* excised from pCH110 by digestion with *Bgl*II and *Bam*HI. This derived a new plasmid, pAc∆*p10_lacZ,* that placed *lacZ* under the control of the *p10* promoter (Figure 3.1 A).

Following ligation and transformation of competent *E.coli,* seven colonies were picked and screened by restriction enzyme digestion (Figure 3.2). Four colonies contained the correct profile of a linearised plasmid giving a single band of about 8 kbp. One of these was selected to purify plasmid DNA and was designated pAc∆*p10*. The correct construction of the plasmid was confirmed by DNA sequencing (data not shown).

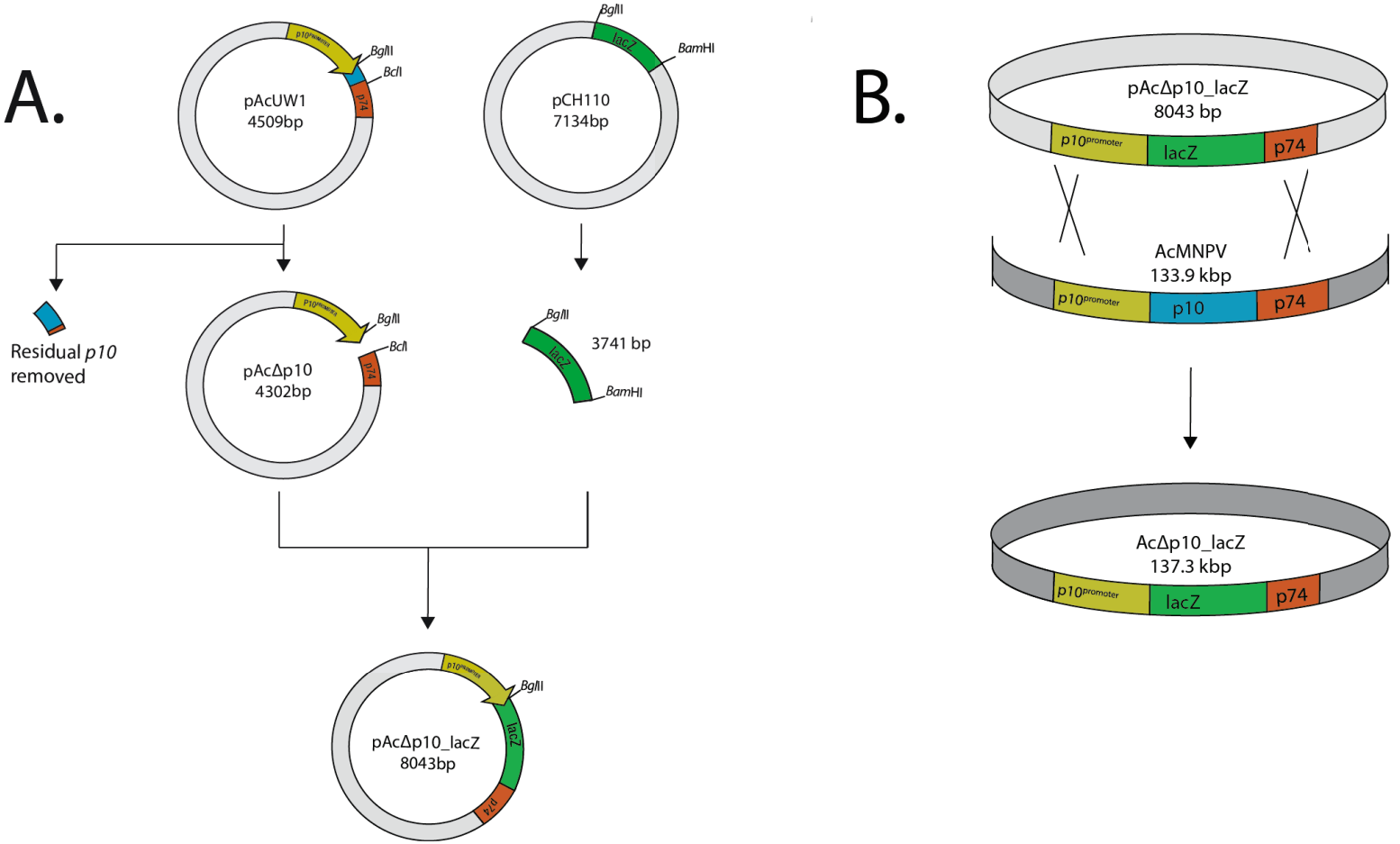

Figure 3.1 Construction of a recombinant *p10*-negative AcMNPV. (A) pAcUW1 was partially-digested with restriction endonucleases *Bgl*II and *Bcl*I to remove remaining *p10* coding region. pCH110 was digested with *Bgl*II and *Bam*H1 to release a *lacZ* fragment. The *lacZ* fragment was ligated into the partially-digested pAcUW1 at the complementary restriction sites *Bgl*II and *Bcl*I/*Bam*H1 (GATC) cleavage site to derive pAc∆*p10_lacZ*. (B) Schematic for co-transfection of insect cells and homologous recombination between pAc∆*p10_lacZ* and AcMNPV DNA to produce Ac∆*p10_lacZ* virus, in which the *p10* coding region has been replaced with *lac*Z.

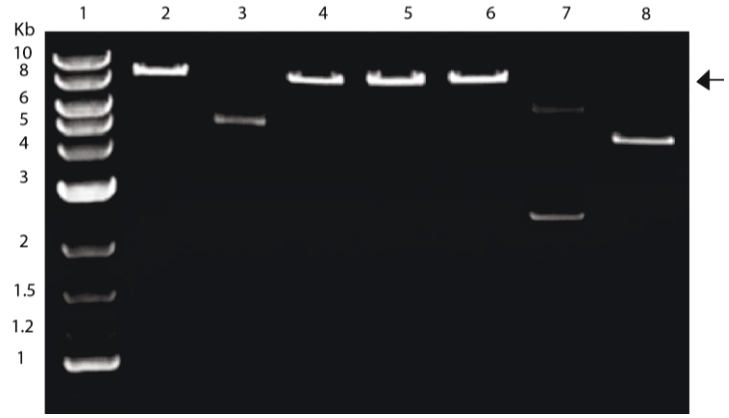

Figure 3.2 Genome analysis of pAcΔP10_*lacZ*. The DNA isolated from seven transformants (lanes 2-8) was digested with *Bgl*II and analysed using a 1% agarose gel. The predicted 8kbp pAcΔP10_*lacZ* fragment (lanes 2 and 4-6) is indicated with a black arrowhead. Molecular size markers are shown, left.

3.2.2 Production of a recombinant AcΔP10_*lacZ* virus

The second phase in the construction of the AcΔ*p10_lacZ* virus was the co-transfection of insect Sf9 cells (Summers and Smith, 1987) with wild-type AcMNPV C6 DNA with pAcΔ*p10_lacZ* plasmid (3.2.1, as described in method 2.3.4. Homologous recombination at the *p10* locus produced the virus designated AcΔ*p10_lacZ* (Figure 3.1 B).

Following co-transfection, the virus harvested from the cell culture media comprised a mixture of wild-type virus and recombinant virus expressing *lacZ*. To obtain a genetically homogeneous stock of recombinant virus, the virus was subjected to three rounds of plaque purification (Method 2.3.5a).

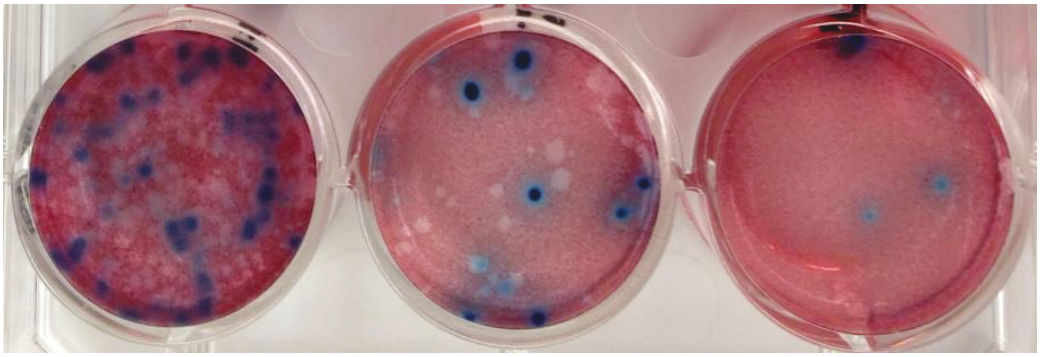

Figure 3.3 Isolation of AcΔ*p10*_lacZ. Representative plaque assay showing serial dilutions of virus harvested from the co-transfection of AcMNPV and pAcΔ*p10_lacZ* DNA. The plates were sequentially stained with X-gal and neutral red to identify those viruses producing β-galactosidase (blue plaques). The white plaques are the parental AcMNPV virus.

Plaques derived from Ac∆*p10_lacZ* were positively identified by the development of a blue colouration as described (Weyer *et al.*, 1990) (Figure 3.3). Clear plaques that developed from parental AcMNPV were identified by additional staining with neutral red. Twelve blue plaques were isolated and re-titrated until no clear plaques were visible. Virus isolated from the final round of plaque-purification was used to infect dishes of Sf9 cells (Method 2.3.3). The media contained budded virus was harvested after five days and was designated recombinant virus passage 0 (P0).

To confirm that plaque-purification had produced genetically homogenous isolates of Ac∆*p10_lacZ,* free from parental virus, PCR analysis and DNA sequencing at the *p10* locus were undertaken. To confirm the structure of the Ac∆*p10_lacZ* genome, PCR targeted at the *p10* locus were performed on twelve P0 recombinants. PCR confirmed: (1) the insertion of *lacZ* and deletion of *p10* coding region by analysis of the PCR fragment size using *p10* flanking primers (pAcLG1 and pAcLG4) (Figure 3.4 A), (2) determined the correct orientation of *lacZ* by using internal primers (pAcLG2 and pAcLG3) with *p10* flanking sequences (pAcLG1 and pAcLG4) (Figure 3.4 B-C). The correct construction of the virus at the *p10* locus was further confirmed by DNA sequencing of two recombinants (data not shown). Two separate P0 stocks of Ac∆*p10_lacZ* were amplified to produce P1 and P2 stocks for purification and characterisation of the virus DNA. Additional PCR analysis by fragment size was performed on the P1 and P2 stocks of Ac∆*p10_lacZ* to re-confirm correct genome structure and the absence of a mixed infection.

Ultra-pure DNA from one Ac∆*p10_lacZ* recombinant was obtained by lysis of budded virus and purification using caesium chloride gradients (Method 2.3.7). The purified Ac∆*p10_lacZ* DNA was used in the production of further recombinant viruses to study the function of P10 (as detailed in Chapters Four and Five).

The PCR analysis described above was specific for the *p10* locus. In order to confirm that there were no other gross changes to the Ac∆*p10_lacZ* DNA genome, virus DNA and wild-type AcMNPV DNA were digested with *Hind*III restriction enzyme and digestion products were analysed using agarose gel electrophoresis (Figure 3.5).

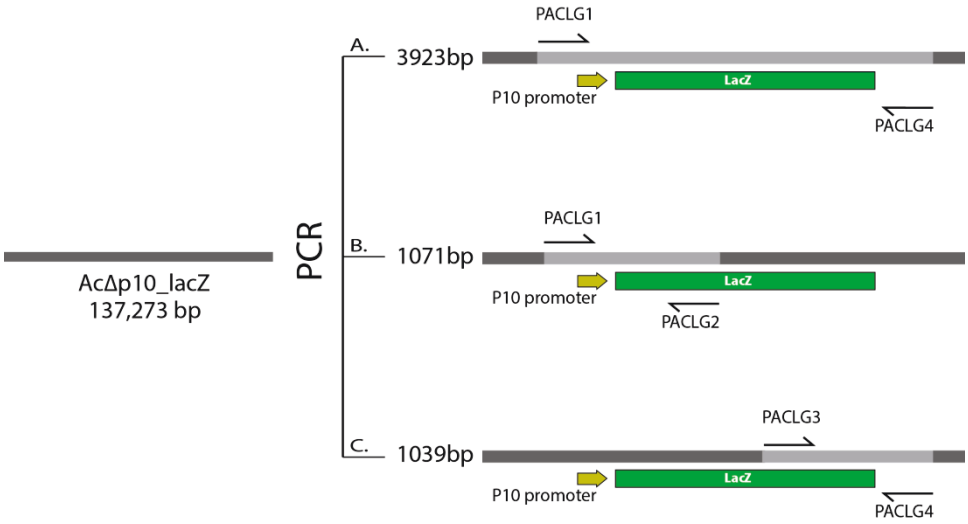

Figure 3.4 Characterisation of AcΔP10_lacZ DNA by PCR. PCR was performed at the expected site of *lac*Z to confirm correct insertion. (A) Shows binding site of primers pAcLG1 (CGGGACCTTTAATTCAACCCAAC) and pAcLG4 (GTGGCGTTTACAGCATTTGT) for PCR amplification of the full-length *lacZ* sequence, including *p10* flanking sequences (3923bp). (B) Shows binding site of primers pAcLG1 and PACLG2 (GTGGCAACATGGAAATCGCTGA) for PCR amplification of N-terminus sequence of *lacZ* and P10 promoter (1071bp). (C) shows binding site of primers PACLG3 (GTGCTGATTACGACCGCTCA) and PACLG4 for PCR amplification of partial C-terminus *lacZ* sequence including flanking region (1039bp).

The *Hind*III profile of AcΔ*p10_lacZ* and AcMNPV DNA showed an identical match of 18 visible bands and two distinct bands that did not correlate due to the presence of *lac*Z and deletion of the *p10* coding region (white arrows in Figure 3.5). These profiles were in agreement with the predicted *Hind*III profile generated by SnapGene® and confirmed that the AcΔ*p10_lacZ* virus DNA contained the additional *lacZ* insert with no other detectable mutations in the virus genome.

To further confirm the genome integrity of AcΔ*p10_lacZ,* a '*p10* rescue' was prepared in which the *p10* coding sequences were reinserted into AcΔ*p10_lacZ*. The rescue virus was constructed as an additional control against unintended mutations in the backbone virus DNA.

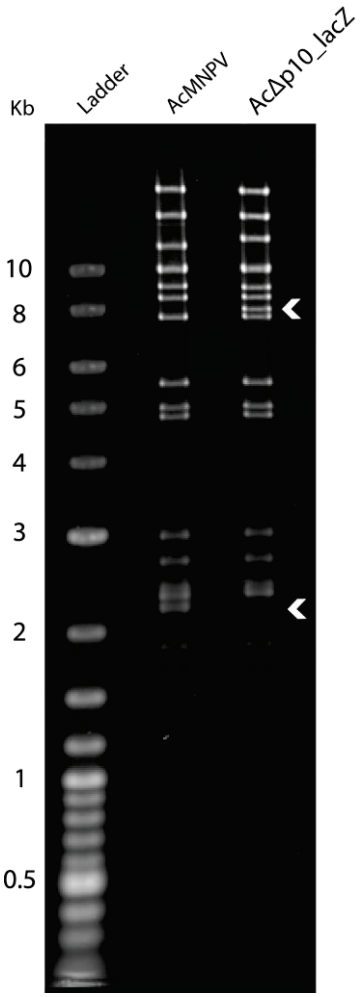

Figure 3.5 Genome analysis of Ac∆*p10_lacZ*. Purified DNA from AcMNPV and Ac∆*p10_lacZ* was digested with *Hind*III and fractionated in a 0.6% agarose gel before staining with Sybr gold. The white arrowheads indicate differences in the two profiles, due to the insertion of *lacZ.* Base pair size is indicated, left.

3.3 Construction of a *p10*-deletion and *p10*-rescue virus using Ac∆*p10_lacZ*

Although Ac∆*p10_lacZ* lacks the complete *p10* coding region, it contains the selectable marker *lacZ* (Section 3.2.1). Since high-level production of β-galactosidase may interfere with native P10 function (Williams *et al.*, 1989), it was necessary to remove the *lacZ* coding sequences from the virus genome prior to further work with this virus. It was also considered prudent to restore the complete *p10* in the Ac∆*p10_lacZ* genome to ensure that the resultant rescue virus behaved as the unmodified AcMNPV. Plasmids that either lacked or contained a complete *p10* coding region were used for the construction of two new recombinant viruses (Figure 3.6) via homologous recombination in Sf9 cells.

3.3.1 Construction of P10-deletion (pAc∆*p10*) and P10-rescue (pAc_*p10*^{Rescue}) plasmids

Two new plasmids containing either a complete *p10*-deletion (pAc∆*p10*) or a *p10*-rescue (pAc_*p10*^{Rescue}) were made using pAcUW1. pAc∆*p10* was constructed by digesting pAcUW1 with *Bgl*II and *Bcl*I and ligating the linear plasmid product prior to transformation and selection in *E. coli* to produce pAc∆*p10* (Figure 3.6 A). pAc_*p10*^{Rescue} was constructed by *Pac*I and *Bcl*I digestion of pAcUW1 to remove the partial *p10* sequence, followed by subsequent insertion of a fragment containing the complete *p10* coding region. The *p10* coding region was amplified from AcMNPV DNA using primers pAcLG1 and pAcLG4 that were complementary to the flanking regions of the *p10* coding sequence. The PCR-generated DNA fragment was purified and digested with *Pac*I and *Bcl*I, prior to ligation into *Pac*I/*Bcl*I-digested pAcUW1, to derive pAc_*p10*^{Rescue} plasmid (Figure 3.6 B). Following ligation and transformation, eight colonies from each construction were picked and screened by restriction enzyme digestion (gel data not shown). Constructs with the correct restriction profile were confirmed by DNA sequencing (data not shown).

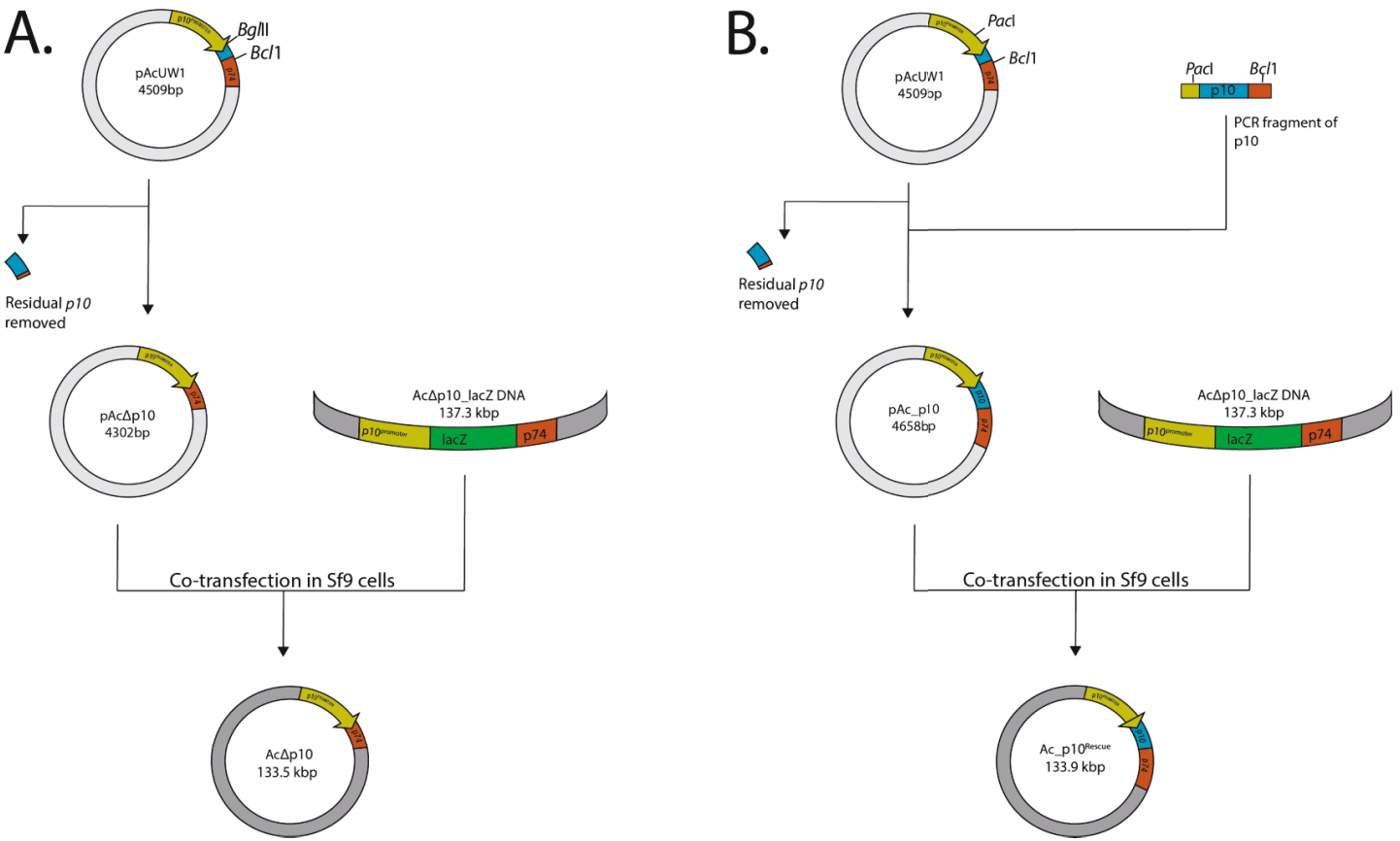

Figure 3.6 Construction of a P10-negative and P10-positive virus. (A) pAcUW1 was partially-digested with restriction endonucleases *Bgl*II and *Bcl*I to remove the remaining *p10* sequence and re-ligated at the complementary cleavage site GATC to derive pAcΔ*p10*. pAcΔ*p10* was then co-transfected with AcΔ*p10_lacZ* in Sf9 cells to construct AcΔ*p10* virus. (B) pAcUW1 was partially-digested with *Pac*I and *Bcl*I to remove the remaining *p10* sequence and then ligated with a PCR fragment, containing *p10* coding sequence, to construct pAc_*p10*^{Rescue}. The PCR fragment was digested with *Pac*I and *Bcl*I prior ligation. Co-transfection and homologous recombination of pAc_*p10*^{Rescue} with AcΔ*p10_lacZ* in Sf9 cells resulted in Ac_*p10*^{Rescue}virus.

3.3.2 Construction of Ac∆*p10 and* Ac*_p10*^{Rescue} virus

The *p10*-deletion virus was made by co-transfection of *Sf*9 cells with pAc∆*p10* and Ac∆*p10_lacZ* DNA (Figure 3.6 A). After 4-5 days, the culture medium, containing a mixture of Ac∆*p10_lacZ,* expressing *lacZ,* and Ac∆*p10* were titrated using a reverse selection approach, whereby only clear plaques were selected for plaque-purification. Clear plaques (in the presence of X-gal) were re-titrated until no blue plaques were detected and a pure stock of Ac∆*p10* was obtained. Twelve clear plaques were selected after the final titration and re-suspended in media prior to infection of Sf9 cells. Media was harvested after 5 days and designated virus passage P0 before being amplified twice to generate a working stock (P2). The Ac*_p10*^{Rescue} virus was produced using the same method as for Ac∆*p10* but used a *p10*-containing plasmid, pAc*_p10*^{Rescue}, for the co-transfection to restore the *p10* coding region in Ac∆*p10_lacZ* (Figure 3.6 B). Twelve P0 virus stocks were produced from the final plaque isolates and were amplified twice to generate a working stock (P2).

As discussed in section 3.2.2, the virus stocks were analysed by PCR and sequenced to confirm the integrity of the Ac∆*p10* and Ac*_p10*^{Rescue} genome (results not shown).

3.4 Characterisation of Ac∆*p10* and Ac*_p10* rescue virus

As highlighted earlier, it is common to examine the functional role of a virus protein by comparing the phenotype when the gene has been deleted with that of the wild-type. The following experiments compared the phenotype of Ac∆*p10*-, Ac*_p10*^{Rescue}- and wild-type AcMNPV-infected cells using a combination of biochemical and microscopy techniques, in order to further elucidate the role of P10 in the AcMNPV replication cycle.

3.4.1 Budded virus production

To determine if budded virus production was affected by deletion of *p10*, a 72-hour, one-step growth curve was performed comparing Ac∆*p10*, Ac*_p10*^{Rescue} and AcMNPV-infected Sf9 cells (Figure 3.7).

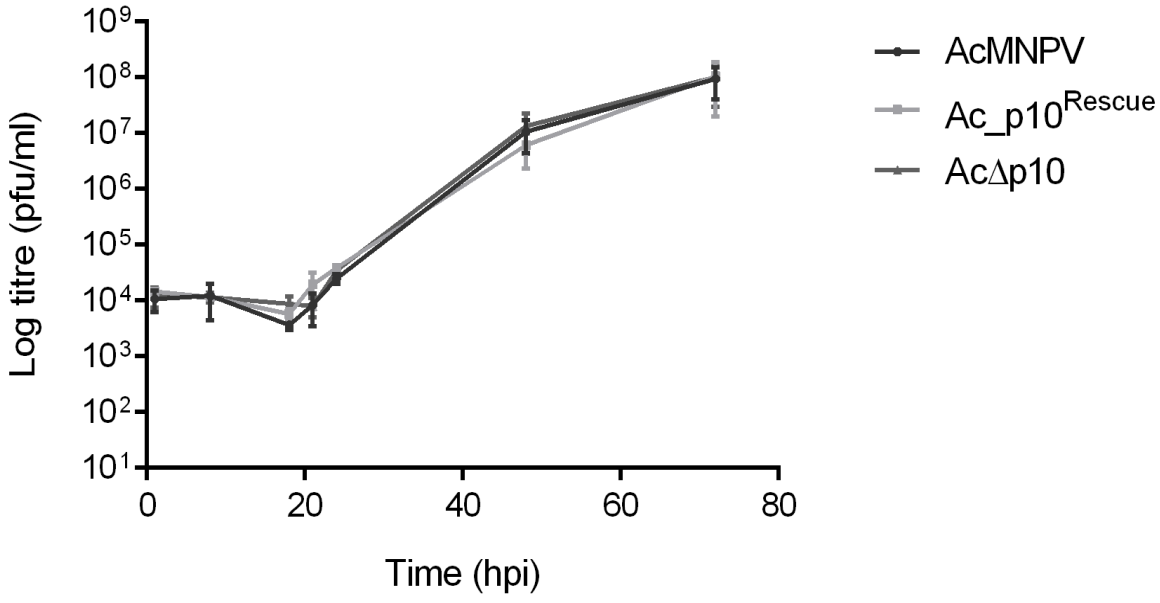

Figure 3.7 One-step growth curve showing budded virus production in Ac∆*p10*, Ac_*p10*^{Rescue} and AcMNPV-infected Sf9 cells. Plaque-titration of culture media for each virus was performed at 1, 8, 18, 21, 24, 48 and 72 hpi to determine virus titre (pfu/ml). Error bars represents mean ± SEM (N=2).

In Figure 3.7, the titres of all three viruses were close to 1 X 10^4 pfu/ml until 20 hpi, when a sharp increase in budded virus production was recorded until 48 hpi. Budded virus production continued to increase until the last time point tested (72 hpi).

A two-way ANOVA test performed on virus titres for Ac∆*p10,* AcMNPV and Ac_*p10*^{Rescue} at each time point confirmed that there was no significant difference in budded virus titres between each of viruses tested (sample p = 0.9951).

3.4.2 Protein synthesis in Ac∆*p10* and Ac_*p10*^{Rescue} -infected T.ni Hi5 cells.

In order to confirm that deletion of *p10* led to absence of P10 protein, and to compare P10 production in wild-type AcMNPV and the rescue virus, *T.ni* Hi5 insect cells seeded at 0.5x10^6 cells/ml were infected with AcMNPV, Ac∆*p10* or Ac_*p10*^{Rescue} at an MOI of 5 pfu/ml and harvested at 24, 48, 72 and 96 hpi. Total protein samples were analysed by SDS-PAGE and stained with Coomassie Brilliant blue to detect total protein (Figure 3.8 A) or transferred to a membrane for Western blotting to detect P10 expression (Figure 3.8 B; Method 2.5.2). Abrogation of P10 production was confirmed by the absence of a 10 kDa band in Ac∆*p10*-infected cells (arrow; Figure 3.8 A). P10 production in wild-type AcMNPV

and the rescue virus was confirmed by detection of a 10 kDa protein (Figure 3.8 A) that was also highlighted using a P10-specific antibody (arrow, Figure 3.8 B).

The anti-P10 antibody was raised in rabbits against a peptide sequence; NH_2-CFELDSDARRGKRSSK (Table 2.6). This peptide region was chosen as it had been previously used to produce an anti-sera that recognised P10 (Patmanidi *et al.*, 2003).

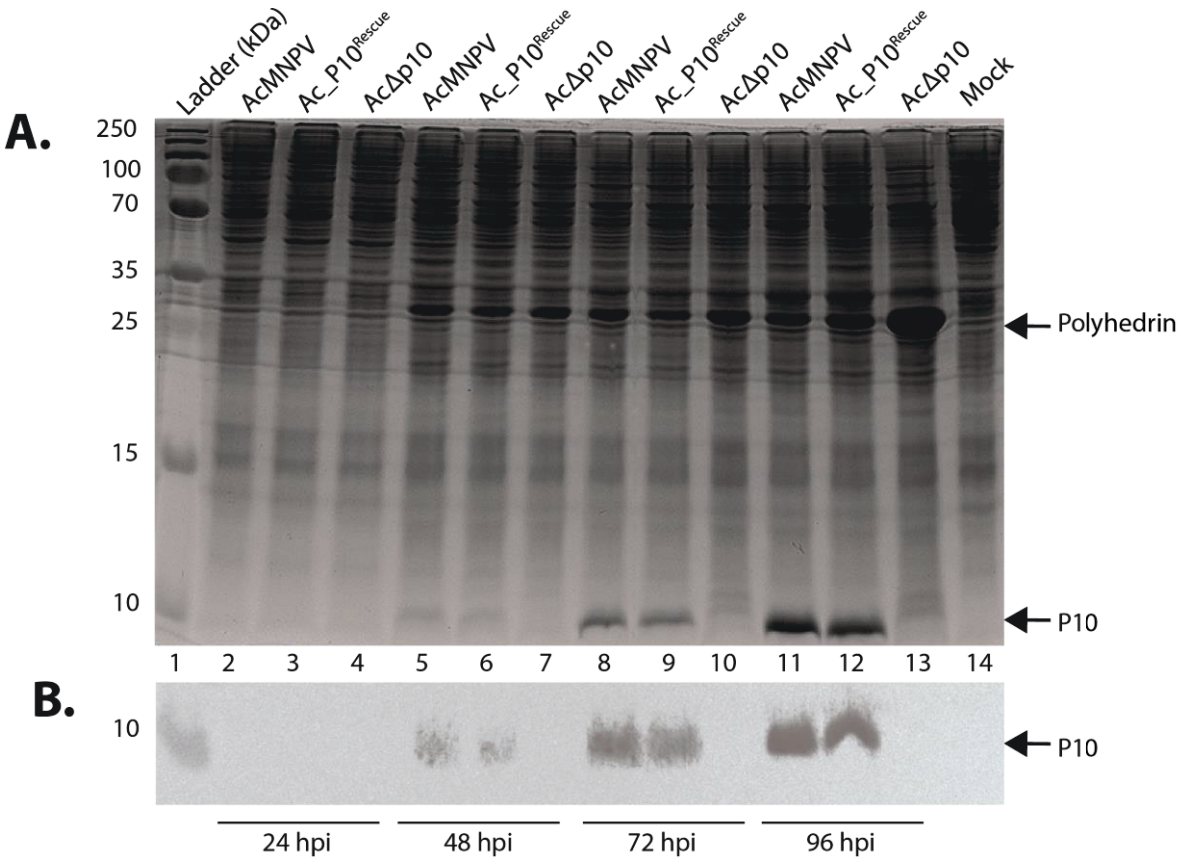

Figure 3.8 Protein synthesis in AcMNPV, Ac∆*p10* and Ac_*p10*^{Rescue} infected T.ni Hi5 cells. Infected cells were harvested at 24, 48, 72 and 96 hpi and total protein fractionated on a 15 % (w/v) SDS-PAGE for either Coomassie staining (A) or western blot analysis (B) with a P10-specific antibody using an alkaline phosphate-conjugated secondary antibody. Alkaline phosphate activity was detected with NBT-BCIP (Methods 2.5.2b). Lanes 1-14 (B) correlate to sample names at top (A). Arrows show expected sizes of P10 and polyhedrin. Ladder size (kDa) is indicated, left.

At 24 hpi, P10 expression was not detected in *T.ni* Hi5 cells by either Coomassie or Western blot for all three viruses (Figure 3.8, lanes 2-4). By 48 hpi, expression levels in Ac_*p10*^{Rescue} and AcMNPV had increased to detectable levels for both Coomassie and Western blot (Figure 3.8, lanes 5-6) and continued to increase at 72 and 96 hpi (Figure 3.8, lanes 8-10 and 11-12, respectively). A P10 associated band was not detected at any time point for Ac∆*p10,* either by Coomassie or Western blot (Figure 3.8, lanes 4, 7, 10 and

13), as expected. Interestingly, at 96 hpi polyhedrin expression was greater in Ac∆*p10*-infected cells compared with wild-type AcMNPV.

3.4.3 Lysis of AcMNPV, Ac∆*p10* and Ac_*p10*^{Rescue} -infected insect cells

A number of functional roles have been suggested for P10, including the lysis of virus-infected cells to release and facilitate dispersal of polyhedra (Williams *et al.*, 1989; van Oers *et al.*, 1993). To examine the role P10 plays in lysis, three different cell lines (*Sf*21, *Sf*9 and *T.ni* Hi5) were infected with wild-type AcMNPV at 5 MOI (Method 2.3.3a) and were imaged using a light microscope at 4 and 7 days post-infection (dpi) (Figure 3.8).

After 4 days, many *T.ni* Hi5 cells infected with AcMNPV had lysed releasing free polyhedra into the media, and by 7 dpi a sharp increase in free polyhedra was observed, completely covering the 35 mm dish (Figure 3.9). In comparison, relatively few free polyhedra were observed in either Sf9 or Sf21 cells at 4 dpi (Figure 3.9). Whilst the numbers of free polyhedra increased by 7 dpi, levels were still much lower than that observed in *T.ni* Hi5 cells (Figure 3.9). Examination of the images in Figure 3.9 suggested that there were more polyhedra per nuclei in *T.ni* Hi5 cells compared with either Sf21 or Sf9 cells. To determine if the number of polyhedra produced in *T.ni* Hi5 cells was statistically higher than in Sf9 cells, occlusion bodies from both cell types were enumerated.

Triplicate dishes of *T.ni* Hi5 ($0.5x10^6$ cells/ml) and Sf9 ($1x10^6$ cells/ml) cells were infected with AcMNPV at 5 MOI and incubated at 28°C (Method 2.3.3a). After five days, the cells and media were harvested and the polyhedra extracted (Method 2.7.4a). Polyhedra were counted using a haemocytometer and averages were compared (Figure 3.10). As both Sf9 and Hi5 plated tissue cultures have shown to be sensitive to cell density, the seeding densities between cell lines were therefore optimised for virus and protein production. The resulting calculations in Figure 3.10 were representative on total production of polyhedra per $0.5x10^6$ cells or per single cell rather than per dish.

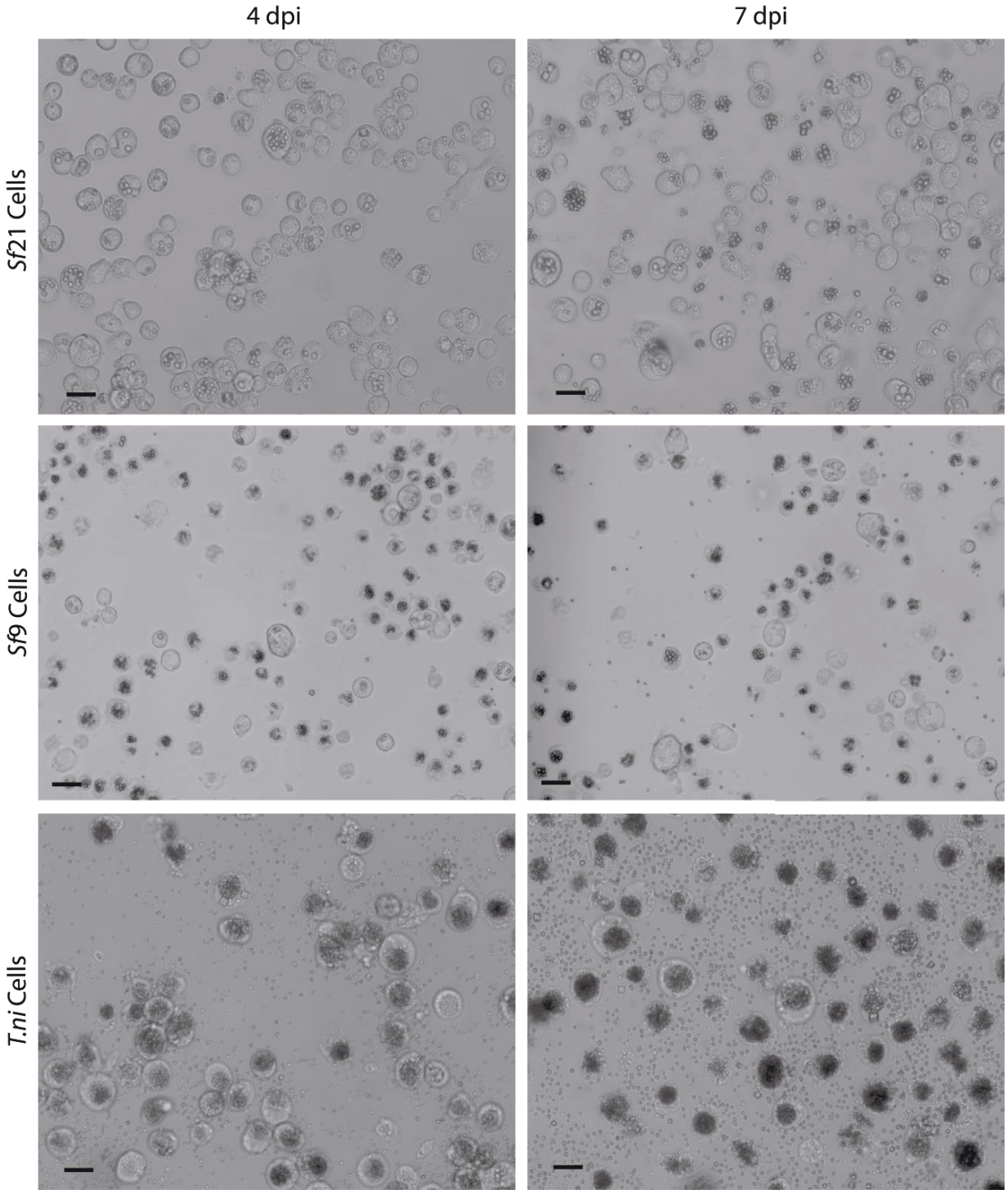

Figure 3.9 AcMNPV-infected cells at four and seven days post-infection. Sf21, Sf9 and *T.ni* cells were infected with AcMNPV (5 MOI) in 35 mm dishes and incubated at 28°C. The cells were imaged using a light microscope Zeiss Axiovert 135 at 4 and 7 dpi to show cell morphology and lysis (100X). Scale bar is 20 µm. *T.ni* Hi5 cells show increased number of free polyhedra compared with either Sf21 or Sf9 cells.

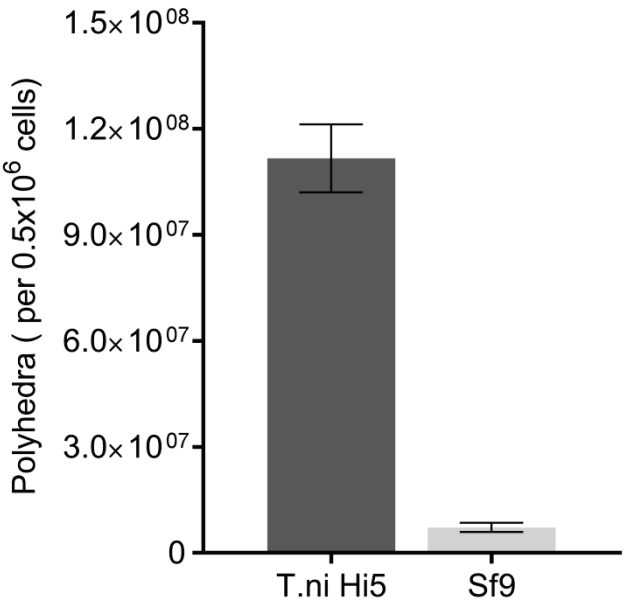

Figure 3.10 Comparison of total polyhedra counts in two different cell lines. Triplicate dishes (n=3) of *T.ni* Hi5 and Sf9 cells were infected with AcMNPV (5 MOI) at $0.5x10^6$ and $1x10^6$ cells per dish, respectively. Five dpi polyhedra were extracted, purified and re-suspended in 1ml PBS. Total polyhedra from infected cell cultures were counted using a haemocytometer giving polyhedra per $0.5x10^6$ cells. Error bars represents mean ± SD

A t-test on polyhedra counts confirmed polyhedra produced by Hi5 ($1.117x10^8$ ± 9.609 $x10^6$ per $0.5x10^6$ cells) were significantly higher ($p<0.0001$) than Sf9 cells ($7.250\ x10^6$ ± 1.299 per $0.5x10^6$ cells) (Figure 3.10). This is equivalent to Hi5 cells producing 234 polyhedra per cell and Sf9 cells with 14.5 polyhedra per cell.

Because of the results obtained in Figures 3.9 and 3.10, and the use of *T.ni* cells to study P10 structures in previous studies (Carpentier *et al.*, 2008), *T.ni* cells were the preferred cell line to further characterise the role of P10 in virus infection.

T.ni Hi5 cells were infected with AcMNPV, Ac_*p10*^{Rescue} or Ac∆*p10* at 5 MOI (Method 2.3.3a) and were imaged at 4, 5, 7 and 14 dpi using a light microscope (Figure 3.11).

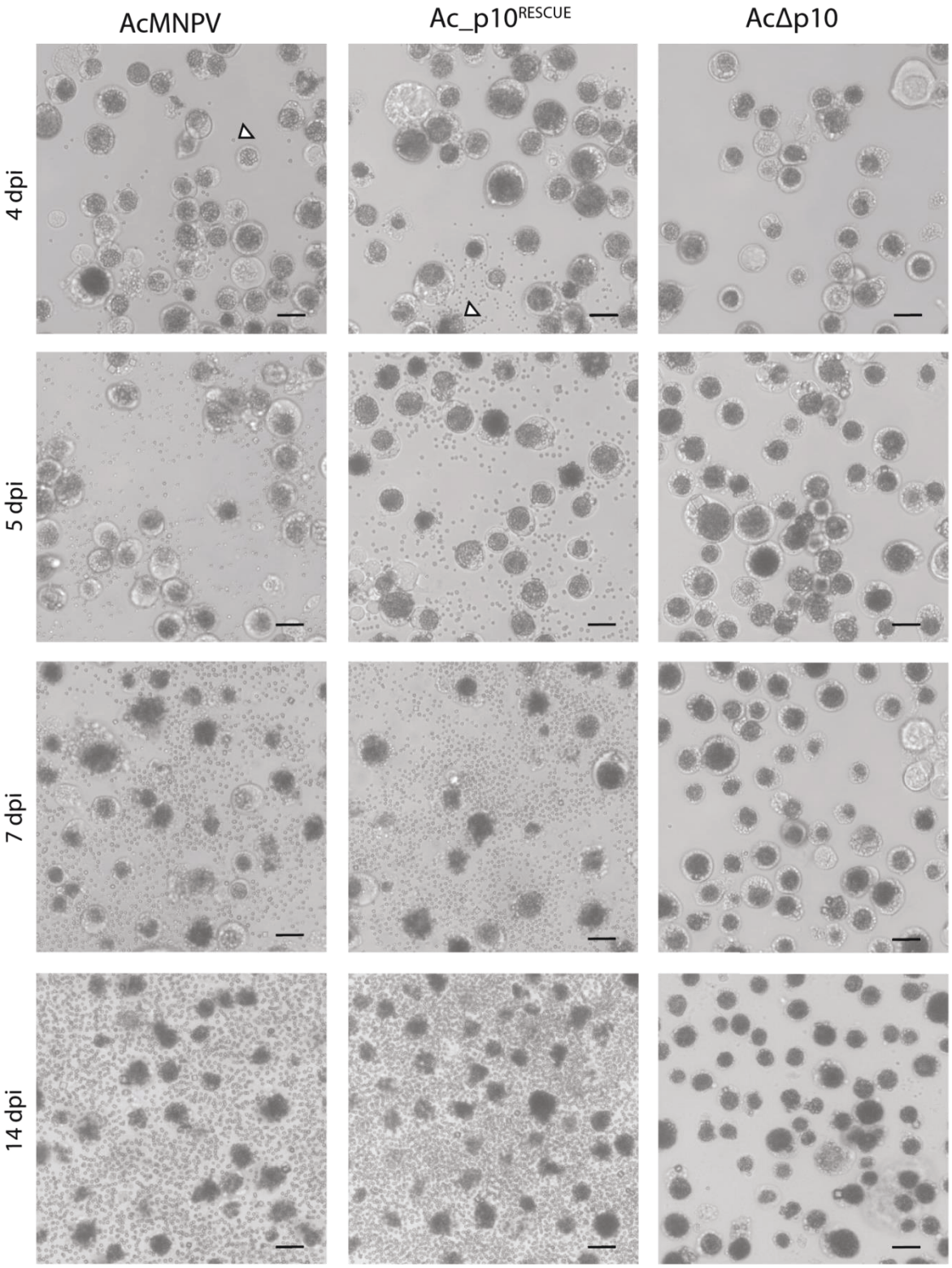

Figure 3.11 Lysis of *T.ni* Hi5 cells infected with AcMNPV, Ac∆*p10* and Ac_*p10*^{Rescue}. *T.ni* Hi5 cells were infected with 5 MOI virus in 35 mm dishes and incubated at 28°C. Cells were imaged at 4, 5, 7 and 14 dpi using a light microscope (Zeiss Axiovert 135) to capture cell morphology and lysis (100X). Free polyhedra as highlighted by white arrows increase from 4-14dpi for only AcMNPV and Ac_*p10*^{Rescue}, no observed free polyhedra were observed for Ac∆*p10*. Scale bar 20µm.

Images in Figure 3.11 show lysis of cells infected with either AcMNPV or Ac_*p10*^{Rescue}, highlighted by the presence of free polyhedra in the medium (see arrows in Figure 3.11). Lysis was observed from 4 dpi for both AcMNPV and Ac_*p10*^{Rescue}, with free polyhedra often located around remnants of an individual cell. The numbers of free polyhedra observed increased sharply over a two week period, with numerous polyhedra covering the dishes when imaged at 14 dpi (Figure 3.11). In comparison, no lysis was observed in Ac∆*p10*-infected cells with an absence of free polyhedra in the cell culture medium, even after two weeks (Figure 3.11).

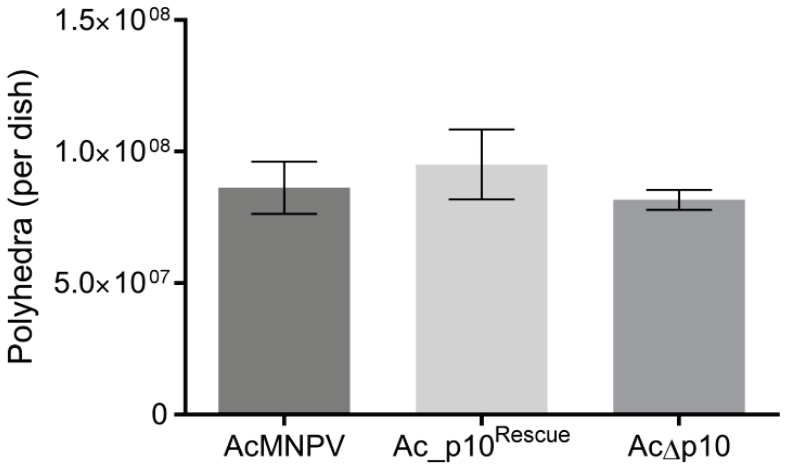

Figure 3.12 Comparison of total polyhedra counts in AcMNPV, Ac_*p10*^{Rescue} and Ac∆*p10*-infected cells. Triplicate dishes (n=3) of *T.ni* Hi5 cells were infected at 5 MOI. At 5 dpi, polyhedra were extracted, purified and re-suspended in 1ml PBS. Polyhedra were counted using a haemocytometer to give total polyhedra per dish. Error bars represents mean ± SD

Total polyhedra counts from AcMNPV, Ac_*p10*^{Rescue} or Ac∆*p10*-infected cells were compared (Figure 3.12). The mean polyhedra counts were between 5 X 10^7 and 1 x 10^8 per dish for each of the three viruses. To confirm that there was no statistical difference between the numbers of polyhedra produced, a one-way ANOVA was performed on the data shown in Figure 3.12. No significant difference between polyhedra was found (p=0.3066), suggesting the absence of P10 has no impact on the number of polyhedra produced.

3.3.4 Confocal microscopy of P10 structure formation during infection of *T.ni* cells

Confocal microscopy was performed on AcMNPV, Ac_*p10*^{Rescue} and Ac∆*p10* infected TN-368 cells at 24hpi (Figure 3.13), 48 hpi (Figure 3.14), 72 hpi (Figure 3.15) and 96 hpi (Figure 3.16) to observe how formation of P10 structures evolved during the early to late phase of infection. Infected or control cells were fixed, stained using a P10 primary antibody and Alexa-fluor 488® secondary antibody (Methods 2.7.1a, 2.7.1b) and imaged using a Zeiss LSM 510 meta laser scanning microscope. Mock-infected cells were included as negative controls (data not shown).

No P10 was detected in Ac∆*p10*-infected cells at any time point studied (Figure 3.13 - 16), as expected due to the absence of *p10*. Infection of cells with Ac∆*p10* was confirmed by the presence of polyhedra using bright-field imaging. P10 was detected at 24 hpi in AcMNPV- and Ac_*p10*^{Rescue} -infected cells (Figure 3.13) and was associated either with a structured network of thin filaments throughout the cytoplasm (Figure 3.13 A-D) or randomly orientated filaments that formed heterogeneous shapes (white arrows in Figure 3.13 B-C).

By 48 hpi, these filamentous structures had thickened and were observed to be more closely associated with the periphery of the nucleus (Figure 3.14 A-D). P10 structures were also seen to twist on themselves and associate with neighbouring P10 structures (white arrow, Figure 3.14 A, D). By 72 hpi, P10 was associated with thick peri-nuclear structures that encapsulated the nucleus (white arrow, Figure 3.15 D), whilst maintaining a complex network of cytoplasmic P10 filaments (Figure 3.15 A, C). Interestingly, the anti-P10 antibody detected P10 associated with polyhedra in the host cell nucleus, providing evidence of an association between P10 and polyhedra during the later phase of infection (white arrow, Figure 3.15 B).

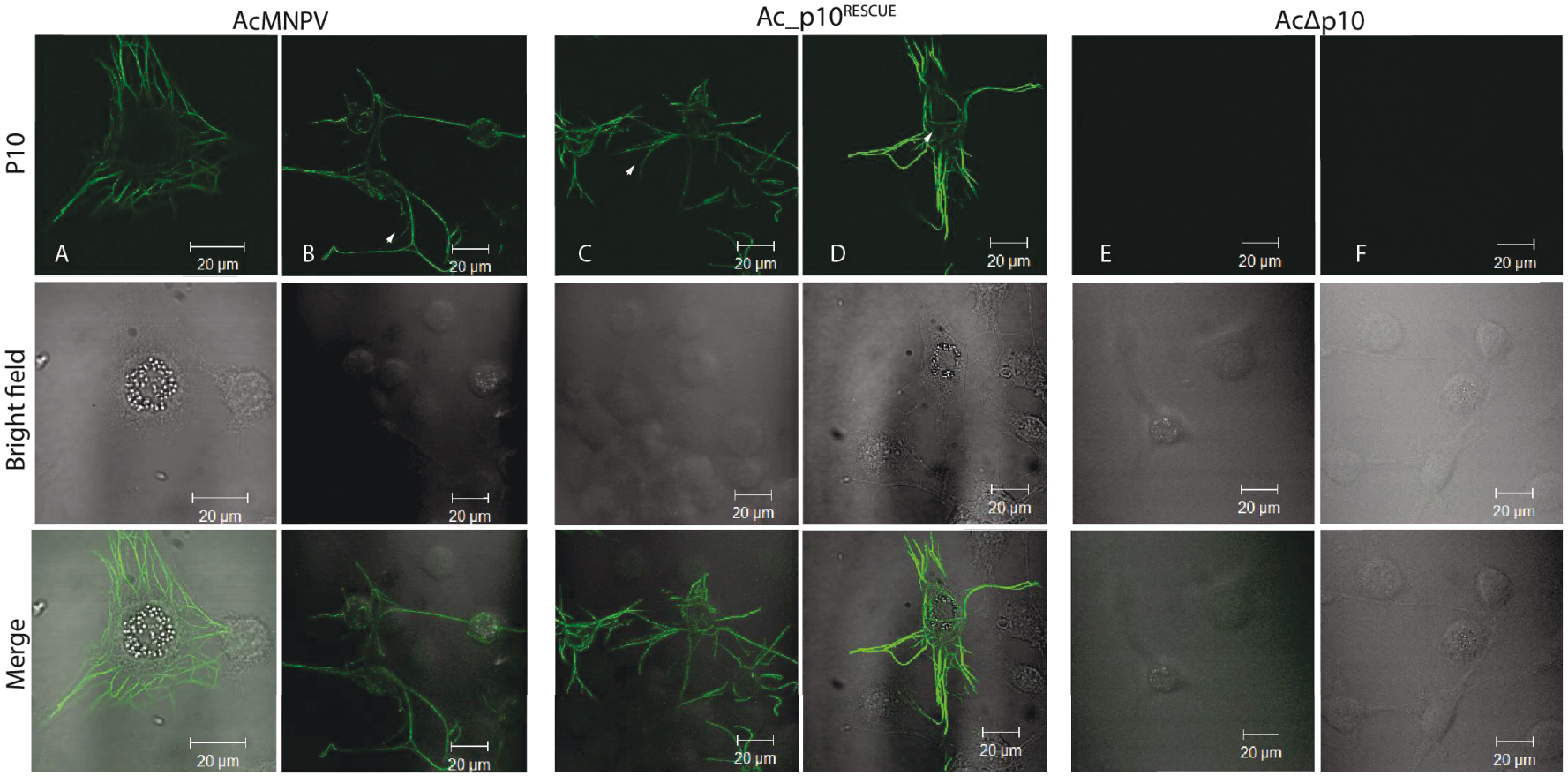

Figure 3.13 Immunofluorescence labelling of P10 structures at 24 hpi. Confocal microscopy of TN-368 cells infected with AcMNPV, Ac_*p10*^{Rescue} and AcΔ*p10* to observe P10 structures (green). Infected cells were fixed at 24 hpi and stained by indirect immunofluorescence using an anti-P10 antibody. A secondary antibody conjugated to an Alexa-fluor 488 was used to visualise P10 structures. White arrows (B,C,D) highlight thin cytoplasmic filamentous P10 structures that branch out. No P10 signal was detected in AcΔ*p10*-infected cells. Scale bar 20µm.

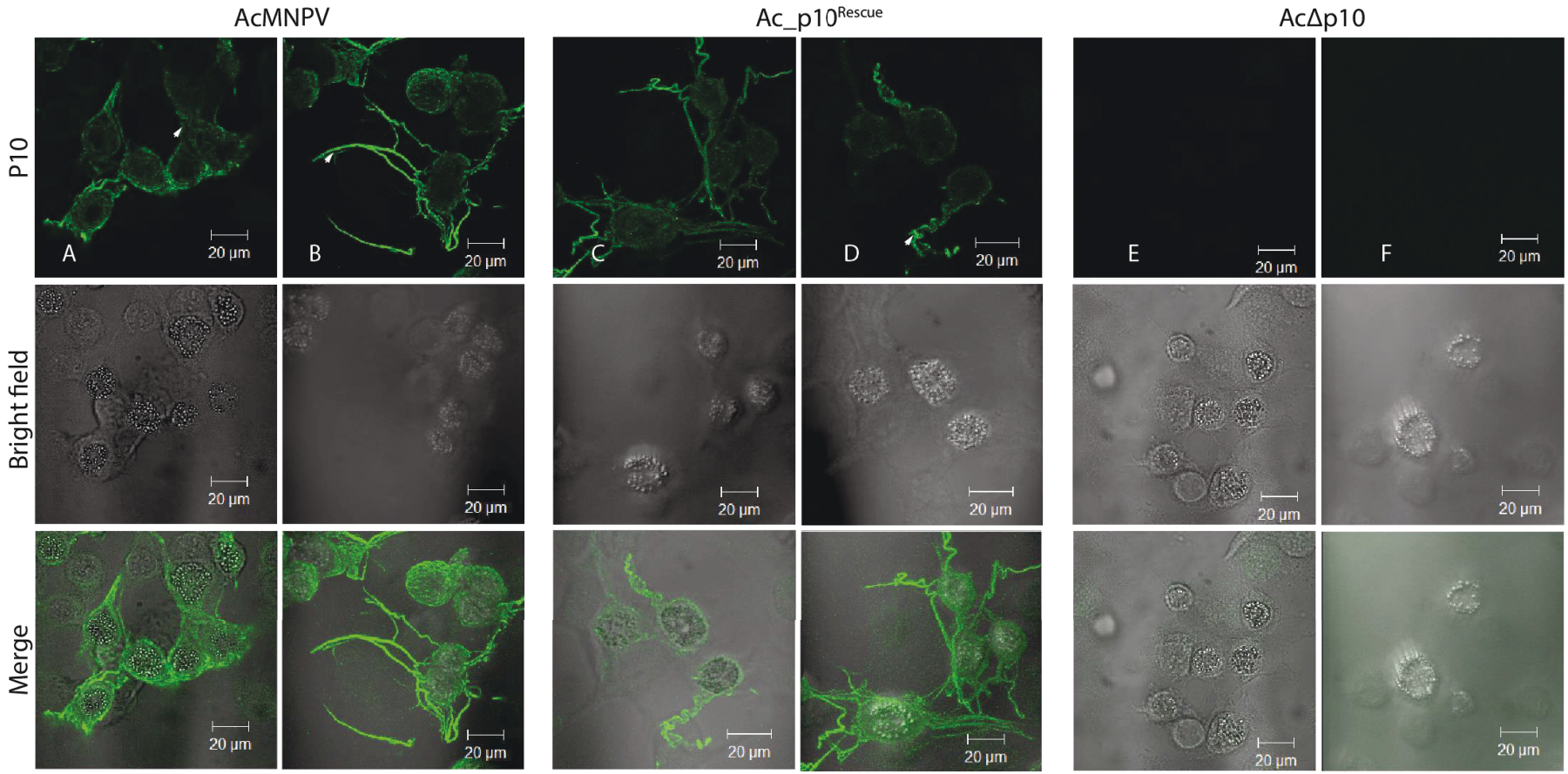

Figure 3.14 Immunofluorescence labelling of P10 structures at 48 hpi. Confocal microscopy of TN-368 cells infected with AcMNPV, Ac_*p10*^{Rescue} and Ac*Δp10* to observe P10 structures (green). Infected cells were fixed at 48 hpi and stained by indirect immunofluorescence using an anti-P10 antibody. A secondary antibody conjugated to a Alexa-fluor 488 was used to visualise P10 structures. White arrows (A,D) show the presence of thicker filamentous P10 structures, that twists on itself. White arrows (B) show thin elongated P10 associated filamentous structures. No P10 signal was detected with Ac*Δp10*. Scale bar 20µm.

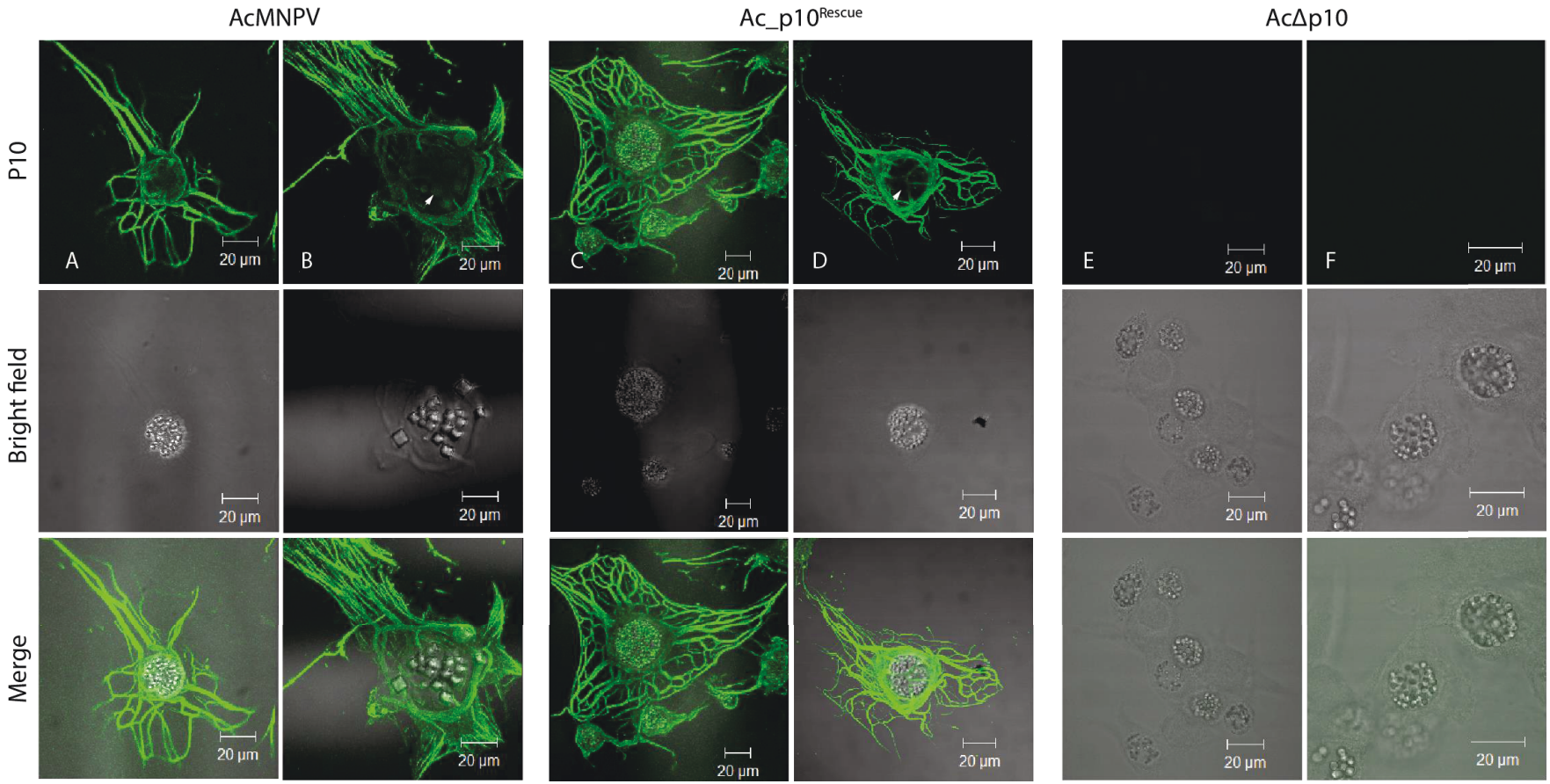

Figure 3.15 Immunofluorescence labelling of P10 structures at 72 hpi. Confocal microscopy of TN-368 cells infected with AcMNPV, Ac_*p10*^{Rescue} and Ac*Δp10* to observe P10 structures (green). Infected cells were fixed at 72 hpi and stained by indirect immunofluorescence using an anti-P10 antibody. A secondary antibody conjugated to a Alexa-fluor 488 was used to visualise P10 structures. cytoplasmic P10 structures Arrow (D) surround the nucleus forming a peri-nuclear cage and thin filaments branching off. White arrow (B) indicates P10 antibody is associating with polyhedra. No P10 signal was detected in Ac*Δp10*-infected cells. Scale bar 20µm.

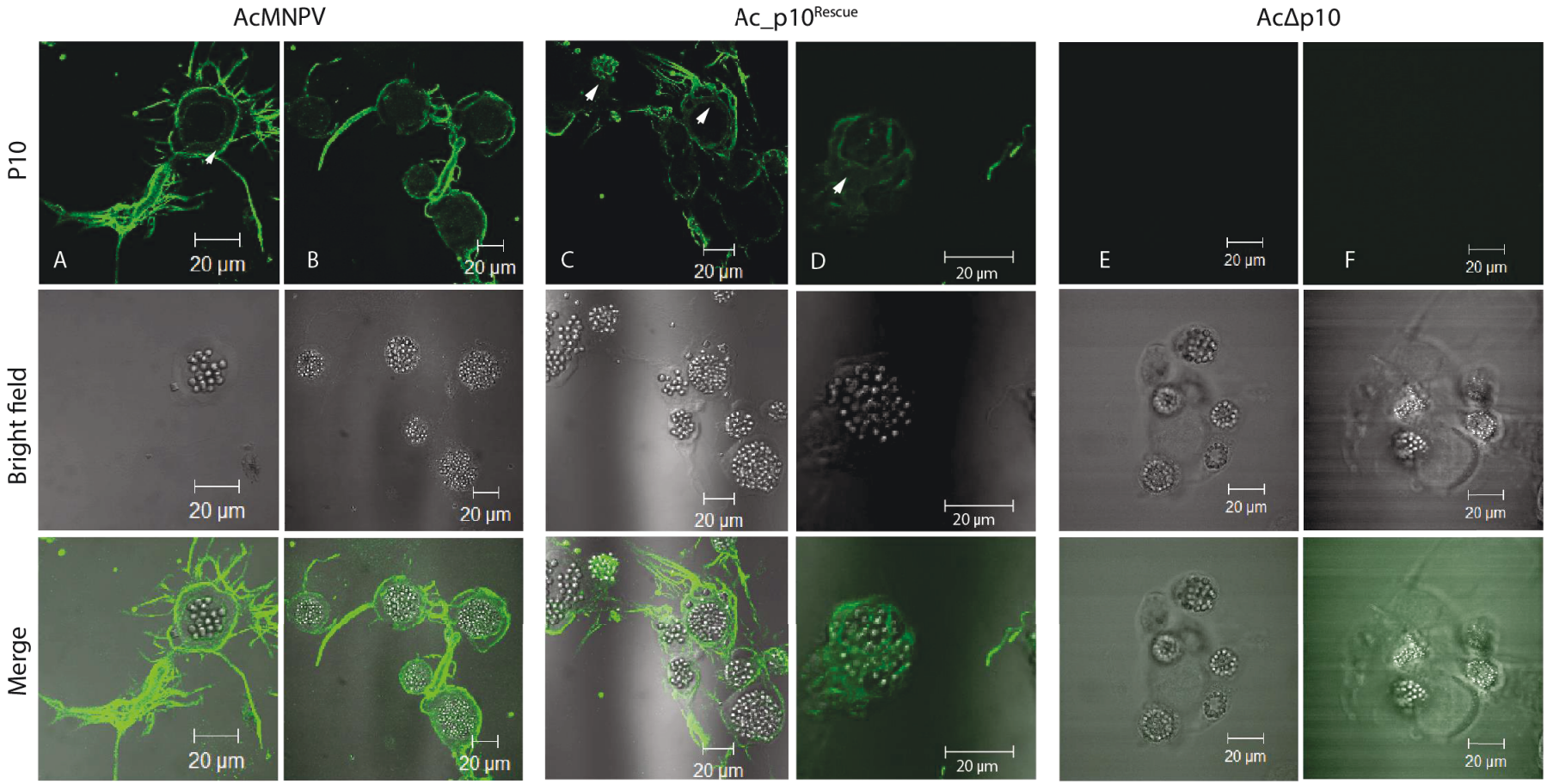

Figure 3.16 Immunofluorescence labelling of P10 structures at 96 hpi. Confocal microscopy of TN-368 cells infected with AcMNPV, Ac_*p10*^{Rescue} and Ac*Δp10* at 96 hpi to observe P10 structures (green). Infected cells were fixed and stained by indirect immunofluorescence using an anti-P10 antibody. A secondary antibody conjugated to a Alexa-fluor 488 was used to visualise P10 structures. White arrows (A) and (D) indicate thick peri-nuclear P10 structure surrounding the nucleus, with the thinner filaments almost absent. The white arrow (C) highlights free polyhedra that associated with P10 antibody. No P10 signal was detected in Ac*Δp10*-infected cells. Scale bar 20µm.

During the later phase of infection (96 hpi), in almost all cells examined, P10 was associated with a thick cage-like structure around the nucleus (Figure 3.16 D) that was often observed as a thick band around the nucleus (Figure 3.16 A, C). The thinner cytoplasmic filaments had also condensed and disassociated from the periphery of the nuclear membrane (white arrow, Figure 3.16 A) resulting in the majority of detectable P10 observed as thick tubular perinuclear (white arrow, Figure 3.16, A, C-D). Interestingly, similar to Carpentier *et al*. (2008), the anti-P10 antibody also detected polyhedra either within the nucleus (Figure 3.15 B-C) or observed outside the nucleus (Figure 3.16 A, C). This is suggestive of an involvement of P10 in polyhedra formation.

Overall, no differences in P10 structures were observed between wild-type AcMPNV and *p10*-rescue virus infected cells.

3.3.5 Transmission electron microscopy of baculovirus infected cells

The use of TEM is common in baculovirus research, allowing ultrastructural characterisation of infected cells. TEM allows the acquisition of high-resolution images of P10 and associated structures in virus-infected cells fixed at various times after infection. By performing TEM on AcMNPV, Ac_*p10*^{Rescue} and Ac∆*p10* infected TN-368 cells, changes to the ultrastructure in the presence and absence of P10 can be observed to offer an insight into the role of P10.

Infected cells were fixed in Epon 812 at 72 hpi using an optimised protocol for detection of P10-associated structures (Method 2.7.2). In particular, this study aimed to investigate further the suggestions that P10 may play a role, alongside electron dense spacers (EDS), in the formation of the PE or calyx (Hess and Falcon, 1978; Chung *et al.*, 1980; Russell and Rohrmann, 1990; Russell *et al.*, 1991; Lee *et al.*, 1996).

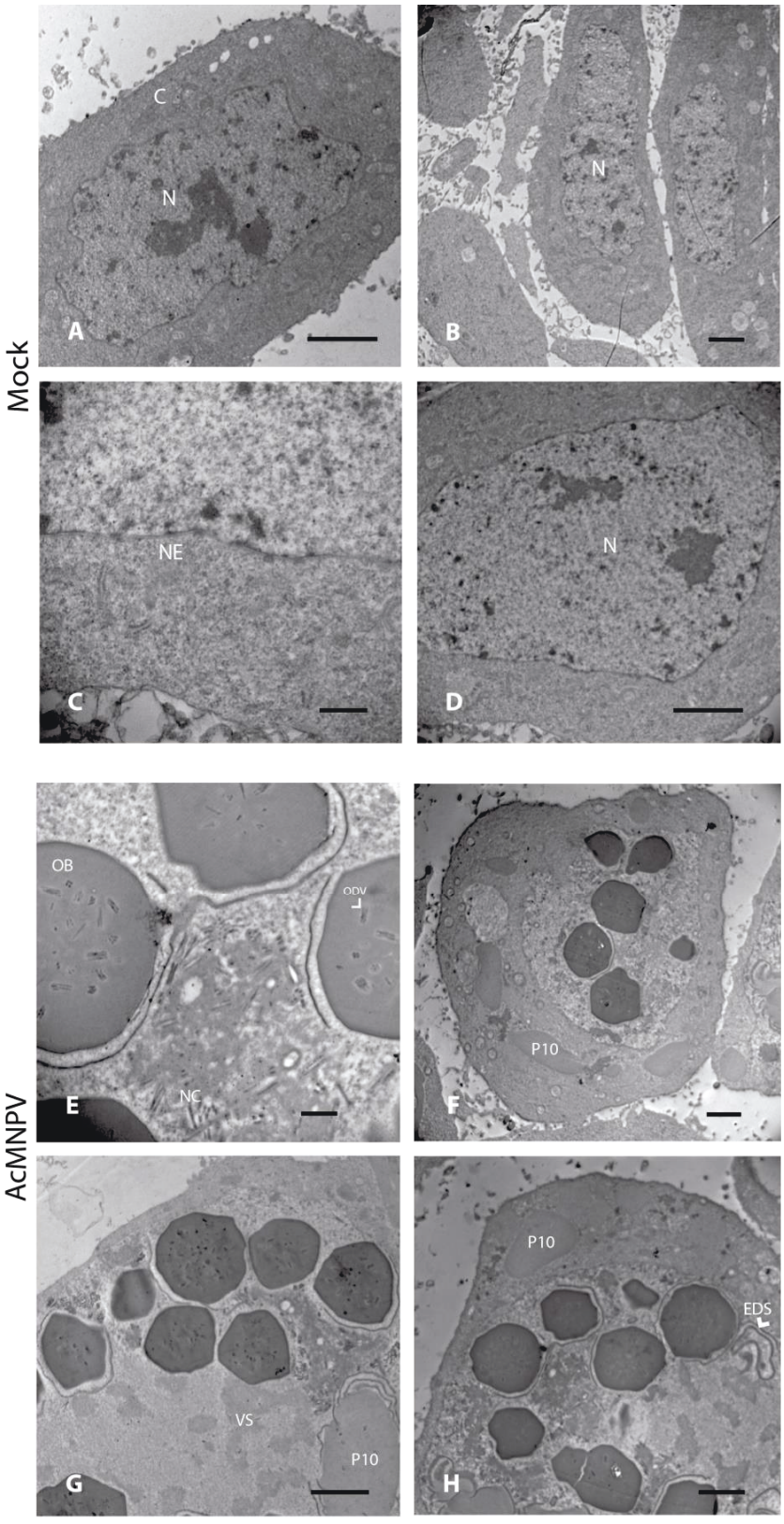

Figure 3.17 Transmission electron microscopy of AcMNPV structures in infected TN-368 cells at 72 hpi. Mock-infected (A-D) cells was observed with no phenotype resemblance of a baculovirus infection; only characteristic cell structures were visible. AcMNPV-infected (E-F) cells show mature polyhedra and P10 fibrous bodies with EDS protruding out of the P10 and wrapping around polyhedra. Abbreviations: C cytoplasm, N nucleus, NE nuclear envelope, NC nucleocapsids, OB occlusion body, ODV occlusion-derived virus (black arrow, E), EDS electron dense spacers (black arrow, H), VS virogenic stroma. Scale bar (A, B, D, F, G and H, 2 μm) or (C, E, 500nm).

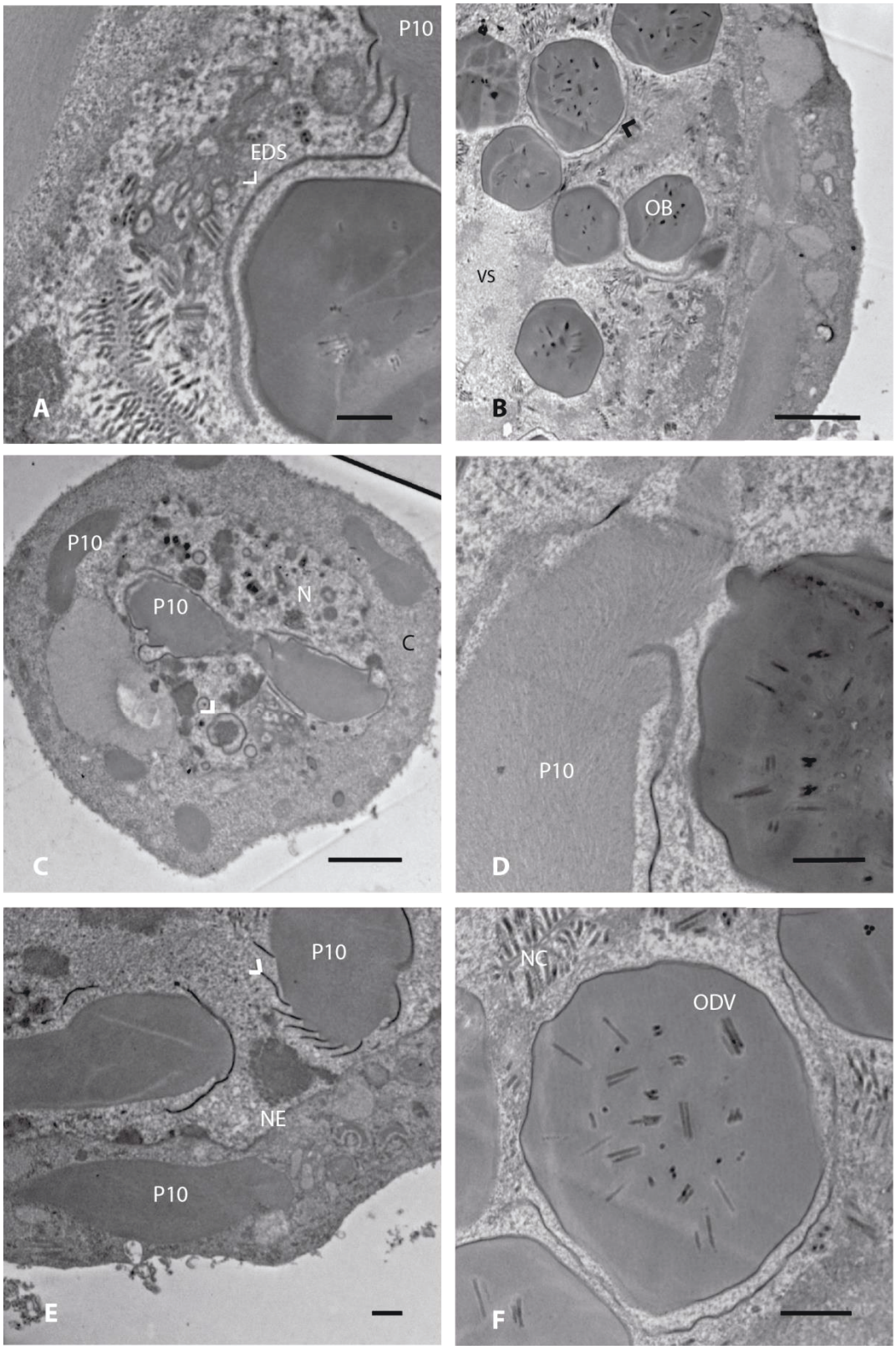

Figure 3.18 Transmission electron microscopy of Ac_*p10*^{Rescue} structures in infected TN-368 cells at 72 hpi. Ac_*p10*^{Rescue} -infected (A-F) cells display characteristic AcMNPV structures as observed in Figure 3.17, with no phenotypic differences observed between Ac_*p10*^{Rescue} and AcMNPV. Abbreviations: C cytoplasm, N nucleus, NE nuclear envelope, NC nucleocapsids, OB occlusion body, ODV occlusion-derived virus, EDS electron dense spacers (arrow, A-C, E). Scale bar: 2 µm (B, C, E) or 500nm (A, D, F).

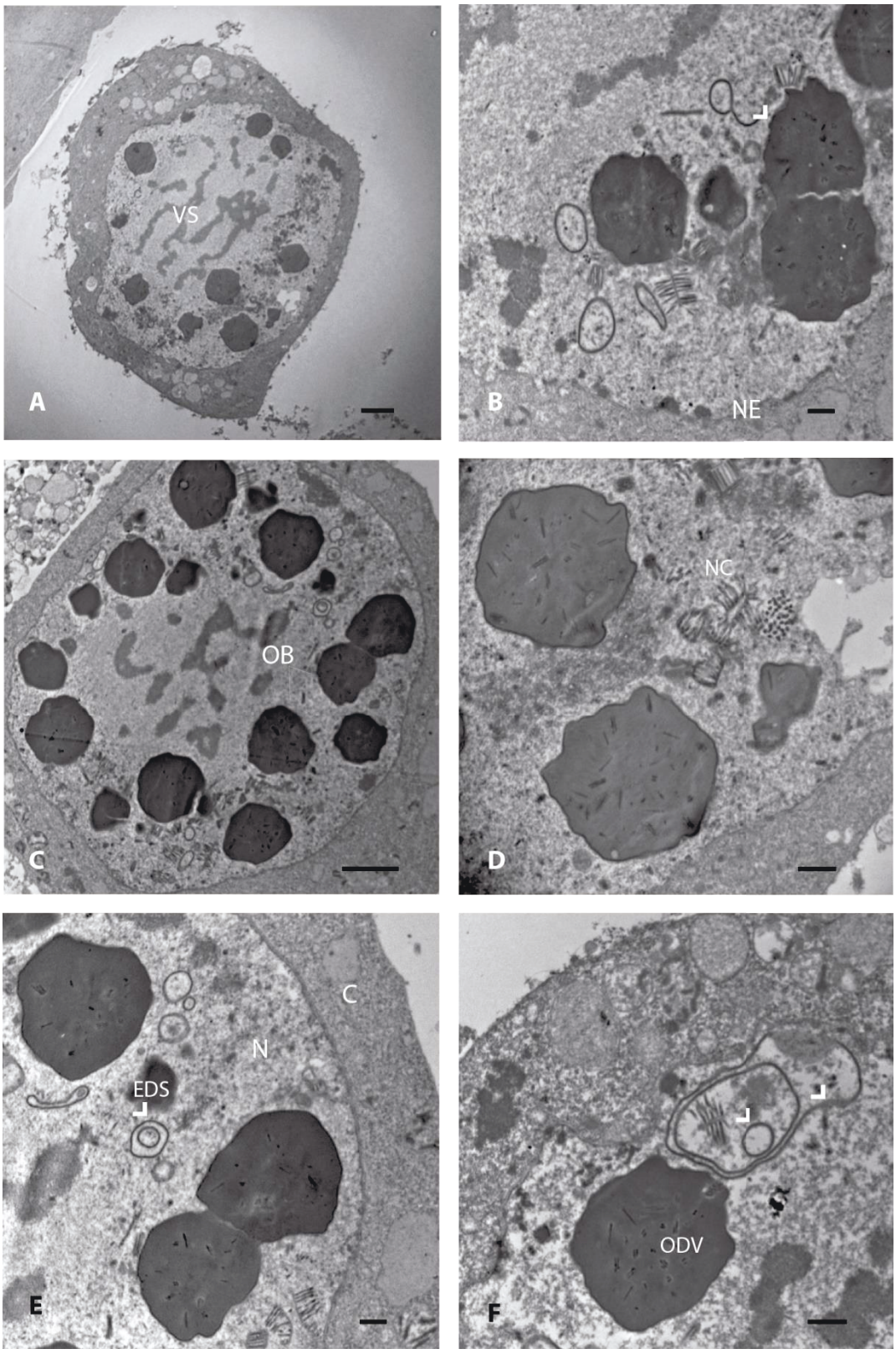

Figure 3.19 Transmission electron microscopy of Ac∆*p10* structures in infected TN-368 cells at 72 hpi. Ac∆*p10*-infected (A-F) cells were observed with polyhedra with a fragmented calyx (Arrow, B) and lacked the closely associated EDS. The EDS continued to form, however they self-associated into ring-like structures (arrow, E). No P10 fibrous bodies were observed. Abbreviations: C cytoplasm, N nucleus, NE nuclear envelope, NC nucleocapsids, OB occlusion body, ODV occlusion-derived virus, EDS electron dense spacers (white arrow, E-F).

The TEM images for mock-infected cells (Figure 3.17, A-D) displayed no phenotype resemblance of a baculovirus infection; only characteristic cell structures were visible. AcMNPV-infected cells (Figure 3.17, E-H) presented commonly associated baculovirus structures: nuclear and cytoplasmic P10 fibrous structures, polyhedra containing ODV embedded in an electron-dense structure, and EDS that associated with both nuclear P10 and polyhedra (black arrow, Figure 3.17 H). Micrographs of Ac_*p10*^{Rescue} (Figure 3.18) displayed the same phenotype as AcMNPV-infected cells, suggesting no change had occurred to the genome backbone during construction of the virus that resulted in a change to the viral structures.

Typical P10 structures were observed as a fibrous-like material with thin EDS protruding and associating with the periphery of polyhedra (Figure 3.18, A-E). This suggests an assocation between P10, EDS and polyhedra, previously noted over 30 years ago (Summers and Arnott, 1969; Chung *et al.*, 1980). This association has been further characterised (see below) and Chapter 6 describes the use of serial TEM sectioning to derive three-dimensional modelling of baculovirus structures.

Ac∆*p10*-infected cells (Figure 3.19) showed distinct differences in the cell phenotype when compared to the viruses expressing *p10* (Figure 3.17 and 3.18). The most identifiable difference was the absence of both nuclear and cytoplasmic fibrous P10 structures (Figure 3.19, A-F). Another major difference was EDS formation. In the absence of P10, the EDS did not associate with the polyhedra as indicated in Figure 3.18 B, E-F (black arrow). Instead, the EDS self-assembled into rings (Figure 3.19 E and F). In addition, polyhedra in Ac∆*p10*-infected cells commonly displayed irregular surfaces (Figure 3.19 B) rather than the smooth surface observed with polyhedra in Ac_*p10*^{Rescue} and AcMNPV-infected cells (Figure 3.17 and 3.18). In other respects, Ac∆*p10*-infected cells displayed many similarities to the Ac_*p10*^{Rescue} and AcMNPV-infected cells with correct packaging of the ODV into polyhedra, a defined virogenic stroma and production of nucleocapsids.

3.3.6 Characterising role of P10 in polyhedral envelope maturation

It has previously been suggested that P10 may play a role in polyhedra maturation through formation of the envelope or calyx (Williams *et al.*, 1989), an hypothesis that is supported by evidence presented in sections 3.3.4 and 3.3.5. However, there is still limited knowledge on the mechanisms that link P10, EDS and calyx formation and the speciifc roles played by EDS and P10. To observe how the polyhedra surface is affected in the absence of P10, SEM was performed on extracted polyhedra from Ac_*p10*^{Rescue} and

AcΔ*p10*-infected TN-368 cells (Method 2.7.4c). The polyhedra were visualised using a Zeiss Merlin 3View SEM to obtain high-resolution (1nm resolution at 15 kV) images of the polyhedra surface, offering detail at previously unattainable resolution. This allowed the polyhedra surface to be imaged in much greater detail than in previous studies, which enabled better characterisation of the impact of the P10 deletion on polyhedra maturation (Figure 3.20).

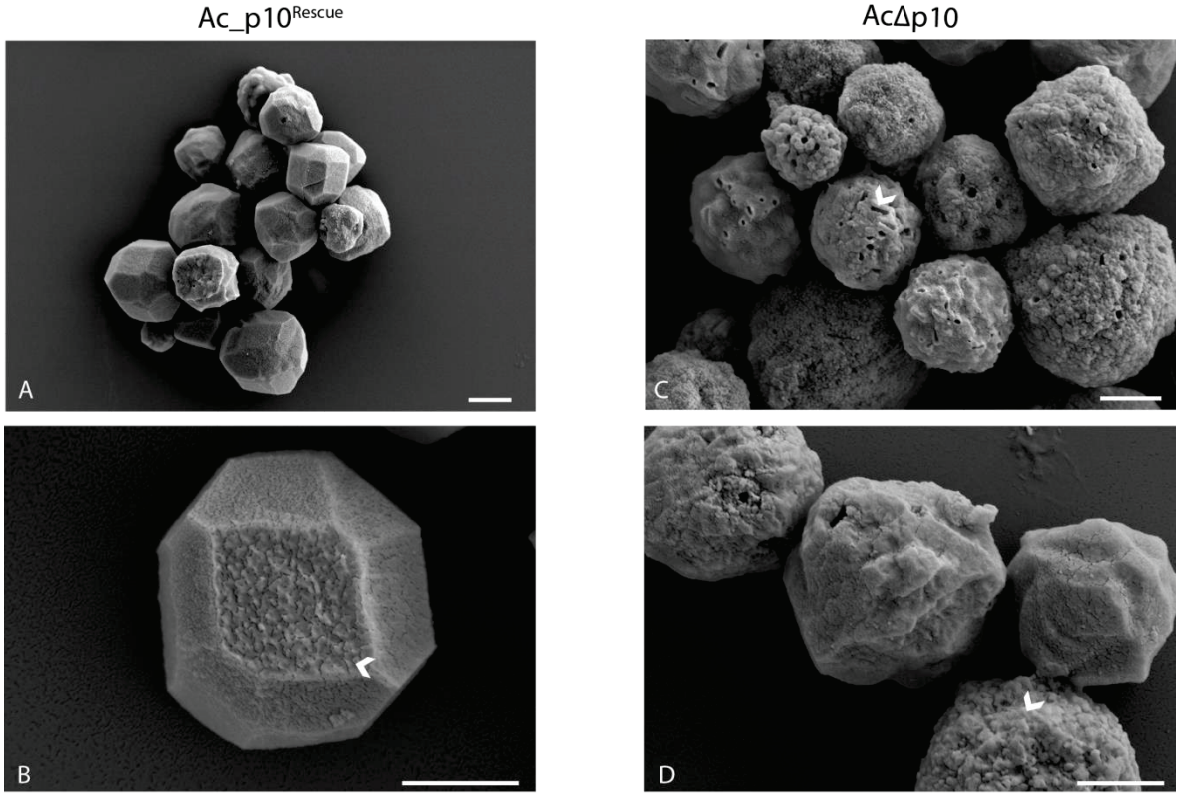

Figure 3.20 High resolution SEM images of calyx morphology on purified polyhedra. SEM images of purified polyhedra from Ac_*p10*^{Rescue} (A-B) and AcΔ*p10*-infected TN-368 cells (C-D) were fixed and imaged using a Zeiss Merlin compact SEM. White arrow (B) shows a close-up polyhedra with textual irregularity, likely from sputter coating. Polyhedra from AcΔ*p10*-infected cells contained polyhedra with pitted (C) and/or rough surface (D) as indicated by white arrow. Captured at extra high tension (EHT) 4.00 kV, variable pressure (VP) 60 Pa. Scale Bar (A) 2μm and (B-D) 1 μm.

SEM images of polyhedra isolated from Ac_*p10*^{Rescue} and AcΔ*p10*-infected cells displayed readily distinguishable morphological differences (Figure 3.20). Polyhedra extracted from Ac_*p10*^{Rescue} cells (Figure 3.20 A and B) predominantly presented a characteristic polyhedron shape with a smooth calyx; a few mis-formed or immature polyhedra were also detected. The rough, flaky texture of polyhedra (white arrow, Figure 3.20 B) is due to the textual irregularity in the gold sputter coating, rather than the polyhedra *per se* (pers. comm. Dr Louise Hughes, Bioimaging Centre Microscopist). Polyhedra extracted from AcΔ*p10*-infected cells exhibited a spherical phenotype that lacked the smooth outer payer (calyx). They often showed a pitted surface (Figure 3.20 C and D), characteristic of an

incomplete calyx and subsequent loss of ODVs during preparation of polyhedral; indicating a lack of ODV stability within polyhedra in the absence of a complete polyhedron envelope (Bischoff and Slavicek, 1999).

Additional SEM images of polyhedra extracted from AcMNPV, Ac_*p10*^{Rescue} and Ac∆*p10*-infected cells were also acquired using a SEM Hitachi S-3400 (images were similar to Figure 3.20, data not shown). This was to enable enough data to perform post-acquisition image processing of polyhedra (n=100) to determine if polyhedra were significantly smaller in the absence of P10. Using image J to calculate size, a cross section measurement of the polyhedra diameter (µm) were recorded and plotted against each other on an XY graph (Figure 3.21).

The size distribution for polyhedra diameter (µm) recorded from AcMNPV, Ac_*p10*^{Rescue} and Ac∆*p10* displayed a positive linear correlation (Figure 3.21 A), indicating polyhedra exhibited a uniformity of shape. The diameter of polyhedra were similar between viruses and primarily clustered between 2-4 µm (Figure 3.20 A).

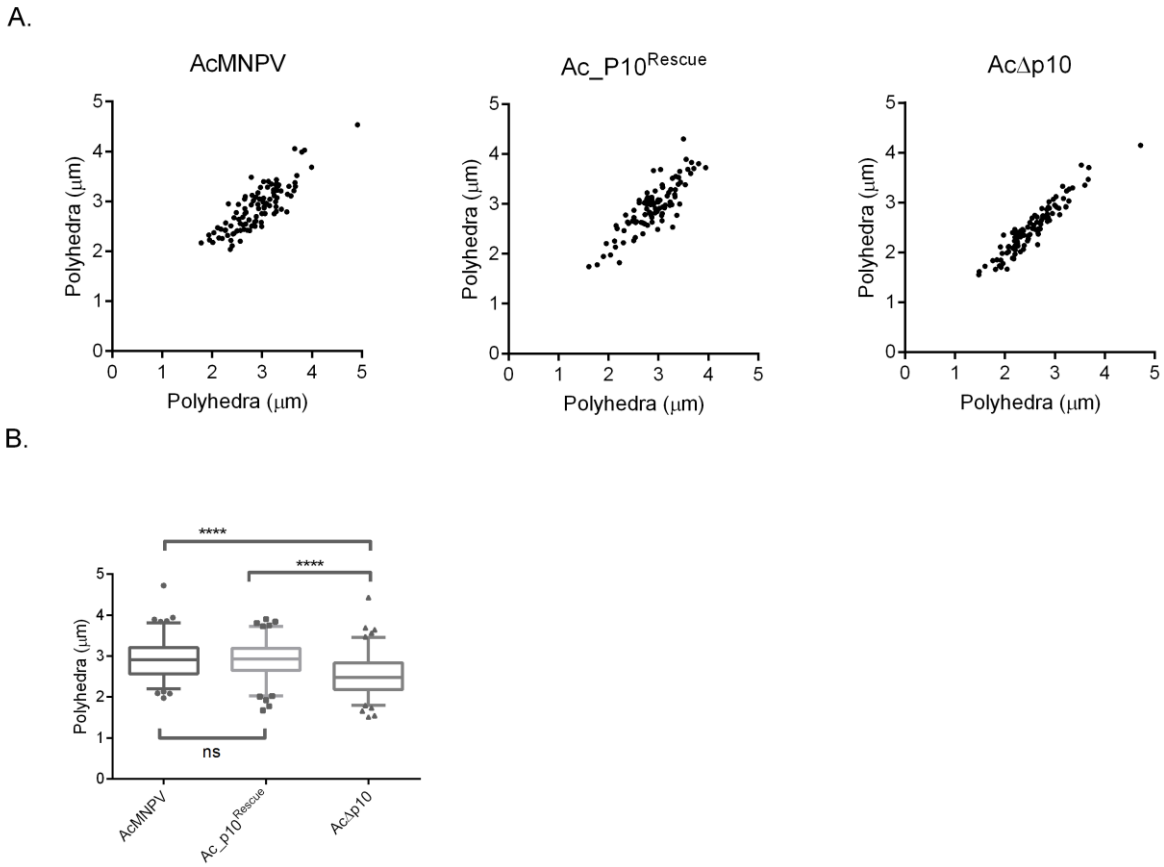

Figure 3.21 Comparative analysis of SEM-imaged polyhedra. (A) Individual XY distribution plots of polyhedra diameters (nm), collected from 100 SEM-imaged AcMNPV, Ac_*p10*^{Rescue} or Ac∆*p10* polyhedra. (B) Box and whiskers plot of mean polyhedra diameter (nm) from AcMNPV, Ac_*p10*^{Rescue} and Ac∆*p10* , n = 100. Bars represent 5-95 % range with outliers plotted. ANOVA represents statistical difference between cohort, **** = < 0.0001 or ns (no significance difference).

The mean polyhedra diameter (µm) was displayed using a box and whiskers plot (Figure 3.21 B) to compare the mean polyhedra size for AcMNPV (mean = 2.896µm), Ac_*p10*^{Rescue} (mean = 2.915µm) and Ac∆*p10* (mean = 2.521µm). To see if the means were significantly different, a one-way ANOVA was performed and the results found a statistical difference between the three viruses ($p<0.0001$, n=3). A Tukey's multiple comparisons post-hoc analysis confirmed the mean size of the Ac∆*p10* (2.521±0.503) polyhedra to be statistically smaller ($p<0.0001$) than both AcMNPV (2.896±0.472) and Ac_*p10*^{Rescue} (2.915±0.447) polyhedra. AcMNPV and Ac_*p10*^{Rescue} showed no statistical difference ($p = 0.9569$) in mean polyhedra size.

3.5 Discussion

Observations of the role P10 plays in polyhedra formation, nuclear stability and lysis, have been documented in this chapter. By using a mix of biochemical and microscopy techniques on newly constructed P10 recombinant viruses (Section 3.2) I hoped to progress previous knowledge of P10 function and produce a validated *p10*-deletion construct that can form the basis for further studies (Chapters 4 and 5).

To examine the possible role of P10 in nuclear stability, confocal microscopy was used to observe P10 structures over time (Section 3.3.4). Microscopy studies used an adherent TN-368 cell line largely due to its large and extensive cytoplasmic volume (Hink, 1970), which allowed complex cytoplasmic structures to be observed more clearly (Carpentier *et al.*, 2008). P10-associated filaments were seen to condense during the later phases of infection to form thicker structures that aligned to form a thick perinuclear cage. It has been postulated that due to the timing of formation of this cage, at 48-96 hpi, this structure may help preserve the integrity (stability) of the nucleus to allow maturation of polyhedra (Carpentier and King, 2009). Once polyhedra have matured, the cage-like structure may undergo a conformational shift, possibly linked to phosphorylation (Raza, 2013), which disrupts the nuclear envelope to liberate polyhedra. Investigations into nuclear lysis in this chapter (Figure 3.11) confirmed that in the absence of P10, and the cage-like structure (Figure 3.13-3.16), polyhedra remain confined within an intact 'nuclear structure' for many days post-infection (even weeks, R D Possee, pers. comm.). To investigate this theory further, an exciting new microscopy technique, serial block face scanning electron microscopy (SBF-SEM), was used to obtain high resolution 3D images of P10 structures (Chapter 6).

P10 was first shown to be a mediator of cell lysis in a study by William et al. (1989), who observed an absence of free polyhedra in the cell culture medium from a recombinant

AcMNPV that did not synthesise detectable levels of P10; compared to wild-type virus that showed many free polyhedra. To explore further the role of P10 in cell lysis, an optimum cell line was required. It was important to use a cell line that represented as closely as possible a 'native infection'. Two cell lines, *Sf9* and *T.ni*, were investigated (section 3.3.3). Sf9 is widely used for wild-type and recombinant AcMPNV propagation (Summers and Smith, 1987; Wang *et al.*, 1992) and Tni (Hi5) cells are commonly used for recombinant protein production studies (Wickham *et al.*, 1992; Davis *et al.*, 1993; Miller, 1997).

It was shown in Figure 3.9 that both cell types infected with AcMNPV displayed the presence of polyhedra within the host cell nucleus after 4 days, including a few free polyhedra observed in the cell medium, suggestive of nuclear lysis. On comparison, Hi5 cells consistently displayed earlier lysis and by 7 dpi there was a notable sharp increase in free polyhedra observed in the cell medium that completely covered the 35 mm dish. Whilst the nuclear lysis was present in infected Sf9 cells, the levels were still statistically lower than that observed in Hi5 cells (Figure 3.9) as calculated by free polyhedra.

This variability is likely to result from different requirements for late/very late expression factor genes, which have a direct impact on *p10* and *polh* promoter activity (Morris and Miller, 1992; Lu and Miller, 1995). Phylogenetic studies on the two cell lines have indicated that *T.ni* represents a closer phylogenetic variance to *Autographa californica*, the 'native' host. *T.ni* Hi5 cells were derived from *Trichoplusia ni* (Cabbage looper), which originated from the same subfamily Plusiinae, as *A. californica* (Alfalfa looper). Whereas *Sf*9 cells originate from *Spodoptera frugiperda* (Fall armyworm moth), which is a different subfamily, Noctuidae (Speidel *et al.*, 1996; Zahiri *et al.*, 2011). For these reasons, *T.ni cells* (either Hi5 or the adherent line TN-368) were chosen to study the role of P10 in the remaining work of this thesis.

P10 has also been implicated in the formation of the PE or calyx, which represents the final stage of polyhedra maturation (MacKinnon *et al.*, 1974; Vlak *et al.*, 1988; Williams *et al.*, 1989; Carpentier *et al.*, 2008). Early microscopy studies by Summers *et al*. (1969) observed an intimate relationship between P10, EDS and the PE. They observed densely stained 'membrane-like' structures (referred to as EDS) associating with both fibrous material (P10) and polyhedra. Interestingly, the paper posed a question that is still unanswered today: by what process and from what source do EDS arise? To determine if P10 played a role in EDS processing, P10 deletion mutants were constructed, however, conflicting results on the whether P10 was required and what role it played in EDS formation were published (Croizier *et al.*, 1987; Vlak *et al.*, 1988; Williams *et al.*, 1989; van Oers *et al.*, 1993). This chapter confirmed that EDS were present in the absence of P10 (Section 3.3.5), confirming that P10 is not a pre-requisite for EDS formation.

In the presence of P10, the EDS were found wrapped around polyhedra (Figure 3.17 – 3.18), supporting the theory P10 has a role in the formation of the PE. Whether EDS are precursors of the PE or represent condensation of extraneous surplus fibrous material has been unclear (Chung *et al.*, 1980); the studies presented in Chapter Six attempt to clarify this further. In the absence of P10 (Figure 3.19), the EDS failed to wrap around the polyhedra, instead they formed ring-like structures that rarely associated with polyhedra (Figure 3.19, black arrow). This suggests that P10 may play a chaperone-like role in transferring the EDS to the surface of maturing polyhedra, which is further examined using SBF-SEM (Chapter 6).

The initial focus of this thesis and chapter was for the successful characterisation of Ac∆*p10_lacZ* (Figure 3.2, 3.5), which can be used to introduce modified *p10* sequences into the virus genome at the natural *p10* locus. Using this system, two recombinant AcMNPV viruses were made, with either the complete deletion or restoration of *p10* coding sequence to the AcMNPV virus genome (Section 3.4). These viruses were consequently characterised to determine the role P10 plays during infection of a host cell. Importantly the validation of Ac∆*p10_lacZ* and P10 work presented in this chapter provided the tools and understanding for future studies of additional P10 variants made using the same system. This work has been presented in Chapters Four and Five.

Chapter Four:

Characterising the specificity of *p10* functions with a bioinformatic and biochemical approach

4.1 Introduction

Bioinformatics has become increasingly popular for analytical analysis of proteins, offering complex computer algorithms for interpretation of aa sequences to rapidly generate complex proteomic information. Due to the increase in computing capabilities and advancements in DNA sequencing, new baculovirus genomes are becoming more publicly available. This increased availability of data has led to an additional 18 new genomes containing recognisable *p10* sequences on NCBI database since the last wide-scale P10 bioinformatics surveys (Carpentier, 2008; Raza, 2013)

To date, 70 complete sequenced baculovirus genomes have been published on NCBI, with 44 alphabaculovirus, 20 betabaculovirus, 1 deltabaculovirus, 3 gammabaculovirus and 2 unclassified baculovirus genomes identified by the taxonomy browser. Of these 70 genomes, a search identified 59 isolates that encoded a recognisable *p10* from alphabaculovirus type I or type II, and betabaculovirus (Table 4.1A, B and C). Interestingly, deltabaculovirus and gammabaculovirus do not encode an identifiable *p10* sequence.

Despite the presence of nearly 60 *p10* sequences within the database, most studies on P10 have focused on AcMNPV. Therefore, similar to previous studies that used either *S. exigua*(Se) MNPV P10 (van Oers *et al.*, 1994) or later *Buzura suppressaria*(Busu) NPV P10 (van Oers *et al.*, 1998) in an AcMNPV genome, alphabaculovirus type ll SfMNPV *p10* was expressed in an alphabaculovirus type I AcMNPV backbone to further explore *p10.* This was to determine if *p10* can be transferred between species and still retain function.

The construction of recombinant virus SfMNPV *p10* in an AcMNPV WT background was initially chosen due to earlier results obtained in Chapter Three. It was observed that WT AcMNPV lysis was greater in *T.ni* cells (Chapter Three) compared to AcMNPV-infected Sf cells, as confirmed by numerous more free polyhedra observed in the AcMNPV-infected Hi5 media. It was postulated that a host cell specific effect between the more natural host, *T.ni* and AcMNPV *p10,* may account for the increased levels of lysis. It was therefore proposed that if SfMNPV *p10* was inserted into AcΔ*p10*_lacZ backbone creating Ac_Sf*p10*, this virus would produce increased lysis of virus-infected Sf cells.

In summary, this study was designed to provide new information on host cell specificity and increase our current understanding on why we observed different lysis profiles in different cell lines (Hi5, Sf9 and Sf21). Furthermore, this study will provide an alternative to the already well-studied AcMNPV type I P10.

4.2 Baculovirus P10 homologues

An updated protein search of the NCBI database identified 59 isolates that encoded a recognisable P10 sequence (Table 4.1). This data provided new information on prior studies on P10 homologues (Carpentier *et al.*, 2008) and warranted new bioinformatic analysis to identify sequence similarities.

The P10 sequences were grouped into three tables for Alphabaculovirus type 1 and II, and Betabaculovirus (Table 4.1 A, B & C respectively).

Table 4.1(A) Alphabaculovirus Type I P10 homologue sequence information

Virus	Orf	Accession number	P10 size (aa)	Date added
Autographa californica nucleopolyhedrovirus_kuzio (HR3 strain)	Orf 137	AAA46726	94	02/08/1993
Autographa californica nucleopolyhedrovirus C6 (AcMNPV)	Orf 137	NP_054167	94	28/03/2016
Antheraea pernyi nucleopolyhedrovirus (ApNPV)	Orf 21	YP_610990	87	08/12/2008
Anticarsia gemmatalis nucleopolyhedrovirus (AgNPV)	Orf 133	YP_803527	93	03/06/2015
Bombyx mandarina nucleopolyhedrovirus (BmNPV)	Orf 121	ACQ57311	70	19/04/2010
Bombyx mori NPV (BmNPV)	Orf 122	NP_047535	70	08/10/2002
Choristoneura fumiferana DEF MNPV (CfMNPV_Def)	Orf 131	NP_932740	89	22/12/2010
Choristoneura fumiferana MNPV (CfMNPV)	Orf 129	NP_848440	81	28/03/2016
Choristoneura murinana alphabaculovirus (ChmuNPV)	Orf 21	YP_008992113	81	04/02/2014
Choristoneura occidentalis alphabaculovirus (CoNPV)	Orf 20	AGR56909	81	28/07/2013
Choristoneura rosaceana alphabaculovirus (CrNPV)	Orf 21	YP_008378374	81	05/08/2013
Condylorrhiza vestigialis MNPV (CoVeNPV)	Orf 20	YP_009118503	93	06/02/2015
Epiphyas postvittana NPV (EpNPV)	Orf 120	NP_203289	85	11/03/2010
Hyphantria cunea nucleopolyhedrovirus (HyCuNPV)	Orf 20	YP_473208	88	18/12/2008
Maruca vitrata nucleopolyhedrovirus (MvNPV)	Orf 105	YP_950835	73	15/09/2008
Orgyia pseudotsugata MNPV (OpMNPV)	Orf 133	NP_046289	90	08/09/2010
Plutella xylostella multiple nucleopolyhedrovirus (PlxyMNPV)	Orf 135	ABE68520	94	29/10/2007
Rachiplusia ou MNPV (RaouMNPV)	Orf 132	AAN28152	94	07/07/2003
Thysanoplusia orichalcea NPV (ThorNPV)	Orf 134	YP_007250541	94	02/01/2013

*AcMNPV_HR3 strain was analysed during this project

Table 4.1(B) Alphabaculovirus Type II P10 homologue sequence information

Virus	Orf	Accession number	P10 size (aa)	Date added
Adoxophyes honmai NPV (AdhoNPV)	Orf 32	NP_818679	92	11/08/2006
Adoxophyes orana nucleopolyhedrovirus (AdorNPV)	Orf 31	YP_002300549	92	30/04/2012
Agrotis ipsilon multiple nucleopolyhedrovirus (AgipMNP)	Orf 150	YP_002268180	81	09/10/2008
Agrotis segetum nucleopolyhedrovirus (AgseNPV_A)	Orf 143	YP_529813	87	07/01/2010
Agrotis segetum nucleopolyhedrovirus B (AgseNPV_B)	Orf 140	YP_009112701	100	21/08/2015
Apocheima cinerarium nucleopolyhedrovirus (ApciNPV)	Orf 100	YP_006607870	88	28/08/2012
Buzura suppressaria nucleopolyhedrovirus (BusuNPV)	Orf 7	YP_009001784	94	13/02/2014
Chrysodeixis chalcites nucleopolyhedrovirus (CcNPV)	Orf 18	YP_249622	88	07/01/2010
Clanis bilineata nucleopolyhedrovirus (CbNPV)	Orf 20	YP_717558	103	06/08/2009
Ecotropis obliqua NPV (EoNPV)	Orf 19	YP_874212	87	24/05/2007
Euproctis pseudoconspersa nucleopolyhedrovirus (EupsNPV)	Orf 50	YP_002854660	90	01/05/2009
Helicoverpa armigera multiple nucleopolyhedrovirus (HearMNPV)	Orf 152	ACH88674	83	30/11/2008
Helicoverpa armigera NPV (HearNPV)	Orf 121	NP_203577	87	01/12/2009
Helicoverpa armigera NPV NNg1 (HearNPV_NNg1)	Orf 20	BAG74585	87	30/11/2009
Helicoverpa armigera nucleopolyhedrovirus G4 (HearNPV_G4)	Orf 21	AAG53764	87	06/11/2007
Helicoverpa zea SNPV (HzSNPV)	Orf 20	AAL56165	87	01/04/2002
Hemileuca sp. Nucleopolyhedrovirus (HespNPV)	Orf 23	YP_008378239	103	28/10/2013
Leucania separata nucleopolyhedrovirus (LsNPV)	Orf 21	YP_758318	108	20/08/2015
Lymantria dispar MNPV (LdMNPV)	Orf 41	NP_047677	77	11/03/2010
Lymantria xylina MNPV (LyxyMNPV)	Orf 37	YP_003517777	77	29/03/2010
Mamestra brassicae multiple nucleopolyhedrovirus (MabrMNPV)	Orf 148	YP_009011213	83	11/03/2014
Mamestra configurata NPV-A (McNPV_A)	Orf 159	NP_613242	85	28/04/2010
Mamestra configurata NPV-B (McNPV_B)	Orf 158	NP_689332	83	23/03/2016
Orgyia leucostigma NPV (OlNPV)	Orf 21	YP_001650931	92	22/04/2008
Pseudoplusia includens SNPV (PsinSNPV)	Orf 19	YP_009116932	87	17/03/2015
Spodoptera exigua MNPV (SpexMNPV)	Orf 130	NP_037890	88	21/08/2015
Spodoptera frugiperda MNPV (SfMNPV)	Orf 132	YP_001036424	105	15/04/2011
Spodoptera litura NPV (SpliNPV)	Orf 19	NP_258287	105	30/11/2009
Spodoptera litura nucleopolyhedrovirus II (SpliNPV_II)	Orf 136	YP_002332832	92	02/12/2008
Trichoplusia ni SNPV (TniSNPV)	Orf 18	YP_308907	91	06/05/2009

Table 4.1 C Betabaculovirus P10 homologue sequence information

Virus	Orf	Accession number	P10 size (aa)	Date added
Adoxophyes orana granulovirus (AdorGV)	Orf 14	NP_872468	116	01/12/2009
Choristoneura occidentalis granulovirus (ChocGV)	Orf 45	YP_654466	104	25/07/2007
Clostera anachoreta granulovirus (CaGV)	Orf 16	YP_004376224	101	28/06/2011
Clostera anastomosis granulovirus (ClanGV)	Orf 16	YP_008719964	102	04/11/2013
Helicoverpa armigera granulovirus (HearGV)	Orf 18	YP_001648987	84	20/07/2011
Pieris rapae granulovirus (PrGV)	Orf 17	YP_003429341	104	14/08/2012
Plutella xylostella granulovirus (PlxyGV)	Orf 2	NP_068221	83	30/11/2009
Pseudaletia unipuncta granulovirus (PsunGV)	Orf 5	YP_003422344	119	01/02/2010
Spodoptera litura granulovirus (SpliGV)	Orf 4	YP_001256955	78	07/01/2010
Xestia c-nigrum granulovirus (XecnGV)	Orf 5	NP_059153	84	11/03/2010

To characterise the P10 sequences presented in Table 4.1 A-C and determine common characteristics, the aa sequences were aligned using T-coffee multiple sequence alignment (Notredame *et al.*, 2000). The sequences were then viewed in Jalview (Figure 4.1). This Java-based software was used to identify conserved regions, quality of read and projected consensus sequences and was annotated with Clustal X default colouring (Figure 4.1).

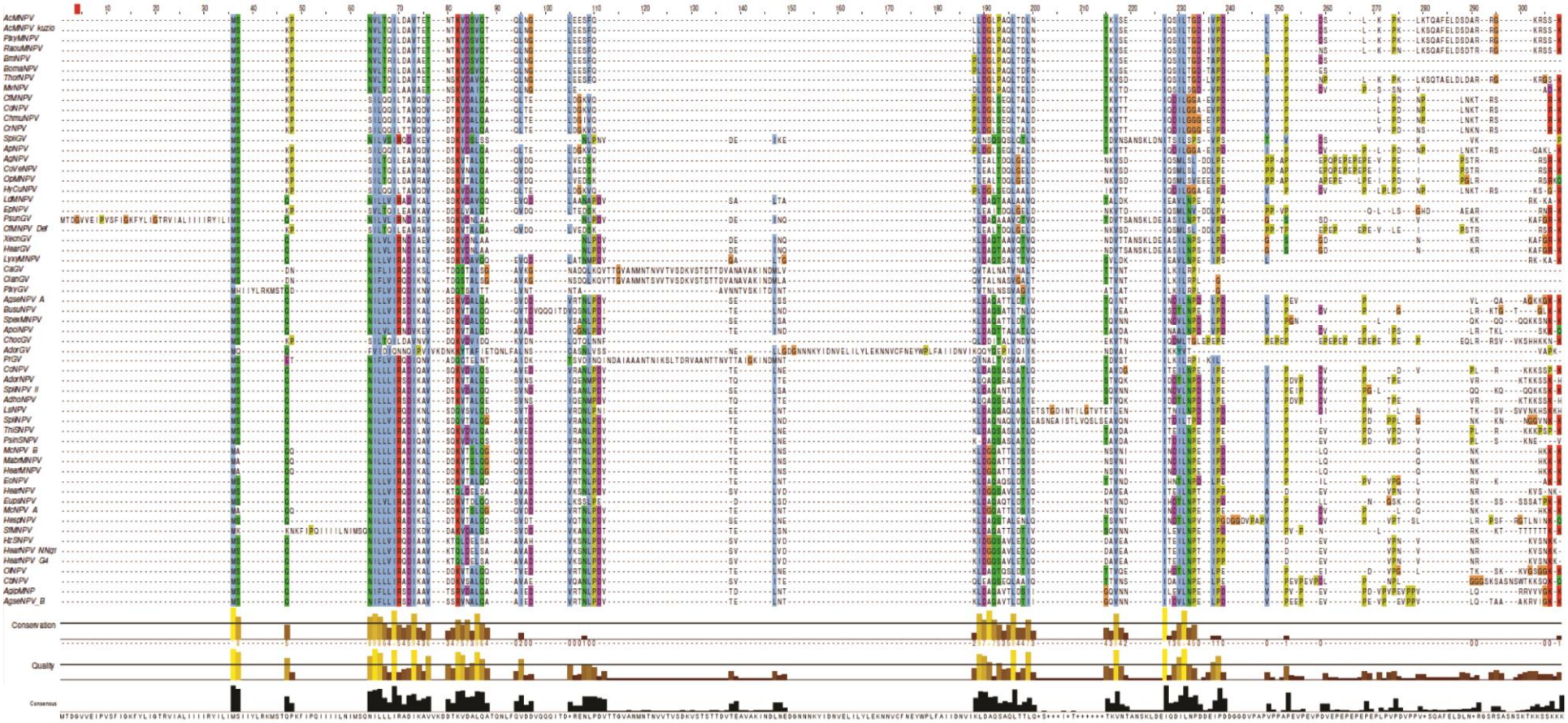

Figure 4.1 Multiple sequence alignment of detectable P10 sequences in Alphabaculovirus and Betabaculovirus. T-coffee multiple sequence alignment of P10 homologues were analysed with Jalview sequence alignment tool that show a higher conservation at the N-terminus. Clustal X default colouring was selected to annotate: positive charge (red), negative charge (magenta), polar (green), hydrophobic (blue), pink (cysteines), prolines (yellow), glycines (orange) aromatic (cyan). Conserved regions and the quality of these regions are indicated by a yellow bar, with a conservation score displaying accuracy of likeliness of the conserved region. A high-resolution image is provided in a CD (Supplementary X) for further identification of specific sequences.

Figure 4.1 shows an alignment of baculovirus P10 sequences found in alphabaculovirus I and II, and betabaculovirus. Analysis confirmed the presence of three primary domains, a more highly conserved region in the N-terminus coiled-coil domain and a proline-rich and basic positive-charged region at the C-terminus (van Oers *et al.*, 1993). Only alphabaculovirus BomaNPV and BmNPV lacked a notable positively-charged region at the C-terminus (Figure 4.1). Interestingly, most betabaculoviruses (SpliGV, PlxyGV, PrGV, ClanGV, CaGV and AdorGV) lacked the characteristic proline-rich and positively-charged domains shown with the other P10 homologues. In Figure 4.1, the quantitative alignment of the all P10 homologues are indicated by the size of the yellow/brown bars (Figure 4.1, consensus). These bars represent a calculated score indicating the associated, conserved physico-chemical properties (Livingstone and Barton, 1993). The higher the score, the more similar the aa are, with * representing identical aa sequence at that location. The bars indicate that the coiled-coil domain contains a more highly conserved aa with a consensus sequence of MSQNILLLI most prevelant (Figure 4.1). The variable domain indicates a greater sequence variation between homologues with only a few commonly related aa's (Figure 4.1).

The possible roles associated with these domains have been discussed in greater detail in chapter one (section 1.4.6, Figure 1.7).

To further characterise these P10 sequences and identify potential evolutionary relationships, phylogenetic studies were carried out on all 59 sequences (Figure 4.2). The aligned P10 sequences shown in Figure 4.1 were sent to ClustalW2-phylogeny for phylogenetic analysis. Default settings were chosen for rooted tree analysis using the neighbour-joining method (Saitou and Nei, 1987). This study importantly provides an update on the previous phylogenetic analysis (Carpentier *et al.*, 2008) to include all recent *p10* sequence data from Alphabaculovirus Type I and II, and Betabaculovirus.

Interestingly, even with a low percentage similarity between P10 proteins, which was often observed below 20% (data not shown), an evolutionary separation still grouped most NPV P10 homologues into group I and group II (Jehle *et al.*, 2006; Miele *et al.*, 2011). This was not seen with LdMNPV and LyxyMNPV, which were grouped into a separate clade containing primarily Alphabaculovirus type I. This is in contrast to genome characterisation that places them as Alphabaculovirus type II (Figure 4.2 *, Miele *et al.*, 2011). Interestingly, Betabaculoviruses were shown in Figure 4.2 to diverge from Alphabaculovirus group I, suggesting a closer evolutionary pattern and common ancestor than had previously been thought. This is in contrast to previous genome phylogeny (based on core genes) that locate betabaculovirus on separate branches or clades to both type I and II Alphabaculovirus (Jehle *et al.*, 2006; Miele *et al.*, 2011).

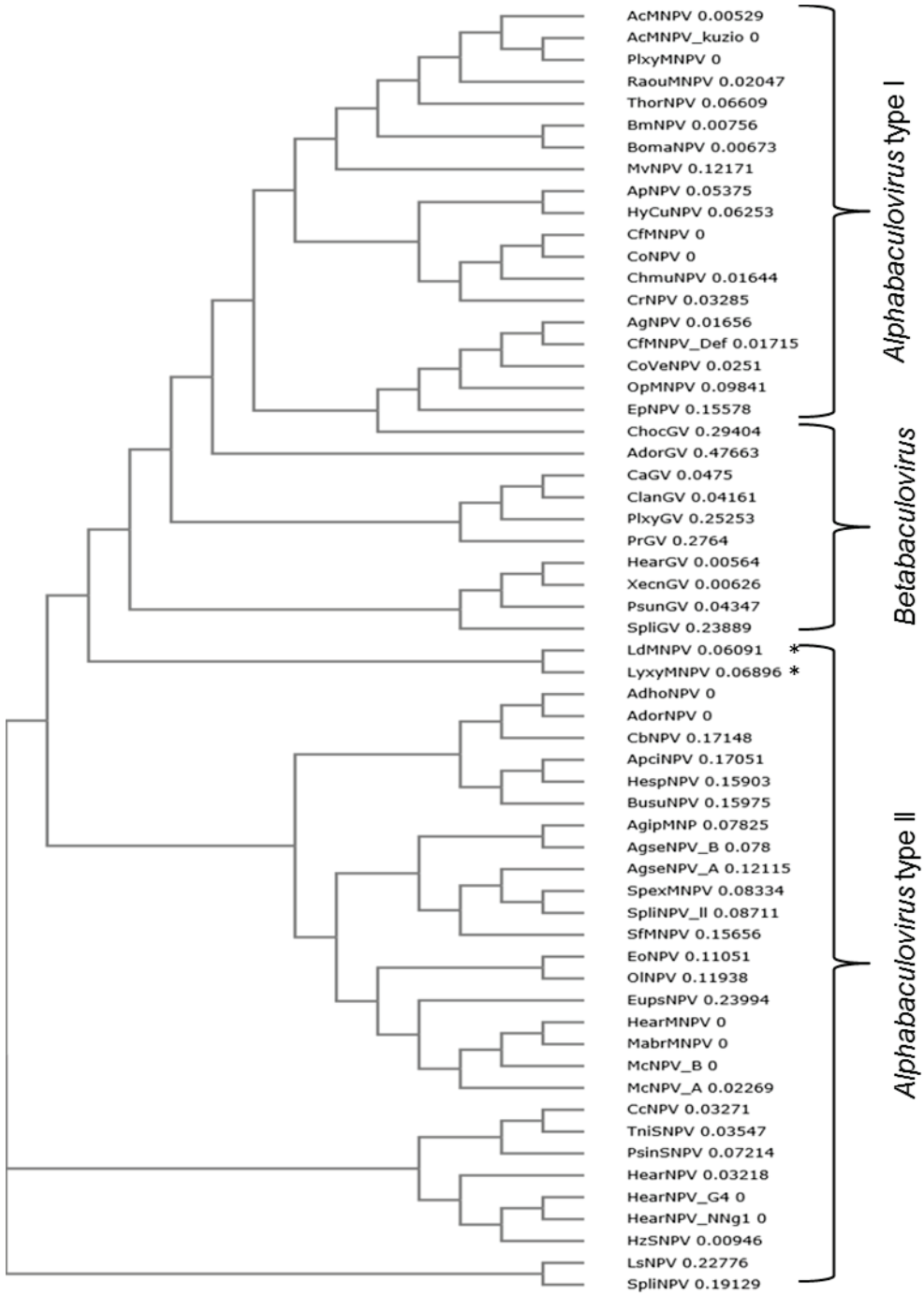

Figure 4.2 Baculovirus P10 phylogenetic tree. Rooted phylogenetic Neighbour-joining tree generated from T-Coffee multiple sequence alignment of P10 and sent to ClustalW2-phylogeny. The P10 sequences of alphabaculovirus type I and type II show a separation. Default phylip format was used with false distance correction, excludes gaps, false percentage identity matrix selected. * indicates location LdMNPV and LyxyMNPV.

However, even though P10 displays distinct groupings (Figure 4.2), it is difficult to determine if this separation presents different characteristics, as not all genomes encoding P10 have been studied in detail. Therefore, it is possible this evolutionary separation shown in Figure 4.2 could indicate varying P10 morphologies and roles.

Furthermore, it was also important to note that phylogenetic trees are only predictive therefore interpretation of Figure 4.2 was only used to theorize relationships.

An alternative phylogenetic tool, T-rex (Appendix 3.1) gave similar results to Figure 4.2 further confirming an evolutionary divergence between group I and group II. The GV were distributed on separate clades and indicates an evolutionary separation.

4.2.2 Functional domains of type I AcMNPV and type II SfMNPV P10

Prior to construction of the recombinant AcMNPV virus expressing SfMNPV P10, a bioinformatic analysis of AcMNPV and SfMNPV P10 was undertaken to define sequence similarities (see Table 4.1). A multiple sequence alignment of AcMNPV and SfMNPV P10 aa sequences was performed using T-coffee software (Notredame *et al.*, 2000) to compare pairwise alignments and identify regions of similarity (Figure 4.3).

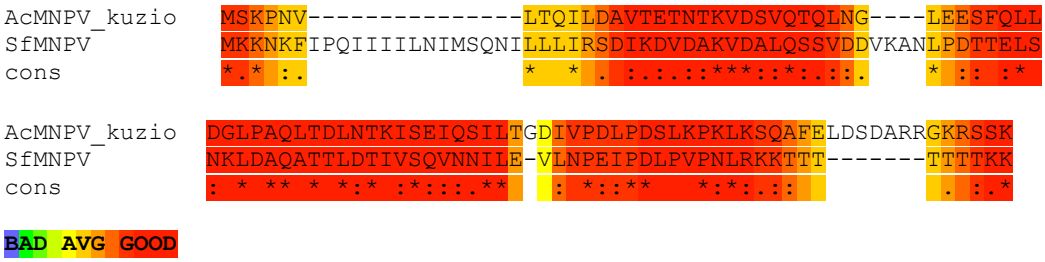

Figure 4.3 Clustal T-Coffee multiple sequence alignment of AcMNPV and SfMNPV P10. Displays the amino acid sequence and alignment between a type I (AcMNPV P10) and type II (SfMNPV P10) alphabaculovirus. The symbols: * single conserved region, : indicates conservation between groups of strong properties and . indicates conservation for weak similar properties.

The clustal T-Coffee alignment in Figure 4.3 displays the 94 aa of AcMNPV aligned with the 104 aa of SfMNPV, with a sequence identity matrix of 29.07%. The alignment proposes that identical conserved regions between homologues are limited to sequences of only one, two or three amino acids including sites of strong and weak conservation (Figure 4.3). Furthermore, Figure 4.3 shows that SfMNPV contained fifteen aa at the N-terminus that were not aligned, whilst seven aa at the C-terminus of AcMNPV did not align. Additional colouration of the aa sequence in Figure 4.3 varying from red (good) to blue (bad), displayed the transitive consistency score (TCS), which is a value of between 1-9 (Chang *et al.*, 2014). The amino-acids coloured in red correlate to a TCS of 5-9 and indicate the trustworthiness of the sequence.

Additional comparisons were also performed on COILS (Lupas *et al.*, 1991) for predicted coiled-coil regions (Figure 4.4). A comparative structural analysis of AcMNPV and

SfMNPV was performed using COILS, which indicated that both P10 structures contained similar positioned coiled-coil regions at the N-terminus (Figure 4.4), which is in agreement with previous analysis (Van Oers *et al.*, 1993; 1997).

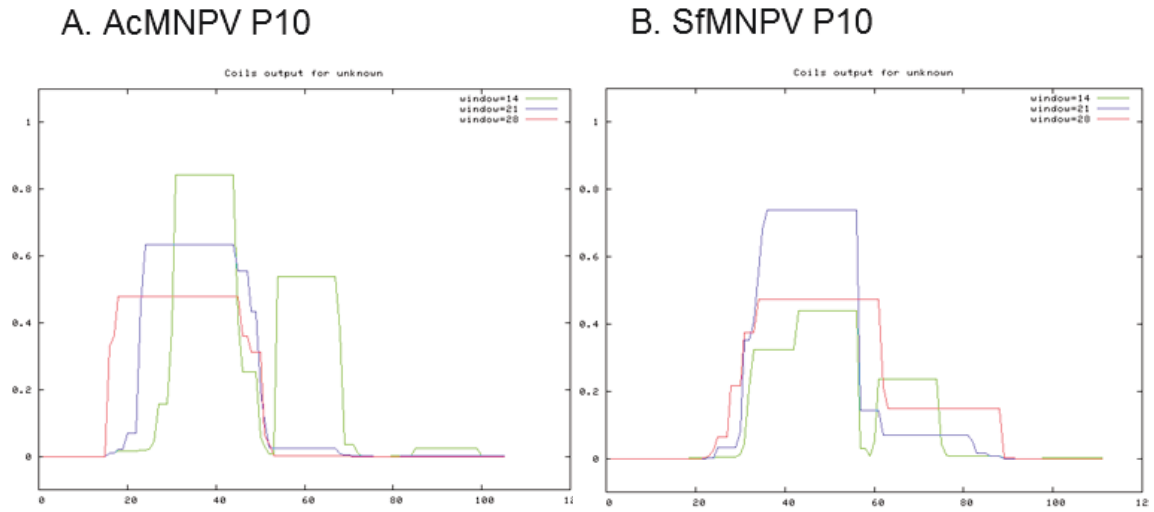

Figure 4.4 Coiled-Coils output for AcMNPV P10 and SfMNPV P10. P10 sequence of AcMNPV and SfMNPV was input into COILS (Lupas *et al.*, 1991), a bioinformatics tool for visualising predicted location for coils in a protein sequences. COILS predicted both P10 sequences to have a coil like structure at the N-terminus coil of the protein.

In addition, further protein analysis was performed with PredictProtein® software for AcMNPV and SfMNPV P10 (Figure 4.5). The results showed a high similarity between the sequences: similar amino-acid composition; secondary structure composition including helix/loop ratio; and solvent accessibility for exposed/buried regions. In addition, gene ontology prediction for both sequences suggested that P10 is a cellular component of virions with a role in occlusion body assembly, with only SfMNPV P10 displaying predictive molecular functions related to nucleotide and compound binding (Figure 4.5 C). Due to the low reliability %, the predictive roles (Figure 4.5 C) are only suggestive and not definitive.

Bioinformatics has become an extremely useful tool for characterising a protein, however as suggested previously, to explore the specificity of *p10* and to determine if associated roles are species-specific, a new virus, Ac_Sf*p10*, was constructed. In this recombinant virus the AcMNPV *p10* was replaced with the SfMNPV *p10* at its natural locus, in what is otherwise a WT AcMNPV.

As discussed earlier, it was proposed that if the host cell interaction with P10 has a direct functional role on the level of lysis, then replacing AcMNPV *p10* with SfMNPV *p10* could increase lysis in Sf cells, possibly to levels similar to that observed in SfMNPV-infected

cells. Therefore, this chapter uses a mixture of biochemical approaches to demonstrate P10 specificity and whether *p10* was functionally interchangeable between viruses, even though AcMNPV and SfMNPV P10 homologues share little sequence homology (Section 4.2.1).

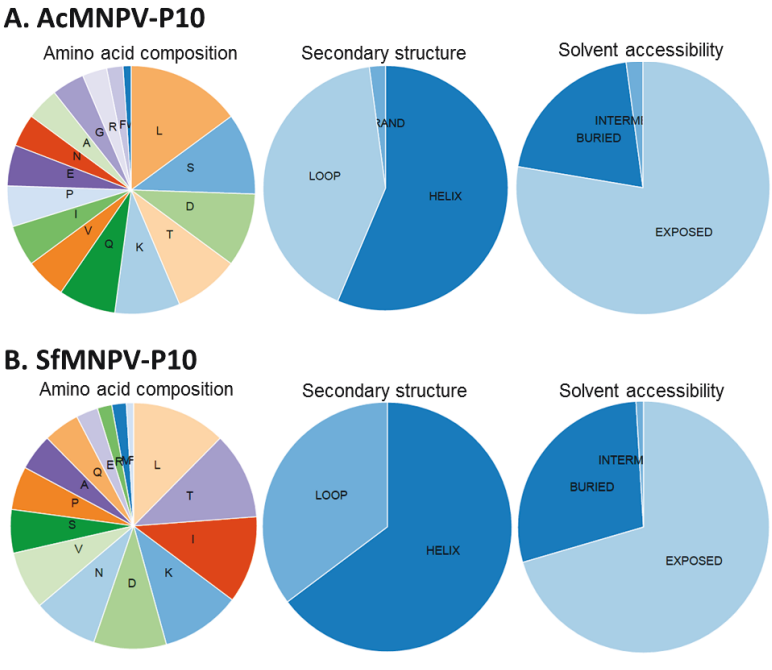

C.

Molecular Function Ontology		
#	GO Term	Reliability (%)
1	Binding	36
2	Nucleotide binding	36
3	Heterocyclic compound binding	36
4	Nucleoside phosphate binding	36
5	Small molecule binding	36
6	Organic cyclic compound binding	36

Figure 4.5 Baculovirus P10 structure annotations. P10 from AcMNPV (A) and SfMNPV (B) were analysed using PredictProtein® for amino acid composition, secondary structure; displaying loop, helix or strand structures. Solvent accessibility identifies ratio of exposed and buried regions. (C) Predicted gene ontology for molecular function of SfMNPV P10.

4.3 Construction of Ac_Sf*p10* virus in which the AcMNPV *p10* coding region is replaced with SfMNPV *p10*

In order to make an Ac_Sf*p10* recombinant virus, a transfer vector containing SfMNPV *p10* coding region was first made and used for homologous recombination in Sf9 cells with Ac∆*p10_lacZ*.

4.3.1 Construction of pAc_Sf*p10*

The transfer plasmid used to replace the AcMNPV *p10* coding region with that of SfMNPV was based on pAcUW1 (Weyer *et al.*, 1990), which contained virus sequences flanking a partial deletion of *p10*. pAcUW1 was digested with *Pac*I and *Hind*III to remove the partial *p10* coding sequence. This was replaced with a PCR-generated SfMNPV *p10* coding sequence, using primers (RDP923 and RDP924, Table 2.9) and SfMNPV DNA as a

template (Figure 4.6 A). Prior to ligation, the PCR fragment was digested with *Pac*I and *Hind*III to generate complementary restriction enzyme sites. This derived a new plasmid, pAc_Sf*p10,* which placed the SfMNPV *p10* coding region under control of the AcMNPV *p10* promoter (Figure 4.6 A).

Following ligation and transformation of competent *E.coli,* eight colonies were picked and screened by restriction enzyme digestion and correct construction of the plasmid was confirmed by DNA sequencing (data not shown).

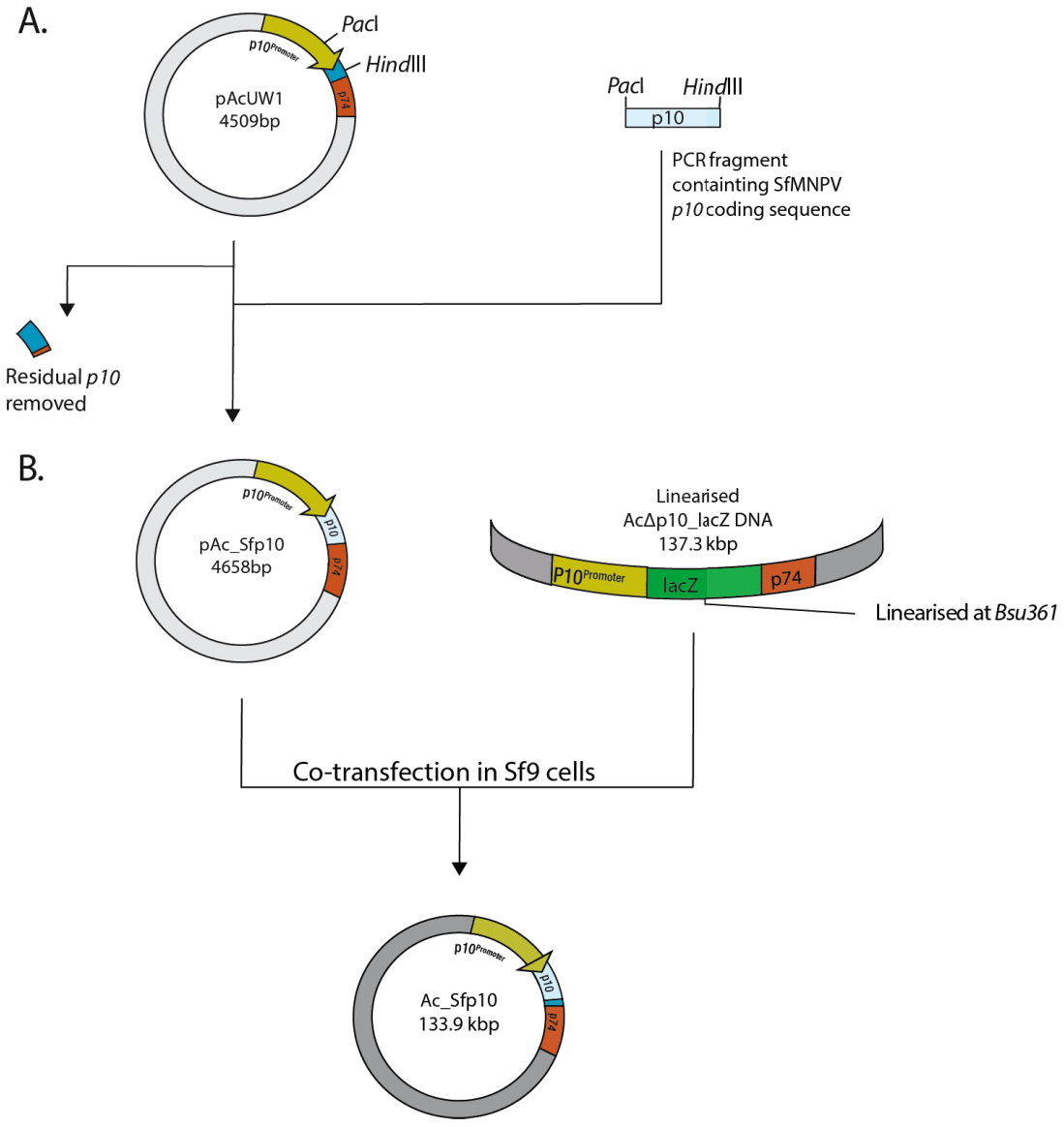

Figure 4.6 Construction of a recombinant AcMNPV virus expressing SfMNPV *p10* coding region under AcMNPV *p10* promoter. (A) pAcUW1 was partially-digested with restriction endonucleases *Pac*I and *Hind*III to remove partial *p10* coding region. The SfMNPV *p10* fragment was amplified using PCR with primers (containing either *Pac*I or *Hind*III) that annealed at the SfMNPV *p10* coding sequence. SfMNPV *p10* fragment was ligated to digested pAcUW1 at complementary *Pac*I and *Hind*III digest sites to form pAc_Sf*p10.* (B) Construction of Ac_Sf*p10* was formed following co-transfection of insect cells with pAc_Sf*p10* and AcΔ*p10_lacZ* DNA, in which lacZ has been replaced with SfMNPV *p10*.

4.3.2 Production of recombinant Ac_Sf*p10* virus

The second phase in the construction for Ac_Sf*p10* virus was the co-transfection of insect (Sf9) cells with pAc_Sf*p10* and Ac∆*p10_lacZ* DNA linearised at the *Bsu*361 site within *lacZ* (Figure 4.6 B, as described in Method 2.3.4), with homologous recombination at the *p10* locus producing virus designated Ac_Sf*p10* (Figure 4.6). This produced a mix of parental *lacZ* (blue) and recombinant Ac_Sf*p10* (colourless) virus when titrated in the presence of X-gal.

Following co-transfection, Ac∆*p10_lacZ,* expressing *lacZ,* and Ac_Sf*p10* were titrated using a reverse selection approach, whereby only clear plaques were selected for plaque-purification. Clear plaques (in the presence of X-gal) were re-titrated until no blue plaques were detected and a pure stock of Ac_Sf*p10* was obtained. Twenty-four clear plaques were selected after the final titration and re-suspended in media prior to infection of Sf9 cells. After 5 days the media was harvested and was designated virus passage P0. To confirm plaque-purification had produced genetically homogenous isolates of Ac_Sf*p10,* free from parental virus, PCR screening at the *p10* locus was undertaken (Figure 4.7).

This was performed on all P0 recombinants to confirm integrity of the Ac_Sf*p10* genome. PCR confirmed: (1) the deletion of *lacZ* and insertion of SfMNPV *p10* coding region by analysis of PCR fragment size using *p10* flanking primers (pAcLG1 and pAcLG4, Figure 4.7 A) and (2) presence of SfMNPV *p10* sequence using specific SfMNPV primers (RDP 923 and RDP 924, Figure 4.7 A). The correct construction of the virus at the *p10* locus was further confirmed by DNA sequencing of recombinants across the *p10* locus (data not shown). After screening, two separate P0 stocks of Ac_Sf*p10* were amplified to produce P1 and P2 working stocks. These virus stocks were also analysed by PCR fragment size (Figure 4.7 B) and DNA sequenced across the *p10* locus to confirm integrity of the Ac_Sf*p10* genome and the absence of a mixed infection.

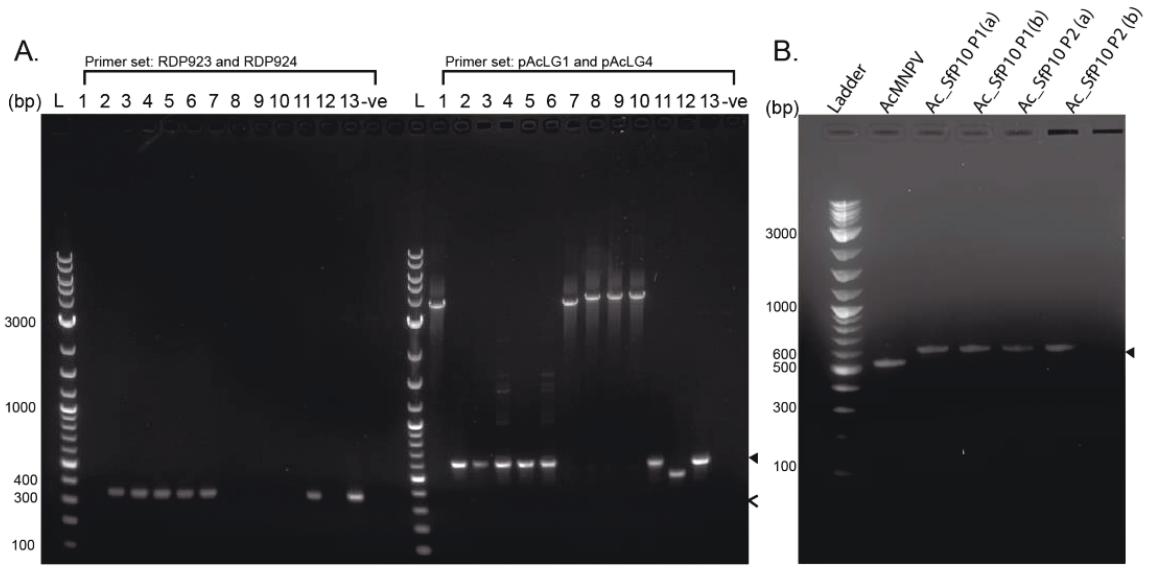

Figure 4.7 Genome analysis of Ac_Sf*p10*. DNA isolated from P0 (A) and P1 and P2 (B) recombinant viruses were characterised by PCR and analysed using 2% agarose gel. Two primer sets were used in (A), RDP923 and RDP924 for a predictive band of 368bp, as indicated by open arrow, and pAcLG1 and pAcLG4 for a predictive band of 630bp, as indicated by a closed arrow. Lanes 1-11 represent homogenous isolates of Ac_Sf*p10,* 12 is an AcMNPV DNA control and 13 is pAcSf*p10* vector, L = 2Log ladder. For (B) pAcLG1 and pAcLG4 primers were used, giving a predictive band of 630bp, as indicated by closed arrow.

4.4 Characterisation of the Ac_SfP10 virus

The following experiments were designed to compare the phenotype of Ac_Sf*p10* with WT AcMNPV-infected cells using a combination of biochemical and microscopy techniques.

4.4.1 Budded virus production

To determine if budded virus production was affected by addition of SfMNPV *p10*, a 72-hour, one-step growth curve was performed comparing BV production from Ac_Sf*p10* and AcMNPV-infected Sf9 cells (Method 2.3.5, Figure 4.8). Sf9 cells were used as they are the preferred cell choice for BV virus production, and provided a direct comparison to budded virus production performed in Chapter Three, Figure 3.7.

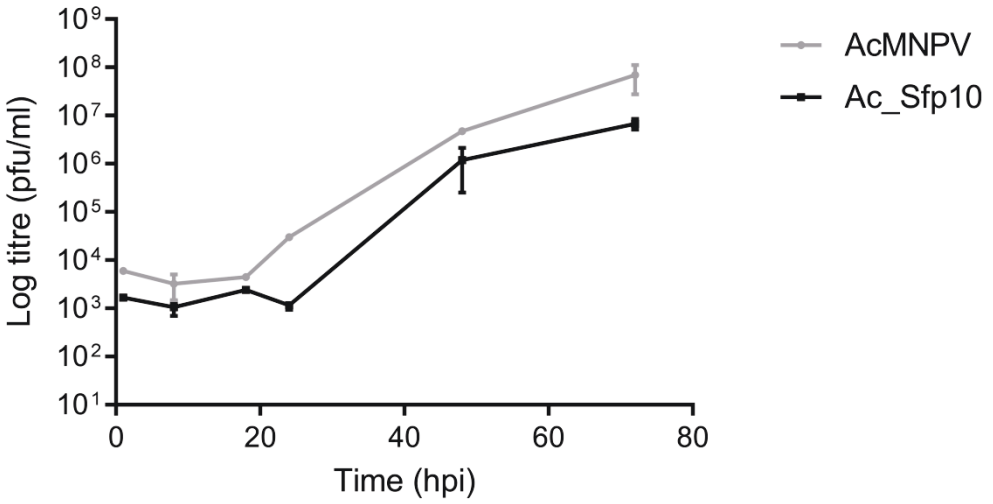

Figure 4.8 One step time course showing budded virus production of Ac_Sf*p10* and AcMNPV in Sf9 cells. Plaque titration of culture media for each virus was performed at 1, 8, 18, 24, 48 and 72 hpi, to determine their budded virus content, Error bars represents mean ± SD (n=2).

Prior to 20 hpi, both viruses showed little increase in BV formation, with Ac_Sf*p10* displaying a slight decrease in BV production compared to AcMNPV. From 20 hpi to 48 hpi, both viruses observed a sharp increase in BV production with a continued increase until the last time point tested at 72 hpi. However, BV production still remained lower for Ac_Sf*p10* compared to AcMNPV at all time points. To test if there was a significance difference in these results, a two-way ANOVA test was performed on each recorded virus titre for AcMNPV and Ac_Sf*p10*. This test confirmed a significant difference in BV titres between the viruses tested ($p = 0.0461$). Post hoc analysis using a Sidak's multiple comparisons test, indicated that the significant difference ($p = 0.0014$) was only observed at 72 hpi. All other time points showed no significant difference, even though an observed difference was seen (Figure 4.8).

4.4.2 Protein synthesis in Ac_Sf*p10*-infected Sf cells.

In order to confirm that the SfMNPV *p10* coding region is expressed when under control of the AcMNPV promoter, Sf9 cells ($1x10^6$ cells/35mm dish) were infected with AcMNPV, SfMNPV or Ac_Sf*p10* at an MOI of 2 pfu/ml (Method 2.3.3a). Infected cells were analysed at 96 hpi by SDS-PAGE and stained with Coomassie blue to detect total protein (Figure 4.9 A) or transferred to a membrane for Western blotting to detect P10 (Figure 4.9 B-C; Method 2.5.2a, 2.5.2b). P10 production was confirmed by detection of a 10 kDa protein (Figure 4.9 A) that was further highlighted using a SfMNPV P10-specific antibody (arrow, Figure 4.9 B). The anti-SfP10 antibody was raised in rabbits against a peptide sequence;

NH_2-CVDDVKANLPDTTEL as advised by GenScript® and the optimal dilution was determined (Table 2.6).

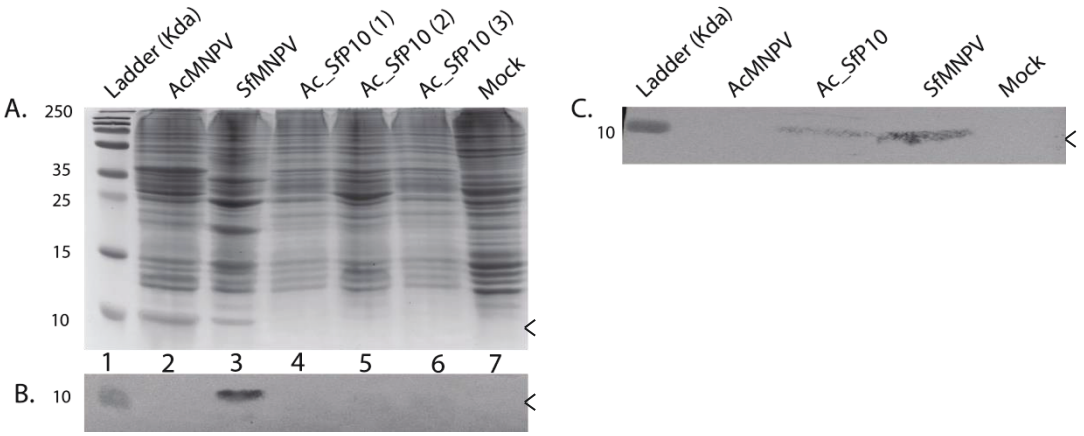

Figure 4.9 Protein synthesis in AcMNPV, SfMNPV and Ac_Sf*p10* infected Sf9 cells. Infected cells were harvested at 96 hpi and total protein fractionated on a 15 % (w/v) SDS-PAGE for either Coomassie staining (A) or western blot analysis (B-C) with a SfMNPV P10-specific antibody using an alkaline phosphate-conjugated secondary antibody. Alkaline phosphate activity was detected with NBT-BCIP (methods 2.5.2b). Lanes 1-7 (B) correlate to sample names at top (A). Three replicates of Ac_SfP10 (1-3) are shown. Virus infected cells in A and B were infected with 2 pfu/cell and 5 pfu/cel in gel C. Arrows show expected sizes of P10. Ladder size (kDa) is indicated, left.

P10 synthesis was observed in AcMNPV- and SfMNPV-infected Sf9 cells by Coomassie staining, which highlighted a P10 associated band at expected size of 10 kDa (arrow, Figure 4.9 A, Lane 2-3). Expression of P10 was undetectable in all three replicates of Ac_Sf*p10*- and mock-infected Sf9 cells (Figure 4.9 A, lanes 4-7). Western blot analysis using a specific SfMNPV P10 antibody (Figure 4.9 B) confirmed the presence of a P10 associated band for only SfMNPV (Figure 4.9 B, lane 3). This confirmed the specificity of the antibody for SfMNPV P10, however, it was not possible to detect P10 in any of the Ac_Sf*p10*-infected cell replicates (Figure 4 B, Lane 4-6). A repeat 15% SDS-PAGE with Western blot (Figure 4.9 C) was performed with AcMNPV-, Ac_Sf*p10*- and SfMNPV-infected Sf9 cells using a higher MOI of 5. This was performed to see if detectable levels of SfMNPV P10 could be observed at a higher MOI (Figure 4.9 C). A P10 associated band was detected for both Ac_Sf*p10* and SfMNPV as indicated by an arrow in Figure 4.9 C, however, decreased band density was observed for Ac_Sf*p10* in comparison to SfMNPV (Figure 4.9 C). This result indicated that SfMNPV P10 was expressed; however, synthesis of SfMNPV P10 was notably lower in Ac_Sf*p10* than WT SfMNPV. Other SDS-PAGE studies showed similar or better expression for P10 in Hi5 cells and Sf21 cells for Ac_Sf*p10* (data not shown) but due to an absence of a detectable P10 in SfMNPV-infected Hi5 cells and low expression in Sf21, Sf9 cells were the preferred choice.

4.4.3 Lysis of insect cells

As P10 has been shown to be essential for nuclear lysis (Williams *et al.*, 1989; van Oers *et al.*, 1993) it was important to determine whether expression of a foreign P10 in an AcMNPV backbone (Ac_Sf*p10*) still resulted in nuclear lysis. By observing lysis in Ac_Sf*p10* infected Sf-cells it will be determined if expression of SfMNPV P10 in its native cell line, *S.frugiperda*, will increase lysis. Answering the question, do we get increased similar lysis to that observed from AcMNPV-infected *T.ni* cells?

It was shown in Chapter Three that different AcMNPV-infected cell lines produced varying characteristics. Infected cells were observed via light microscopy to have contrasting lysis profiles and polyhedra production. It was, therefore, important when interpreting lysis and cell phenotype from Ac_Sf*p10*, AcMNPV and SfMNPV infections to compare them in a variety of different cell lines. This will indicate whether a host cell specific interaction with a native (SfMNPV) P10 causes increased lysis or whether Ac_Sf*p10* has the same effect in all cell types.

To study this impact *Sf*21, Sf9 ($1x10^6$ cells/35mm dish) and Hi5 ($0.5x10^6$ cells/35mm dish) cells were infected with AcMNPV, SfMNPV and Ac_Sf*p10* at 5 MOI (Method 2.3.3a). The infected cells were then imaged using a light microscope Zeiss Axiovert 135 at 5 and 7 dpi.

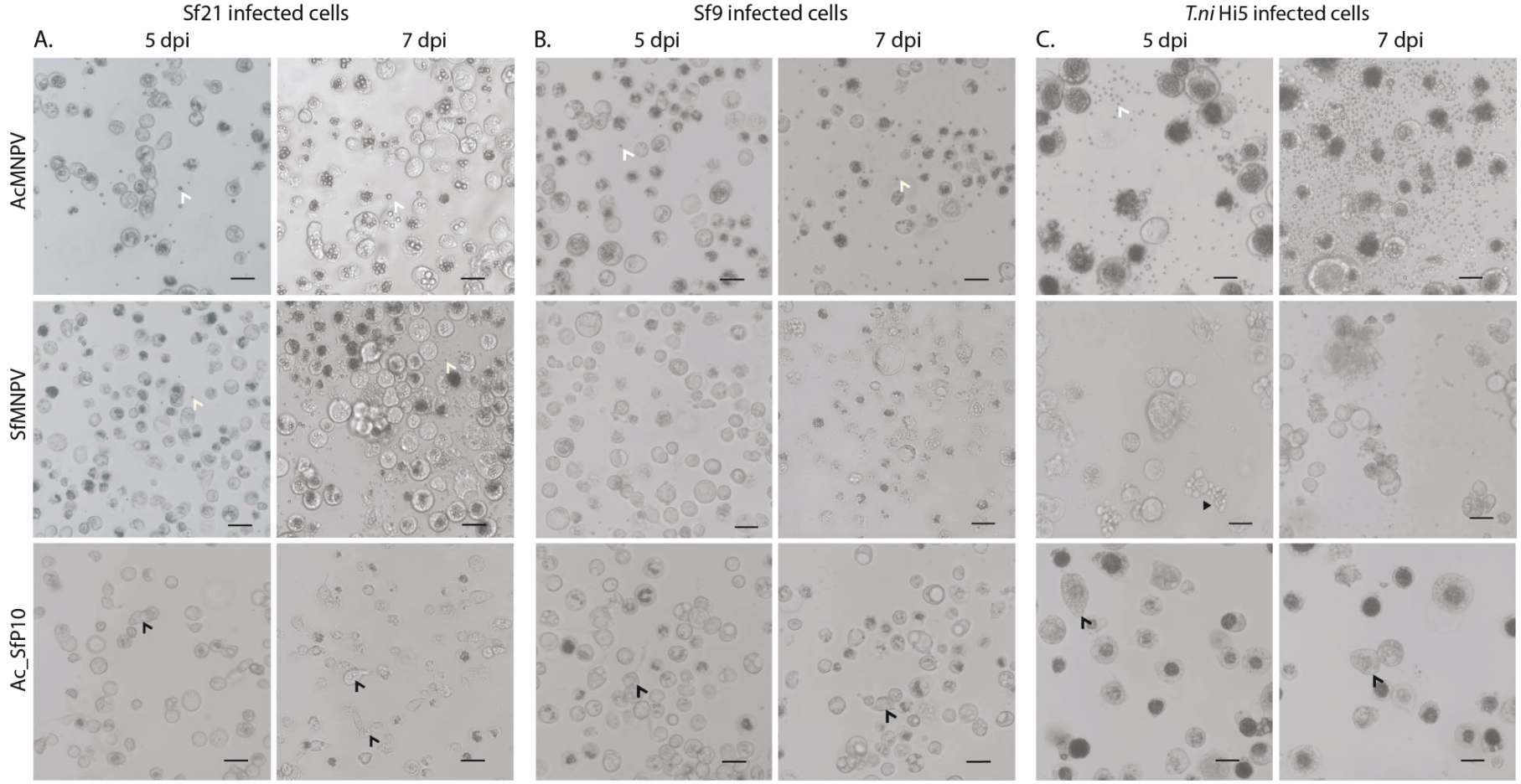

Figure 4.10 AcMNPV, SfMNPV and Ac_Sf*p10* infected (A) Sf21, (B) Sf9 and (C) *T.ni* Hi5 cells at five and seven days post-infection. Cells were infected with AcMNPV, SfMNPV or Ac_Sf*p10* (5 MOI) in 35 mm dishes and incubated at 28°C. The cells were imaged using a light microscope Zeiss Axiovert 135 at 5 and 7 dpi to show cell morphology and lysis (100X). Both AcMNPV and SfMNPV infected cells show normal signs of nuclear lysis, which is in contrast to Ac_SfP10 infected cells. In all cell lines Ac_SfP10 infected cells displayed a toxic effect with no sign of nuclear lysis and reduced polyhedra. Scale bar is 20 µm. White arrow indicates free polyhedra, black arrow highlights granulated or deformed cell.

After 5 dpi, AcMNPV- or SfMNPV-infected Sf21 cells were observed by light microscopy and displayed characteristic signs of baculovirus infection, as discussed previously in Chapter Three. The cells presented with enlarged nuclei and contained multiple polyhedra within the nucleus. Furthermore, these infected cells showed the presence of multiple free polyhedra in the media, suggestive of nuclear lysis (white arrow, Figure 4.10 A). In comparison to AcMNPV and SfMNPV, the majority of Ac_Sf*p10* infected cells lacked polyhedra and no free polyhedra were observed in the cell media. On further analysis, Ac_Sf*p10*-infected Sf21 cells looked stressed and deformed (black arrow, Figure 4.10 A), a characteristic that was not observed in AcMNPV- or SfMNPV-infected Sf21 cells.

By 7 dpi, the number of free polyhedra observed in AcMNPV- or SfMNPV-infected cell medium had increased, with the enumeration of free polyhedra observed to be similar or even higher in SfMNPV- than AcMNPV-infected Sf21 cells (white arrow, Figure 4.10 A). In-contrast, Ac_Sf*p10*-infected cells continued to show no sign of lysis, with more cells appearing granulated and with a continued delay in polyhedra production. The polyhedra that were observed appeared noticeably smaller (black arrow, Figure 4.10 A, 7 dpi), which was confirmed in Figure 4.13.

Repeat infections using alternative cell lines, Sf9 and Hi5, gave similar results to Sf21 cells at both 5 and 7 dpi (Figure 4.10), with the exception of SfMNPV-infected Hi5 cells, which showed a complete absence of polyhedra. Instead infections with SfMNPV caused cell apoptosis at both 5 and 7 dpi, with no visible sign of baculovirus replication (black arrow, Figure 4.10 C, SfMNPV).

At 5 dpi, nuclear lysis, as determined by free polyhedra, was observed in both AcMNPV- and SfMNPV-infected Sf9 cells and the polyhedra observed in the media of SfMNPV-infected Sf9 cells were few and more sparsely distributed (Figure 4.10, B, SfMNPV). This decrease in polyhedra for SfMNPV was possibly due to slight differences in characteristics between each Sf cell line. However, during the same experiment it later became apparent that the SfMNPV-infected Sf9 cells (left for ten days) were contaminated. It is therefore possible that earlier imaged SfMNPV-infected Sf9 cells could also have been contaminated which may have caused delay in viral replication and thus lysis (Figure 4.10 B, SfMNPV). By 7 dpi, both AcMNPV-infected Sf9 and Hi5 cells displayed a continued increase in free polyhedra with enumeration of free polyhedra in cell medium greater in infected Hi5 cells (white arrow, Figure 4.10 C, AcMNPV).

In contrast to AcMNPV-infected Sf9 and Hi5 cells and SfMNPV-infected Sf9 cells, Ac_Sf*p10*-infected Sf9 and Hi5 cells at 5 dpi, 7 dpi and even 14 dpi (data not shown) failed to lyse (Ac_SfP10, Figure 4.10 B-C). In comparison to Ac_SfP10-infected Sf21 cells

(Figure 4.10 A, Ac_SfP10), most cells lacked polyhedra and often looked granulated or misshapen (Figure 4.10 B-C, Ac_SfP10).

In summary, SfMNPV P10 appeared to have a detrimental impact on lysis. Thus this study (Section 4.4.3) failed to support the hypothesis that expression of SfMNPV P10 in an AcMNPV genome would increase lysis in a native cell line.

4.4.4 Characterisation of P10 structures

Confocal microscopy was performed on AcMNPV- and Ac_SfP10-infected TN-368 cells at 96 hpi (Figure 4.12) to observe formation of P10 structures during the late phase of infection. The adherent TN-368 was chosen as it has inherently been best for studying P10 structures (Carpentier *et al.*, 2008). Infected or control cells were fixed and stained using either an AcMNPV P10 (for AcMNPV infected cells) or a SfMNPV P10 (for Ac_SfP10 infected cells) primary antibody and Alexa-fluor 488® secondary antibody (Methods 2.7.1a). Stained cells were imaged at 96 hpi using a Zeiss LSM 510 meta laser scanning microscope. Ac∆*p10* and mock-infected cells were included as negative controls for expression of P10 (data not shown). SfMNPV infected TN-368 cells were not studied as a control as SfMNPV causes apoptosis in *T.ni* cells.

AcMNPV P10 was detected at 96 hpi in almost all cells examined and displayed the formation of a thick cage-like structure that wrapped around the nucleus (white arrow, Figure 4.11 A-B). The results were characteristic of earlier confocal imaging at 96 hpi performed in Chapter Three (Figure 3.16, AcMNPV). In comparison, detection of SfMNPV P10 was limited to only a few cells, with P10 observed forming a combination of limited thin cytoplasmic filaments (white arrow, Figure 4.11 C) or thicker undefined aggregate structures (white arrow, Figure 4.11 D).

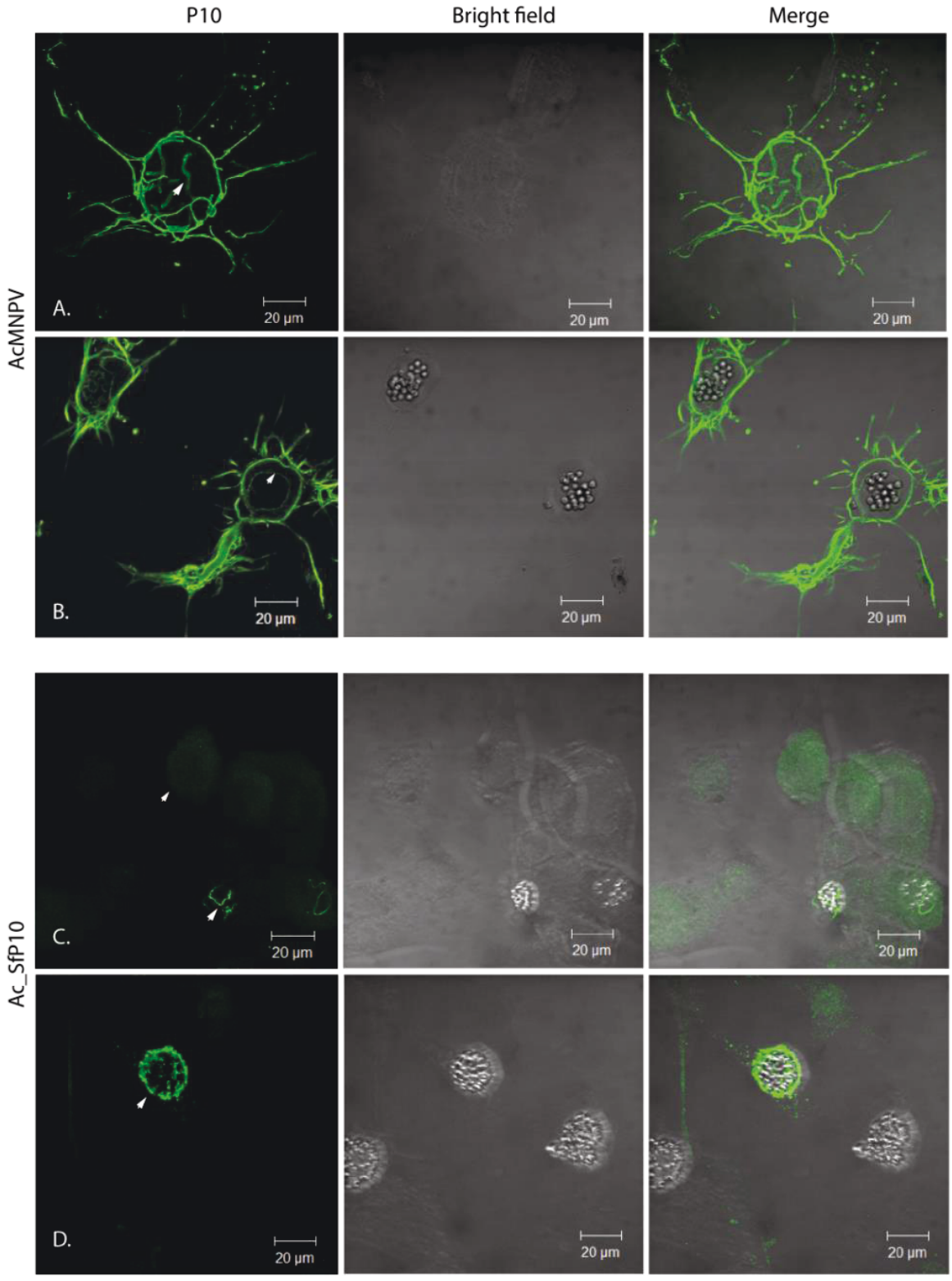

Figure 4.11 Immunofluorescence labelling of P10 structures at 96 hpi. Confocal microscopy of TN-368 cells infected with AcMNPV or Ac_Sf*p10* to observe P10 structures (green). Infected cells were fixed at 96 hpi and stained by indirect immunofluorescence using either an AcMNPV or SfMNPV anti-P10 antibody. Ac_SfP10 infected cells were observed with reduced P10 structures that remained as thin filaments or as P10 aggregates around the nucleus. White arrows (A, B) highlight thicker AcMNPV P10 structures, and (C, D) highlight thin filament structures and P10 aggregates. Scale bar 20µm.

Confocal analysis performed at earlier time points, including 24, 48 and 72 hpi (data not shown) were unable to detect Ac_Sf*p10* P10 structures (24 hpi and 48 hpi). P10 presented as thin cytoplasmic filaments or aggregates at 72 hpi similar to those shown in Figure 4.11 C. Data suggest that expression of SfMNPV P10 within the AcMNPV backbone form structures that differ to those of native AcMNPV P10 (Figure 4.11 A). It is possible that the low expression levels (Figure 4.9) could have affected formation of these structures and is a theory further explored in Chapter Five.

It was observed during confocal analysis with SfMNPV P10 antibody that a high level of unspecific background was often present (white arrow, Figure 4.11-C) and future work would benefit from optimisation of conditions.

4.4.5 Characterising the role of P10 in polyhedral envelope maturation

To observe how polyhedra produced in Ac_Sf*p10*-infected cells might be affected by this foreign P10 protein, SEM was performed on extracted polyhedra from AcMNPV and Ac_Sf*p10*-infected TN-368 cells (Method 2.7.4c). The polyhedra were then visualised using a Hitachi S-3400 SEM to obtain high-resolution images of the polyhedra surface (Figure 4.12). To complement prior work in Chapter Three (Section 3.3.6) TN-368 cells were chosen.

SEM images of polyhedra isolated from AcMNPV or Ac_Sf*p10*-infected cells displayed distinguishable morphological differences (Figure 4.12). With polyhedra extracted from AcMNPV-infected cells predominantly presenting a characteristic polyhedron shape with a smooth calyx (white arrow, Figure 4.12 A-B); only a few malformed or immature polyhedra were detected. In contrast, polyhedra extracted from Ac_Sf*p10*-infected cells exhibited a range of phenotypes, primarily with small polyhedra that contained a pitted surface (white arrow, Figure 4.12, C-D) characteristic lacking calyx (Figure 3.20). A small percentage (~5-10%) of polyhedra were still observed to be larger with a more characteristic polyhedron shape. Another characteristic noted was that extracted Ac_Sf*p10* polyhedra often clumped together (Figure 4.12 C-D), suggesting that the absence of the calyx could result in adhesive properties and prevent dispersal.

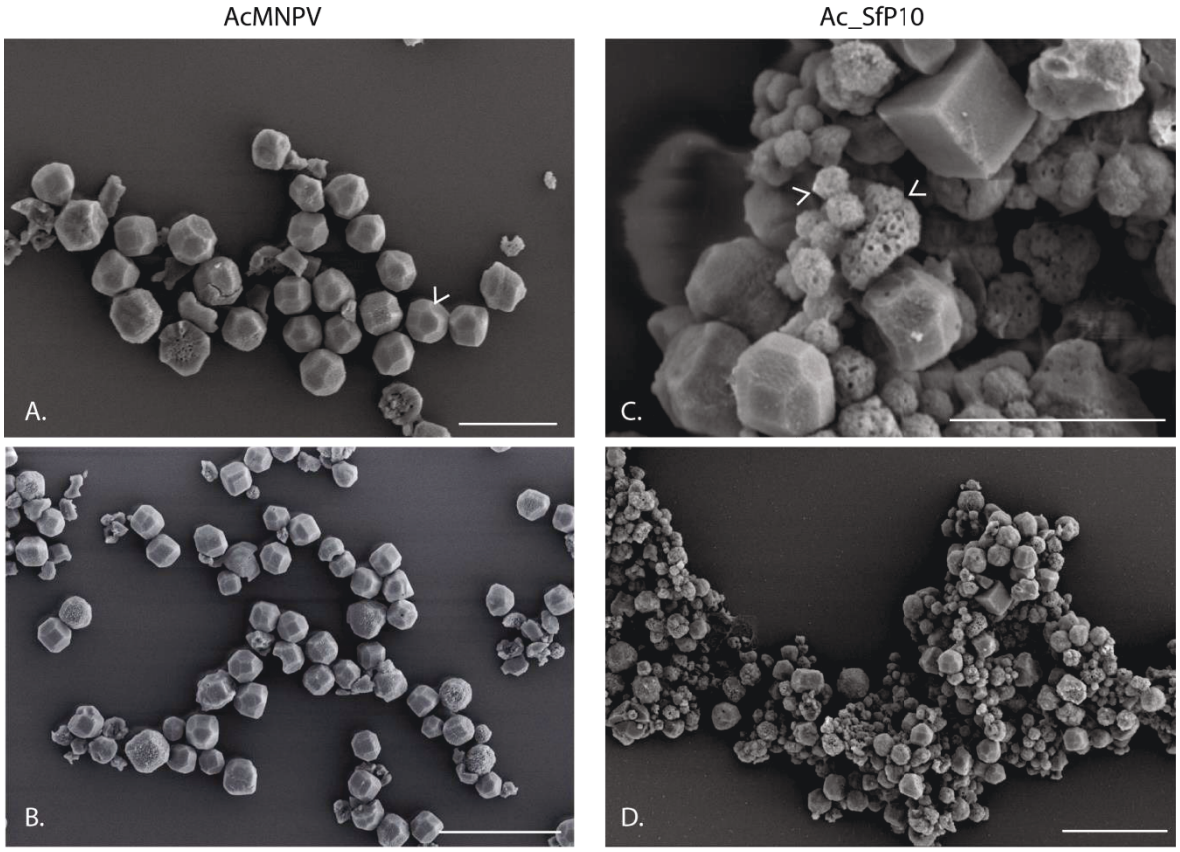

Figure 4.12 High resolution SEM images of calyx morphology on purified polyhedra. SEM images of purified polyhedra from AcMNPV (A-B) or Ac_Sf*p10*-infected TN-368 cells (C-D) were fixed and imaged using SEM Hitachi S-3400. White arrows (C) show a close-up of polyhedra displaying smaller polyhedra often with a pitted surface. All images were captured at 5.00 kV. Scale Bar (A, B & D) 10µm and (C) 5µm.

Post-acquisition image processing of 100 polyhedra was performed using Image J to determine if imaged AcMNPV or Ac_Sf*p10* polyhedra collected in Figure 4.13 were significantly different. To calculate size, a cross section of the polyhedra diameter (µm) was measured and plotted against each other (Figure 4.13). The size (µm) distribution of polyhedra shown in Figure 4.13 A displayed a positive linear correlation, indicating a uniformity of shape for both AcMNPV and Ac_Sf*p10*. However, a difference in size was clearly observed for extracted polyhedra from AcMNPV or Ac_Sf*p10* (Figure 4.13 A), with AcMNPV polyhedra diameters clustered between 2µm and 4µm (mean = 2.891) and Ac_Sf*p10* at 1-2 µm (mean=1.219). These data are also presented using a box and whiskers plot (Figure 4.13 B), which confirmed a greater median and higher diameter range for AcMNPV compared to Ac_Sf*p10*.

To determine if this observed variation (Figure 4.13) was statistically different, a t-test was performed. The result confirmed SfMNPV P10 (1.219±0.336) was significantly smaller than AcMNPV (2.891±0.473). Therefore, confirming that SfMNPV P10 had a significant impact on polyhedra size when compared to the expressing WT AcMNPV P10.

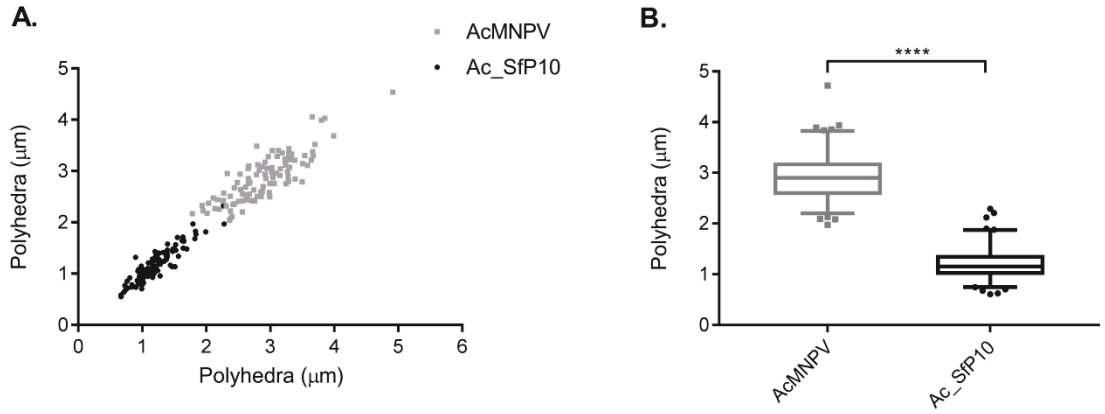

Figure 4.13 Comparative analysis of SEM-imaged polyhedra. (A) Individual XY distribution plots of AcMNPV (grey) and Ac_Sf*p10* (black) polyhedra diameters (nm), collected from 100 SEM-imaged polyhedra. (B) Box and whiskers plot of mean polyhedra diameter (nm) from AcMNPV and Ac_Sf*p10*, n = 100. Bars represent 5-95 % range with outliers plotted. t-test represents statistical difference between cohort, **** = < 0.0001.

4.5 Characterising Ac_Sf*p10* with the construction of a new recombinant virus, Ac∆*p10*_lacZ^{Rescue}

To determine if the phenotypic characteristics and lower BV titres of Ac_Sf*p10*-infected Sf21 cells (Figure 4.8, 4.10) resulted from inserting a foreign *p10* or as a result of additional mutations to the backbone virus, the construction of a new recombinant virus, Ac∆*p10*_lacZ^{Rescue} was made.

Traditionally a rescue virus would reinsert the AcMNPV P10 sequence, but because this would result in the absence of a selectable marker, it was decided therefore, *lacZ* would be reinserted. This will ensure that what is reproduced is the P10 minus phenotype, which was already characterised in Chapter Three.

4.5.1 Construction of an Ac∆*p10*_lacZ^{Rescue} recombinant virus rescue virus

The construction of Ac∆*p10*_lacZ^{Rescue} was made by transfecting Ac_SfP10-infected Sf9 cells with pAc∆*p10*_lacZ plasmid DNA at 18 hpi, (see Figure 4.14, Methods 2.3.4). After 5dpi, the cell medium containing a mixed infection was harvested and titrated by plaque assay to isolate recombinant virus Ac∆*p10*_lacZ^{Rescue}. By implementing a plaque purification method that selected blue plaques, in the presence of X-gal, Ac∆*p10*_lacZ^{Rescue} was positively selected (Method 2.3.5a). From each plaque assay, twelve blue plaques were isolated and re-titrated until no clear plaques were visible. Virus isolated from the final round of plaque-purification was then used to amplify virus by

infecting dishes of Sf9 cells (Method 2.3.3a). Virus was harvested after five days and was designated recombinant virus passage 0 (P0).

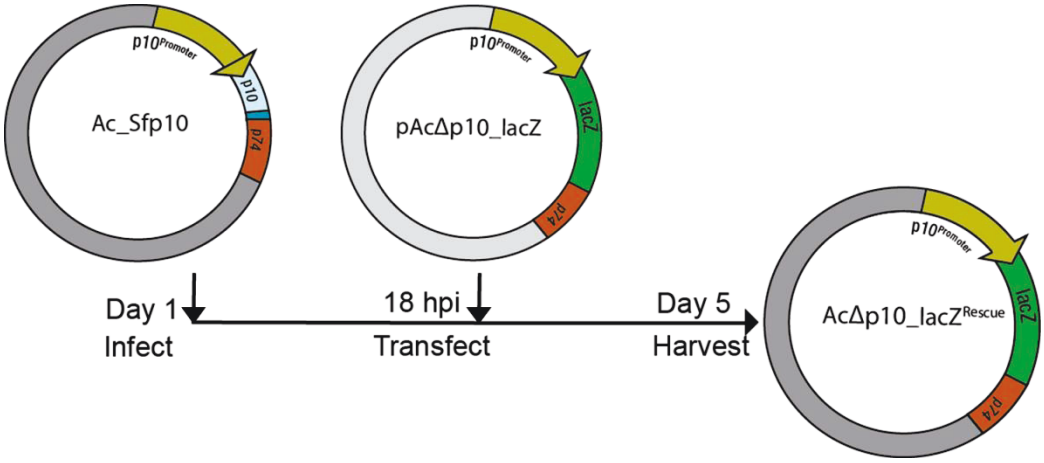

Figure 4.14 Construction of Ac∆*p10*_lacZ^{Rescue} virus replacing SfMNPV-*p10* with lacZ. Ac∆*p10*_lacZ^{Rescue} was constructed by a process of infecting Sf9 cells with Ac_SfP10 and then transfecting with pAc∆*p10*_lacZ plasmid DNA 18 hpi.

To confirm plaque-purification had produced genetically homogenous isolates of Ac∆*p10*_lacZ^{Rescue}, free from parental virus, PCR analysis and DNA sequencing across the *p10* locus were undertaken (data not shown) as stated in Chapter 3.3.2 for Ac∆*p10_lacZ.* Two P0 virus stocks with correct genome were amplified to generate a working stock (P2).

4.5.2 Budded virus production

To determine if normal BV production was rescued in AcΔSfP10_*lacZ*^{Rescue}, virus titres were compared between AcMNPV, Ac_*p10*^{Rescue}, Ac_Sf*p10* and AcΔSfP10_*lacZ*^{Rescue} (Figure 4.16). Sf9 cells were infected at 0.1 MOI in shake cultures (1x10^6 cells/ml) and T75 flats (3x10^6/dish) and incubated at 28°C for 5 days (Method 2.3.3). Both shake and flat cultures have been used as it was noted in earlier studies that production of Ac_Sf*p10* BV varied between each method. After incubation, the media was harvested and virus titres were confirmed by plaque-assay (Method 2.3.5a)

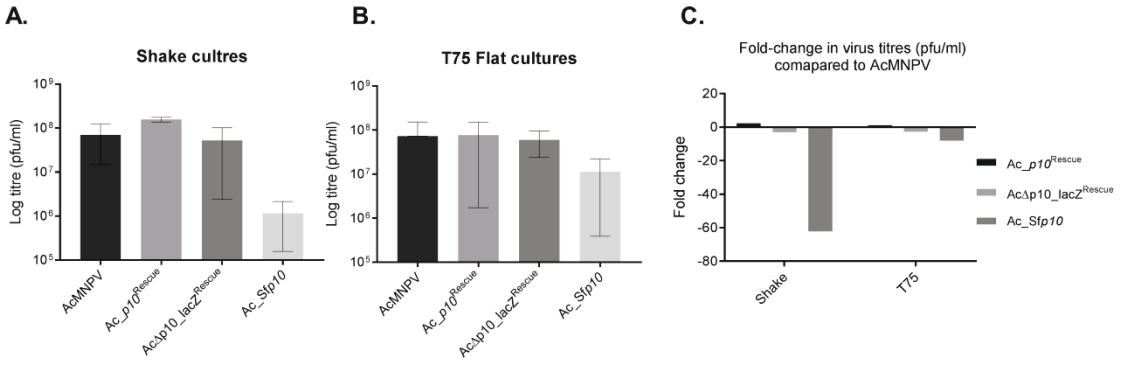

Figure 4.15 Comparison of virus titres (pfu/ml) for AcMNPV, Ac_*p10*^{Rescue}, Ac_Sf*p10* and AcΔSfP10_lacZ^{Rescue}. Plaque-titration of infected Sf9 cell culture media at 5 dpi was performed to determine virus titre (pfu/ml) in either (A) shake cultures or (B) T75 Flats. A shift in calculated titres (fold-change) (C) was calculated against AcMNPV virus. (n =2), error bars represents mean ± SD.

The BV titres (pfu/ml) from shake cultures for AcMNPV (7.00x10^7 pfu/ml), Ac_*p10*^{Rescue} (1.57x10^8 pfu/ml) and AcΔSfP10_*lacZ*^{Rescue} (5.23x10^7 pfu/ml) gave similar titres, with only Ac_Sf*p10* (1.6x10^6 pfu/ml) showing a notable decrease in virus titre (Figure 4.15 A). In comparison, the BV titres (pfu/ml) obtained from the T75 flats gave similar results to shake cultures, with AcMNPV (7.30x10^7 pfu/ml), Ac_*p10*^{Rescue} (7.69x10^7 pfu/ml) and AcΔSfP10_*lacZ*^{Rescue} (5.98x10^7 pfu/ml) giving similar readings. Interestingly, Ac_Sf*p10* gave a higher titre then previously observed in the shake cultures of 1.13x10^7 pfu/ml (Figure 4.15 B). However, this was still consistently lower than the other three viruses harvested from the T75 flats. These results therefore suggest that the expression of SfMNPV P10, rather than other mutations made to the backbone virus, is resulting in the low BV titres.

To enumerate this change in BV production, the fold-change in recombinant virus titres was compared to the WT AcMNPV virus (Figure 4.15 C). The results confirmed a 1- and 2-fold increase in virus titres for Ac_*p10*^{Rescue} in shake and flat cultures respectively, with AcΔSfP10_*lacZ*^{Rescue} showing only a 1-fold decrease for both shake and flat cultures. However, Ac_Sf*p10* showed a 61-fold decrease in shake cultures and a 6-fold decrease in flat cultures, further indicating the impact SfMNPV P10 has on BV titres. But interestingly indicates shake cultures maybe less favourable for BV production in Ac_Sf*p10*-infected cells.

4.5.3 Lysis of AcMNPV, Ac_*p10*^{Rescue}, Ac_Sf*p10* and AcΔSfP10_*lacZ*^{Rescue} - infected insect cells

To characterise lysis in AcMNPV, Ac_*p10*^{Rescue}, Ac_Sf*p10* or AcΔSf*p10_lacZ*^{Rescue} cell infections, Hi5 cells were infected at 5 MOI (method 2.3.3a) and imaged using a light microscope at 4, 7 and 10 dpi (Figure 4.16). The infected cells were observed at different time points to characterise whether the *lacZ* rescue virus would produce the characteristic P10 minus infection (Figure 3.11), or show the toxic-like effects previously observed with Ac_Sf*p10* infected cells (Figure 4.10). Therefore, confirming whether expression of SfMNPV P10 or additional mutations to the genome was having this observed effect on cells during infection.

By 4 dpi, AcMNPV, Ac_*p10*^{Rescue}, Ac_Sf*p10* and AcΔSf*p10_lacZ*^{Rescue} infected Hi5 cells showed a majority of cells containing multiple polyhedra in the nucleus, with free polyhedra observed with AcMNPV and Ac_*p10*^{Rescue} (black arrow, Figure 4.17). However, similar to previous Ac_Sf*p10* lysis results (Figure 4.10), ~40-50% of infected cells lacked polyhedra and looked granulated and misshapen (Figure 4, red arrow). By 7 and 10 dpi, the number of free polyhedra observed in the cell medium had increased dramatically in AcMNPV- and Ac_*p10*^{Rescue}-infected cells, whilst Ac_Sf*p10*- and AcΔSf*p10_lacZ*^{Rescue} – infected showed no signs of nuclear lysis (Figure 4.16). This was expected with the P10 minus AcΔSf*p10_lacZ*^{Rescue} virus, as deletion of P10 inhibits nuclear lysis (Vlak *et al.*, 1988; Williams *et al.*, 1989). Similar to observations at 4 dpi, a large percentage of Ac_Sf*p10*-infected cells (~30-40%) lacked polyhedra and continued to look granulated and misshapen (red arrow, Figure 4.16), suggestive of a toxic effect.

Due to this observed variation in phenotype between Ac_Sf*p10* and AcΔSf*p10_lacZ*^{Rescue} infected cells, which more closely related to the phenotype of AcMNPV and Ac_*p10*^{Rescue}, it can be proposed that SfMNPV-P10 results in this toxic effect.

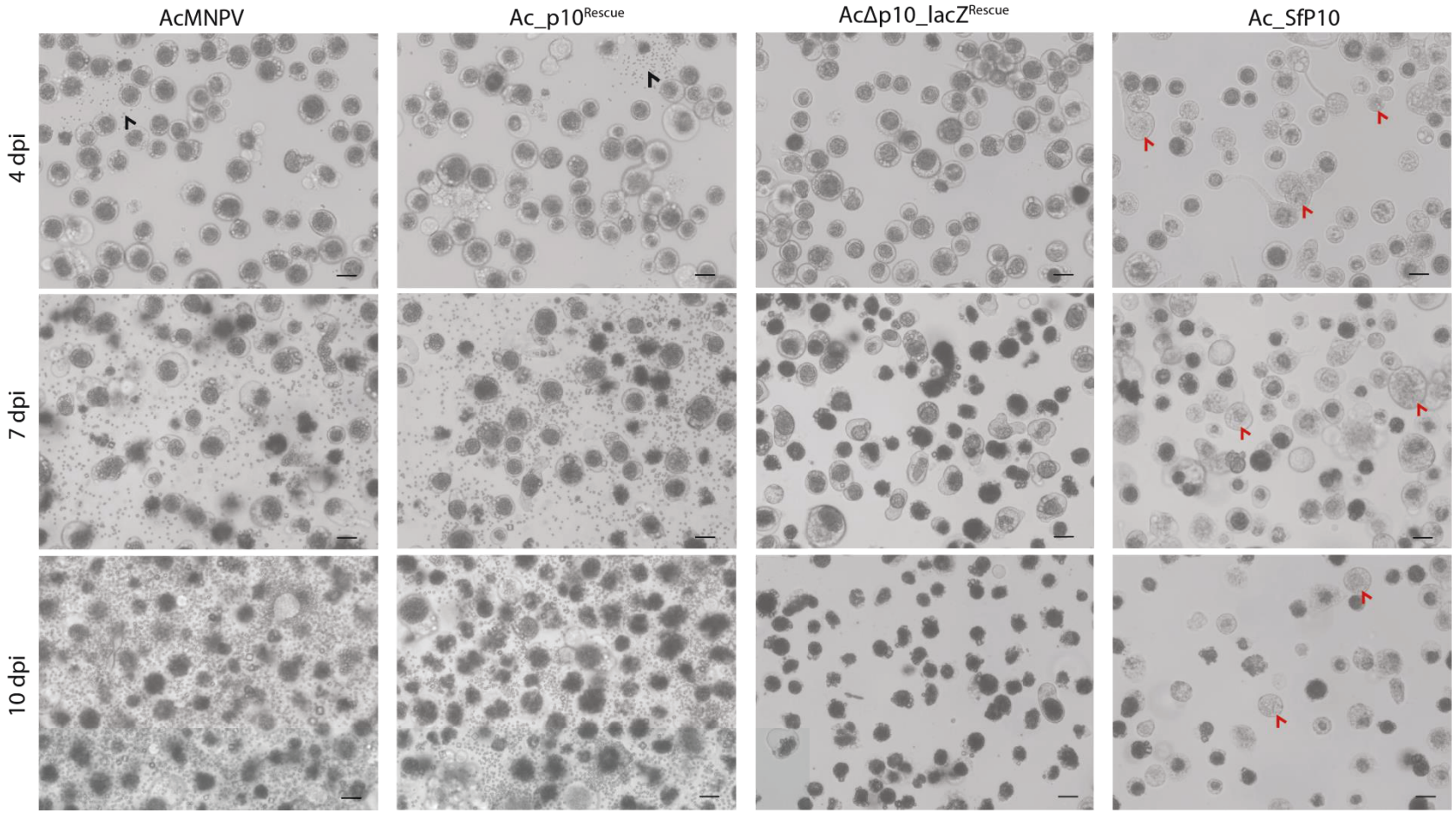

Figure 4.16 AcMNPV, Ac_*p10*^{Rescue}, Ac_Sf*p10* and AcΔSf*p10*_lacZ^{Rescue} infected *T.ni* Hi5 cells at four, seven and 10 days post-infection. Cells were infected with AcMNPV, Ac_*p10*^{Rescue}, Ac_Sf*p10* and AcΔSf*p10*_lacZ^{Rescue} (5 MOI) in 35 mm dishes and incubated at 28°C. AcMNPV and Ac_*p10*^{Rescue} infected cells showed characteristic infection with numerous polyhedra produced and signs of nuclear lysis, black arrows (AcMNPV and Ac_P10^{Rescue}) highlight free polyhedra in media. Ac_Sf*p10* infected cells became granulated and misshapen and showed reduced polyhedra formation with no sign of nuclear lysis. Red arrows (Ac_SfP10) shows partially infected cells lacking mature polyhedra. AcΔSf*p10*_lacZ^{Rescue} infected cells were observed with normal polyhedra. The cells were imaged using a light microscope Zeiss Axiovert 135 to show cell morphology and lysis (100X). Scale bar is 20 µm.

To determine if the decrease in polyhedra formation for Ac_Sf*p10* infected cells (Figure 4.16) was statistically relevant, the total polyhedra were enumerated. The polyhedra were purified from a 35mm dish containing Hi5 or Sf9 cells infected with AcMNPV, Ac_*p10*^{Rescue}, Ac_Sf*p10* or AcΔSf*p10_lacZ*^{Rescue} at 5 dpi. It was decided to analyse both cell lines as it was shown in Chapter Three that polyhedra production is statistically different between cell these lines. Therefore, it was interesting to observe polyhedra production in both cell lines, as one cell line might be more sensitive to Ac_Sf*p10* infection.

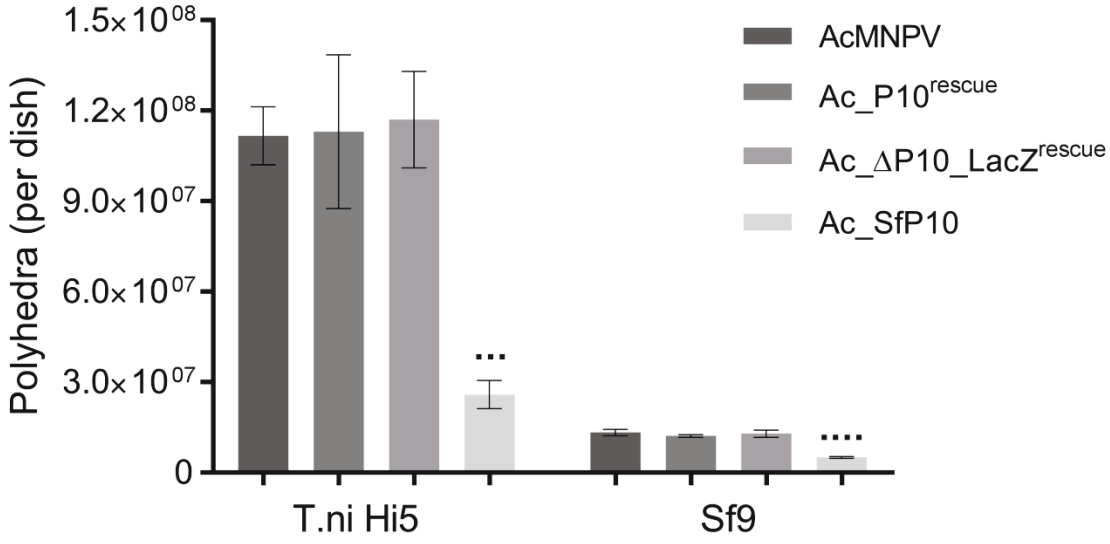

Figure 4.17 Comparison of total polyhedra counts in two different cell lines. Triplicate dishes of *T.ni* Hi5 and *Sf9* cells (0.5x10^6 and 1x10^6 cells/35mm dish respectively) were infected with AcMNPV, Ac_*p10*^{Rescue}, Ac_Sf*p10* and AcΔSf*p10_lacZ*^{Rescue} (5 MOI). Five dpi, polyhedra were extracted, purified and re-suspended in 1ml PBS. Polyhedra were counted using a haemocytometer to derive polyhedra per dish. Error bars represents mean ± SD (n=3) for each cell line. ***(*) indicates significant difference.

Figure 4.17 displays the mean polyhedra counts for AcMNPV, Ac_*p10*^{Rescue}, Ac_Sf*p10* and AcΔSf*p10_lacZ*^{Rescue}-infected cells that were enumerated between 2.6x10^7 and 1.1x10^8 per dish for Hi5 infected cells and between 4.9x10^6 and 1.3x10^7 per dish for Sf9 infected cells (Figure 4.17). The results showed an increase in polyhedra production for all viruses in Hi5 cells compared with Sf9, which was similar to previous comparisons between the two cell lines (Figure 3.10). However, on comparison of polyhedra production between viruses, Ac_Sf*p10* was considerably lower for both cell lines (Figure 4.17). Enumerated polyhedra collected from other AcMNPV, Ac_*p10*^{Rescue} and AcΔSf*p10_lacZ*^{Rescue} were comparable in both cell lines.

To determine if this was statistically relevant, a one-way ANOVA was performed on the data presented in Figure 4.18. The ANOVA confirmed a statistical difference between viruses in both Hi5 (p=0.003***) and Sf9 (p=<0.001****) cells. A Tukey's multiple comparisons post-hoc analysis confirmed the polyhedra produced in Ac_Sf*p10*-infected *T.ni* Hi5 (2.587x107 ± 4.688x10^6) and Sf9 cells (5.000x10^6 ± 3.555x10^5) were statistically lower (p<0.001) than to AcMNPV (1.117x10^8 ± 9.609x10^6 and 1.327x10^7 ± 1.079x10^6), Ac_*p10*^{Rescue} (1.130 x10^8 ± 2.545x10^7 and 1.215x10^7 ± 4.500x10^5) and AcΔSfP10_*lacZ*^{Rescue} (1.171x10^8± 1.598x10^7 and 1.290x10^7±1.153x10^5) respectivly. However, AcMNPV, Ac_*p10*^{Rescue} and AcΔSfP10_*lacZ*^{Rescue} showed no statistical variation (Figure 4.17), confirming SfMNPV-P10 had a significant impact on polyhedra production.

4.5.4 Cell viability of AcMNPV, Ac_*p10*^{Rescue}, Ac_Sf*p10* and AcΔSfP10_*lacZ*^{Rescue} cell cultures

A cell viability test was performed on AcMNPV, Ac_*p10*^{Rescue}, Ac_Sf*p10* and AcΔSfP10_*lacZ*^{Rescue} to determine if the observed toxic effect shown with Ac_Sf*p10* negatively impacted cell viability. A trypan blue exclusion assay was performed on Sf9 cells seeded at 1x10^6 cells/ml and infected with AcMNPV, Ac_*p10*^{Rescue}, Ac_Sf*p10* and AcΔSf*p10_lacZ*^{Rescue} at MOI of 0.1. Counts were taken at 24, 48, 72, 96 and 120 hpi from three separate aliquots (Method 2.7.8).

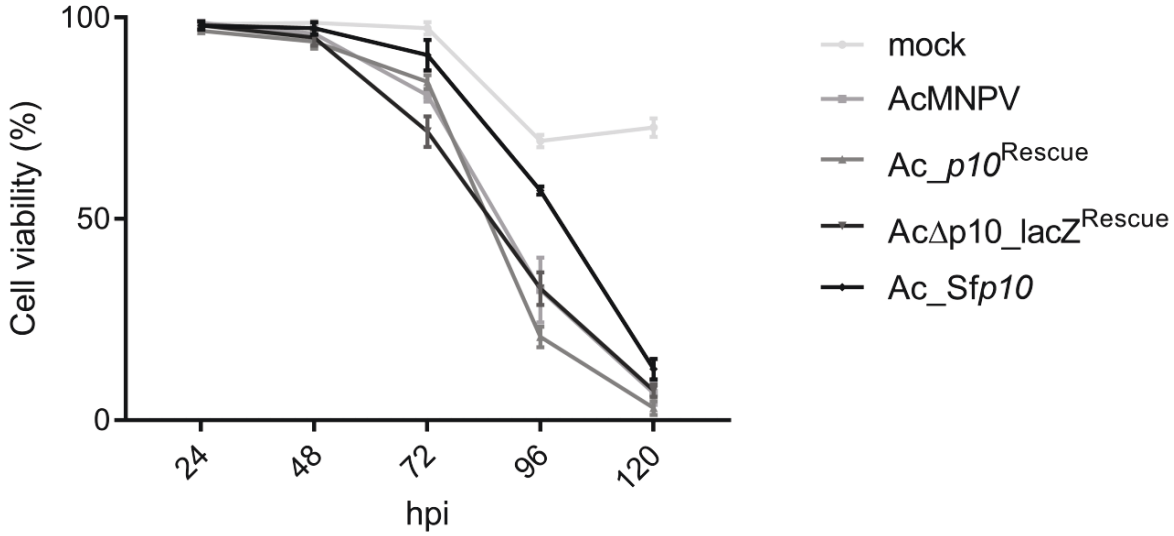

Figure 4.18 Effect of SfMNPV P10 on cell viability. Sf9 cells were infected with AcMNPV, Ac_*p10*^{Rescue}, Ac_Sf*p10* or AcΔSf*p10_lacZ*^{Rescue} at a MOI of 5. Cell viability was measured using trypan blue exclusion method at 24, 48, 72, 96 and 120 hpi (n=1). Error bars represents mean ± SD of 3 repeat measures.

Figure 4.18 displays a general decline in cell viability for AcMNPV, Ac_*p10*^{Rescue}, Ac_Sf*p10* and AcΔSf*p10_lacZ*^{Rescue}, gradually decreasing from 24-120 hpi. Cell viability was similar between viruses at each recorded time. Interestingly, cell viability for Ac_Sf*p10* showed the opposite to the expected result. Rather than increasing the rate of cell death, a slight delay in cell death was observed when compared with AcMNPV, Ac_*p10*^{Rescue} and AcΔSf*p10_lacZ*^{Rescue}. However, further repeats would be required for statistical relevance.

4.6 Discussion

This chapter has characterised the formation of Ac_Sf*p10,* a recombinant AcMNPV genome in which the *p10* coding sequence was replaced with a foreign *p10* from SfMNPV. This was performed with the proposal that expression of SfMNPV P10 would increase nuclear lysis of Ac_Sf*p10*-infected Sf cells compared with WT AcMNPV.

This chapter found a number of interesting characteristics for Ac_Sf*p10* infected Sf21, Sf9, and Hi5 cells that differed from WT AcMNPV. The recombinant virus Ac_Sf*p10* failed to cause lysis in each cell line and interestingly produced less polyhedra (often deformed) with P10 expression and BV titres were notably decreased. Confocal microscopy further observed that P10 fibril structures were either absent or decreased in size. This indicates that insertion of SfMNPV *p10* in an AcMNPV genome had a dramatic impact on infection and highlights a species-specific functionality for P10. This was confirmed by a failure to detect the usual characteristics associated with P10: failure to form the nuclear cage-like structure, failure to facilitate maturation of polyhedra with a calyx, and failure to detect nuclear lysis (Carpentier *et al.*, 2008).

One early suggestion for the observed effects associated with SfMNPV P10 was the inadvertent introduction of additional mutations during construction. This was ruled out when comparisons with AcΔSfP10_*lacZ*^{Rescue}-infected cells, made from the same backbone, gave phenotype characteristics of a P10 minus virus (Chapter Three). This therefore strongly suggests that expression of SfMNPV P10 in AcMNPV was the contributing factor to the observed effects during this study.

Interestingly, the results observed with Ac_Sf*p10* contrasted with the previous literature that characterised the specificity of baculovirus *p10* function. Previous studies made recombinant viruses in which the coding region of AcMNPV-*p10* was replaced with either SeMNPV-*p10* (van Oers *et al.*, 1994) or BusuNPV-*p10* (van Oers *et al.*, 1998). Unlike Ac_Sf*p10,* these viruses expressing SeMNPV-P10 (AcCR1) or BusuNPV-P10 (AcMVO7)

displayed normal formation of P10 fibrous structures with a characteristic phenotype of a WT-AcMNPV infected cell. However, a similar characteristic to Ac_Sf*p10* was shown with these recombinant viruses, in which infected cells failed to lyse. It was suggested by the authors that other viral factors were required to interact with P10 of the same species to initiate nuclear lysis (van Oers *et al.*, 1994; van Oers *et al.*, 1998).

An alternative interpretation, as highlighted from the bioinformatic study (Figure 4.3), is that the poor sequence identity shared between P10 homologues could have an impact on function, specifically lysis (Section 1.4.6). It is possible the less conserved proline rich domain, suggested to play a role in nuclear lysis (van Oers *et al.*, 1993) is not recognisable between species. Therefore, It is likely virus-specific factors are unable to recognise foreign P10 that enable nuclear disintegration; furthermore, this theory could also answer why lysis was not observed in AcCR1 and AcMVO7.

An additional theory proposed for the absence of lysis, is that sufficient accumulation of P10 is required before nuclear lysis can occur, therefore low expression levels of the foreign P10 are insufficient for nuclear lysis (van Oers *et al.*, 1998). This is similar to Ac_Sf*p10*-infected cells, where low levels of P10 where detected by both Coomassie and Western blots (Figure 4.9). This proposed symbiotic relationship between levels of P10 and nuclear lysis is further explored in Chapter Five and was shown that a concomitant relationship was observed between P10 expression and nuclear lysis. It was postulated during this study that the low P10 expression levels caused the malformed or absent P10 associated fibrous structures. It was therefore postulated that the failure of the thicker mature P10 structures in Ac_Sf*p10*-infected cells might also be a reason for the absence of lysis. This proposal was further supported in Chapter Five and Six, which indicated that the dynamic remodelling of the perinuclear cage during the later phases of infection is crucial for lysis.

In contrast to the variable domain, the majority of alphabaculovirus and betabaculovirus also share a high sequence identity in the conserved P10 coiled-coil domain (Wilson *et al.*, 1995; Carpentier *et al.*, 2008). This region forms a recognisable α-helical protein chain (Crick, 1952; Crick, 1953) and has been implicated in aggregation and formation of the P10 fibrous bodies in both HearNPV and AcMNPV (Dong *et al.*, 2005; Dong *et al.*, 2007). It is plausible that the more highly conserved region is, therefore, likely to retain function, as the foreign species is more likely to encode this sequence. This is seen with the continued production of fibrous structures by van Oers *et al*. (1994; 1998) and partially with Ac_Sf*p10* (Figure 4.11 C-D). Furthermore, as indicated by Dong *et al*. (2005; 2007), the functional role of P10 coiled-coil domain in fibrous body formation was shown not to

require other viral factors and suggests why some function of the SfMNPV P10 is retained in AcMNPV backbone.

Another characteristic of Ac_Sf*p10* was the decrease in BV production. It has been previously shown that deletion of *p10* does not affect BV production (Croizier *et al.*, 1987; Vlak *et al.*, 1988). Therefore, it is unclear why insertion of SfMPV-*p10* at the *p10* locus would have an impact on BV production (Figure 4.15). It is possible the harmful effects of the SfMNPV P10 on Ac_Sf*p10* infected host cells (Figure 4.10 and 4.16) resulted in decreased BV titres (Figure 4.17). Interestingly it was also noted that BV titres from Ac_Sf*p10* infected cells were higher in T75 flats than in shake cultures, which characteristically give higher titres and are favoured for virus production. It is plausible the harmful effect of the SfMNPV P10 was less pronounced in T75 flats, offering more favourable conditions to the cells and/or virus. This is possibly due to the mechanism of growing virus cultures in shake cultures, which result in both decreased aeration (Wong *et al.*, 1994) and poorer quality of BV particles (Hattori *et al.*, 2016). It could simply be the vigorous effect of the shake cultures combined with impact of the SfMNPV P10 on the infected cells, which causes damage to the cell integrity early on in infection.

In conclusion, it is clear from this chapter that SfMNPV P10 does not increase lysis of Sf cells, further suggesting that particular roles of P10, such as lysis, are host-specific. It would be interesting to determine what viral or host cell factors interact with P10 to promote lysis and to confirm if lysis is isolated to the variable domain. This could therefore help develop a more targeted approach to understand the mechanisms of P10 and characterise the structural domains of P10 further.

Chapter Five:

Modulation of *p10* expression and its effect on virus-infected cell lysis

5.1 Introduction

AcMNPV genes are temporally regulated over four main phases: immediate early, delayed early, late and very late (Rohel and Faulkner, 1984). There are two major proteins expressed in the very late phase, polyhedrin and P10, the latter of which was originally identified as a small hyper-expressed protein by Vlak *et al*. (1981). In a similar manner to polyhedrin, P10 has been shown to accumulate from 12 hpi to 66 hpi (Rohel and Faulkner, 1984) and together these two proteins form the majority of cell mass very late in infection (Weyer and Possee, 1988). Both very late proteins have roles commonly associated with the final stages of infection, including occlusion of ODV within polyhedrin to form polyhedra (Smith *et al.*, 1983a), and cell lysis (Williams *et al.*, 1989; van Oers *et al.*, 1993)

Interestingly, neither of these proteins are essential for *in vitro* virus replication, and both genes can be deleted from the virus genome with no effect on formation of infectious virus particles (Smith *et al.*, 1983a; Vlak *et al.*, 1988; Williams *et al.*, 1989). This feature has been exploited by using the hyper-expressed promoters for expression of foreign proteins as reviewed by Possee (1997) and more recently van Oers *et al*. (2015)

The polyhedrin gene promoter requires the complete 5' leader sequence for maximum expression (Matsuura *et al.*, 1987), with data suggesting the presence of 69 bp upstream of the ATG translation start codon is required to facilitate optimal expression. This includes 20 bp upstream and 49 bp downstream from the mRNA cap site (Howard *et al.*, 1986; Possee and Howard, 1987). The *p10* promoter also requires complete integrity of the 5' leader sequence, with deletions downstream of the transcription initiation site (mRNA CAP) showing a reduction in efficiency (Weyer and Possee, 1988). A reduction in transient expression of chloramphenicol acetyltransferase (CAT) was observed (by thin layer chromatography) with progressive deletions from the *p10* ATG codon to the transcription start (TAAG) site (Weyer and Possee, 1988). Similar results were also shown by Scheper *et al.* (1997), further providing evidence of the requirements for a complete *p10* promoter leader sequence for maximum gene expression. Interestingly, deletions made upstream of the *p10* initiation TAAG sequence had little impact on gene expression (Weyer and Possee, 1989).

This chapter uses information available from these previous studies to modulate *p10* expression to determine the effect of different levels of protein production on P10 function. Therefore, a set of recombinant viruses containing a series of deletions downstream of the *p10* TAAG motif were constructed, whilst retaining the *p10* coding sequence.

The aim of the study was to answer three main questions: (1) Is P10 synthesis modulated by progressive deletions to the promoter? (2) Does this affect the functional role of P10? And (3) Do characteristic P10 structures still form? Overall the aim was to determine whether hyper-expression of P10 is crucial for its function during infection.

5.2 Construction of a series of *p10* promoter deletion viruses

This chapter describes the construction of ten recombinant viruses, nine of which contain progressive deletions made to the *p10* 5' leader promoter sequence, from the ATG codon to the TAAG motif (Figure 5.1). A control virus, containing the complete promoter sequence was also constructed. First, a series of transfer vectors containing deletions in the *p10* promoter were constructed and then recombinant viruses were recovered by co-transfecting Sf9 cells with the transfer vector DNA and Ac∆*p10_lacZ DNA* (Chapter 3). This ensured that the promoter and coding sequence of *p10* was inserted at its natural locus within the AcMNPV genome.

5.2.1 Construction of a series of *p10* transfer vectors containing promoter deletions

A series of deletions were made in the DNA encoding the 5' untranslated sequence of *p10* mRNA (Fig. 5.1). These were constructed using a two-step PCR. In the first round, a common oligonucleotide primer (PrimeLG_ECOR1_F, Table 2.9) binding upstream of the *p10* transcription start site was paired with one of a number of primers (Table 2.9) that bound at various points upstream of the *p10* ATG translation initiation codon (Figure 5.2 A). These products were then used as templates in a second round of reactions using PrimeLG_ECOR1_F and a series of unique primers that added the first 18 bp of the *p10* coding region to the product (Figure 5.2 A).

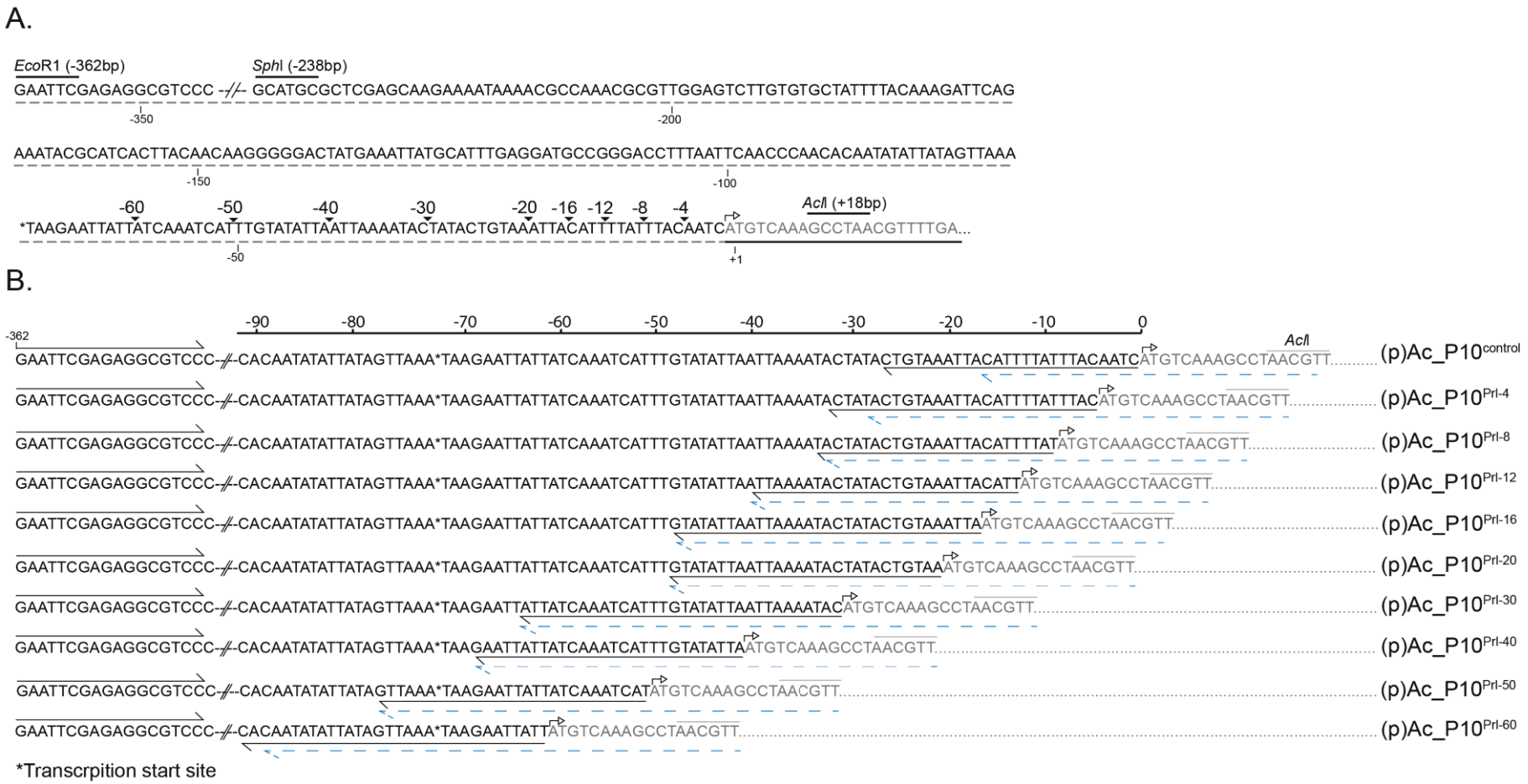

Figure 5.1 Nucleotide sequence of *p10* promoter leader sequence. (A) Indicates site for a series of deletions made to the promoter sequence from *transcription initiation (mRNA CAP) and location of relevant restriction digest sites. (B) Displays nucleotide sequence of PCR fragments made using a two-step PCR to generate a series of promoter deletions as indicated in (A). The black arrows indicate binding of primer set for the first PCR round, and the dotted blue line was use for the second PCR round and was used in combination with the forward primer upstream of the *p10* transcription start. The *p10* coding region starts at the ATG start codon as indicated by the open arrow, is highlighted as grey text and underlined with a black line in (A).

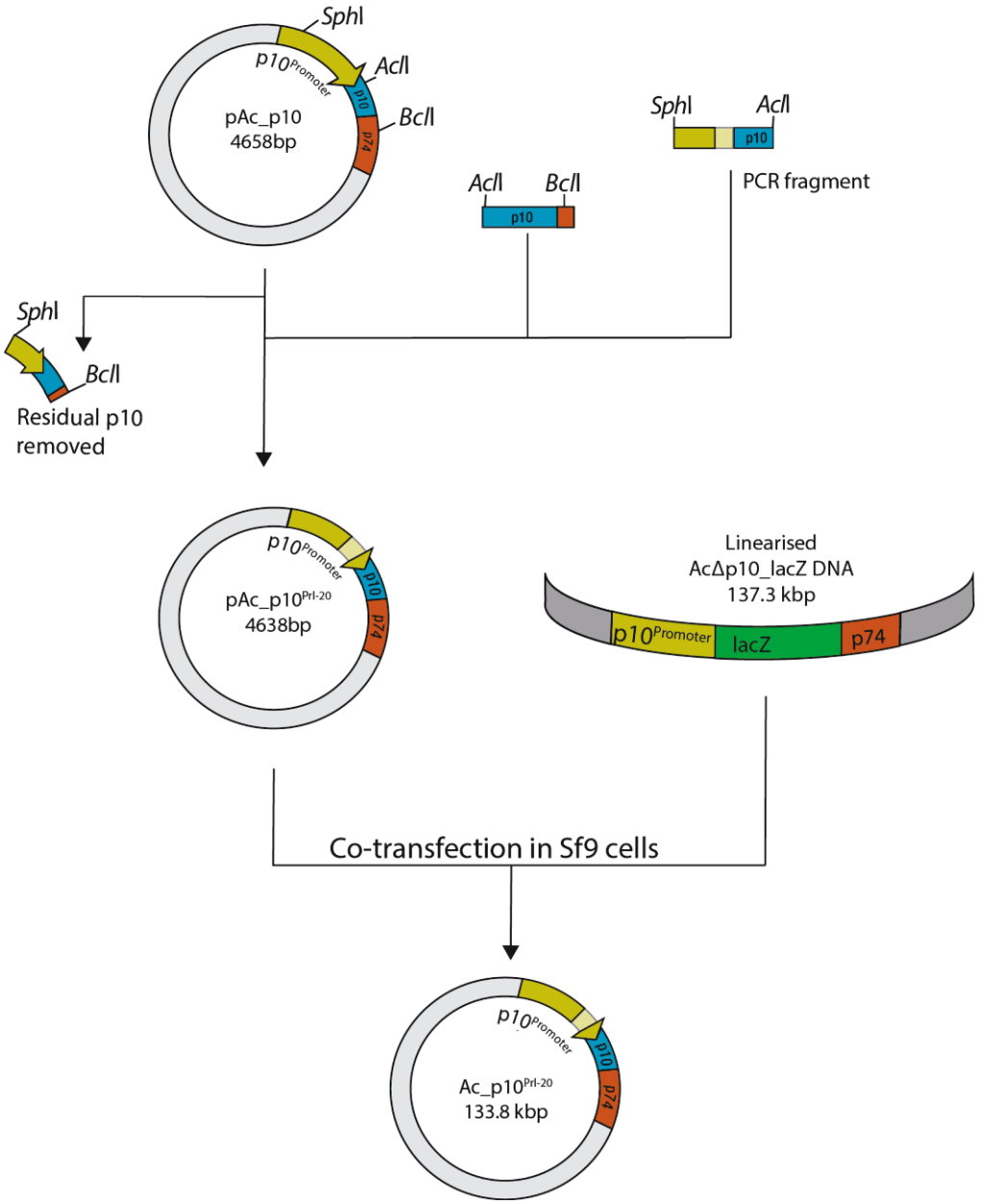

Figure 5.2 Construction of a series of recombinant AcMNPV viruses containing *p10* promoter deletions. pAc_*p10*^{Rescue} was digested with restriction endonucleases *Sph*I and *Bcl*I to remove the remaining *p10* coding region. A series of PCR fragments containing promoter deletions (Figure 3.1) were digested with *sph*I and *Acl*I and *p10* fragment derived from *Acl*I and *Bcl*I digested pAc_*p10*^{Rescue} was ligated to *SphI*/*Bcl*I digested pAc_*p10*^{Rescue} plasmid, to derive a series of deletion transfer vectors: pAc_P10^{control},pAc_P10^{prl-4}, pAc_P10^{prl-8}, pAc_P10^{prl-12}, pAc_P10^{prl-16}, pAc_P10^{prl-20}, pAc_P10^{prl-30}, pAc_P10^{prl-40}, pAc_P10^{prl-50}, pAc_P10^{prl-60}.

The PCR-generated DNA fragments (Figure 5.2 A) were purified, digested with *Sph*I and *Acl*I and characterised by gel electrophoresis (Figure 5.2 B), which confirmed an expected size range of 196-236 bp. These DNA fragments were then ligated individually in a triple ligation that also included pAc_*p10*^{Rescue}, digested with *Sph*I and *Bcl*I, and an *Acl*I/*Bcl*I fragment purified from the same plasmid to reconstitute the *p10* gene with a series of

deletions in the 5' untranslated coding region (Figure 5.2C). This resulted in 10 transfer vectors as listed in Figure 5.1; all constructs were confirmed by restriction endonuclease mapping (Figure 5.3) and DNA sequencing (data not shown).

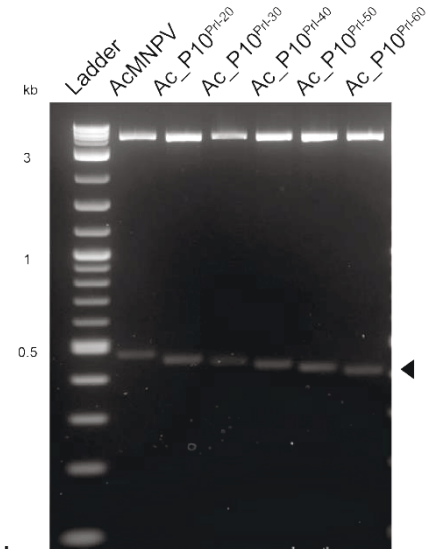

Figure 5.3 Genome analyses of pAc_P10^{prl-20}, pAc_P10^{prl-30}, pAc_P10^{prl-40}, pAc_P10^{prl-50}, pAc_P10^{prl-60}. Isolated DNA from transformants was digested with *Sph*I and *Hind*III, and analysed using a 1% agrose gel. A predicted 476-416bp band is shown by black arrow.

5.2.2 Production of a series of recombinant AcMNPV containing deletions in the *p10* promoter sequence

The second phase in the construction of viruses containing a series of deletions in the *p10* promoter was the co-transfection of insect (Sf9) cells with *Bsu*361-linearised Ac∆*p10_lacZ* DNA (Figure 5.2C) and each of the promoter deletion transfer plasmids or the control plasmid from 5.2.1 (as listed in Figure 5.1).

At 4-5 days post-transfection, the culture media comprising of a mixture of parental Ac∆*p10_lacZ* virus and appropriate recombinant promoter deletion virus were titrated by plaque-assay to separate the two virus types. Parental viruses produced blue plaques in the presence of X-gal (Weyer *et al*., 1990) and recombinant virus produced clear plaques. Twelve clear plaques were isolated and re-titrated (plaque-purified, Method 2.3.5a) until only clear plaques were visible. Virus isolated from the final round of plaque-purification was used to infect dishes of Sf9 cells (Method 2.3.3) to amplify virus stocks, designated P0. The nine promoter deletion viruses and one control virus were designated as shown in Figure 5.1.

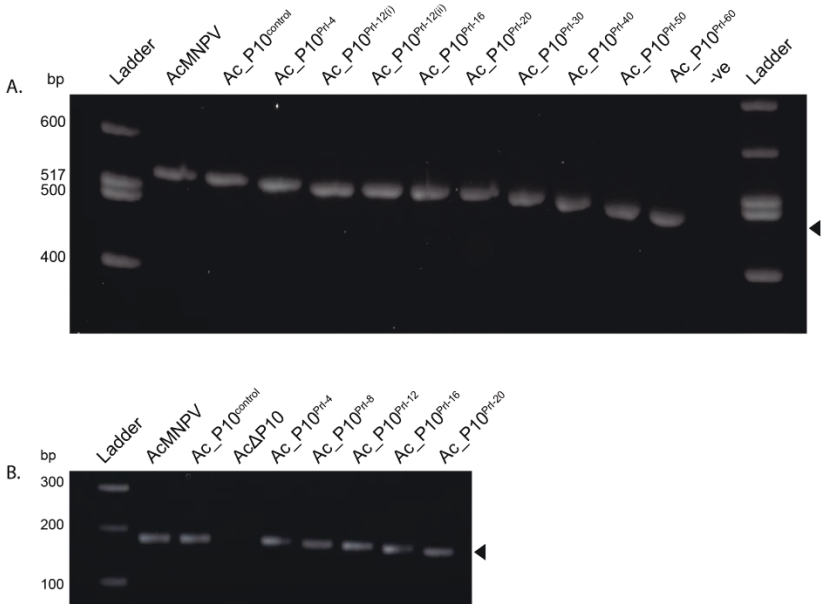

Figure 5.4 Genome analyses of *p10* promoter deletion viruses. DNA isolated from P0 recombinant viruses were characterised by PCR and analysed using 2% agarose gel. The predicted banding of (A) 545-485bp and (B) 181-161bp fragment is indicated by black arrowhead.

To confirm the plaque-purification process had produced genetically homogenous isolates, free from Ac∆*p10_lacZ,* PCR analysis and DNA sequencing at the *p10* locus was undertaken. PCR targeted at the *p10* locus was performed on twelve isolates of the 10 P0 recombinant viruses. PCR confirmed: (1) the insertion of *p10* coding region by analysis of the PCR fragment size using *p10* flanking primers (pAcLG1 and pAcLG4; Figure 5.4A); and (2) successful deletion of desired promoter sequences by using internal primers (pAcLG1 and pAcLG12; Figure 5.4B). The correct construction of the virus at the *p10* locus was further confirmed by DNA sequencing (data not shown).

Two separate P0 stocks of each recombinant were amplified to produce P1 and P2 stocks (Method 2.3.3) with additional PCR analysis (Method 2.6.5) by fragment size performed to correct genome structure and the absence of a mixed infection (data not shown).

5.3 Characterisation of the *p10* promoter deletion viruses

5.3.1 Analysis of P10 synthesis

To confirm that deletions of the promoter sequence led to modulation of P10 protein levels, when compared to P10 production in wild-type AcMNPV and control virus, Hi5 insect cells ($0.5x10^6$ cells/ml) were infected with AcMNPV, Ac_*p10*^{control} and deletion recombinants (Figure 5.1) at an MOI of 5 (Method 2.3.3a). The cells and culture media were harvested at 96 hpi.

Total protein samples were analysed by SDS-PAGE and stained with Coomassie blue (Figure 5.5 A) or transferred to a membrane for Western blotting to detect P10 protein (Figure 5.5 B; Method 2.5.2). P10 production was confirmed by detection of a 10 kDa protein (Figure 5.5B, arrow) highlighted using a P10-specific antibody. The anti-P10 antibody was raised in rabbits against a peptide sequence: NH_2-CFELDSDARRGKRSSK (Table 2.6). This peptide region was chosen as it had been previously used to produce an anti-serum that recognised P10 (Patmanidi *et al.*, 2003). A control AcMNPV P10-minus virus (AcΔP10) was also used.

To confirm that alterations to the *p10* promoter had not affected virus replication, cathepsin production was monitored using a cathepsin-specific antibody raised in Guinea-pigs against a peptide sequence: NH_2-CFELDSDARRGKRSSK (Table 2.6) and previously used with success to produce an anti-sera that recognised cathepsin (Raza, 2013). This cathepsin-specific antibody detected 35.5, 32 and 27.5 kDa bands, as expected (Figure 5.5 B).

Detectable levels of P10 were observed in both Coomassie and Western blots of infected Hi5 cells, with both AcMNPV and Ac_P10^{control} forming a thick P10 associated band (Figure 5.5 A-B, lanes 1-2). In contrast, a progressive decrease in expression of P10 was observed from P10^{prl-4} to P10^{prl-20} (Figure 5.5 A-B, lanes 3-7); with P10 expression below detection limits for Ac_P10^{prl-16} and Ac_P10^{prl-20} by Coomassie staining (Figure 5.5 A, lanes 6-7). Interestingly, Ac_P10^{prl-12} displayed higher expression levels than that expected from neighbouring deletions, with a band density more comparable to AcMNPV and Ac_P10^{control} (Figure 5.5 A-B, lane 5). A P10 associated band was not detected for Ac∆*p10* or deletion viruses Ac_P10^{prl-30} to Ac_P10^{prl-60} either by Coomassie or Western blot (Figure 5.5 C).

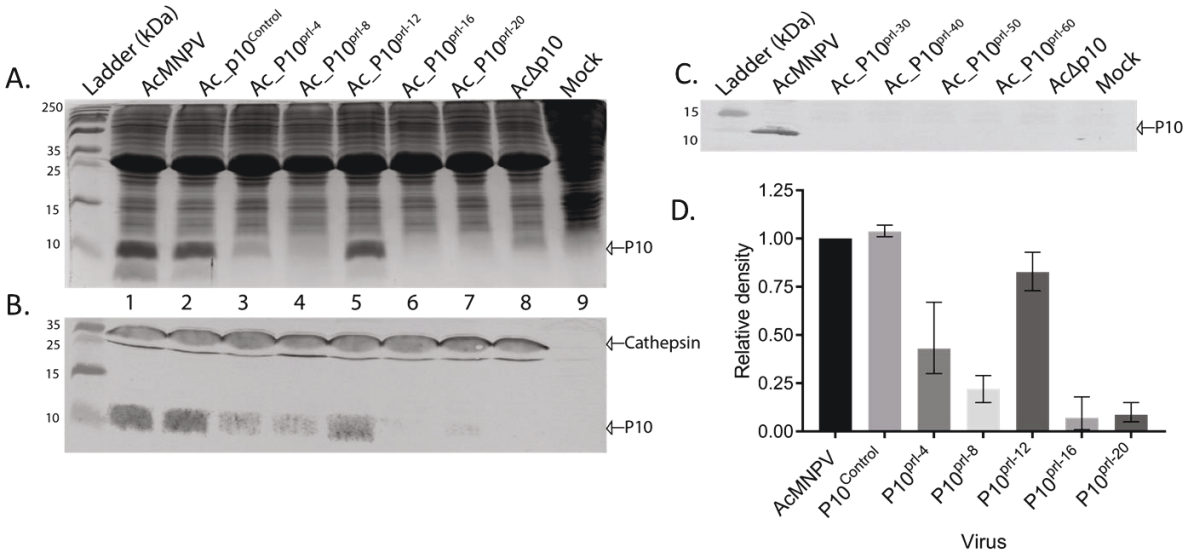

Figure 5.5 Protein syntheses in AcMNPV and *p10* promoter deletion recombinant viruses. Infected Tni368 cells were harvested at 96 hpi and total protein fractionated on a 15 % (w/v) SDS-PAGE for either Coomassie staining (A) or western blot analysis (B and C) with P10 and cathepsin-specific antibodies using an alkaline phosphatase-conjugated secondary antibody. Alkaline phosphatase activity was detected with NBT-BCIP (Methods 2.5.2). Lanes 1-9 (B) correlate to sample names at top (A). Arrows show expected sizes of P10 and cathepsin. Ladder size (kDa) is indicated, left. (D) The mean relative P10 band density for AcMNPV, Ac_P10^{Control} Ac_P10^{prl-4}, Ac_P10^{prl-8}, Ac_P10^{prl-12}, Ac_P10^{prl-16} and Ac_P10^{prl-20} were calculated from a series of Western blots (n=3). Error bars represents mean ± SD.

To characterise the observed decrease in expression, the average P10 band density from three separate western blots was recorded using imageJ (Figure 5.5C) for AcMNPV, Ac_P10^{control}, Ac_P10^{prl-4}, Ac_P10^{prl-8}, Ac_P10^{prl-12}, Ac_P10^{prl-16} and Ac_P10^{prl-20}. The results confirmed data in Figure 5.5 A-B, showing P10 expression decreased with progressively removed nucleotides. Results for Figure 5.5 C gave a 2.5 and 4.5 fold decrease in native *p10* expression for Ac_P10^{prl-4} and Ac_P10^{prl-8}. With expression further decreasing to a 14.3 and 12.5 fold decrease for Ac_P10^{prl-16} and Ac_P10^{prl-20} (Figure 5.5 D). However, as observed in Figure 5.5 A-B, Ac_P10^{prl-12} did not follow this observed expression decrease, with only a 1.2 fold decrease in P10 synthesis.

5.3.2 Lysis of AcMNPV, Ac_P10^{control}, Ac_P10^{prl-4}, Ac_P10^{prl-8}, Ac_P10^{prl-12}, Ac_P10^{prl-16} and Ac_P10^{prl-20}–infected insect cells

As discussed previously, a number of functional roles have been suggested for P10, including nuclear lysis of virus-infected cells to release and facilitate dispersal of polyhedra (Williams *et al.*, 1989; van Oers *et al.*, 1993). In the absence of P10, nuclear lysis does not occur and polyhedra are not released into the culture medium (see Chapter

Three). To determine whether particular levels of P10 are required for nuclear lysis and release of free polyhedra, Hi5 cells were infected with wild-type AcMNPV, Ac_P10^{control}, AcΔP10, Ac_P10^{prl-4}, Ac_P10^{prl-8}, Ac_P10^{prl-12}, Ac_P10^{prl-16} and Ac_P10^{prl-20} at 5 MOI (Method 2.3.3a) and were imaged using a light microscope at 4, 7 and 14 dpi (Figure 5.6).

After four days, signs of lysis were noted in Hi5 cells infected with AcMNPV, Ac_P10^{control}, Ac_P10^{prl-4}, Ac_P10^{prl-8}, Ac_P10^{prl-12} (Figure 5.6), however, no signs of nuclear lysis or free polyhedra were observed in Ac_P10^{prl-16}, Ac_P10^{prl-20} or Ac∆*p10* infected cells (Figure 5.6). By seven dpi, the numbers of free polyhedra observed in the media of infected cells had increased, and a few free polyhedra were also observed for both Ac_P10^{prl-16} and Ac_P10^{prl-20} (Figure 5.6). The number of free polyhedra continued to increase from seven to 14 dpi (Figure 5.6). However, it was noted (Figure 5.6) that there were fewer free polyhedra in the media from all infected cells containing promoter deletions, apart from Ac_P10^{prl-12}. At all-time points Ac_P10^{prl-12} displayed similar levels of lysis to AcMNPV and Ac_P10^{control}. Examinations of the images suggest a correlation between a general decrease in free polyhedra (Figure 5.6) with progressively removed nucleotides from the *p10* promoter (Figure 5.1).

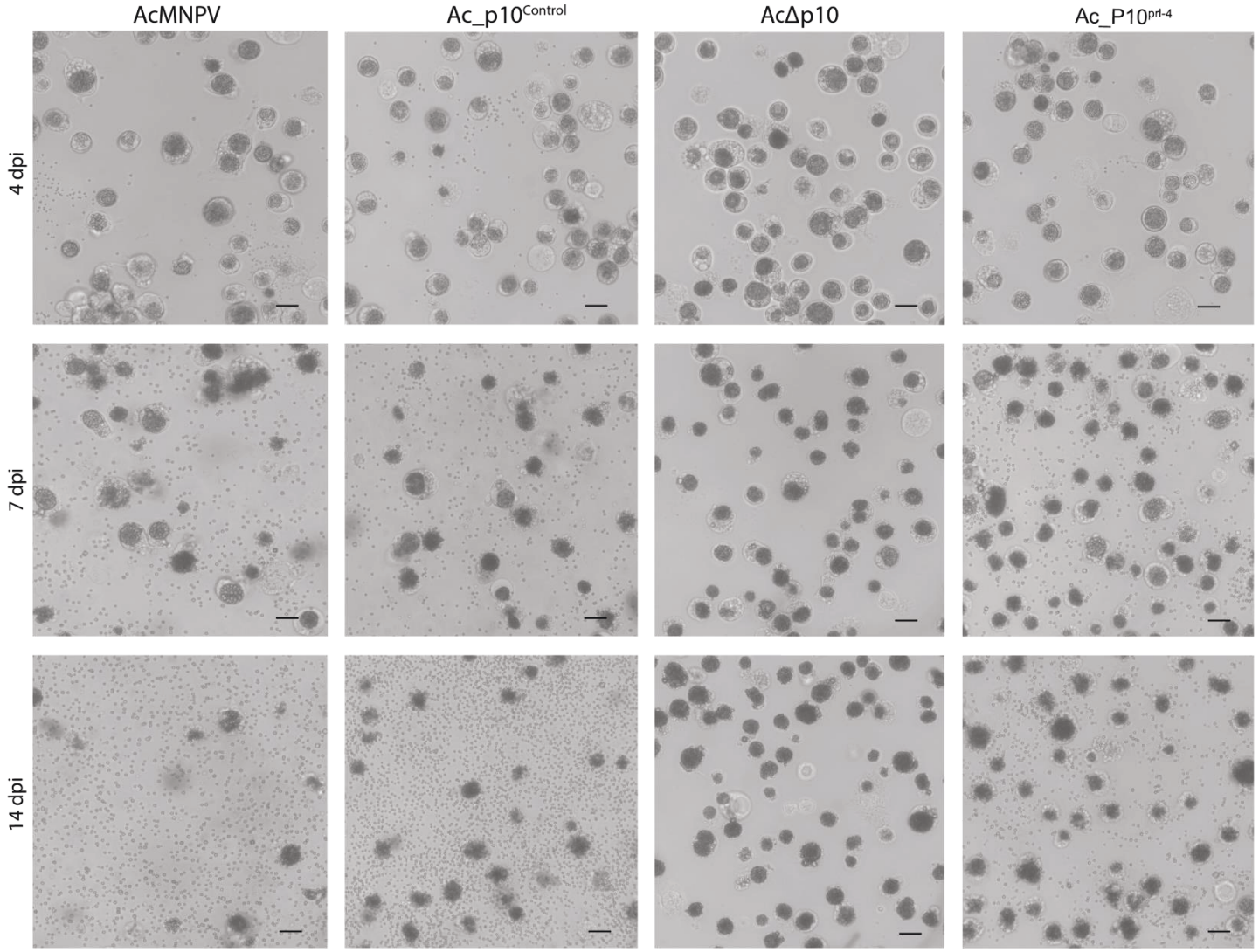

Figure 5.6 *T.ni* Hi5 infected cells at four, seven and fourteen days post-infection.

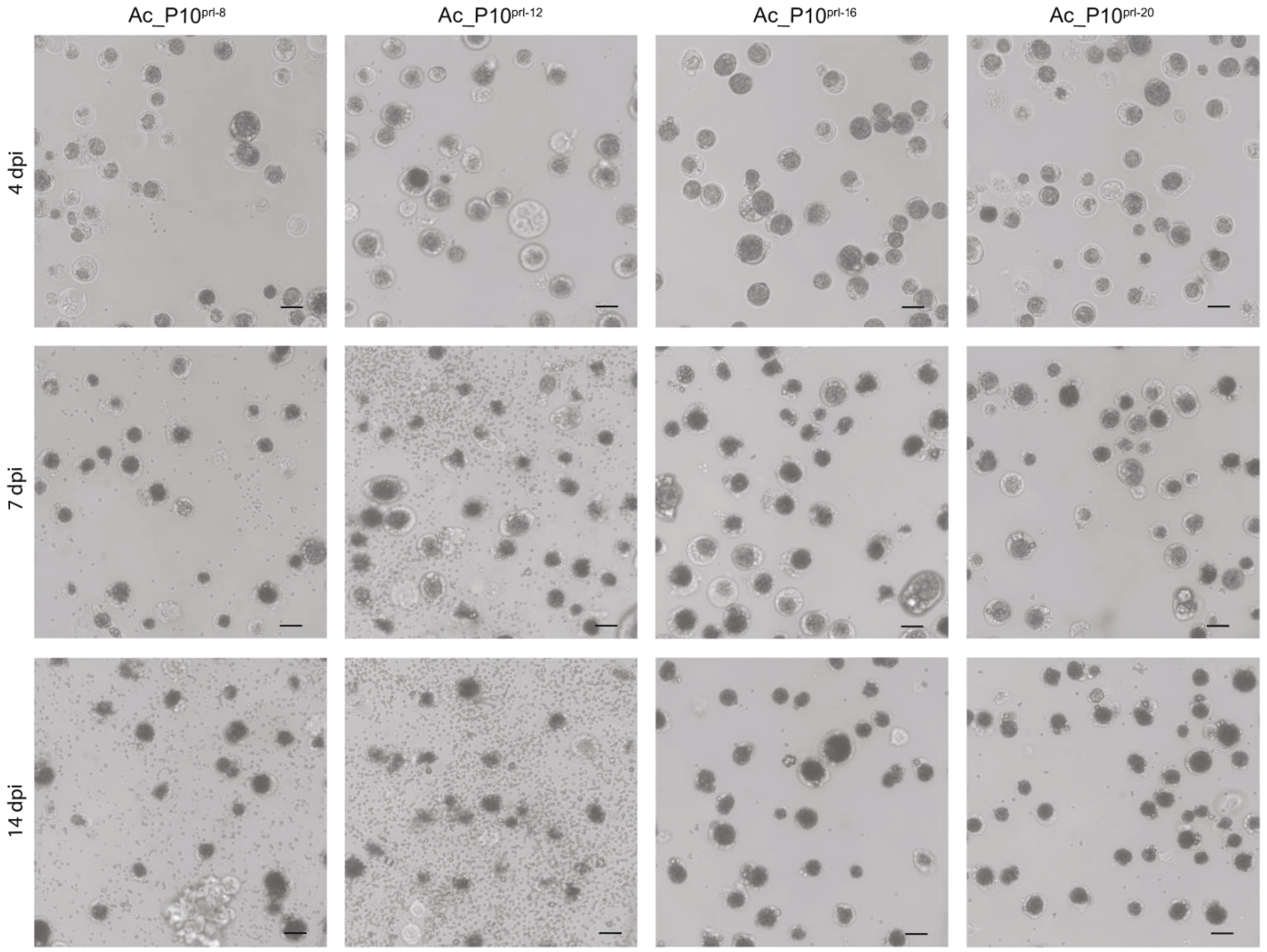

Figure 5.6 (continued) *T.ni* Hi5 infected cells at four, seven and fourteen days post-infection. *TN-368* cells were infected with AcMNPV or recombinant viruses (5 MOI) in 35 mm dishes and incubated at 28°C. AcMNPV and Ac_P10^{control} infected cells lysed by 4 dpi with numerous free polyhedra observed after 14 dpi. All infected cells with a recombinant viruses containing a base-pair deletion were observed with fewer free polyhedra in the media, apart from Ac_P10^{prl-12}. This suggest a correlation between a general decrease in free polyhedra (Figure 5.6) with progressively removed nucleotides from the *p10* promoter The cells were imaged using a light microscope Zeiss Axiovert 135 at 4, 7 and 14 dpi to show cell morphology and lysis (100X). Scale bar is 20 µm.

To determine if the number of free polyhedra was statistically lower in promoter deletion recombinants, post-acquisition image processing of occlusion bodies from 10 images from each virus were enumerated using image J (Figure 5.7).

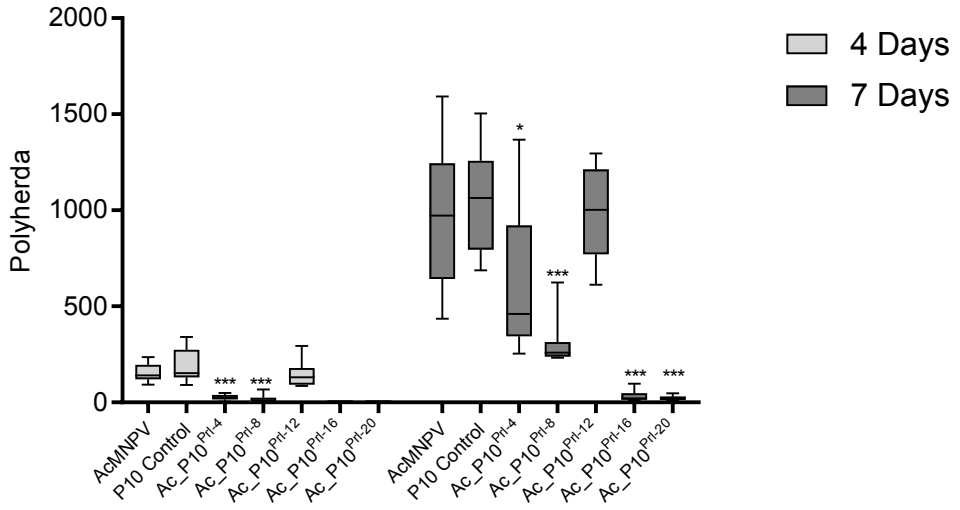

Figure 5.7 Observed free polyhedra from virus-infected *T.ni* Hi5 cells at four, seven and fourteen days post-infection. *T.ni* cells were infected with AcMNPV (5 MOI) in 35 mm dishes and incubated at 28°C. The cells were imaged using a light microscope Zeiss Axiovert 135 at 4, 7 and 14 dpi to show lysis (100X). Box and whiskers plot of mean free observed polyhedra from a total of ten separate images per virus. Scale bar is 20 µm.

Figure 5.7 indicates that nuclear lysis at 4 and 7 dpi (data from 14 dpi not shown), as indicated by free polyhedra in the medium, decreases with progressive deletions made to the *p10* promoter (Figure 5.3). This enumeration of free polyhedra confirmed results shown in Figure 5.6, with all deletion recombinants apart from Ac_P10^{control} or Ac_P10^{prl-12}, statistically less than AcMNPV at 4 and 7 dpi. Therefore, confirming that a reduction in *p10* expression, as confirmed by Western blot (Figure 5.5), has a concomitant effect on lysis (Figure 5.6 and 5.7).

5.3.3 Confocal microscopy of P10 structure formation during infection of *T.ni* cells with promoter deletion viruses

Confocal microscopy was performed on AcMNPV, Ac_P10^{control}, Ac_P10^{prl-4}, Ac_P10^{prl-12}, Ac_P10^{prl-16} and Ac_P10^{prl-20} infected TN-368 cells at 96 hpi (Figure 5.8) to observe formation of P10 structures during late phase of infection. Infected or control cells were fixed, stained using a P10 primary antibody and Alexa-fluor 488® secondary antibody (Methods 2.7.1a) and imaged using a Zeiss LSM 510 meta laser scanning microscope (Methods 2.7.1b). AcMNPV, Ac∆*p10* and mock-infected cells were included as positive and negative controls for expression of *p10* (data not shown).

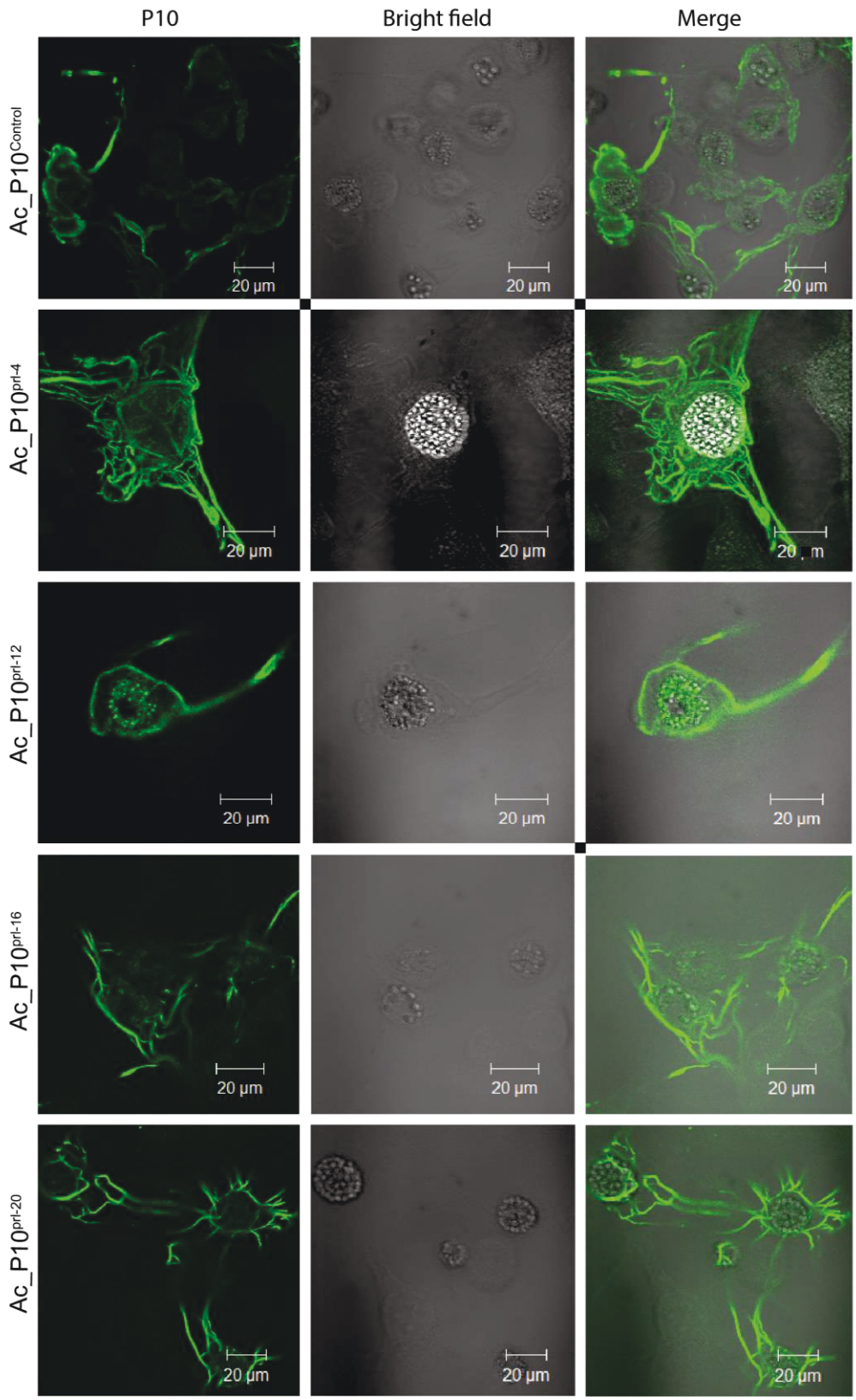

Figure 5.8 Immunofluorescence labelling of P10 structures at 96 hpi. Confocal microscopy of TN-368 cells infected with Ac_P10^{control}, Ac_P10^{prl-4}, Ac_P10^{prl-12}, Ac_P10^{prl-16} and Ac_P10^{prl-20} to observe P10 structures (green). Both Ac_P10^{control} and Ac_P10^{prl-12} infected cells showed the formation of thick peri-nuclear tubular structures. Ac_P10^{prl-4}, Ac_P10^{prl-16} and Ac_P10^{prl-20} infected cells were observed with thinner cytoplasmic filamentous structures with reduced number of cells observed with P10 associated structures (Ac_P10^{prl-16} and Ac_P10^{prl-20}). Scale bar 20µm.

During the later phase of infection (96 hpi), P10 was observed in almost all cells examined for AcMNPV, Ac_P10^{control}, Ac_P10^{prl-4}, Ac_P10^{prl-12}, Ac_P10^{prl-16} and Ac_P10^{prl-20}. Overall, no differences in P10 structures were observed between wild-type AcMNPV, Ac_P10^{control} and Ac_P10^{prl-12} virus-infected cells. P10 was shown associated with a thick cage-like structure around the nucleus (Figure 5.8) that was often observed as a thick band around the nucleus. Cells infected with Ac_P10^{prl-4} lacked this characteristic thick perinuclear structure, instead presenting as thinner cytoplasmic filaments located around the nucleus and branching out in the cytoplasm (Figure 5.8). These thin cytoplasmic structures were also observed for Ac_P10^{prl-16} and Ac_P10^{prl-20}, however, P10 did not show the close association with the periphery of the nucleus (Figure 5.8) as seen with AcMNPV, Ac_P10^{control}, Ac_P10^{prl-4}, Ac_P10^{prl-12} infected cells.

5.4 Discussion

This chapter presents an alternative approach to observing the functional role of P10 by determining how the levels of P10 expression effects protein function and answer the question: Why P10 is produced at such high levels? Unlike previous papers looking at promoter integrity expressing CAT (Weyer and Possee, 1988; Scheper *et al.*, 1997), this chapter looked at expressed P10 itself under a series of promoter deletions.

The main finding of this chapter was the fact that if we modulate P10 expression, a critical amount of P10 is required for virus-infected nuclear lysis. This confirmed a dependency of P10 function on the *p10* promoter, requiring the full integrity of promoter for maximum expression. Synthesis of P10 was determined by Western blot (Figure 5.5), which highlighted that deletions of only 4 bp caused a substantial decrease in expression and became undetectable with deletions made to the promoter of 30 bp or more. Previous studies examining the *p10* promoter also showed a similar decrease in expression, observing a concomitant reduction in expression with progressive deletions made to the promoter in the 5' non coding region (Weyer and Possee, 1988; Scheper *et al.*, 1997).

Importantly it was observed in the deletion recombinants expressing ≥2.5 fold decrease in P10 expression that the characteristic thick peri-nuclear cage was either immature or absent, therefore indicating that sufficient protein is required to make the P10 cage. In the absence of this cage-like structure a reduction or absence in nuclear lysis was observed by recombinant virus-infected cells and suggests that the formation of the cytoplasmic P10 cage structure is could play an important role in nuclear lysis.

This hypothesis is explored further in Chapter Six, where modelling of P10 structures highlight the formation of a dynamic cage-like structure that changes shape over time in a manner that facilitates lysis from 96 hpi (Chapter Six).

Interestingly, Hi5 cells infected with Ac_P10^{prl-}12 gave comparable levels of P10 expression to both AcMNPV and Ac_P10 control, which was in contrast to other deletions made to the promoter regions (Figure 5.5 C). On review of similar P10 deletions by Possee *et al*. (1987) and Scheper *et al*. (1997), they did not note similar characteristics. However, it is important to note that identical deletions to the promoter were not made, and they observed CAT reporter gene expression.

A search for studies relating to promoter expression did not find many similar results relating to that observed above. One similar study by Blissard *et al*. (1991) made eleven 5' deletions to the regulatory region of a *gp64* promoter-fusion (CAT). They observed varied CAT activity between deletions in three different cell lines. The authors proposed the *gp64* promoter contained both negative and positive regulatory elements, and the removal of such regions could influence expression (Blissard and Rohrmann, 1991). However, how the removal of 12 nucleotides from the P10 promoter would display a positive effect on expression is still speculation.

One alternative theory is that Ac_P10^{prl-12} contains an undetectable mutation or forms part of a mixed infection that increases expression. However, as this virus was made twice, with the *p10* region determined by both PCR and DNA sequencing at each virus passage, it is unlikely this is the case. To determine the cause for this anomaly in expression, further experiments have been proposed in the final discussion chapter.

A number of theories have been proposed that could result in the observed decrease in *p10* expression as a result of increasing bp deletions. It has been identified that very-late gene promoters (*p10* and polyhedrin gene) have the addition of a unique 'burst' sequence located between the TAAG signal and translational start site, which is suggested to enhance very-late transcription (reviewed in Vanarsdall *et al*., 2004). Therefore, the bp deletions made within this sequence is likely to have deleterious effect on expression. Furthermore, these deletions could disrupt the interaction of very late factor-1 with *p10* promoter, which is suggested to be essential for high levels of expression for very late genes of P10 and polyhedrin (Vanarsdall *et al.*, 2004).

It has also been identified that the *p10* gene contains four overlapping transcripts with possible polyadenylation signals on three or four of these (Rankin *et al.*, 1986). The bp promoter deletions would likely disrupt these 5' polyadenylation termination signals and

overlapping transcripts at *p10,* thus disrupt P10 function. This is most notably with the 1100bp transcript that extends *p26* sequence and terminates immediately prior to the ATG translation site (Liu *et al.*, 1986; Rankin *et al.*, 1986).

In the study it can be concluded that P10 requires complete integrity of *p10* promoter for maximum expression and importantly i have determined that as protein levels decrease, the P10 cage structure is diminished with a concomitant decrease in nuclear lysis.

Chapter Six:

Serial block-face scanning electron microscopy to reconstruct three-dimensional virus structures in AcMNPV-infected cells

6.1 Introduction

Methods to image baculovirus structures in virus-infected cells have historically used light microscopy, as early as 1856 by Maestri and Cornalia as reviewed by Benz (1986). More recently confocal microscopy (Quant-Russell *et al.*, 1987; Volkman and Zaal, 1990; Alaoui-Ismaili and Richardson, 1998; Patmanidi *et al.*, 2003), or EM for the study cell ultrastructure at high-resolution (Bergold, 1947; Bergold, 1950; Hughes, 1950; Summers and Arnott, 1969) have been used to progress the understanding of baculoviruses. Whilst confocal microscopy allows reconstruction of three dimensional (3D) images at low resolution, there is a gap at present in the reconstruction of large volume 3D images from high-resolution 2D micrographs (Hughes *et al.*, 2014). This chapter presents a solution that bridges confocal microscopy and high-resolution EM for 3D imaging of AcMNPV-infected cells.

Confocal microscopy is an optical imaging technique for observing live or fixed cells that allows acquisition of 3D images using Z-stacking functions (Patmanidi *et al.*, 2003; Carpentier *et al.*, 2008). The limitation of the technique has always been the low resolution, which has had implications for imaging cell ultrastructure. Therefore, high-resolution imaging of cell or virus ultrastructures has commonly used TEM, in which images are prepared from ultra-thin slices cut from embedded tissue (Summers and Arnott, 1969; Vlak *et al.*, 1988; Williams *et al.*, 1989). Unlike the 3D possibilities of using confocal microscopy, TEM is conventionally 2D; meaning much of the detailed structural information is not captured and is limited to ~80nm sections.

Systems to solve the limitations of conventional TEM have been developed and include serial-section TEM (ssTEM) (Birch-Andersen, 1955; Sjöstrand, 1958; Ware and Lopresti, 1975) or tilt-series based tomography (Hoppe, 1981; Baumeister, 2002; Shi *et al.*, 2015), which provide mechanisms to model small data sets in 3D in high-resolution. Serial-section TEM involves the process of cutting and imaging serial sections from a resin-embedded sample as a single ribbon. Each section is individually imaged by TEM and post-processed for data analysis. This method has been highly successful and has been attributed to the 3D reconstruction of the retinal rod synapse (Sjöstrand, 1958), dendritic spine (Harris, 1999) and even whole organisms with the nematode *Caenorhabditis elegans* (White *et al.,* 1986). This process is however, labour-intensive and time-intensive, often requiring a high degree of expertise to minimise artefacts such as compression, alignment issues, loss of sections and stain precipitation. Alternatively, tilt-series based electron tomography can be automated, enabling imaging of 350-1000 nm thick sections at a series of different tilts. Similar to ssTEM, it relies on manual serial

sectioning from resin-embedded samples and is limited to small volumes (Shi *et al.*, 2015).

The automatic acquisition of near TEM resolution images has become a reality with the introduction of new SEM-based imaging systems: Focussed ion beam (FIB) and serial-block face SEM (SBF-SEM). These techniques use field emission SEM (FEG-SEM) with backscattered electron imaging on resin blocks (Kittelmann *et al.*, 2016) with the automatic image and sectioning of a single resin block (Figure 6.1). The benefit of which is a new automated approach to generating high-resolution images that minimises the need for human interaction during image capture (reviewed in Hughes *et al*. 2014; Kittelmann *et al*. 2016). This reduces the need for image realignment and minimises human-induced artefacts during processing (Hughes *et al.*, 2014).

The FIB-SEM uses gallium ion beam milling to section the resin block face with Z-resolution as fine as 5nm. The major issue is the time-consuming process of milling and the limited region of imaging (~50μm^2) making it optimal for small volumes. The SBF-SEM uses an automated microtome (3View) system that contains a diamond knife in the SEM chamber for the serial sectioning of 30-200 nm thin slices (Figure 6.1) (Leighton, 1980; Denk and Horstmann, 2004; Starborg *et al.*, 2013). SBF-SEM benefits from quicker acquisition and collection of larger sample volumes (600x600x600μm), making it suited to larger datasets such as virus-infected cells. The main drawback when compared to FIB-SEM is a slightly decreased resolution; however, this is minimal and still allows near-TEM image quality (Figure 6.2).

This chapter will focus on the optimisation of SBF-SEM for the generation of high resolution images of AcMNPV-infected TN-368 cells, to facilitate the reconstruction of 3D virus structures including P10, EDS and polyhedra. It is planned that providing new information on these structures, and their association with each other and the cell ultrastructure, will aid our understanding of their roles in virus infection.

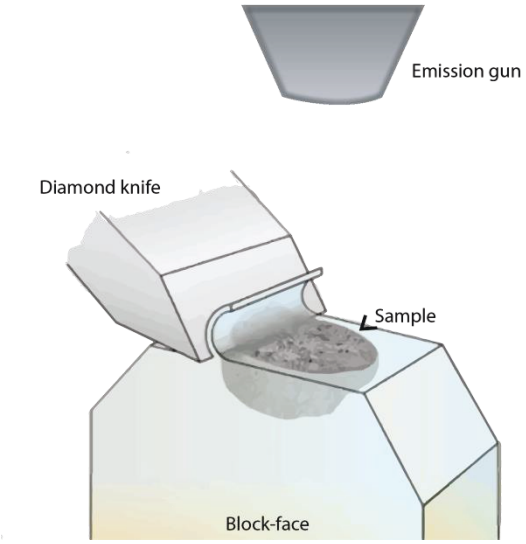

Figure 6.1 Automated 3View system for imaging block-face by SBF-SEM. This comprises an automated system for sectioning from a resin block-face in an SEM chamber. Adapted from Julia Kuhl (2016) from www.somedonkey.com.

6.2 Sample preparation, imaging and post-acquisition optimisation of AcMNPV- infected TN-368 cells

As no published SBF-SEM methods for baculoviruses or insect cells were available, a protocol for primary fixation, post-fixation, dehydration and resin embedding was developed (Method 2.7.3). These methods were based on previous SBF-SEM applications (Starborg *et al.*, 2013; Hughes *et al.*, 2014), TEM fixation methods and communication with Dr Louise Hughes. The main objectives were to achieve a suitable cell pellet for sectioning and generate good contrast in the final images. To achieve these objectives, six main steps were optimised: (1) sample fixation (Section 6.2.1 and 6.2.2); (2) sample preparation (Section 6.2.3); (3) data acquisition (Section 6.2.4); (4) data processing (Section 6.2.5); (5) data analysis (Section 6.2.5) and (6) visualisation (Section 6.2.6) for reconstruction of the 3D models of AcMNPV ultrastructure in infected insect cells (Figure 6.2).

To produce a resin embedded cell pellet that could be imaged using SBF-SEM, protocol optimisation was performed on AcMNPV-infected TN-368 cells at 96 hpi and fixation quality was assessed by TEM. These steps are discussed in Section 6.2.1-6.2.6. The final optimised method (Methods 2.7.3) was then used to image AcMNPV-infected TN-368 cells at 24, 48, 72 and 96 hpi using SBF-SEM.

6.2.1 Fixation and preparation of AcMNPV-infected TN-368 cell pellet

The initial focus was to obtain a good standard of fixation and resin embedding of baculovirus-infected insect cells. Sample preparation included a rapid microwave fixation method (Method 2.7.2 and 2.7.3) for both the primary and secondary fixation stages. This protocol was chosen because it had been successfully used with plant cells and had achieved significant reduction in processing time (Heumann, 1992; Zechmann and Zellnig, 2009). The microwave fixation method involved six 5 second full power (850 W) blasts, each separated by a 30 second incubation period for both the primary and secondary fixation steps. For comparison, a separate cell pellet was fixed in the conventional manner, with two-hour incubations (data not shown). The results between microwave and standard fixation methods were compared by TEM, which displayed a similar quality of image (results not shown). On the basis of reduced processing time, the microwave fixation was the preferred option during this study.

The initial sectioning of cell pellets was difficult because pellets were soft, especially in cell rich areas. To try to obtain harder pellets with better resin penetration, incubation times for resin-embedding (Method 2.7.2 and 2.7.3) were increased from 15 to 30 minutes with final 60-minute incubation. Furthermore, centrifugations of the microfuge tubes at resin infiltration were increased from 2 to 4 minutes to increase the infiltration of resin. These changes gave a harder pellet that was easier to section and produced good quality ultrathin sections (for example, Figure 6.2 A-B).

Resin polymerisation was also optimised, after comparing different polymerisation times, it was shown that Epon 812 resin benefited from longer incubations. Mock-infected TN-368 cells were shown to polymerise sufficiently at 100ºC for 1-2 hours, however, this was insufficient for baculovirus-infected TN-368 cells. It was noted during sectioning that the baculovirus-infected TN-368 cells remained soft, which was postulated to result from the large virus structures impeding polymerisation. By changing the incubation to 70ºC for 18-24 hours, successful polymerisation allowed for a harder resin-block. The optimised steps in Section 6.2.1 were implemented for both SBF-SEM (Methods 2.7.3) and TEM (Methods 2.7.2).

6.2.2 Contrast enhancement for SBF-SEM imaging of AcMNPV-infected TN-368 cells

It was shown by Starborg *et al*. (2013) that the addition of a second osmium tetroxide step for the staining of cell pellets generated increased contrast as a result of increased electron scattering. Therefore, the cell pellet was treated with an additional 2% osmium tetroxide stain and incubated for 40 minutes at RT. Samples imaged with the additional osmium stain displayed enhanced contrast and resolution for improved structure identification (for example, Figure 6.2).

Another benefit of using the additional osmium tetroxide staining step was a decrease in sample charging. Unlike traditional SEM, where electrostatic charge is minimised by the grounding effect of a gold coating, the SBF-SEM 3View system exposes the resin block face after each slice thus making it prone to charging in the absence of heavy metals (Wilke *et al.*, 2013; Hughes *et al.*, 2014).

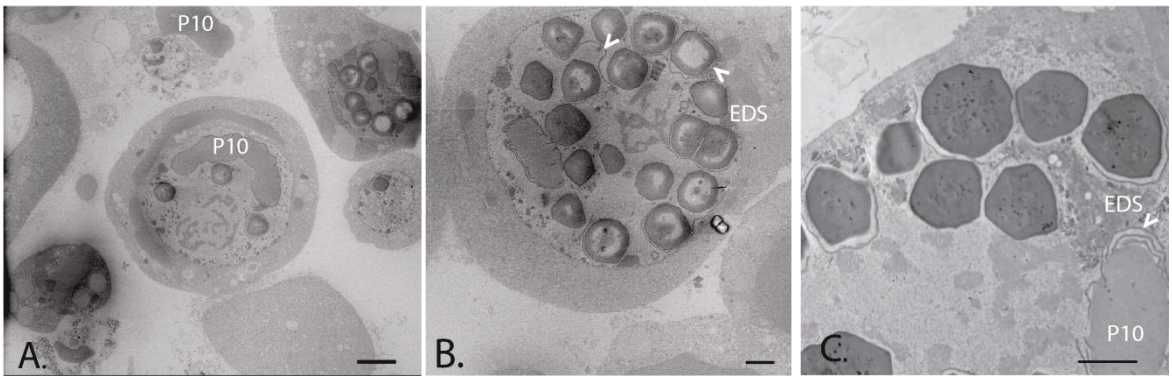

Figure 6.2 Scanning and transmission electron microscopy image of an AcMNPV-infected TN-368 cell at 96 hpi. Comparing two EM methods (A-B) SBF-SEM and (C) TEM for resolution and contrast with P10 and electron dense structure (EDS, arrow) highlighted. Bars represent, 5µm A and 2µm B, C.

6.2.3 Preparation of resin-embedded samples for imaging by SBF-SEM

After fixation, staining and embedding, a sample was mounted onto a flat surface specimen pin used for the SBF-SEM 3View system. The polymerised resin block was shaped to a small isosceles trapezoid using a fine jewellers saw and razor blade (1.5-2mm) in height and small enough (~3mm) to fit on the pin. A conductive adhesive resin (Circuitworks conductive epoxy, #CW2400, ITW Chemtronics, Georgia, USA) was used to mount the sample on the pin and was cured for one hour at 70ºC or overnight at RT. The resin block was further trimmed using a PT-PC PowerTome Ultramicrotome (RMC™) with a glass or diamond knife to smooth the block face.

The sample was then loaded onto a Zeiss Merlin compact field emission gun SEM (FEG-SEM) with variable pressure (VP) mode and a Gatan 3View 2 XP system and aligned to the diamond knife of the 3View stage. A final check was conducted to ensure that the resin block face was being cut at the correct angle.

6.2.4 Data acquisition of resin-embedded sample for imaging by SBF-SEM

The acquisition of data was performed by Dr Louise Hughes using imaging parameters under her advisement for the SBF-SEM. System preferences were chosen to give the highest final image resolution without damaging the resin block (Table 6.1).

Table 6.1 Imaging parameters for acquisition of data by SBF-SEM

Imaging parameters	AcMNPV-infected cells			
	24 hpi	48 hpi	72 hpi	96 hpi
Accelerating voltage	4kV	4kV	4kV	4kV
Horizontal field width	82µm	41 µm	75 µm	64 µm
Pixel size	15x15nm	7.6x7.6nm	6.9x6.9nm	12x12nm
Slice thickness	100nm	100nm	100nm	100nm
Dwell time	3µs	3µs	3µs	3µs
Aperture size	30µm	30µm	30µm	30µm
Chamber pressure	0.23 torr	0.23 torr	0.34 torr	0.23 torr
Digital Micrograph	Version: 2.31.743.0	Version: 2.31.743.0	Version: 2.31.743.0	Version: 2.31.743.0
Variable pressure	40Pa	30Pa	45Pa	40Pa
Sections	150-700	150-700	150-700	150-700

At each time point (24, 48, 72 and 96 hpi) one pellet was imaged with a total of 150-700 sections collected. For each section, the SBF-SEM was set to capture images of the block-face at four different regions. After completion, the resin block was stored at RT in case further imaging was required.

6.2.5 Data processing of acquired images from SBF-SEM

The raw image datasets of 150-700 sections were acquired using Digital Micrograph (Gatan, Oxfordshire, UK) format (dm4). These images were then converted to obtain stacked image files (mrc) for data processing using a free iMOD© software package

(Kremer *et al.*, 1996). Once converted, the data settings were updated to give the image size in Angstroms for X, Y and Z (slice thickness).

If required a number of optimisations steps could be performed. This included alignment of stacked images, which used an automated system (etomo, part of the iMOD package) with default parameters, rotation and translation selected. Image enhancement and data trimming was also possible through iMOD as well as AMIRA if required. It was also required, due to the large data size of the stacked image file, to bin the file in 2D, this decreases the file size and allows for more stable software analysis.

6.2.6 Data analysis of SBF-SEM processed data

Image processing was performed using the 3D modelling program AMIRA (FEI™, Cambridge, UK) that allowed both automatic and manual isolation of baculovirus structures (Figure 6.2 A-B). The segmentation function combining the trace and threshold function was used to highlight/select structures of interest in each slice (Figure 6.3 B). This process was repeated over sequential sections containing the structures of interest (See Appendix; Supplementary CD, stacked image).

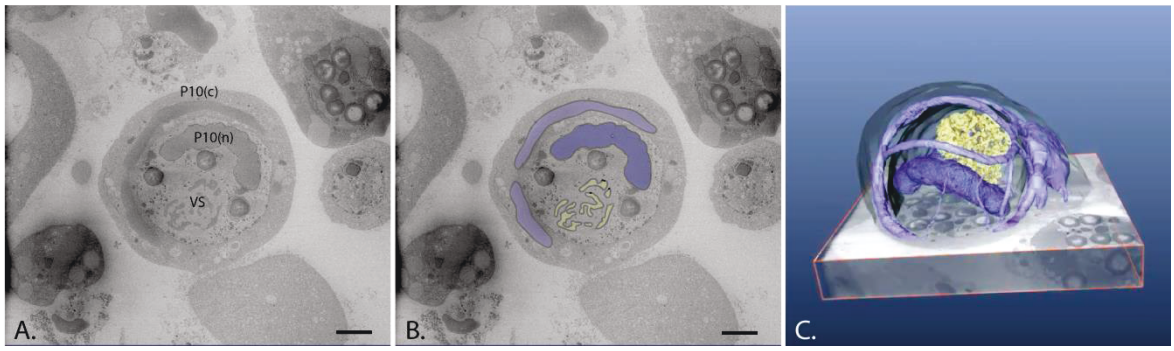

Figure 6.3 Generation of a 3D surface rendered image of AcMNPV-infected Tni368 cells. (A) SBF-SEM image of AcMNPV-infected TN-368 cell at 96 hpi. (B) Structures of interest (P10 = blue, virogenic stroma = yellow) highlighted using AMIRA segmentation software. (C) Surface rendered 3D model of structures created using Amira from highlighted regions (B). Key: (c) cytoplasm, (n) nucleus, VS virogenic stroma. Scale Bar = 5µm.

6.2.6 Modelling and visualisation of image-stacks for virus structures in AcMPNV-infected TN-368 cells

Data analysis of structure(s) in Amira generated a surface rendered 3D model by using an image generate and surface view function (Figure 6.3 C). It was possible to alter the surface to change the level of smoothing, colour, transparency, and shadows, as well as

other visual effects for model enhancement. Another useful function was 3D measurement and surface volume, which was used to estimate the size and volume of structures (Figure 6.4 A-B).

6.3 High-resolution 3D models of P10 structures from AcMNPV-infected TN-368 cells

AcMNPV P10 structural models were generated from AcMNPV-infected TN-368 cells at 24, 48, 72 and 96 hpi (Method 2.7.2a) as outlined in Section 6.2. Each time point included two figures of a single cell, a SEM image of the infected cell with a partial reconstruction of P10 and a complete 3D model of the P10 structures. This included the relative position of the nucleus (N), nuclear membrane (NM) and the cytoplasm (C) (Figures 6.4 to 6.11). Additional models (Appendix 1.1-1.4; Appendix 2.1-2.3) for each time point and film at 96 hpi (Appendix; Supplementary CD, P10 structures) are presented in Appendix.

Data acquisition of P10 structures at 24 hpi were imaged at an accelerating voltage of 4kV with a variable pressure of 40 pascal (Pa) (Table 6.1). A total of 308 slices were imaged at a Z-thickness of 100nm and horizontal field width (HFW) of 82µm with pixel size of 15x15nm. SEM images of the surface resin block (Figure 6.4 A) and later image-stacks (Figure 6.4 B) produced high resolution with excellent contrast, allowing partial model automation for P10 structures.

By 24 hpi, the AcMNPV-infected TN-368 cells presented phenotypic signs of baculovirus infection with a large virogenic stroma (VS) containing interspersed nucleocapsids (NC) (Figure 6.4 A-B). Surface reconstruction of P10, recognisable from its distinct fibrous structure (Figure 6.5 A arrow), displayed a long thin formation, positioned in the nucleus (light blue) and cytoplasm (dark blue) (Figure 6.4 C-E).

Complete P10 surface rendered images (Figure 6.5) are shown with the cytoplasmic membrane removed to display the full morphology of the P10 structures. The nuclear and cytoplasmic P10 structures remained independent of each other (Figure 6.5 A-C), separated by the host nuclear membrane (Figure 6.5 D-E). Cytoplasmic P10 presented as a thin filamentous structure that branched off at acute angles within the cytoplasm (Figure 6.5 A-E). Nuclear P10 was observed as a single thin worm-like structure in close proximity to the nuclear membrane (Figure 6.5 D-E). The differences in the two P10 structures may indicate differing roles for nuclear and cytoplasmic P10.

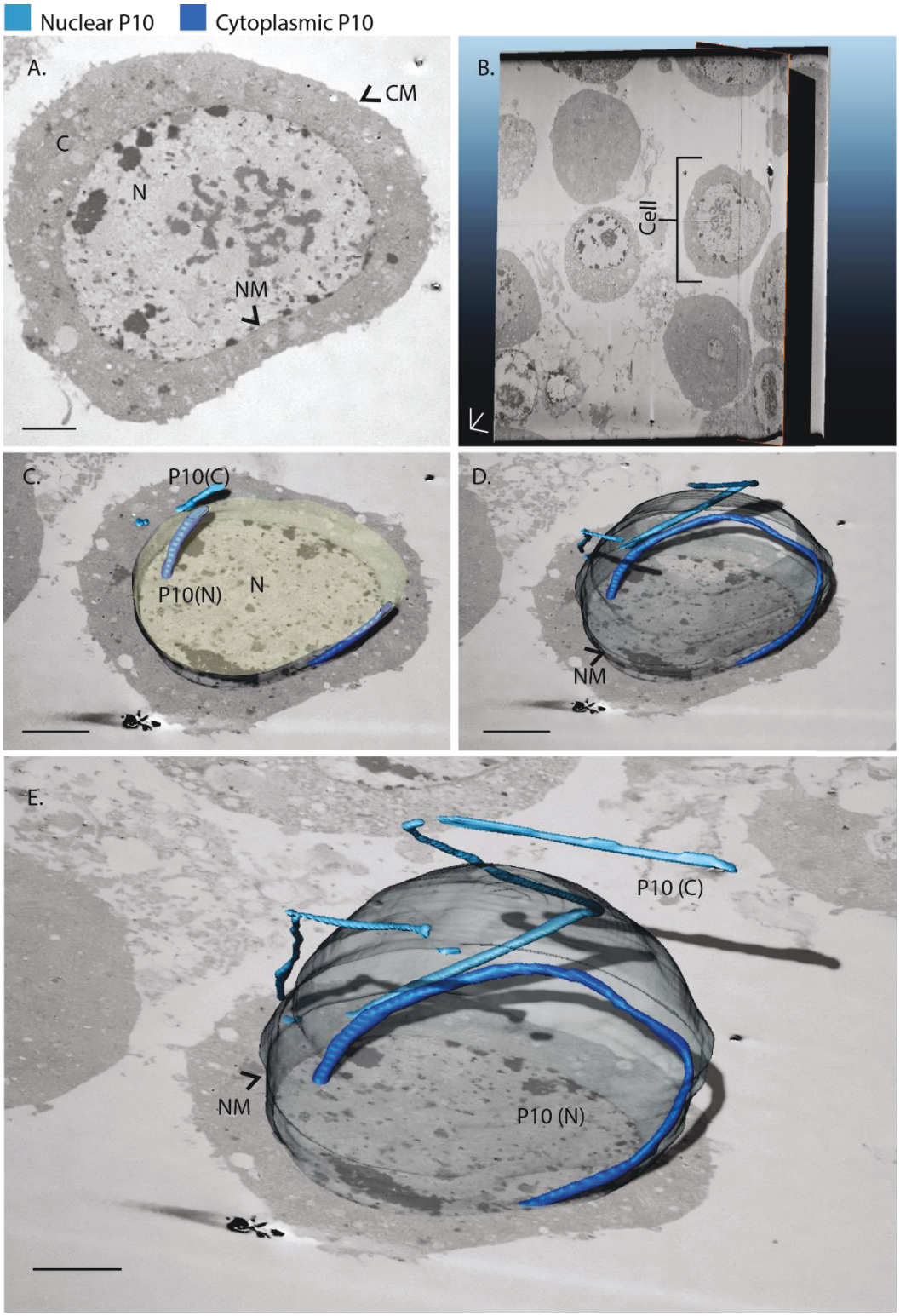

Figure 6.4 Serial-block face scanning electron microscopy of AcMNPV structures in infected TN-368 cells at 24 hpi. AcMNPV-infected TN-368 cells were harvested at 24 hpi and fixed in Epon 812. 100nm thick sections were imaged automatically using the 3View system on the Zeiss Merlin compact field emission gun SEM (A) and grouped to make a stacked image file (.mrc) (B). A segmentation function on Amira was used to build up surface rendered images of P10 (C-E). Abbreviations: C cytoplasm, N nucleus, NM nuclear membrane, CM cytoplasmic membrane. Scale bar = 3μm.

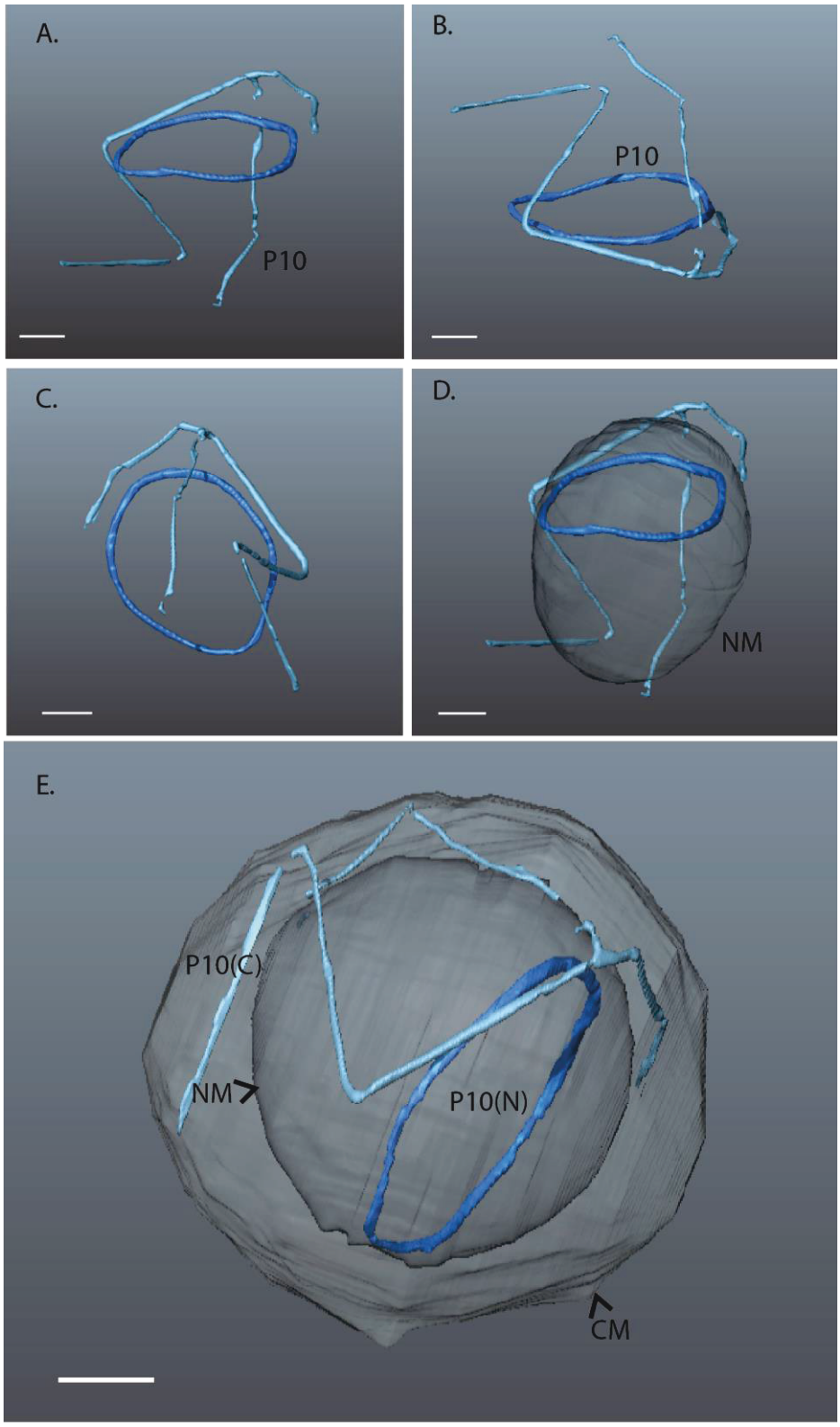

Figure 6.5 Serial-block face scanning electron microscopy of AcMNPV structures in infected TN-368 cells at 24 hpi. P10 structures formed as thin cytoplasmic and nuclear structures that were observed to branch off randomly. Nuclear P10 formed a halo structure. Surface generated images for P10 were generated from stacked images using Amira (A-E). Abbreviations: C cytoplasm, N nucleus, NM nuclear membrane, CM cell membrane. Scale bar = 3μm.

Data acquisition of P10 at 48 hpi was imaged at an accelerating voltage of 4kV with a variable pressure of 30Pa (Table 6.1). Data processing was performed on 620 slices at a Z-thickness of 100nm, HFW of 41µm and pixel size of 7.6x7.6nm. SEM images of the surface resin block (Figure 6.6 A) and later image-stacks (Figure 6.6 A) produced high-resolution images with excellent contrast to allow partial model automation for P10 structures.

AcMNPV infection at 48 hpi displayed a characteristic virus phenotype commonly associated with the late phase of infection, with polyhedra, P10, VS and EDS structures observed (Figure 6.6 A-B). Partial reconstruction of P10 in Figure 6.6 C-E showed that separate P10 structures were maintained both in the nucleus and membrane, separated by the nuclear membrane (Figure 6.6 C&E, arrow).

Full reconstruction of P10 showed distinct cytoplasmic and nuclear P10 structures (Figure 6.7 A-C), separated by the nuclear membrane (Figure 6.7 D-E, arrow). Cytoplasmic P10 displayed larger structures than modelled at 24 hpi, forming a branched structure that wrapped around the nucleus on the outside of the nuclear membrane (Figure 6.7 A-E). It is referred here as a ‘cage-like’ structure. This perinuclear structure displayed a complex network of thin filaments that were shown to accumulate at a polar region (Figure 6.7 A). Nuclear P10 (Figure 6.7 B) had increased in diameter from 24 hpi to form a single large elongated shape that was observed throughout much of the nucleus (Figure 6.7 D).

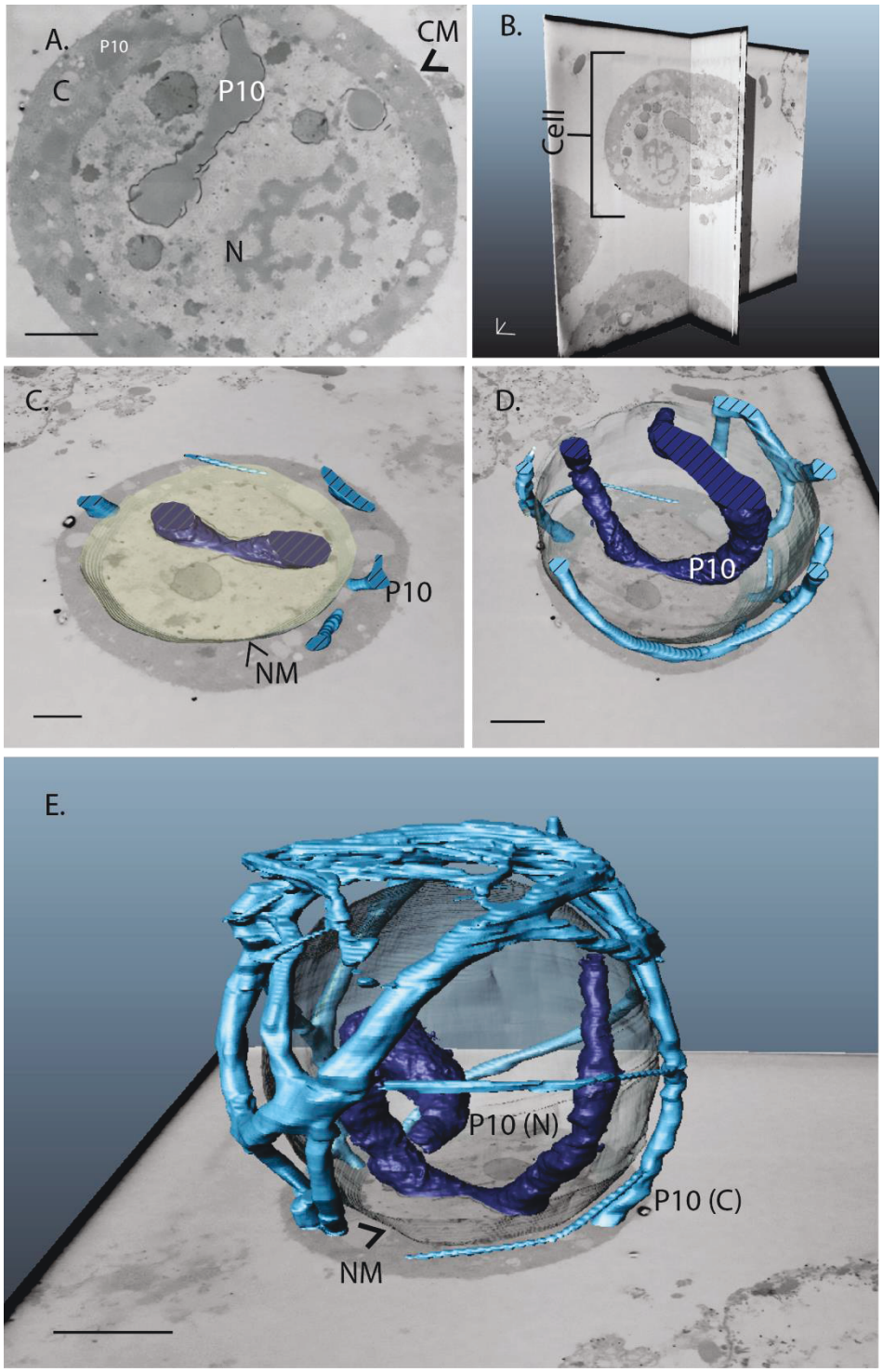

Figure 6.6 Serial-block face scanning electron microscopy of AcMNPV structures in infected TN-368 cells at 48 hpi. AcMNPV-infected TN-368 cells were harvested at 48 hpi and fixed in Epon 812. 100nm thick sections were imaged automatically using the 3View system on the Zeiss Merlin compact field emission gun SEM (A) and grouped to make a stacked image file (.mrc) (B). A segmentation function on Amira was used to build up surface rendered images of P10 (C-E). Abbreviations: C cytoplasm, N nucleus, NM nuclear membrane, CM cell membrane. Scale bar = 3µm.

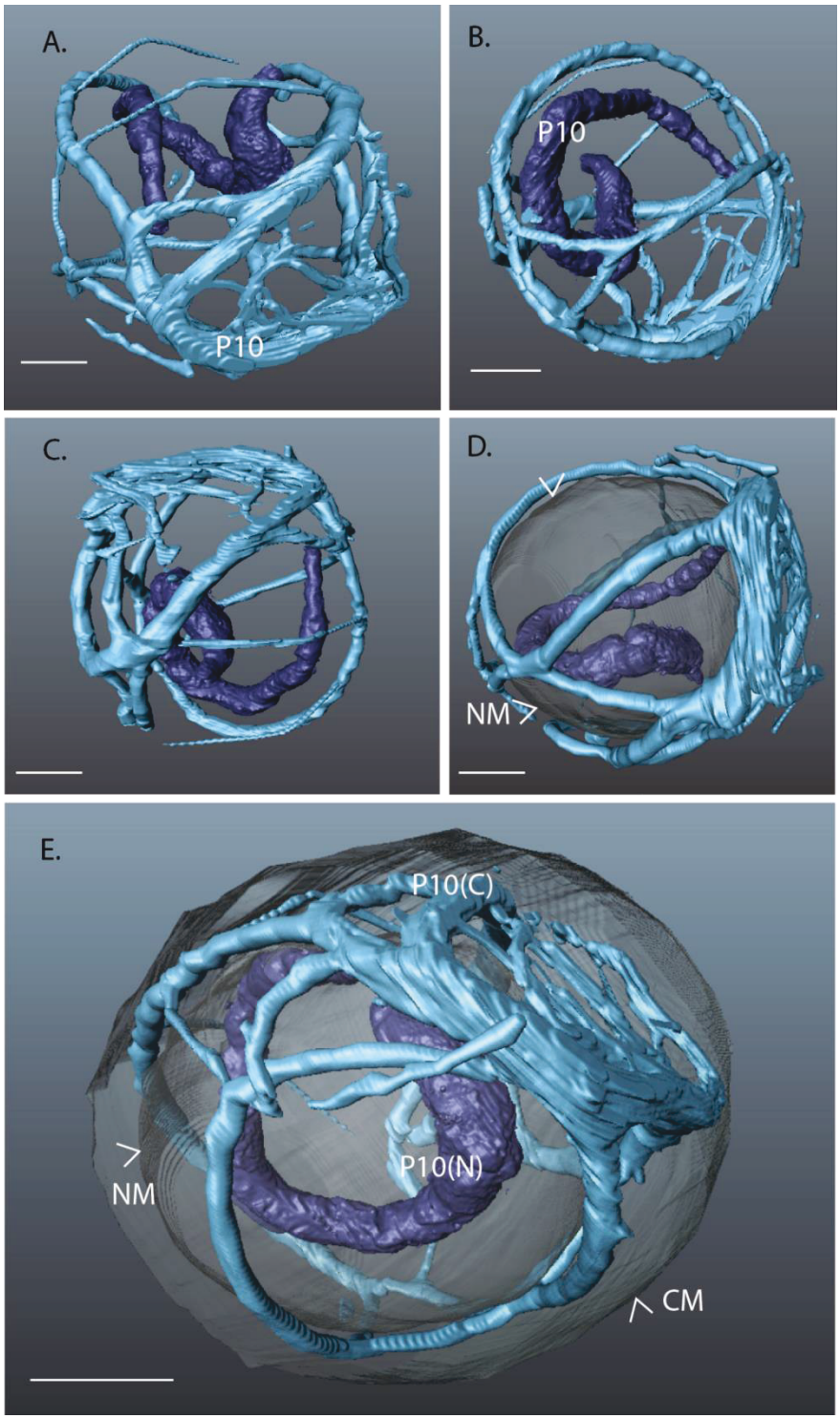

Figure 6.7 Serial-block face scanning electron microscopy of AcMNPV structures in infected TN-368 cells at 48 hpi. Cytoplasmic P10 formed a peri-nuclear cage structure the remained separated from nuclear P10. Nuclear P10 formed a thick worm-like structure. Surface generated images for P10 were generated from stacked images using Amira (A-E). Abbreviations: C cytoplasm, N nucleus, NM nuclear membrane, CM cell membrane. Scale bar = 3μm.

Data acquisition of P10 at 72 hpi was imaged at an accelerating voltage of 4kV with a variable pressure of 45Pa (Table 6.1). Data processing was performed from 540 slices at a Z-thickness of 100nm, HFW of 75µm and pixel size of 6.9x6.9nm. SEM images of the surface resin block (Figure 6.8 A) and later image-stacks (Figure 6.8 B) produced high resolution images with excellent contrast. This allowed identification of the virus ultrastructure and partial model automation for P10 structures.

AcMNPV infection at 72 hpi displayed characteristics of the very late phase of infection with the presence of mature polyhedra, P10 structures and production of EDS that were aligned both with P10 and polyhedra (Figure 6.8 A-B). P10 structures at 72 hpi were sometimes observed as white structures (Figure 6.8 A) rather than the expected dark grey. This is likely due from difficulties with stain penetrating into the full depth of the P10 structures or from delayed imaging, which allowed regions to de-stain. Partial reconstruction of cytoplasmic and nuclear P10 structures (Figure 6.8 C-D) showed that they remained separated by the nuclear membrane (Figure 6.8 C&E arrows).

This separation was further shown in 3D generated models of complete P10 structures in Figure 6.9, confirming that these structures remain independent throughout the virus replication cycle. The cytoplasmic P10 maintained its characteristic perinuclear structure however, in contrast to 48 hpi; the P10 filaments had condensed to form fewer, thicker tubules (Figure 6.8 A-E). This suggests cytoplasmic P10 is a dynamic structure that is able to rearrange itself over time, possibly in relation to its role. Similar to 48 hpi, nuclear P10 was observed forming thick worm-like structures, which were observed close to the periphery of the nuclear membrane (Figure 6.9). This is likely to minimise disruption to the polyhedra and virogenic stroma.

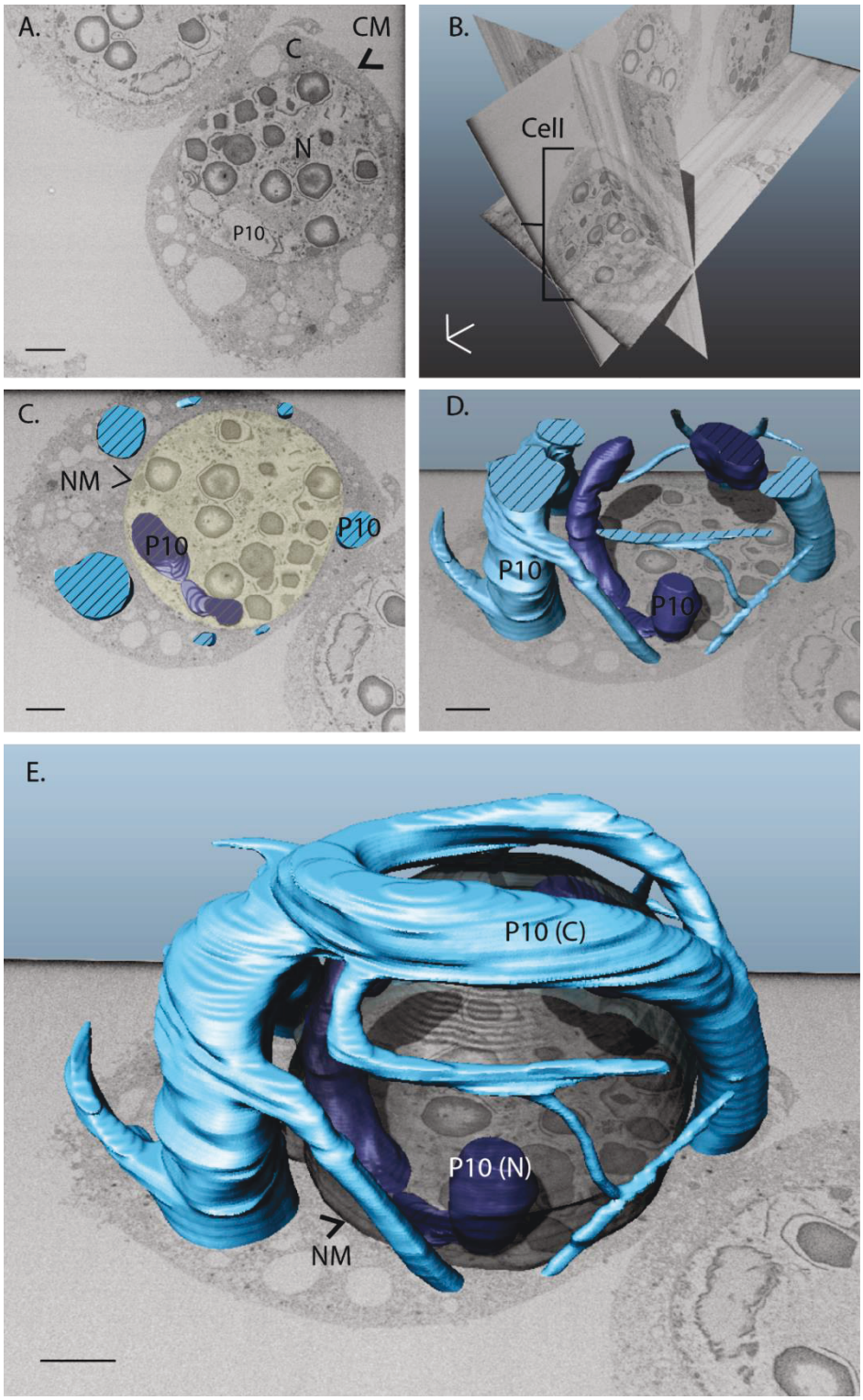

Figure 6.8 Serial-block face scanning electron microscopy of AcMNPV structures in infected TN-368 cells at 72 hpi. AcMNPV-infected TN-368 cells were harvested at 72 hpi and fixed in Epon 812. 100nm thick sections were imaged automatically using the 3View system on the Zeiss Merlin compact field emission gun SEM (A) and grouped to make a stacked image file (.mrc) (B). A segmentation function on Amira was used to build up surface rendered images of P10 (C-E). Abbreviations: C cytoplasm, CM cell membrane, N nucleus, NM nuclear membrane. Scale bar = 3µm.

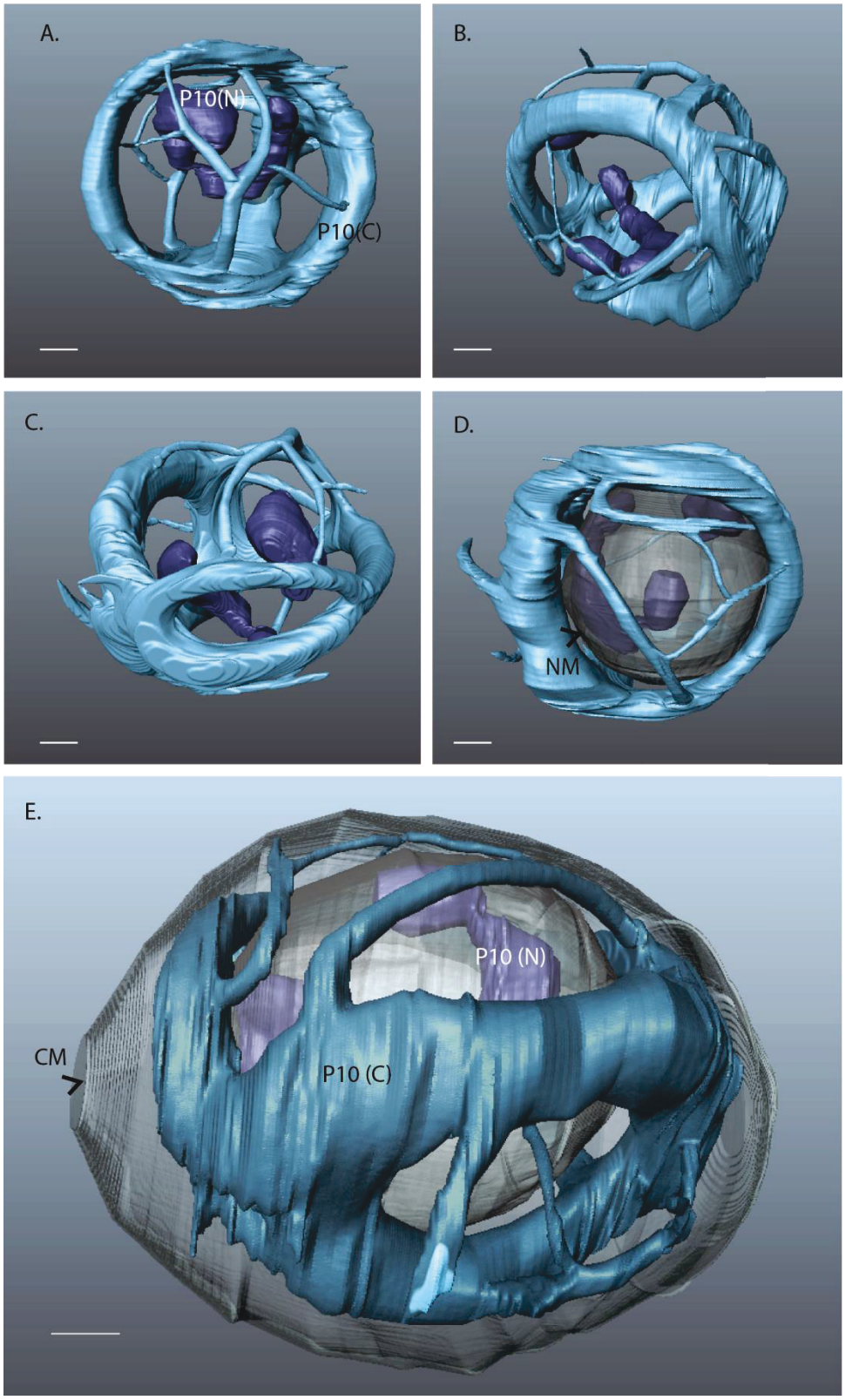

Figure 6.9 Serial-block face scanning electron microscopy of AcMNPV structures in infected TN-368 cells at 72 hpi. Cytoplasmic P10 had condensed to form as thicker tubular structures. Nuclear P10 remained as a thick fibrous body, separate from the cytoplasmic P10. Surface generated images for P10 were generated from stacked images using Amira (A-E). Abbreviations: C cytoplasm, N nucleus, NM nuclear membrane, CM cell membrane. Scale bar = 3μm.

Data acquisition of AcMNPV-infected TN-368 cells at 96 hpi was performed at an accelerating voltage of 4kV with a variable pressure of 40Pa (Table 6.1). Data processing was performed on 427 slices at a Z-thickness of 100nm, HFW of 64µm and pixel size of 12x12nm. SEM images of the surface resin block (Figure 6.10 A) and later image-stacks (Figure 6.10 B) produced suitably high-resolution images with excellent contrast. This allowed identification of the virus ultrastructure and partial model automation for P10 structures.

At 96 hpi the AcMNPV-infected cells continued to display phenotypic characteristics of very-late phase baculovirus infection with continued formation of P10, EDS and the formation of mature polyhedra (Figure 6.10 A). In addition, there were visible signs of lysis, as indicated by free polyhedra observed in-between cells (data not shown), which is consistent with lysis observed in TN-368 cells with light microscopy. Similar to 72 hpi, polyhedra were observed with an unstained centre, again suggesting a problem with impregnation of the polyhedra with stain (Figure 6.10 A-B). As with previous time points, partial reconstruction of P10 formed distinct structures, both in the nucleus and cytoplasm (Figure 6.10 C&E) observed P10 separated by the nuclear membrane (Figure 6.10 E, arrows).

Surface rendered images of cytoplasmic P10 (Figure 6.11) showed that some reminence of a perinuclear cage structure were present however; this was distinctly different from cytoplasmic sturctures observed at 48-72 hpi. P10 displayed a continued decrease in branching with formation of a single large aggregate at a polar region of the host cell (Figure 6.11). This aggregated mass remained in close association to the nuclear membrane (Figure 6.11 D-E, arrow) with thin filaments branching off (Figure 6.11). Nuclear P10 maintained its characteristic long thick tube-like appearance forming a worm-like feature (Figure 6.11 A-C) that became shaped by the virogenic stroma and densely packed polyhedra (Figure 6.14).

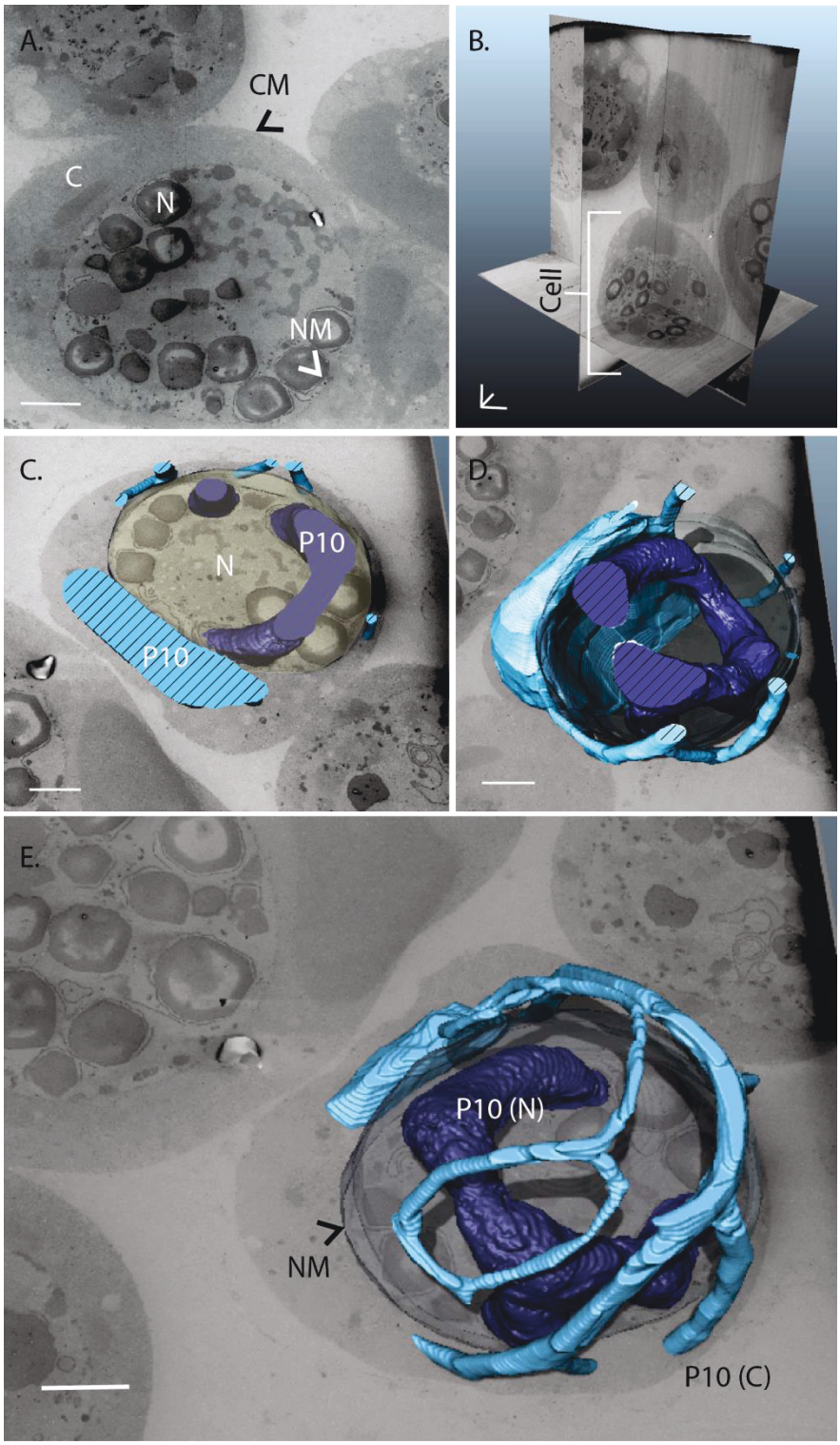

Figure 6.10 Serial-block face scanning electron microscopy of AcMNPV structures in infected TN-368 cells at 96 hpi. AcMNPV-infected TN-368 cells were harvested at 96 hpi and fixed in Epon 812. 100nm thick sections were imaged automatically using the 3View system on the Zeiss Merlin compact field emission gun SEM (A) and grouped to make a stacked image file (.mrc) (B). A segmentation function on Amira was used to build up surface rendered images of P10 (C-E). Abbreviations: C cytoplasm, N nucleus, NM nuclear membrane. Scale bar = 3μm.

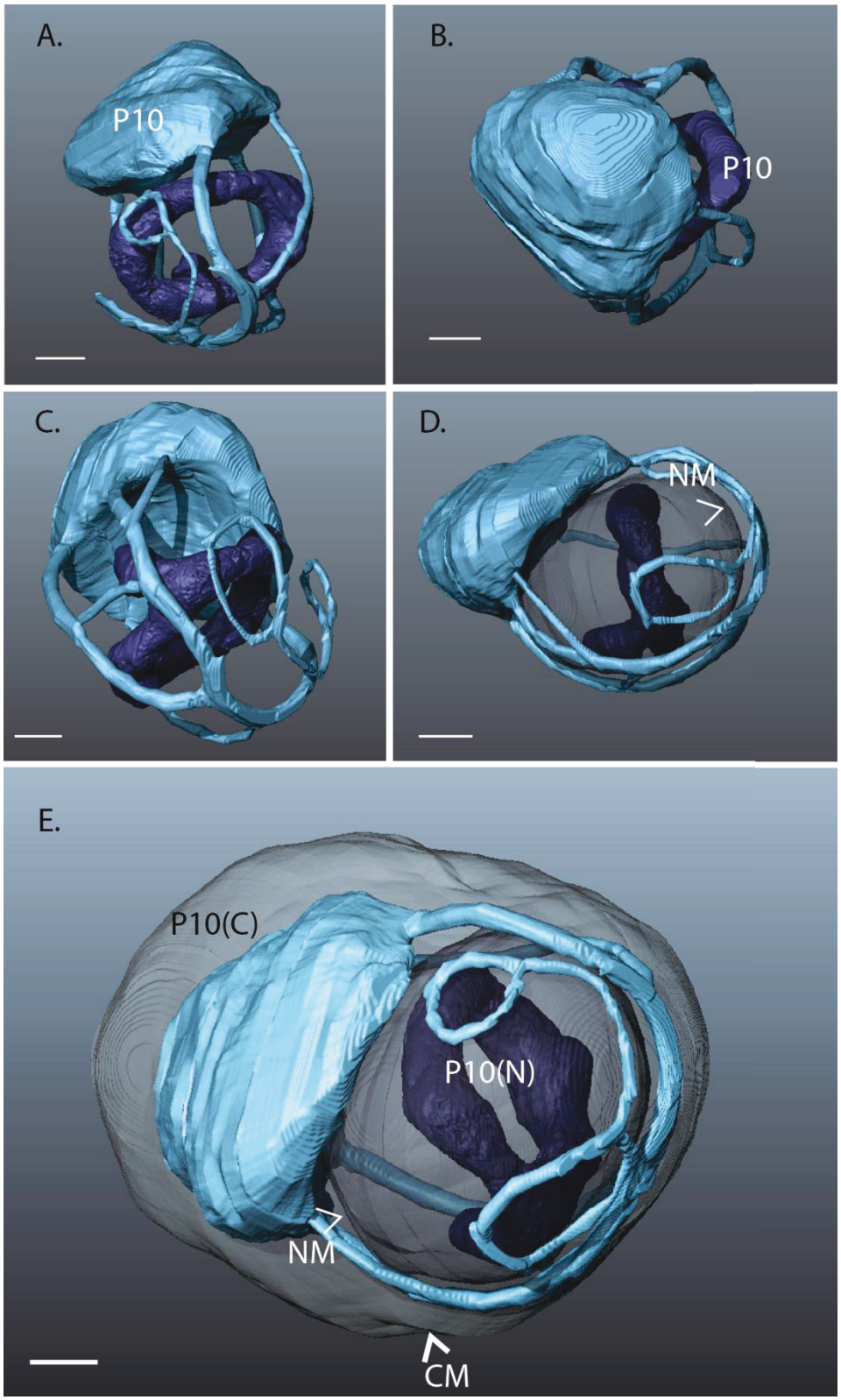

Figure 6.11 Serial-block face scanning electron microscopy of AcMNPV structures in infected TN-368 cells at 96 hpi. The cytoplasmic P10 formed a large polarised P10 mass with a thin fibrils branching off and around the nucleus. Nuclear P10 formed a thick worm like feature that formed around the inside of the nuclear membrane. Surface generated images for P10 were generated from stacked images using Amira (A-E). Abbreviations: C cytoplasm, N nucleus, NM nuclear membrane, CM cell membrane. Scale bar = 3μm.

6.3.1 Three-dimensional measurements and volumetric data from SBF-SEM models of AcMNPV P10 structures

The surface generated images displayed in section 6.3 were used to determine size variations in P10 over time, providing additional data to support the structural observations of P10 between 24 and 96 hpi. Using the 3D measurement function in Amira, the diameter of the cytoplasmic and nuclear P10 structures were recorded at 10 separate locations. The range of measurements and mean reading was recorded and displayed using a bar chart (Figure 6.12 A). Structural volumes were calculated using the 'Surface area function' on Amira. This calculates total volume of structures (nm^3).

Due to the varied sizes of the TN-368 cells (Hink, 1970), relative volume percentage of P10 structures, cytoplasm and nucleus to total cell volume were plotted, as this provided a more representative approach (Figure 6.12 B).

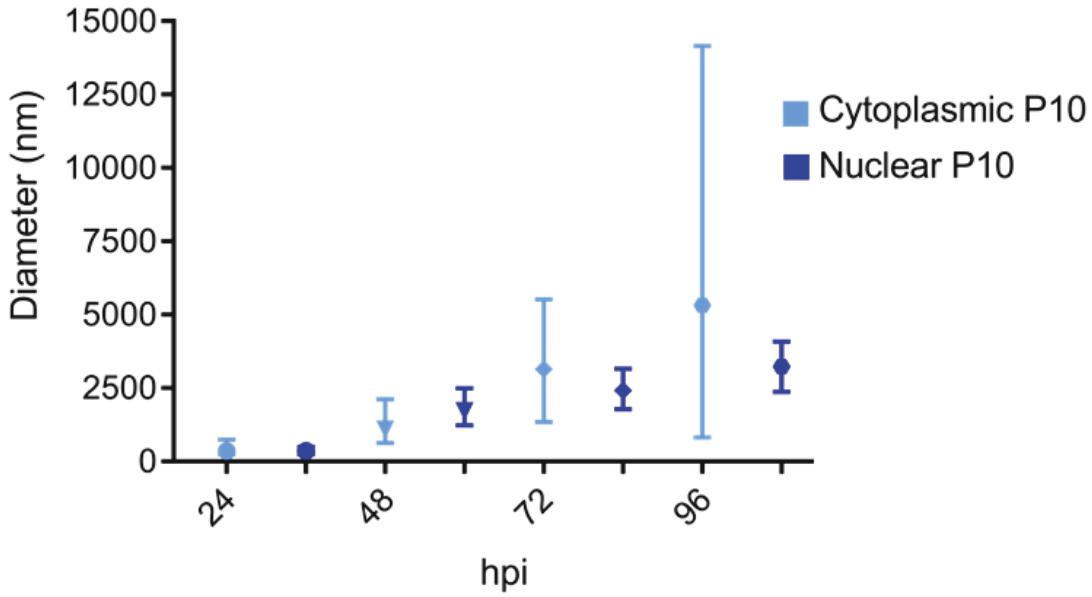

Figure 6.12(A) Comparison of P10 diameters in AcMNPV- infected TN-368 cells. Surface generated models of P10 from stacked imaged data at 24, 48, 72 and 96 hpi were used to record the random diameter measurements of P10 3D structures (cytoplasmic and nuclear) (n=10). This gave a cross-section of P10 structures at different regions of the cell.

At 24 hpi, cytoplasmic P10 had a mean diameter of 362nm (n=10) with a range from 242nm to 749nm. Nuclear P10 was similar, with a mean diameter of 354nm (n=10) and range of 244-489nm (Figure 6.12A). Volumetric data of P10 confirmed structures at 24 hpi

were smaller than later time points, with cytoplasmic and nuclear P10 structures making up 0.11% of the total cell volume, 0.05% and 0.06%, respectively (Figure 6.12 B).

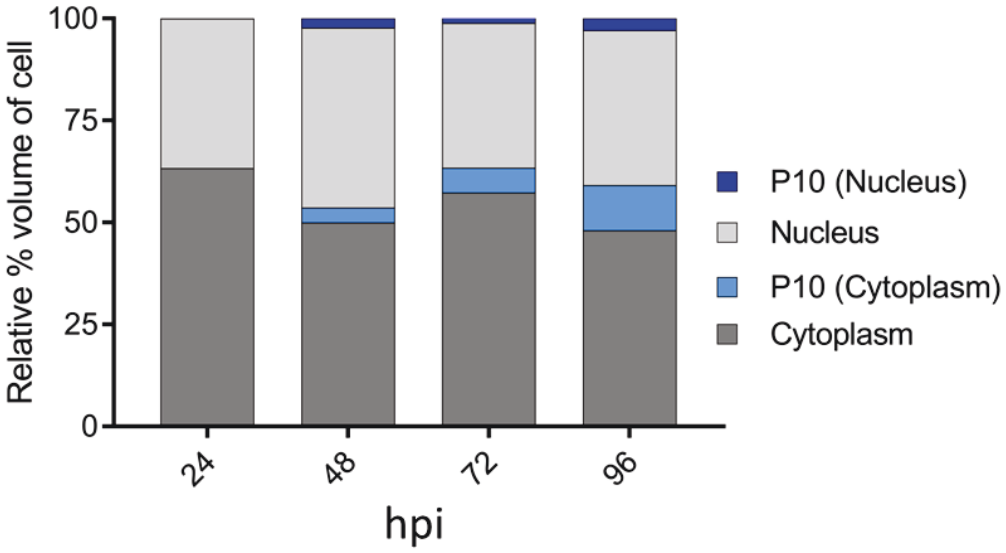

Figure 6.12(B) Volumetric analysis of P10 structures in AcMNPV-infected TN-368 cells. Surface generated models of P10 from stacked imaged data at 24, 48, 72 and 96 hpi were used to calculate the relative % volume of P10 structures (cytoplasmic and nuclear) in comparison to total cell volume.

By 48 hpi, cytoplasmic P10 had nearly tripled in size to a mean diameter of 1097nm (n=10) and range of 632nm to 2120nm (Figure 6.12A). This trend was replicated with nuclear P10, with a mean of 1719nm (n=10) and range of 1234nm to 2488nm (Figure 6.4A). Volumetric readings identified a considerable % volume increase in both cytoplasmic P10 at 3.64% and nuclear P10 at 2.28% (Figure 6.12 B). These volumetric readings confirmed a 54-fold increase in P10 (cytoplasmic and nuclear), with structures making up 5.92% of the total cell volume overall.

By 72 hpi, cytoplasmic P10 showed a continued increase in diameter with a mean of 3142 nm (n=10) and range of 1349 nm to 5517 nm. Nuclear P10 was similar to 48 hpi, with a mean of 2417 nm (n=10) and range of 1784 nm to 3156 nm (Figure 6.12A). Volumetric readings confirmed a continued increase of cytoplasmic P10 structures, with cytoplasmic P10 making up 6.08% of the total cell volume (Figure 6.12 A). In contrast, a slight decrease in the nuclear P10 volume (1.16%) was observed from 48 hpi (Figure 6.12B). This still however, represents an overall relative % volume of P10 (cytoplasmic and nuclear) 7.24% for, a 1.2-fold increase in volume (Figure 6.12 B).

During the very late phases of infection (96 hpi), the shift in the cytoplasmic P10 structure (Figure 6.11) showed a dramatic increase in diameter of the large polarised mass, with maximum reading of 14151nm. In contrast, the thinner filaments shown to wrap around the nucleus (Figure 6.11) were recorded between 814nm and 1585nm, giving a total and mean reading of 5317nm (n=10, Figure 6.4 A). Due to the range in recorded measurements, the volumetric data gave a more representative approach. As shown in Figure 6.13 a representative % increase were displayed for both cytoplasmic and nuclear P10 structures. Overall, nuclear P10 only showed a little increase in relative % volume of the total cell volume from 48 hpi, with % volume of nuclear P10 structures at 96 hpi at 2.86%, whereas cytoplasmic P10 was recorded at 11.12%. This represented a continued increase in overall relative % volume for P10 (cytoplasmic and nuclear) of 13.98% giving a combined 1.9-fold increase from 72 hpi and a 128-fold increase from 24 hpi (Figure 6.12 B).

In summary, Figure 6.12 A and B provides evidence to a continually evolving structure for cytoplasmic and nuclear P10 from 24 hpi to 96 hpi. The recordings of the P10 diameters alongside relative % volumes of the total cell indicate a continual growth for both cytoplasmic and nuclear P10. Importantly this further confirmed the relative size of the prominent polarised cytoplasmic P10 mass observed in Figure 6.11 E, P10 (C) was substantially larger than at other recorded time points (24 hpi-72 hpi).

6.4 High-resolution 3D models of electron dense spacers (EDS) and polyhedra structures in AcMNPV-infected TN-368 cells

An association between P10, EDS and polyhedra was first noted in TEM images by Summers & Arnott (1969), and later from papers observing baculovirus-infected cells by (MacKinnon *et al.*, 1974; Chung *et al.*, 1980). It was suggested by these authors that EDS may act as precursors to polyhedra envelope formation and they proposed a functional role for EDS in polyhedra calyx formation. Therefore, the extent of this association is unclear and the relationship between EDS, P10 and polyhedra remains relatively unknown.

Using the large volume of stacked-image data collected for AcMNPV-infected TN-368 cells at 24, 48, 72 and 96 hpi (Figures 6.6 to Figure 6.11), it was possible to model in 3D this intimate relationship between EDS, P10 and polyhedra. Therefore providing an

excellent opportunity to re-examine the relationship between these AcMNPV virus structures and identify how P10, EDS and polyhedra interact with each other (Figure 6.13).

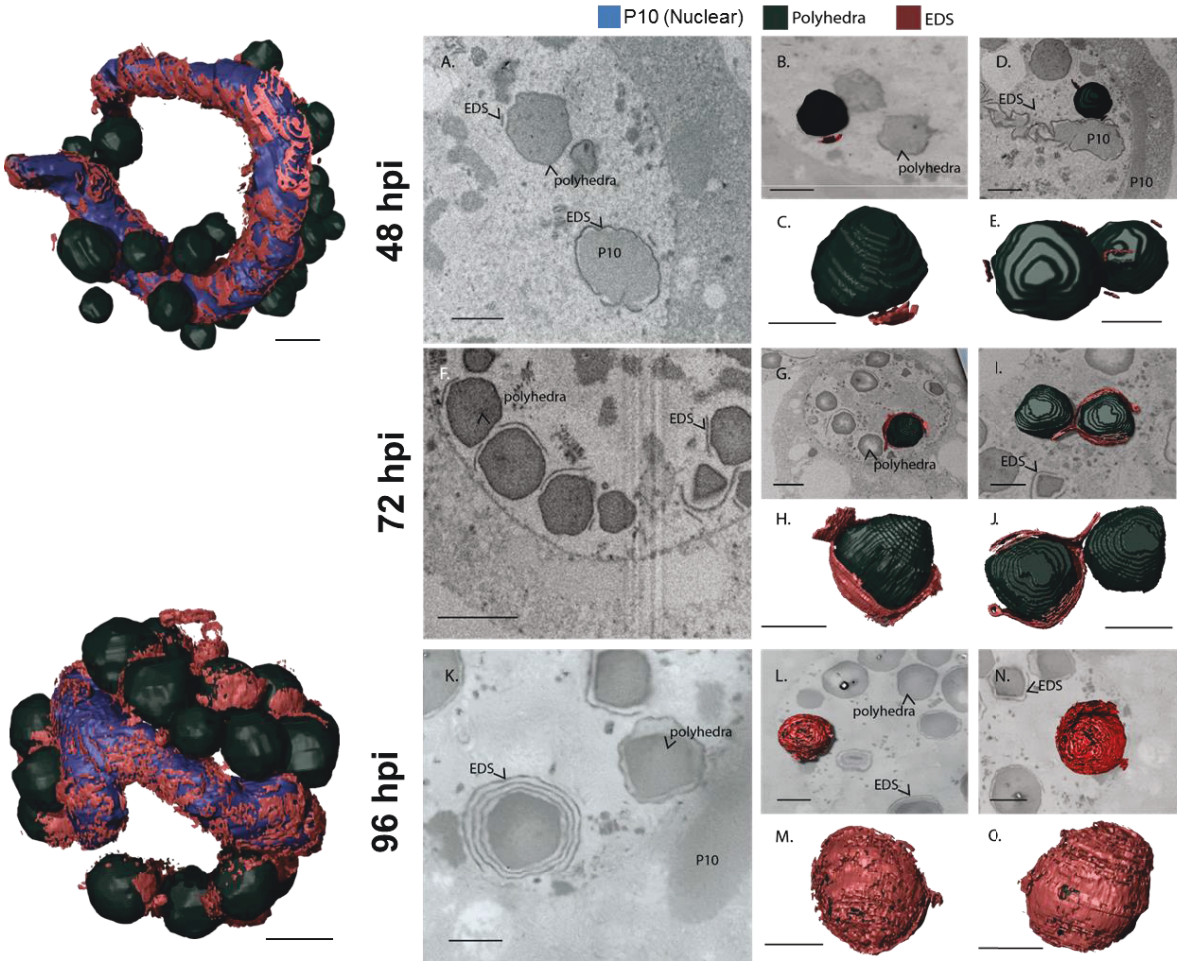

Figure 6.13 Serial-block face scanning electron microscopy of P10 and polyhedra with associated EDS. AcMNPV-infected TN-368 cells were harvested at 24, 48, 72 and 96 hpi and fixed in Epon 812. Surface generated images for P10, EDS and polyhedra were generated from stacked images using Amira. The EDS (red) were observed in close association with Nuclear P10 (blue) at each time point. The EDS were modelled forming sheet like structures. The EDS were found surrounding polyhedra (black) at 48 hpi (A-E), 72 hpi (F-J) and 96 hpi (K-O), with polyhedra becoming surrounded by the EDS. No EDS were seen to associate with polyhedra at 24 hpi. Abbreviations: EDS electron dense spacers. Arrows have been used to highlight polyhedra and EDS. Scale bar = 3 μm.

At 24 hpi, polyhedra were just starting to form, and whilst there was some associated EDS with P10 (as observed in Figure 14), there was no association with the immature

polyhedra. By 48 hpi EDS (red-brown) were observed surrounding large parts of the nuclear P10 (blue, Figure 6.13) with smaller sheets of EDS found in close association to a small percentage (~20-30%) of fully formed polyhedra (dark grey, Figure 6.13 A-E). By 72 hpi; EDS continued to form with more spacers shown surrounding the nuclear P10 and branching off. The EDS were also observed to cover larger regions of the polyhedra (Figure 6.13 F-J) with complete regions of the polyhedra fully encased by the spacers (Figure 6.13 H). By 96 hpi, the EDS were observed to cover the majority of the nuclear P10 (Figure 6.13) and found around the periphery of at least 70-80% of polyhedra with ~50% of polyhedra completely encapsulated within the EDS (Figure 6.13, L-O). Interestingly, the continued production of EDS often resulted in multiple layers around a single polyhedra (Figure 13 K), and furthermore, as observed at all time points, a small gap between the EDS and polyhedra was present (Figure 6.13 A, F, K).

These models provided new evidence showing the complete encapsulation of polyhedra by EDS, thus providing further evidence to this intimate association between P10, EDS and polyhedra and a possible mechanism for the involvement of EDS in calyx formation. It is important to also note, as highlighted in Figure 6.13 L, a small number of polyhedra at 96 hpi (15-20%) remained absent of EDS.

6.5 Three-dimensional reconstruction of AcMNPV-infected cells

Models of virogenic stroma (yellow), polyhedra (black), nuclear P10 (dark blue), EDS (red), nuclear membrane (grey) and cytoplasmic P10 (light blue) were generated to provide insight into the development and association of these structures during the replication cycle of AcMNPV virus in TN-368 cells. The 3D reconstruction of major AcMNPV structures were generated from SBF-SEM image stacks of AcMNPV-infected TN-368 cells at 24, 48, 72 and 96 hpi. Refer to Appendix for supplementary videos at 24, 48, 72 and 96 hpi.

The reconstruction of the AcMNPV virus structures in Figure 14 successfully show 3D models of the virogenic stroma (i), polyhedra (ii), nuclear P10 (iii), EDS (iv) within the nuclear membrane (v), which is surrounded by the cytoplasmic P10 (v).

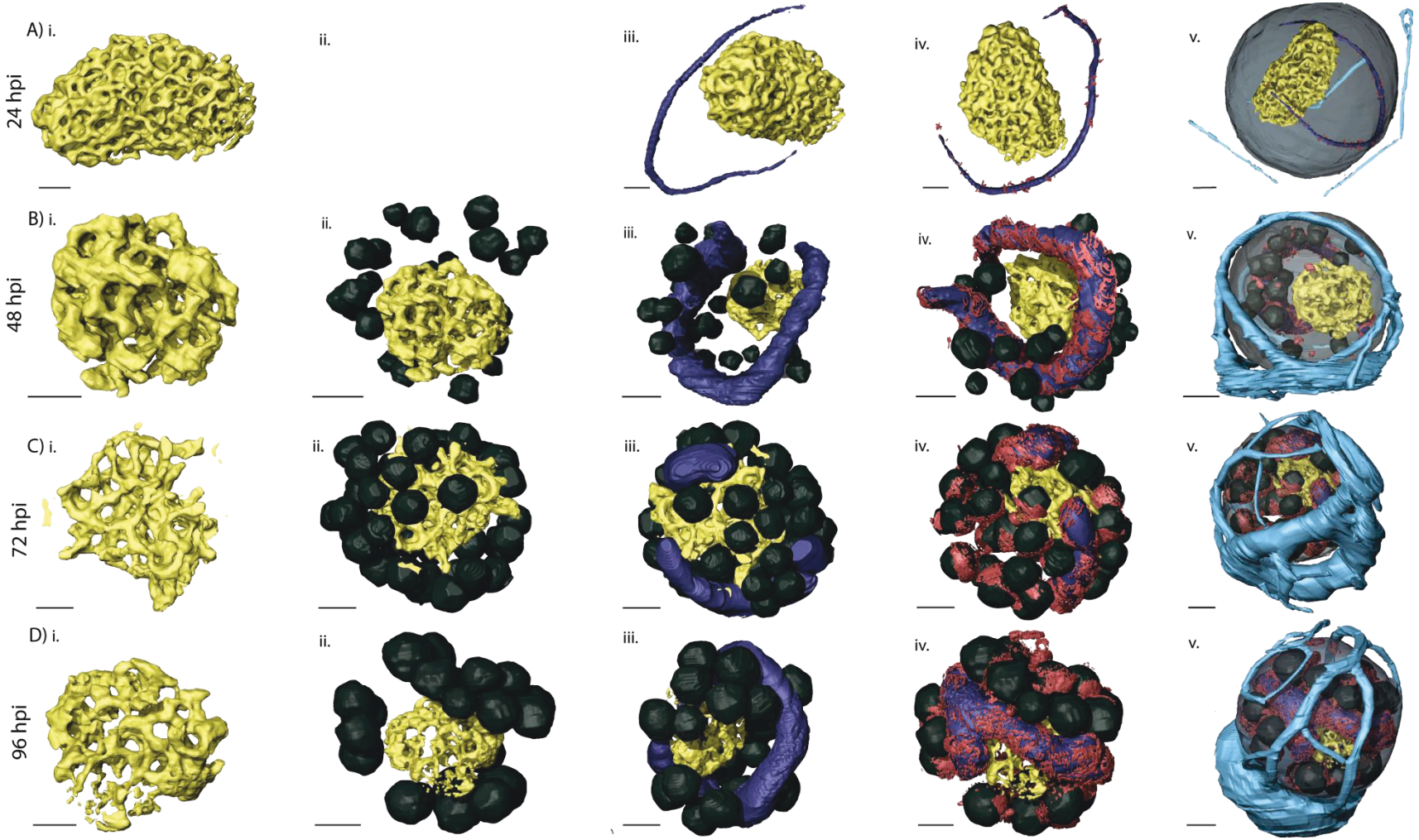

Figure 6.14 Serial-block face scanning electron microscope of AcMNPV structures. Stacked image files of AcMNPV infected *T.ni* cells were used for 3D modelling of AcMNPV to show structure formation and association at different time points; 24, 48, 72 and 96 hpi (A-D). Nuclear P10 forms a worm-like structure that is forms around and in between the virogenic stroma and polyhedra. The EDS form in close association with nuclear P10 as early 24 hpi and continues to form around nuclear P10 and polyhedra from 48 hpi. Virogenic stroma (i) yellow, Polyhedra (ii) black, P10 (iii & v) light and dark blue, electron dense structures (iv) red and nuclear membrane (v) light grey. Scale bar 3 μm.

Virogenic Stroma

The 3D model of the virogenic stroma in Figure 14 (i) demonstrated that this structure was present at all time points, forming a homogenous structural network of electron-dense matter that expanded across much of the nucleus (Figure 14 A(i)-D(i)). Even though the virogenic stroma is present at the later stages (72-96 hpi), the 3D model indicated the structure was more fragmented and less defined (Figure 14 C(i) & D(i)).

Polyhedra

Polyhedra were first detected as an irregular electron dense mass at 24 hpi (Figure 6.4 E), however, it was only at 48hpi that polyhedra developed into its recognisable shape (Figure 6.13), and was shown interspersed throughout the nucleus (Figure 6.14 B(ii)-D(ii)).

Nuclear P10

Nuclear P10 structures were observed as early as 24hpi as thin-like structures (Figure 14 A(iii)). From 48 hpi onwards, P10 had thickened and was observed in-between the polyhedra and around the outside of the virogenic stroma.

EDS

EDS were present as early as 24 hpi and was seen wrapping around nuclear P10. The EDS were observed in greater quantities from 48 hpi, wrapping around nuclear P10 and starting to associate with polyhedra. By 72 hpi and 96 hpi the EDS continue to form around P10, with the excess EDS forming large spiral-like structures that protrude off P10. Furthermore, as noted in Figure 13 the polyhedra became completely encapsulated within the EDS by 96 hpi.

Nuclear membrane and cytoplasmic P10

The host cell nucleus was modelled at each time point to delineate between virus structures within the nucleus and cytoplasm (Figure 14, from A(v) to D(v)). This further confirmed that cytoplasmic and nuclear P10 remained separate with the reconstruction of cytoplasmic P10 highlighting a dynamic perinuclear cage that evolves during AcMNPV infection (Figure 14 A(v)-D(v)).

6.6 Discussion

This chapter has provided an exciting new opportunity for baculovirus research with the introduction of a new microscopy technique that has allowed for generation of high-

resolution 3D modelling for AcMNPV structures in TN-368 cells. Due to this new field in baculovirus research, this chapter used the prototype virus, AcMNPV and developed a usable system for the collection of large high-resolution volume of data from infected TN-368 cells. With the successful sectioning of whole cells, it became possible to combine SBF-SEM with programs such as iMOD and Amira for the successful 3D reconstruction of the infected cell ultrastructure (reviewed in Kittelmann *et al*. 2016)

The initial focus of this chapter was to build on previous P10 work, where already excellent confocal microscopy-generated 3D images of P10 in TN-368 cells were acquired by immune staining (Carpentier *et al.*, 2008). The negatives associated with this approach resulted in lower resolution of the confocal microscopes and difficulty to image P10 in relation to other virus structures (Patmanidi *et al.*, 2003; Carpentier *et al.*, 2008). Furthermore, confocal microscopy lacked the ability to observe the cell ultrastructure, which has been possible with TEM. The introduction of SBF-SEM makes it possible to resolve these issues and offer previously unparalleled 3D structural information on P10, with the successful sectioning, scanning and modelling of the AcMNPV-infected cells.

6.6.1 The two P10 structures and their independent function

SBF-SEM showed for the first time the independent formation of two distinct P10 structures, identifying the formation of a cytoplasmic filamentous structure and nuclear worm-like structure (Figure 6.4 to Figure 6.11). The reconstruction of these two P10 structures displayed variations in shape, location (Figure 6.4 to Figure 6.11), size (Figure 6.12 A and B) and association with other structures (Figure 6.14). This exciting new research has offered new levels of information on P10 sturctures during baculovirus infection and have provided new insights into P10s role in lysis, nuclear stability and polyhedra maturation.

Nuclear stability

It was previously postulated that the formation of the characteristic perinuclear P10 ‘cage-like’ structure played a role in nuclear stability and nuclear lysis (Carpentier and King, 2009), but due to low-resolution images and lack of detail, this remained largely speculation. The introduction of SBF-SEM allowed high-resolution structural reconstruction of cytoplasmic P10, for greater resolution. 3D models of cytoplasmic P10 were shown to form a perinuclear structure at 48-72 hpi that may support the view (Carpentier and King, 2009) that this structure helps maintain nuclear integrity during the final stages of the virus replication cycle, for example, allowing polyhedra to fully mature.

Nuclear lysis

However, during the later phase of infection (96 hpi+) an increase in P10 volume and size was observed (Figure 6.12 A-B), combined with formation of a large polarised P10 mass on the perinuclear cage (Figure 6.11). This shift in structure and continued increase in size is postulated to provide a mechanism for lysis by destabilising or tearing of the nucleus. This is supported by the timing of this event that coincides with nuclear lysis of AcMNPV-infected *T.ni* cells as observed by light microscopy (Figure 3.9). Additionally, it was also observed in Chapter Three and historically (Williams *et al.*, 1989; van Oers *et al.*, 1993) that deletion of *p10* results in both the absence of P10 associated structures and nuclear lysis. This indicates an importance for P10 in lysis. However, previous studies have shown that lysis can still occur in the absence of an identifiable P10 structures (van Oers *et al.*, 1993). On further analysis of the recombinant virus used (AcMO13), it was noted that deletions were made to the C-terminus of P10, which was shown by Dong *et al*. (2005; 2007) by both TEM and confocal analysis that P10 structures continued to form. It will be imperative to confirm this data, with future work discussed in more detail in Chapter Seven.

Polyhedra maturation

The structure formed by nuclear P10, is tube-like and twists through-out the nucleus. It is not continuous with cytoplasmic P10 at any stage. Nuclear P10 is likely to play a role in polyhedra maturation. This is based on the intimate relation shown between P10, EDS and polyhedra, where P10 was observed to associate with EDS during the later phase of infection (Figure 6.13 and Figure 3.17, 3.18). Furthermore, the EDS observed around polyhedra have shown to play a possible role in calyx maturation (Hess and Falcon, 1978) as indicated in Chapter Three (Figure 3.19). Observations of AcΔ*p10*-infected Hi5 cells found that both the EDS failed to wrap around polyhedra and polyhedra contained a fragmented calyx (Figure 3.20).

To characterise this possible relation between EDS and calyx formation, SBF-SEM, with the benefit of 3D modelling and high degree of accuracy, was used to determine the association between EDS and polyhedra. The SBF-SEM models of EDS and polyhedra (Figure 6.13; 6.14) identified that EDS show increased relation with polyhedra from 48 hpi and completely encapsulate the polyhedra by 96 hpi. This intimate connection supports a functional role in calyx formation by a process of condensing and compression (Hess and Falcon, 1978) .

As observed in Figure 6.14, a small number of polyhedra at 96 hpi (15-20%) remained absent of EDS. This is possibly due to the limitations in the modelling software, as during

the surface rendering of the 3D models in figure 14, EDS detail was lost. It was also highlighted that some polyhedra remained absent of EDS even at 96 hpi (Figure 3.17; 3.18 and Figure 6.10). One possibility is that these polyhedra formed later, therefore the EDS that associates with the more mature polyhedra, had not yet attached to the polyhedra. An alternative and more likely explanation is some polyhedra remain absent of EDS. This theory could therefore answer why in previous SEM images of AcMNPV polyhedra (Chapter 3.20, AcMNPV), a similarly small percentage of polyhedra remained absent of a calyx. This is because similar to the P10-minus virus, in the absence of the associated EDS around the polyhedra, the PE cannot form.

In summary, this Chapter has presented that SBF-SEM provides a exciting new technique for obtaining high-resolution 3D structural information. The quality of the data obtained during this study has been in keeping with previous SBF-SEM studies (Denk and Horstmann, 2004; Hughes *et al.*, 2014; Gluenz *et al.*, 2015; Kittelmann *et al.*, 2016) and importantly recent baculovirus EM 3D modelling (Shi *et al.*, 2015). This technique has highlighted the extensive EDS association with polyhedra, previously only speculated from EM micrographs and confirmed the formation of two independent P10 structures.

It is postulated from this study that the formation of these two P10 structures provide a mechanism to their functional role, with cytoplasmic P10 playing a role in nuclear stability followed by lysis, whereas, nuclear P10 and the association with EDS display a functional role in calyx formation.

Chapter Seven:
Discussion

7.1 Introduction to P10

The baculovirus P10 protein has been the subject of interest over the previous 40 years, with studies identifying P10 as an abundant protein under control of a hyper-expressed very late promoter.

It was shown from early EM images taken of baculovirus-infected insect cells that large fibrous structures were present both in the nucleus and cytoplasm. It was identified, with the sequencing of the P10 gene and subsequent immunofluorescence and *p10* deletion studies, that these striking structures were associated with P10. Studies on P10 also indicated a multifunctional role for the protein, suggesting a role in polyhedra maturation, nuclear stability and nuclear lysis. The specific action and underlying mechanisms of these functional roles have however, largely remained a mystery.

The previous chapter highlights how the novel use of SBF-SEM in baculovirus research has both confirmed previous P10 and virus structure work performed using TEM and confocal microscopy, whilst providing significantly increased detail. These new findings strongly provide clear evidence that cytoplasmic and nuclear P10 are not one continuous structure. This thesis proposes that each distinct structure suggests a mechanism for their role in polyhedra maturation, nuclear stability and lysis. It was furthermore confirmed that strong *p10* promoter activity and subsequent accumulation of P10 to high levels is required for the successful formation of these structures and the proper function of P10.

These findings are now discussed in greater detail leading to new insights into the role of P10 in polyhedra maturation, calyx formation and nuclear lysis.

7.2 Discussion of research model

The aim of this thesis was to take a closer look at historical work, using new recombinant *p10* viruses and modern techniques to explore in greater depth the functional roles of P10 in baculovirus-infected cells.

This thesis sought to build on earlier experimental approaches, by providing a system that enabled variants of *p10* to be inserted under the *p10* promoter at its natural locus, importantly with no other changes to the AcMNPV genome. This ensured any functional changes observed can be directly be attributed to the loss of *p10*. Furthermore, it was important to start from a known virus, AcMNPV, for construction of the recombinant

viruses. This was to prevent additional unknown factors that could influence the characterisation of the virus.

By using this platform, the P10 story was primarily characterised in TN-368 and Hi5 cells. These were chosen as they have shown to be a more relevant model system for the study of P10 in AcMNPV-infected cells. This was observed in Chapter Three with AcMNPV-infected Hi5 cells showing significantly increased polyhedra and signs of lysis compared to Sf cells. TN-368 were also the preferred choice for microscopy imaging of P10 structures due to the large cytoplasmic volume of the cell morphology, which has allowed the P10 structures to be imaged more easily (Carpentier *et al.*, 2008).

One important aspect of this thesis was to continue the work performed by Carpentier *et al*. (2008) and use the developing microscopy field to further explore our understanding of baculoviruses P10, specifically AcMNPV. This was especially relevant since P10 structures almost certainly relate to its function. Therefore, the use of SBF-SEM, a high-resolution SEM microscope was used for the 3D modelling of sub-cellular structures.

This study was the first introduction of this technique to baculovirus research and offers previously unparalleled 3D structural information on P10 and other virus structures.

7.3 Discussion of thesis results and future research

In this thesis, the study of P10 has been described in detail, with new techniques and methods providing a unique insight into P10 structures and their role.

7.3.1 The role of P10 in polyhedral envelope (calyx) formation

It was proposed from early studies, as discussed in this thesis, that P10 plays a role in polyhedra maturation. This was first noted from TEM studies on baculovirus structures (Summers and Arnott, 1969; Chung *et al.*, 1980), where it was suggested that P10 was closely associated with EDS (van der Wilk *et al.*, 1987; Russell and Rohrmann, 1990; van Lent *et al.*, 1990; Russell *et al.*, 1991; Gross *et al.*, 1994), which surround the polyhedra to help form the PE by a process of condensing and compression (Hess and Falcon, 1978).

Similar observations were repeated during this thesis, which confirmed an intimate association between P10, EDS and polyhedra. This was shown from TEM images of AcMNPV and P10-rescue virus-infected cells that showed EDS surrounding the periphery of nuclear P10 and polyhedra. Further, key evidence supporting this association was

gained from the AcMNPV *p10*-deletion mutant (Chapter Three), where TEM images of AcΔ*p10*-infected TN-368 cells lacked fibrous P10 structures, and polyhedra formed with a fragmented PE. SEM analysis of extracted polyhedra in Chapter Three also confirmed that polyhedra contained a pitted and rough surface and indicates that P10 is required for PE formation.

Even though a number of publications comment on an association between P10, EDS and the PE (van der Wilk *et al.*, 1987; van Lent *et al.*, 1990; Russell *et al.*, 1991; Gross *et al.*, 1994), there little evidence for a mechanism to explain the role of P10 in calyx formation; some papers have been sceptical of its involvement at all (van Oers *et al.*, 1993).

By using a combination of TEM, SEM and SBF-SEM for the generation of high-resolution 3D models, new insights into the role P10 and EDS play in the formation of the PE are proposed. As first observed in Chapter Three, the absence of P10 structures had a profound effect on the wrapping of EDS around the periphery of polyhedra. Instead, EDS were observed to wrap onto themselves, forming self-aggregated spherical structures. This suggests that EDS require the presence of P10 to associate with polyhedra. Thus the role of P10 is to enable EDS to associate with polyhedra forming a mature calyx. In the absence of P10, EDS fail to associate with polyhedra leaving them malformed and pitted calyx.

This proposal that EDS association with polyhedra is required for PE formation was further supported by SBF-SEM on AcMNPV-infected TN-368 cells. By using SBF-SEM it became possible to generate high-resolution 3D models of complete P10, EDS and polyhedra structures (Chapter Six), which has not previously been performed. This new method further emphasised the level at which EDS associates with both P10 and polyhedra, with models at 96 hpi displaying the P10 and polyhedral surface to be covered by the EDS. Therefore, SBF-SEM provides new evidence to suggest the continued wrapping of the EDS around the polyhedra provide a mechanism for calyx formation and provides evidence that P10 plays a chaperone-like role in transferring the EDS to the surface of maturing polyhedra as previously indicated (Hess and Falcon, 1978).

Potential leads into new research

It is not clear how P10 plays this chaperone role, but is indicated that putative binding sites for EDS on P10 could account for this close association between structures (van Oers and Vlak, 1997). It is therefore thought this association could enable the restructuring of EDS to form around the periphery of polyhedra. Further evidence is

required to provide evidence for this proposal and to determine how these specific interactions between P10 and EDS occur.

One possibility would be to identify potential binding sites identified through computational sequence and domain comparisons, and then create point and domain mutants to study their effects on EDS formation and polyhedra maturation. This could be complemented with biochemical and microscopy-based protein-protein interaction approaches (e.g. Fluorescence Resonance Energy Transfer) and immunocytochemistry. A search with PredictProtein® suggests that aa's 1, 62, 69 and 72 on AcMNPV P10 are potential binding sites that would provide a starting point for this work.

It would be beneficial to generate crystals for X-ray crystallography to determine the atomic structure and molecular structure of P10. With crystallographic structures widening our understanding of site directed mutagenesis, enzyme mechanisms and specificity of protein-ligand interactions as a few interesting areas for initial research (Smyth and Martin, 2000). X-ray crystallography has already been used with success in the study of AcMNPV polyhedrin (Coulibaly *et al.*, 2009). Initial work has been started, with the construction of an N-terminus his-tagged recombinant P10 virus. However, issues arose when trying to generate enough soluble P10 protein for purification, but this will be revisited in due course.

An alternative approach will be to characterise the possible relationship between the temporal alignment of the PE around the periphery of the polyhedra and EDS formation around polyhedra. One possible suggestion to achieve this would be to use a combination of SEM on extracted polyhedra and TEM on partially digested polyhedra (to allow observation of the PE) at different time points post-infection. This will identify how and when the PE develops, which can be cross-referenced against the SBF-SEM data already obtained. This will provide new information on whether calyx formation/maturation (assessed using SEM and TEM data) is proportional to EDS coverage (as shown by SBF-SEM). Thereby, giving evidence for the involvement for EDS in polyhedra maturation.

As a final note, SEM has shown to provide a valuable tool for characterising polyhedra, however, with the introduction of new high-resolution SEM's (Chapter Three) that provide previously unattainable detail, current methods need to be re-examined to exploit the advances in technology. It was identified in Chapter Three that the process of gold-sputter coating for sample coating can produce a "flaky" surface. One possible solution would be the use of Chromium, which could offer reduced charging and continuous surface film (Dr. Louise Hughes, pers. comm). Additionally, it would be beneficial to determine the minimal

sample processing required reducing sample artefacts and thus allowing more precise changes to be observed.

7.3.2 P10's role in nuclear stability and nuclear lysis

One further aim of this thesis was to address the functional role that P10 plays in nuclear stability (Carpentier *et al.*, 2008; Carpentier and King, 2009) and lysis (Williams *et al.*, 1989; van Oers *et al.*, 1993). It has been shown historically and during this thesis that P10 has a role in nuclear stability prior to lysis, however, the mechanisms behind this process are not well understood (reviewed in Carpentier and King, 2009). Therefore, the introduction of new techniques during this study has provided an excellent opportunity to further understanding of P10.

From comparative analysis of P10-positive and P10-minus virus in Chapter Three, it was clear that the synthesis of P10 was required for lysis of host cells. When P10 was deleted polyhedra failed to be released from the nucleus of infected cells, thus confirming previous studies identifying P10 is required for nuclear lysis (Williams *et al.*, 1989; van Oers *et al.*, 1993). As well as comparing a P10-positive and P10-minus virus, the construction of a new recombinant AcMNPV virus containing SfMNPV P10 was studied in Chapter Four to further explore cell-specific effects of P10 in lysis. In Chapter Four It was hypothesised that if the host-specific interaction with AcMNPV P10 caused increased lysis in the more native Hi5 cell line, then host-specific interaction with SfMNPV P10 (in the AcMNPV genome) in the native Sf9 and Sf21 cell line would increase lysis when compared to AcMNPV. However, during characterisation of the SfMNPV P10 recombinant virus a number of uncharacteristic observations were made, including the absence of nuclear lysis. This absence of lysis was similar to previous P10 substitutions in AcMNPV by van Oers *et al*. (1994) and van Oers *et al*. (1998), who also suggested other host cell factors, were required for the involvement of P10 for nuclear lysis.

Interestingly, during this study of SfMNPV P10, it became apparent that two factors could be causing the lack of lysis. Firstly, the level of synthesis of SfMNPV P10 was decreased when compared to both SfMNPV and AcMNPV and secondly, no typical P10 structures could be observed by confocal microscopy.

The possible role P10 structures play in nuclear lysis

Recent literature has provided a strong indication for the role for P10 structures in both nuclear stability and lysis by the use of confocal microscopy (Carpentier *et al.*, 2008). To explore this theory and provide new insight, the introduction of SBF-SEM microscope provided the relevant tools to progress our understanding (Chapter Six). By characterising the P10 structures using SBF-SEM, it was observed that two distinct independent P10 structures were identified: cytoplasmic and nuclear P10. Modelling of whole cells, identified the formation of thin fibrous cytoplasmic filaments at 24 hpi that developed into thicker perinuclear tubular structures (48-72 hpi), described in this thesis as a 'cage' like structure. Finally, by 96 hpi, the cytoplasmic P10 structures remodelled to form an enlarged polarised cytoplasmic P10 mass, with thin fibrils that branched out from it and wrapped around the nucleus. From these results it is likely that the close proximity of the cytoplasmic P10 'cage' like structure to the nuclear membrane provides a functional purpose. This 'cage' structure was also observed by Carpentier *et al*. (2008), who indicated that it has a role in nuclear stability, serving to both stabilise and protect the nucleus allowing the polyhedra to mature. This still however, raises the question to whether these structures also play a role in lysis, and if so how?

One possibility is the dramatic dynamic shift of the P10 fibrous bodies at 96 hpi from the perinuclear structure to a thick polarised P10 mass could result in nuclear lysis. One possibility is that the formation of the large P10 mass destabilises or tears the nucleus, thus facilitating the release of polyhedra. This is further supported from light microscopy of AcMNPV-infected TN-368 cells that show signs of nuclear lysis also at 96 hpi.

Some previous published data conflicts with the theory that P10 structures are involved in lysis (van Oers *et al*., 1993). In this study it was observed that nuclear lysis still occurred in a partial *p10*-deletion AcMNPV recombinant virus (AcMO13), which lacked the C-terminal 15 aa of P10. Importantly, electron micrographs of AcMO13 labelled with antiserum, complexed to Protein A-gold and subjected to silver enhancement did not detect P10 associated structures. More recent by work Dong *et al*. (2005; 2007), however, has challenged the proposal that carboxyl-terminus deletions would prevent formation of the P10 structures. This study showed that C-terminal deletions of up to 21 aa in HearNPV P10 and 29 aa in AcMNPV P10 still formed associated P10 structures, as confirmed by TEM (Dong *et al.*, 2005) and confocal microscopy (Dong *et al.*, 2007).

Therefore, to confirm if P10 structures could provide a mechanism for nuclear lysis, clarification is needed as to whether P10 structures play a functional role during infection. This is supported from the high degree of structural homology observed between P10

(van Oers and Vlak, 1997) and suggests an evolutionary pressure to preserve the P10s characteristic structure. This is still observed between *p10* that share a low sequence homology (van Oers *et al.*, 1994; van Oers *et al.*, 1998).

The importance of high levels of P10 for lysis to occur

In order to determine if the accumulation of high levels of P10 is a requirement for the protein's array of functions, a number of *p10* promoter deletions were created, to modulate expression of P10 and characterise the effect of reduced P10 levels (Chapter Five). By observing P10 expression and function it was indicated that there was a dosage effect between P10 synthesis and function. These observations highlight the importance of the strength of the *p10* promoter, suggesting that synthesis of P10 is required at a high level in order to form P10 structures that in turn mediate function. Confocal microscopy analysis demonstrated that a decrease in P10 synthesis resulted in a decrease in the development of P10 structures. This was confirmed by a noticeable absence of thicker tubules at 96 hpi when more than 12 bp's of the promoter was deleted. This supports to the hypothesis that the cage structure could have a role in nuclear lysis as discussed in Chapter Six.

It was noted that within the set of promotor deletions that the recombinant virus that contained the deletion of 12 nucleotides (Ac_P10$^{prl\text{-}12}$) gave similar P10 expression levels and function to AcMNPV and control P10 virus. To determine if this is an anomaly, it would be interesting to make some further point base pair deletions, possibly from -8bp to –16bp, to see is this change is gradual or whether there is a cut off. A further possibility would be to use these constructs to determine if similar expression profiles are reproduced with a reporter protein that can be measured in sensitive assays e.g. GFP or CAT expression. It would also be interesting to perform further research with the promoter deletion mutants to look at RNA levels. This would determine if RNA levels remain high in the deletion mutants and confirm if the P10 levels could be down to translation.

Furthermore, TEM characterisation, to complement the confocal analysis, combined with SEM for analysis of the PE would also be valuable in further characterisation of these recombinant viruses.

New research to characterise P10's role in lysis

To achieve this, the construction of a new set of AcMNPV deletions similar to van Oers *et al*. (1993) and Dong *et al*. (2007) is required, which will enable confirmation using TEM, confocal and light microscopy if P10 associated fibrous structures are required for nuclear

lysis. To compliment this work it would be really exciting to develop an additional set of recombinant viruses to characterise the earlier hypothesis that cytoplasmic and nuclear P10 structures each have varied roles. It would be interesting to construct mutants that could separately associate into either nuclear or cytoplasmic P10 structures. This would enable me to determine if both structures are important in polyhedra maturation, nuclear stability and lysis, or if they have independent roles, as currently expected. One potential way to do this is to identify, and then mutate, potential nuclear localisation or retention motifs (likely at the N-terminus) or cleavage sites that enable the separation of sequences. One potential indication that cleavage of P10 occurs is a potential lower migrating band that appears below P10 during SDS-PAGE as seen on many occasions during my research and in previous studies (Lee *et al.*, 1996). Recent work indicated this could be an artefact from protease digestion (Carina Bannach, pers comm, Insect Virology Research Group) and therefore warrants further confirmation, possibly by sequencing of the lower migrating band.

Some new and exciting avenues of research to characterise the role of these P10 structures has resulted from recent discussions with Mercedes (Tim Graves, personal communication). It was indicated that computational software could be used to map force distribution through P10. Therefore, enabling me to identify whether this change from a ‘cage’ like structure to a polarised P10 mass could result in a directional shift in force that could ultimately initiate nuclear disintegration. This could further be complimented experimentally using techniques such as atomic force microscopy, where forces required to lyse cells can be measure with high accuracy.

Live-cell imaging has often been a fruitful approach to investigating proteins. Recent work performed by Raza., (2013) in her thesis characterised a small fluorescent protein iLOV. Her work developed a recombinant P10 virus that contained an carboxyl-terminus iLOV fusion for real time imaging of P10 structures. This recombinant virus successfully expressed P10 structures, but was indicated that the fusion of iLOV impacted the correct structural formation. Therefore, it was proposed the addition of iLOV near to the microtubule binding domain might be causing an interference with the P10s association with microtubules to form the filamentous P10 structures. Thus, an alternative iLOV recombinant P10 virus fusion at the N-terminus was constructed. Unfortunately I had little success with this virus, as filamentous P10 structures failed to form, with only large iLOV-P10 aggregates observed. It is possible fusion of iLOV at the N-terminus impacted the coiled-coil domain, which has been suggested to have role in formation of P10 structures. going forward with the P10 it will be of great use to optimise a live-cell imaging technique

to further characterise the formation of P10 structures and the potential role it plays during host cell infection.

7.4 Proposal for large scale analysis of P10

I think one of the major steps required to progress the *p10* story, which has largely been studied in cell cultures, would be to perform large field studies to characterise the effects of a P10 deletion on a larger scale. Smaller *in vivo* studies have been documented, but these indicated *p10* was not vital for survival. This therefore raises the question: what is the evolutionary importance of *p10*? It could be argued that the continued gene conservation of P10 suggests an evolutionary importance, even though it has a seemingly insignificant function (Reviewed in Carpentier and King, 2009). This proposes that the function must be important in some aspect of viral propagation to be maintained. One theory is that P10 is required for optimum dispersal of the polyhedra, either due to increased dispersal of polyhedra during liquefaction or reduce the effect of aggregation of polyhedra. A commonly observed feature in P10 deletion mutants. P10 would thus provide a beneficial selection criteria for the survival and spread of the virus. Therefore, to elucidate this characteristic it would be interesting to map the distribution of *p10* deletion virus, to see if over generations there is a negative impact in comparison to the WT virus. Unfortunately due to regulatory and legislation steps, and the possible interaction and competition with other viruses makes this proposal difficult.

7.5 Concluding comments

In examining the role of this protein, the thesis has concentrated on identifying the mechanism of action of multifunctional P10. Although definitive answers to “the functional role of P10 during baculovirus infection of an insect cell,” remain, my findings provide further evidence to P10 function and contribute to current knowledge, which will progress our understanding of this protein.

Over the last few decades our understanding of P10 has continued to progress and its complex nature makes it an intriguing puzzle to solve. This project made progress in unravelling the mystery of this small yet intriguing protein by making use of the new advancements in available technology.

It was confirmed, using a set of new recombinant P10 viruses, that the expression of P10 was required for lysis of insect cells, with expression of P10 having a host and species specific role. Furthermore, through targeted promoter modifications it was established that the full integrity of the P10 promoter is required for normal levels of expression, with results suggesting there is a dosage effect between P10 synthesis and function. This is the first instance of targeted control of P10 expression through modification of its native promoter, and provides evidence that hyper-expression from the P10 promoter is a functional necessity for the protein.

Finally, this thesis successfully used SBF-SEM on whole virus-infected cells to generate high-resolution 3D models of P10, as well as other AcMNPV virus structures. These techniques offered new insights into the close spatial relationship between P10, EDS and polyhedra, and provides evidence for a proposed mechanism for nuclear lysis based on the remodelling of P10 at the latter stages of infection.

Hopefully the work presented in this thesis will help define P10 and provide the stepping stone to understanding the mechanisms behind P10's many functions.

Appendix

Supplementary CD data

A number of videos have been provided to support the data shown in Chapter Six. The videos were all made from SBF-SEM collected data that were modelled and then animated using Amira. If a CD is not present please get in touch on email: 12083983@brookes.ac.uk or leograves@hotmail.com.

Supplementary data_Stacked image_96 hpi: Video showing a collection of stacked slices obtained from AcMNPV-infected TN-368 cells using SBF-SEM

Supplementary data_24 hpi full cell_1: Video showing the 3D reconstruction of AcMNPV-infected TN-368 cell at 24 hpi highlighting baculovirus structures discussed in Figure 6.14 (A).

Supplementary data_48 hpi full cell_1: Video showing the 3D reconstruction of AcMNPV-infected TN-368 cell at 48 hpi highlighting baculovirus structures discussed in Figure 6.14 (B).

Supplementary data_72 hpi full cell_1: Video showing the 3D reconstruction of AcMNPV-infected TN-368 cell at 72 hpi highlighting baculovirus structures discussed in Figure 6.14 (C).

Supplementary data_96 hpi full cell_1: Video showing the 3D reconstruction of AcMNPV-infected TN-368 cell at 96 hpi highlighting baculovirus structures discussed in Figure 6.14 (D).

Supplementary data_96 hpi full cell_2: Video showing the 3D reconstruction of AcMNPV-infected TN-368 cell at 96 hpi highlighting the baculovirus structures discussed in Figure 6.14 (D).

Supplementary data_96 hpi P10 structures: Video showing the 3D reconstruction of AcMNPV-infected TN-368 cell at 96 hpi highlighting the formation of P10 structures as discussed in Figure 6.10; 6.11.

Appendix One: Additional High-resolution 3D models of P10 structures from AcMNPV-infected TN-368 cells

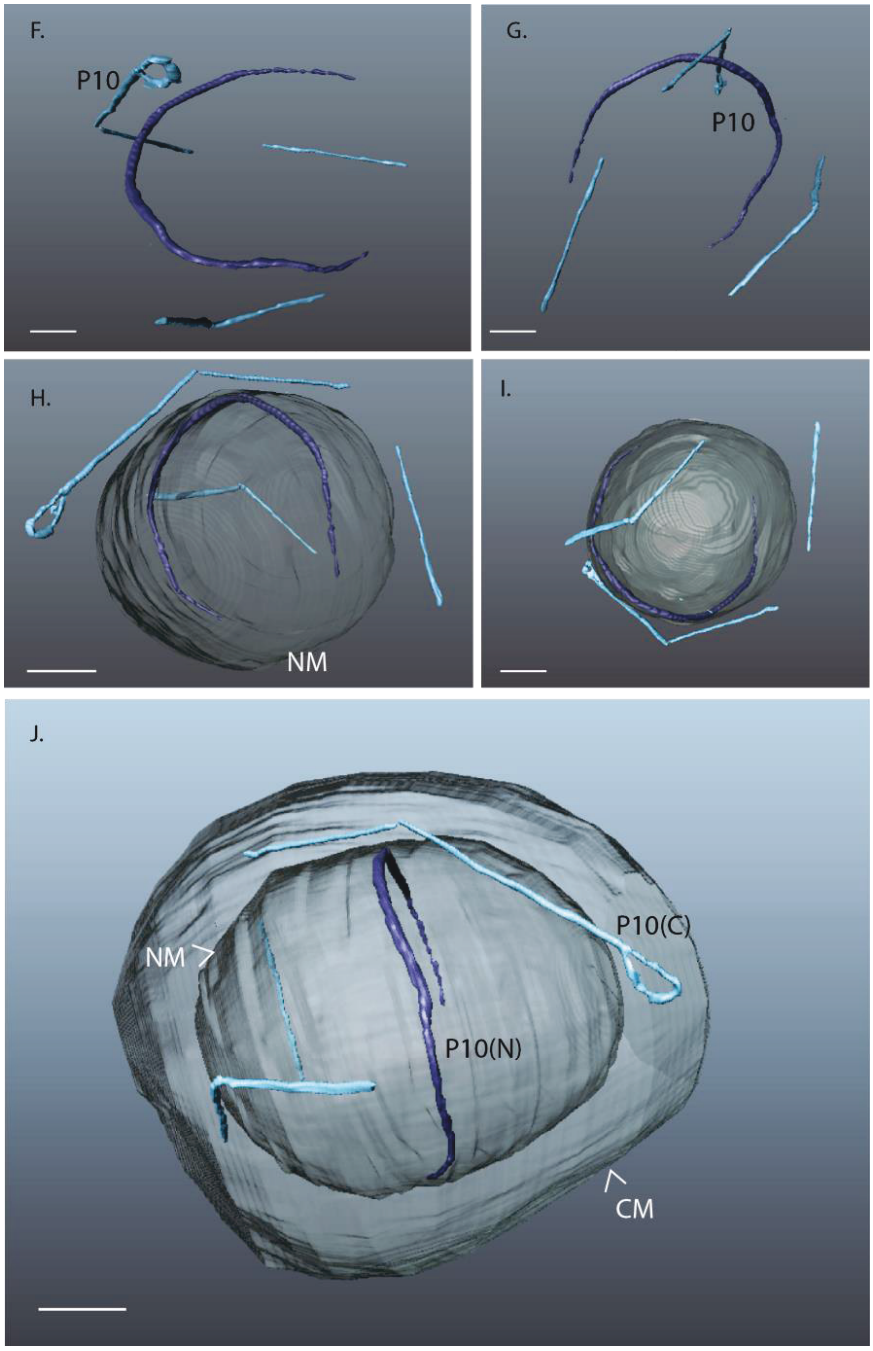

Appendix 1.1 Serial-block face scanning electron microscopy of AcMNPV structures in infected TN-368 cells at 24 hpi. AcMNPV-infected TN-368 cells were harvested at 24 hpi and fixed in Epon 812. 100nm thick sections were imaged automatically using the 3View system on the Zeiss Merlin compact field emission gun SEM. Surface generated images for P10 were generated from stacked images using Amira (A-E). Abbreviations: C cytoplasm, N nucleus, NM nuclear membrane, CM cell membrane. Scale bar = 3μm.

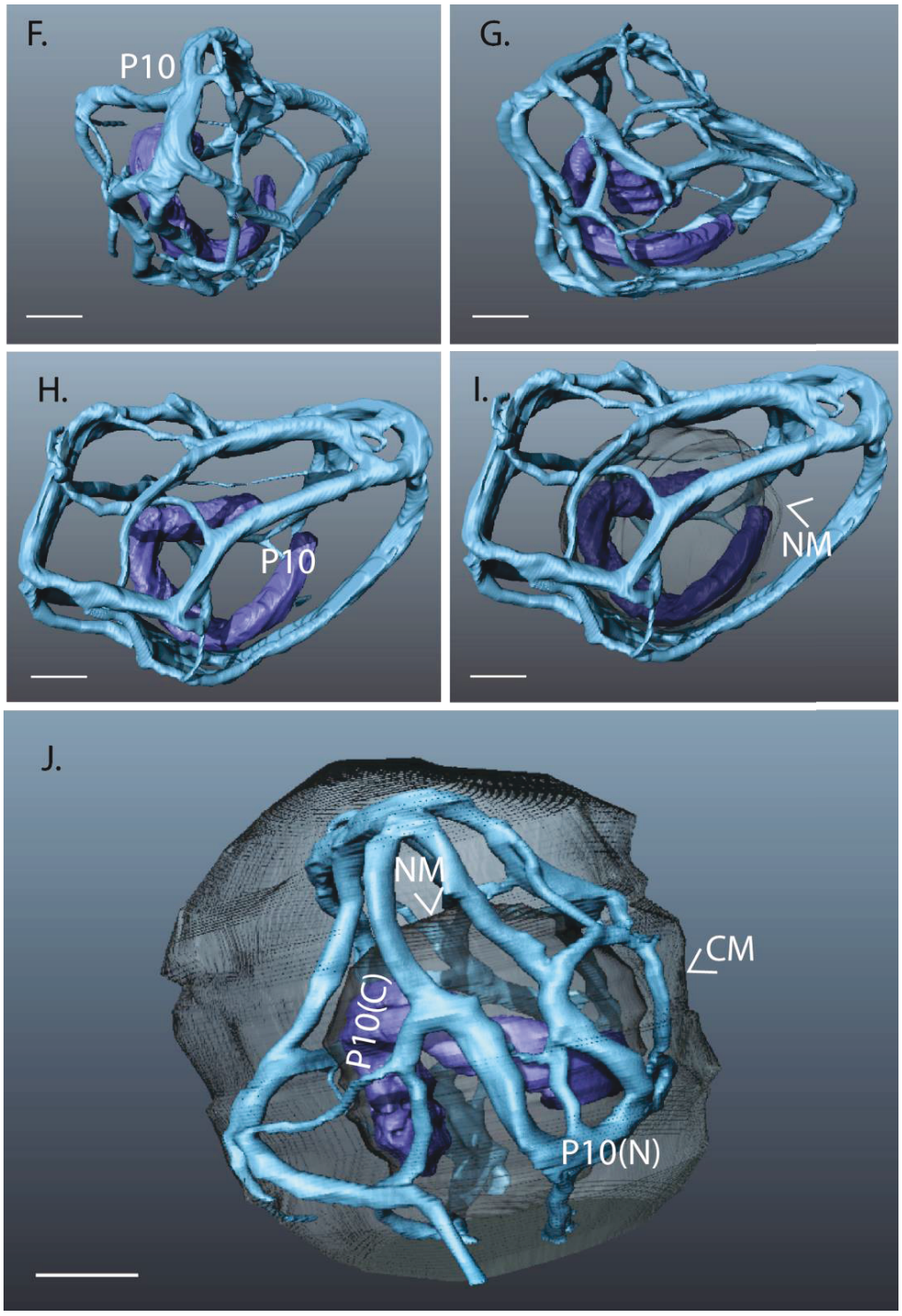

Appendix 1.2 Serial-block face scanning electron microscopy of AcMNPV structures in infected TN-368 cells at 48 hpi. AcMNPV-infected TN-368 cells were harvested at 48 hpi and fixed in Epon 812. 100nm thick sections were imaged automatically using the 3View system on the Zeiss Merlin compact field emission gun SEM. Surface generated images for P10 were generated from stacked images using Amira (A-E). Abbreviations: C cytoplasm, N nucleus, NM nuclear membrane, CM cell membrane. Scale bar = 3µm.

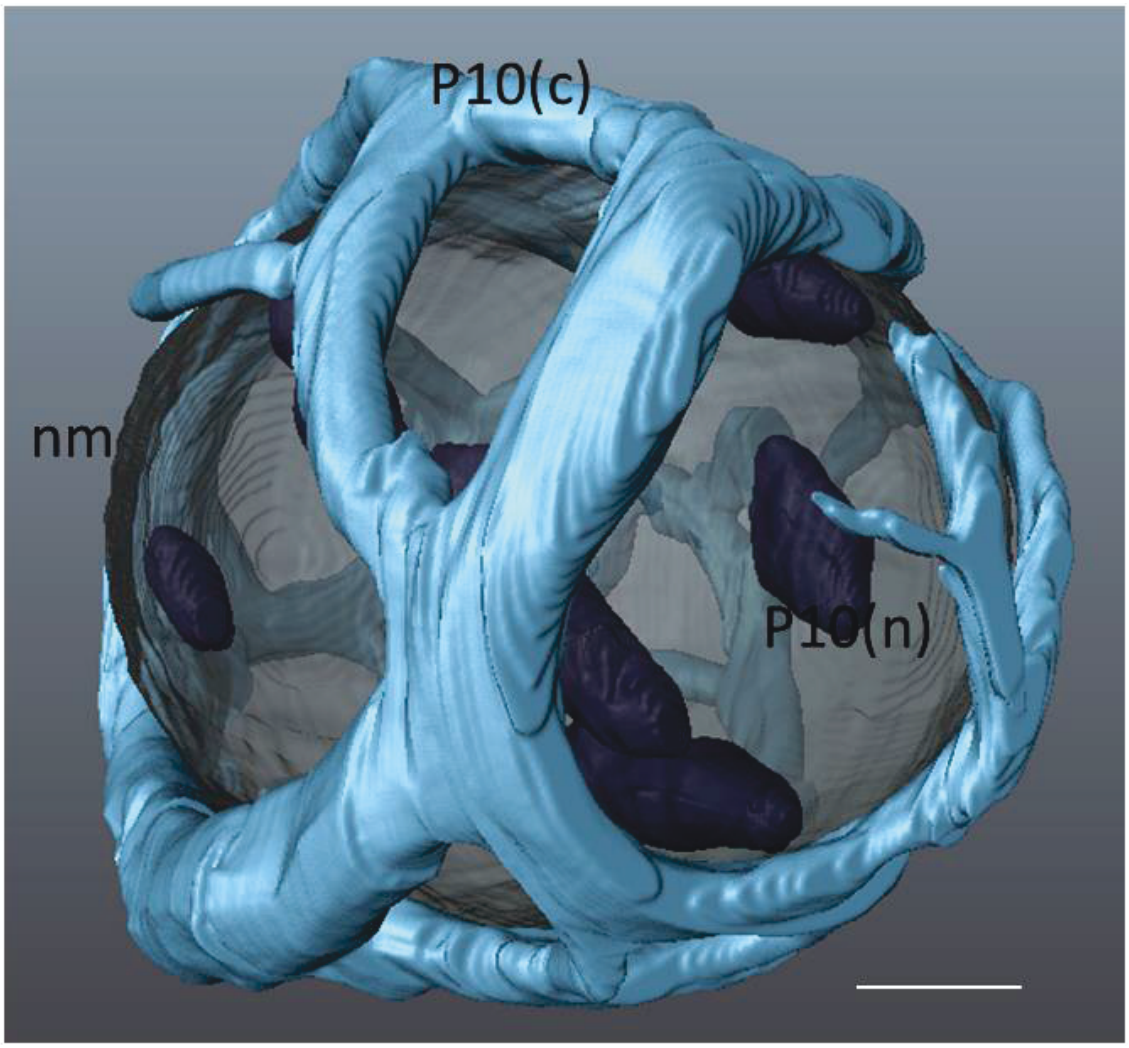

Appendix 1.3 Serial-block face scanning electron microscopy of AcMNPV structures in infected TN-368 cells at 72 hpi. AcMNPV-infected TN-368 cells were harvested at 72 hpi and fixed in Epon 812. 100nm thick sections were imaged automatically using the 3View system on the Zeiss Merlin compact field emission gun SEM. Surface generated images for P10 were generated from stacked images using Amira (A-E). Abbreviations: c cytoplasm, n nucleus, nm nuclear membrane. Scale bar = 3µm.

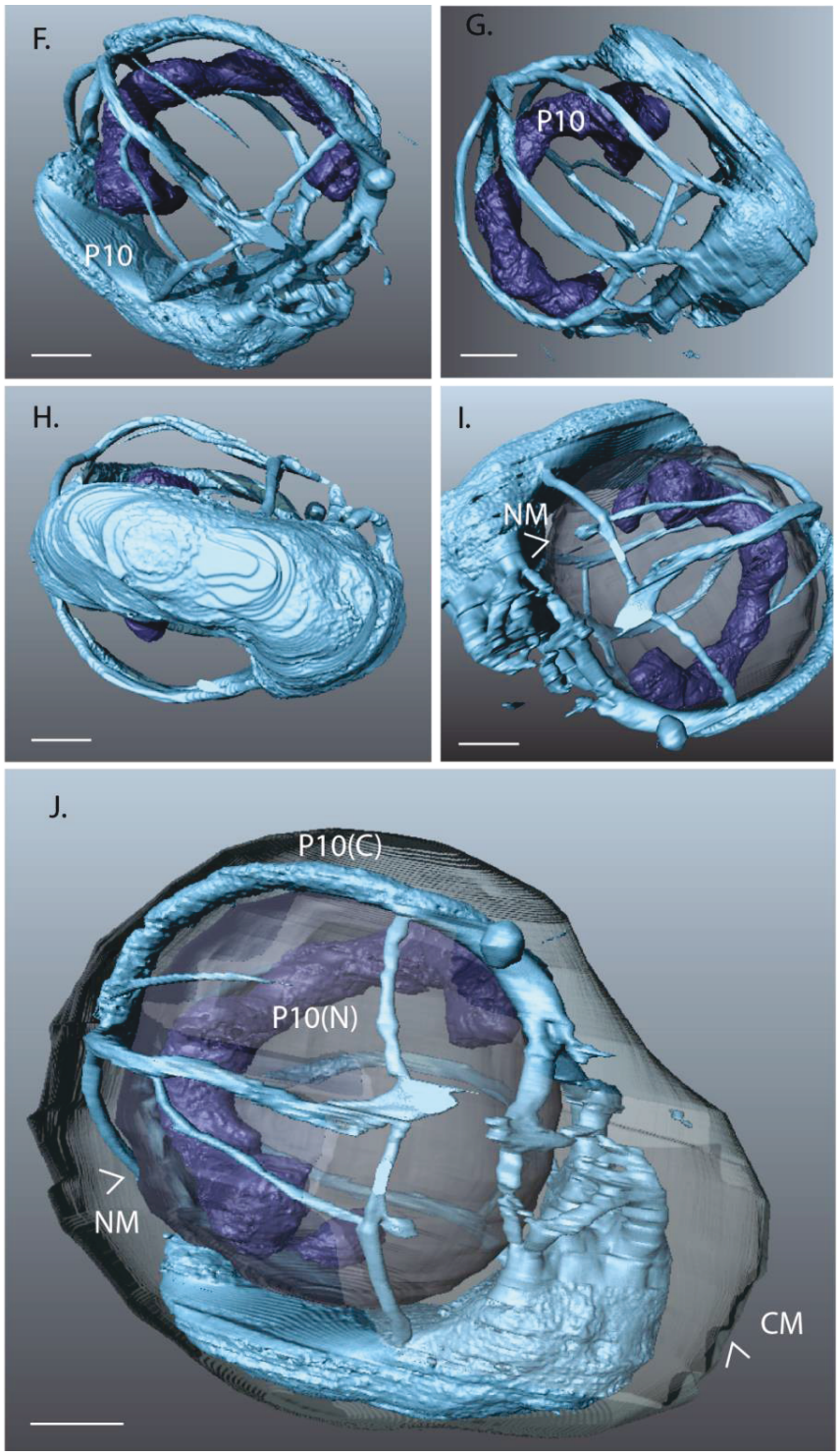

Appendix 1.4 Serial-block face scanning electron microscopy of AcMNPV structures in infected TN-368 cells at 96 hpi. AcMNPV-infected TN-368 cells were harvested at 96 hpi and fixed in Epon 812. 100nm thick sections were imaged automatically using the 3View system on the Zeiss Merlin compact field emission gun SEM. Surface generated images for P10 were generated from stacked images using Amira (A-E). Abbreviations: C cytoplasm, N nucleus, NM nuclear membrane, CM cell membrane. Scale bar = 3μm.

Appendix Two: Stereoscopic images of P10 structures

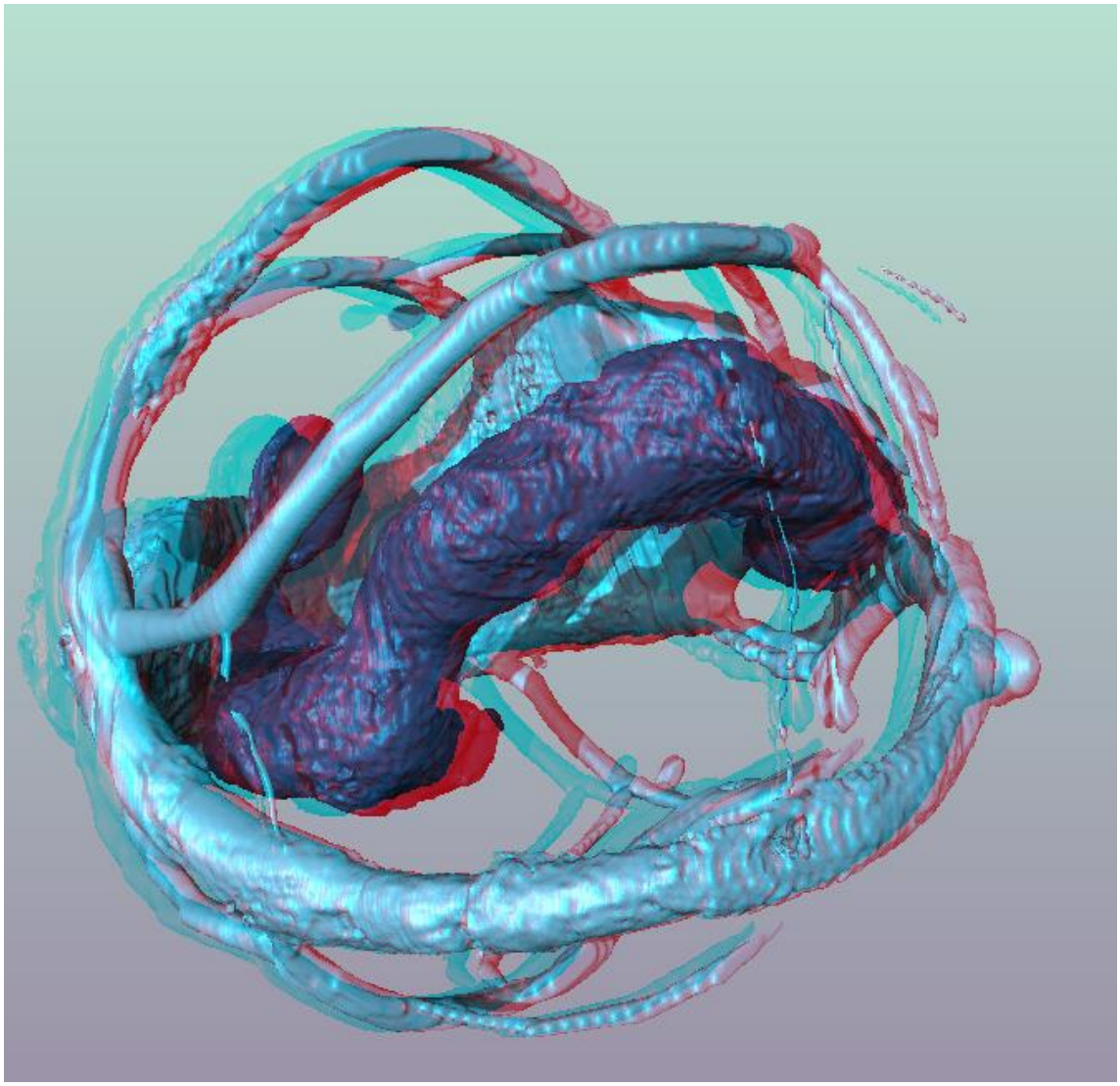

Appendix 2.1 Stereoscopic 3D image of AcMNPV structures in infected TN-368 cells at 96 hpi. Use 3D glasses provided

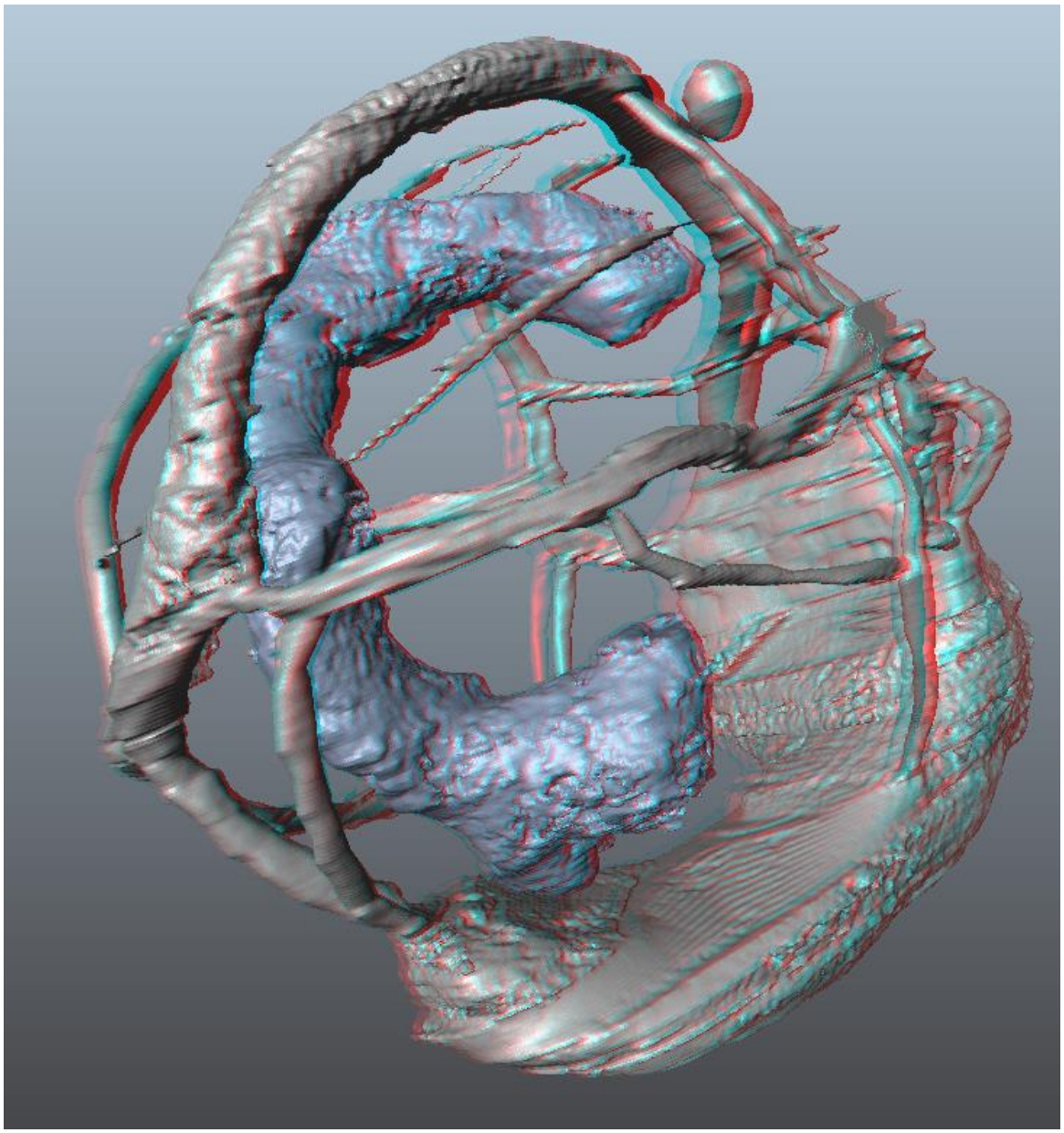

Appendix 2.2 Stereoscopic 3D image of AcMNPV structures in infected TN-368 cells at 96 hpi. Use 3D glasses provided**.**

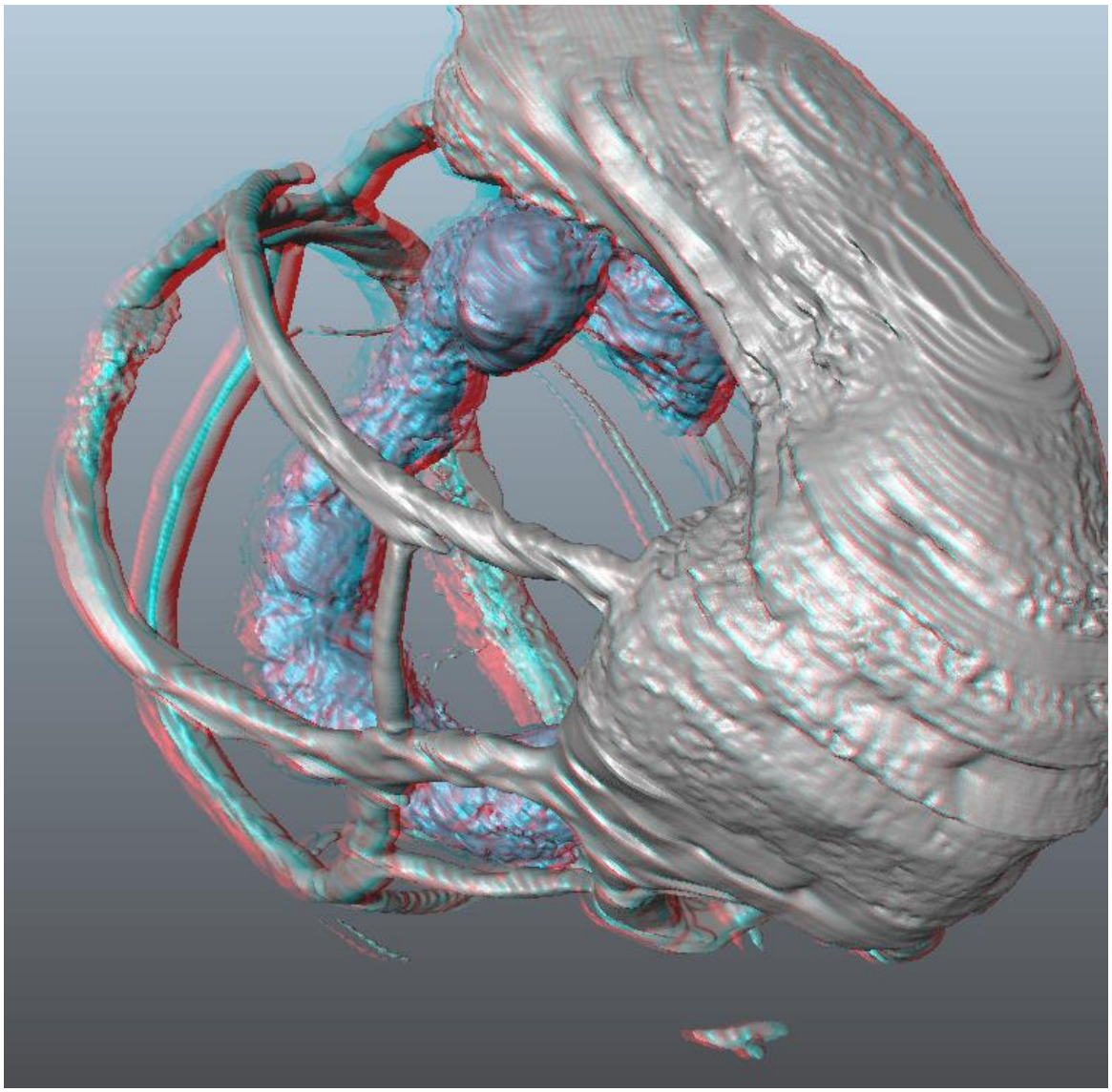

Appendix 2.3 Stereoscopic 3D image of AcMNPV structures in infected TN-368 cells at 96 hpi. Use 3D glasses provided**.**

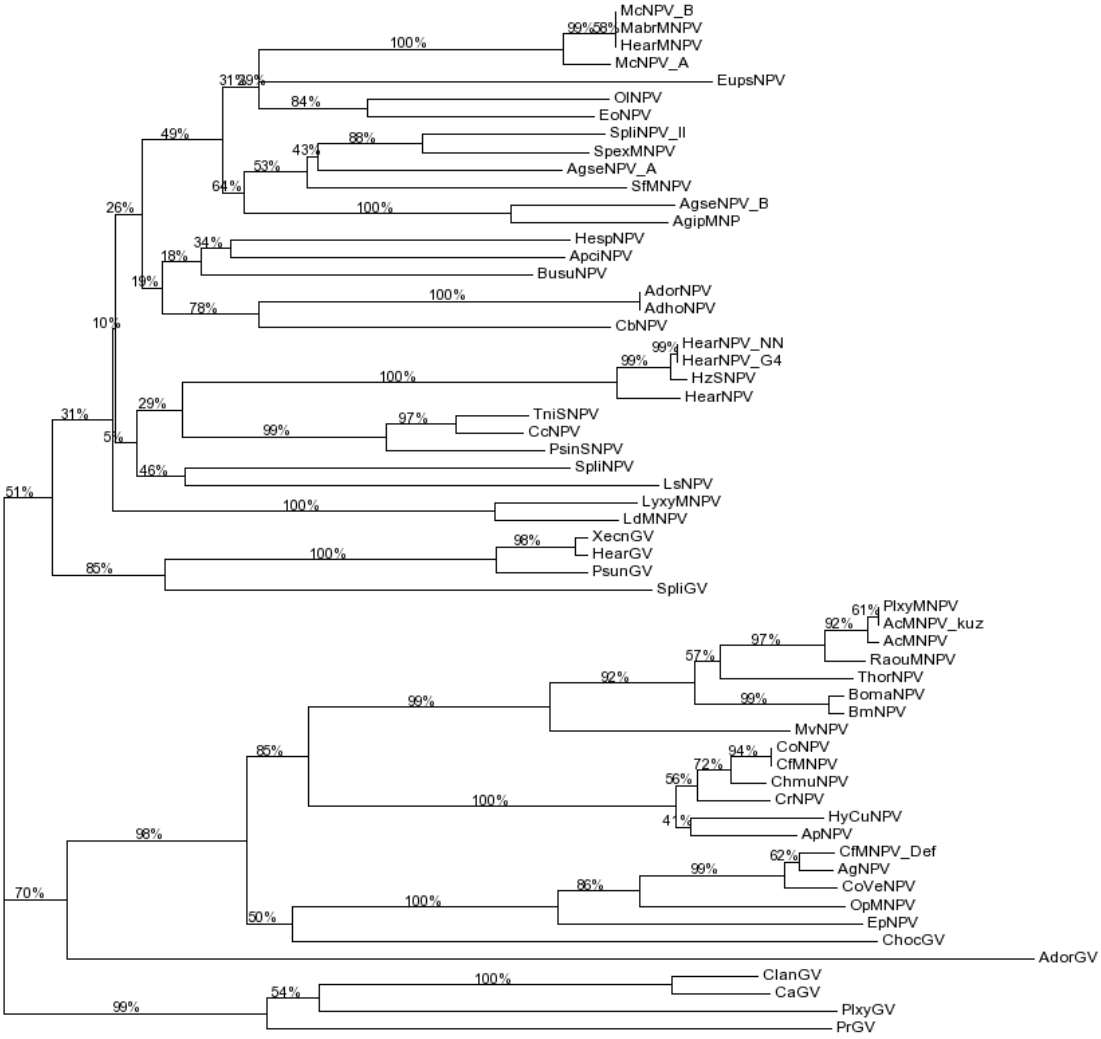

Appendix 3.1 Baculovirus P10 phylogentic tree. Displays a neighbour-joining phylogenic tree using T-Rex on generated T-coffee multiple aligned P10 sequences. Default Phylip format was used with a bootstrap value of 1000. The tree shows a distinct separation into two clades.

REFERENCES

Ackermann, H. and Smirnoff, W. (1983). A morphological investigation of 23 baculoviruses. *Journal of Invertebrate Pathology* 41(3), 269-280.

Adang, M. J. and Miller, L. K. (1982). Molecular cloning of DNA complementary to mRNA of the baculovirus *Autographa californica* nuclear polyhedrosis virus: Location and gene products of RNA transcripts found late in infection. *Journal of Virology* 44(3), 782-793.

Agriculture and Agri-Food Canada. (2013). *Biopesticide Database Directory* [Online]. [Accessed: 01 September 2016] Available: https://www5.agr.gc.ca/MPDD-CPM/search-recherche.do?lang=eng.

Alaoui-Ismaili, M. H. and Richardson, C. D. (1998). Insect virus proteins (FALPE and *p10*) self-associate to form filaments in infected cells. *Journal of Virology* 72(3), 2213-2223.

Arnott, H. J. and Smith, K. M. (1967). An ultrastructural study of the development of a granulosis virus in the cells of the moth *Plodia interpunctella* (Hbn.). *Journal of Ultrastructure Research* 21(3-4), 251-268.

Au, S., Wu, W. and Pante, N. (2013). Baculovirus nuclear import: open, nuclear pore complex (NPC) sesame. *Viruses* 5(7), 1885-1900.

Baumeister, W. (2002). Electron tomography: Towards visualizing the molecular organization of the cytoplasm. *Current Opinion in Structural Biology* 12(5), 679-684.

Benz, G. A. (1986). Introduction: Historical Perspectives. In*:* Granados, R. R. and Federici, B. A. (eds.) *The biology of Baculoviruses.* Boca Raton, Florida: CRC Press. 1-35.

Bergold, G. (1947). Die isolierung des polyeder-virus und die natur der polyeder. *Zeitschrift für Naturforschung B* 2(3-4), 122-143.

Bergold, G. H. (1950). The multiplication of insect viruses as organisms. *Canadian Journal of Research* 28(1), 5-11.

Bergold, G. H. (1953). On the nomenclature and classification of insect viruses. *Annals of the New York Academy of Sciences* 56(3), 495-516.

Bianchi, F. J., Snoeijing, I., Van Der Werf, W., Mans, R. M., Smits, P. H. and Vlak, J. M. (2000). Biological activity of SeMNPV, AcMNPV, and three AcMNPV deletion mutants against *Spodoptera exigua* larvae (Lepidoptera: Noctuidae). *Journal of Invertebrate Pathology* 75(1), 28-35.

Bilimoria, S. (1986). Taxonomy and identification of baculoviruses. In*:* Granados, R. R. and Federici, B. A. (eds.) *The Biology of Baculoviruses.* Boca Raton: CRC Press. 44-53.

Birch-Andersen, A. (1955). Reconstruction of the nuclear sites of *Salmonella typhimurium* from electron micrographs of serial sections. *Microbiology* 13(2), 327-329.

Bischoff, D. S. and Slavicek, J. M. (1999). Impact of deletion of the *Lymantria dispar* nucleopolyhedrovirus PEP gene on viral potency: expression of the green fluorescent protein prevents larval liquefaction. *Biological Control* 14(1), 51-59.

Blissard, G. W. and Rohrmann, G. F. (1990). Baculovirus Diversity and Molecular-Biology. *Annual Review of Entomolgy* 35, 127-155.

Blissard, G. W. and Rohrmann, G. F. (1991). Baculovirus gp64 gene expression: analysis of sequences modulating early transcription and transactivation by IE1. *Journal of Virology* 65(11), 5820-5827.

Blissard, G. W. and Wenz, J. R. (1992). Baculovirus gp64 envelope glycoprotein is sufficient to mediate pH-dependent membrane fusion. *Journal of Virology* 66(11), 6829-6835.

Boucias, D. G. and Pendland, J. C. (1998). Baculoviruses. In*:* Boucias, D. G. and Pendland, J. C. (eds.) *Principles of Insect Pathology.* Norwell, New York: Kluwer Academic Publishers. 111-146.

Braunagel, S. C. and Summers, M. D. (2007). Molecular biology of the baculovirus occlusion-derived virus envelope. *Current Drug Targets* 8(10), 1084-1095.

Carpentier, D. C. (2008), *The baculovirus P10 Protein: Exploring an enigma,* Oxford Brookes University, PhD Thesis, Oxford.

References

Carpentier, D. C., Griffiths, C. M. and King, L. A. (2008). The baculovirus P10 protein of *Autographa californica* nucleopolyhedrovirus forms two distinct cytoskeletal-like structures and associates with polyhedral occlusion bodies during infection. *Virology* 371(2), 278-291.

Carpentier, D. C. J. and King, L. A. (2009). The long road to understanding the baculovirus P10 protein. *Virologica Sinica* 24(4), 227-242.

Carstens, E. B. and Ball, L. A. (2009). Ratification vote on taxonomic proposals to the International Committee on Taxonomy of Viruses (2008). *Archives of Virology* 154(7), 1181-1188.

Chang, J.-M., Di Tommaso, P. and Notredame, C. (2014). TCS: a new multiple sequence alignment reliability measure to estimate alignment accuracy and improve phylogenetic tree reconstruction. *Molecular Biology and Evolution* 31(6), 1625-1637.

Cheley, S., Kosik, K. S., Paskevich, P., Bakalis, S. and Bayley, H. (1992). Phosphorylated baculovirus *p10* is a heat-stable microtubule-associated protein associated with process formation in Sf9 cells. *Journal of Cell Science* 102(4), 739-752.

Chiu, E., Coulibaly, F. and Metcalf, P. (2012). Insect virus polyhedra, infectious protein crystals that contain virus particles. *Current Opinion in Structural Biology* 22(2), 234-240.

Chung, K., Brown, M. and Faulkner, P. (1980). Studies on the morphogenesis of polyhedral inclusion bodies of a baculovirus *Autographa californica* NPV. *Journal of General Virology* 46(2), 335-347.

Cohen, C. and Parry, D. A. (1994). Alpha-helical coiled coils: more facts and better predictions. *Science* 263(5146), 488-489.

Coulibaly, F., Chiu, E., Gutmann, S., Rajendran, C., Haebel, P. W., Ikeda, K., Mori, H., Ward, V. K., Schulze-Briese, C. and Metcalf, P. (2009). The atomic structure of baculovirus polyhedra reveals the independent emergence of infectious crystals in DNA and RNA viruses. *Proceedings of the National Academy of Sciences* 106(52), 22205-22210.

Cox, M. M. (2012). Recombinant protein vaccines produced in insect cells. *Vaccine* 30(10), 1759-1766.

Crick, F. H. (1952). Is α-keratin a coiled coil? *Nature* 170, 882-883.

Crick, F. H. (1953). The packing of α-helices: simple coiled-coils. *Acta Crystallographica* 6(8), 689-697.

Croizier, G., Gonnet, P. and Devauchelle, G. (1987). Localisation cytologique de la protine non structurale P10 du baculovirus de la polydrose nuclaire du lepidoptere *Galleria mellonella* L. *Comptes rendus de l'Academie des Scienes* 305(19), 677-681.

Daimon, T., Katsuma, S. and Shimada, T. (2007). Mutational analysis of active site residues of chitinase from *Bombyx mori* nucleopolyhedrovirus. *Virus Research* 124(1), 168-175.

Danquah, J. O., Botchway, S., Jeshtadi, A. and King, L. A. (2012). Direct interaction of baculovirus capsid proteins VP39 and EXON0 with kinesin-1 in insect cells determined by fluorescence resonance energy transfer-fluorescence lifetime imaging microscopy. *Journal of Virology* 86(2), 844-853.

Davis, T., Wickham, T., Mckenna, K., Granados, R., Shuler, M. and Wood, H. (1993). Comparative recombinant protein production of eight insect cell lines. *In Vitro Cellular & Developmental Biology-Animal* 29(5), 388-390.

Denk, W. and Horstmann, H. (2004). Serial block-face scanning electron microscopy to reconstruct three-dimensional tissue nanostructure. *PLoS Biology* 2(11), e329.

Dent, D. R. (1993). The use of *Bacillus thuringiensis* as an insecticide. In*:* Jones, G. (ed.) *Exploitation of Microorganisms.* London: Chapman and Hall. 19-44.

Dong, C., Li, D., Long, G., Deng, F., Wang, H. and Hu, Z. (2005). Identification of functional domains required for HearNPV P10 filament formation. *Virology* 338(1), 112-120.

Dong, C., Deng, F., Li, D., Wang, H. and Hu, Z. (2007). The heptad repeats region is essential for AcMNPV P10 filament formation and not the proline-rich or the C-terminus basic regions. *Virology* 365(2), 390-397.

Dutta, S. (2010). Biopesticides: an ecofriendly approach for pest control. *Journal of Pharmacy and Pharmaceutical Sciences* 4(6), 250-265.

Fang, M., Nie, Y. and Theilmann, D. A. (2009). AcMNPV EXON0 (AC141) which is required for the efficient egress of budded virus nucleocapsids interacts with beta-tubulin. *Virology* 385(2), 496-504.

Fuxa, J. (1982). Prevalence of viral infections in populations of fall armyworm, *Spodoptera frugiperda,* in southeastern Louisiana. *Environmental Entomology* 11(1), 239-242.

Garavaglia, M. J., Miele, S. a. B., Iserte, J. A., Belaich, M. N. and Ghiringhelli, P. D. (2012). The ac53, ac78, ac101, and ac103 genes are newly discovered core genes in the family Baculoviridae. *Journal of Virology* 86(22), 12069-12079.

Gerhardson, B. (2002). Biological substitutes for pesticides. *Trends in Biotechnology* 20(8), 338-43.

Gluenz, E., Wheeler, R. J., Hughes, L. and Vaughan, S. (2015). Scanning and three-dimensional electron microscopy methods for the study of *Trypanosoma brucei* and *Leishmania mexicana* flagella. *Methods in Cell Biology* 127, 509-542.

Granados, R. R. (1978). Early events in the infection of *Heliothis zea* midgut cells by a baculovirus. *Virology* 90(1), 170-174.

Granados, R. R. and Lawler, K. A. (1981). *In vivo* pathway of *Autographa californica* baculovirus invasion and infection. *Virology* 108(2), 297-308.

Gross, C. H., Russell, R. L. and Rohrmann, G. F. (1994). *Orgyia pseudotsugata* baculovirus *p10* and polyhedron envelope protein genes: analysis of their relative expression levels and role in polyhedron structure. *Journal of General Virology* 75 (5), 1115-1123.

Haas-Stapleton, E. J., Washburn, J. O. and Volkman, L. E. (2004). P74 mediates specific binding of *Autographa californica* M nucleopolyhedrovirus occlusion-derived virus to primary cellular targets in the midgut epithelia of *Heliothis virescens* larvae. *Journal of virology* 78(13), 6786-6791.

Harrap, K. (1972). The structure of nuclear polyhedrosis viruses: I. The inclusion body. *Virology* 50(1), 114-123.

Harrap, K. A. and Payne, C. C. (1979). The structural properties and identification of insect viruses. *Advances in virus research* 25, 273-355.

Harris, K. M. (1999). Structure, development, and plasticity of dendritic spines. *Current Opinion in Neurobiology* 9(3), 343-348.

Hattori, T., Nakanishi, K., Mori, T., Tomita, M. and Tsumoto, K. (2016). The method used to culture host cells (Sf9 cells) can affect the qualities of baculovirus budding particles expressing recombinant proteins. *Bioscience, Biotechnology, and Biochemistry* 80(3), 445-451.

Hawtin, R. E., Zarkowska, T., Arnold, K., Thomas, C. J., Gooday, G. W., King, L. A., Kuzio, J. A. and Possee, R. D. (1997). Liquefaction of *Autographa californica* nucleopolyhedrovirus-infected insects is dependent on the integrity of virus-encoded chitinase and cathepsin genes. *Virology* 238(2), 243-253.

Henderson, J., Faulkner, P. and Mackinnon, E. (1974). Some biophysical properties of virus present in tissue cultures infected with the nuclear polyhedrosis virus of *Trichoplusia ni*. *Journal of General Virology* 22(1), 143-146.

Hess, R. T. and Falcon, L. (1978). Electron microscope observations of the membrane surrounding polyhedral inclusion bodies of insects. *Archives of Virology* 56(1-2), 169-176.

Heumann, H.-G. (1992). Microwave-stimulated glutaraldehyde and osmium tetroxide fixation of plant tissue: ultrastructural preservation in seconds. *Histochemistry* 97(4), 341-347.

Hink, W. (1970). Established insect cell line from the cabbage looper, *Trichoplusia ni*. *Nature* 226, 466-467.

Hitchman, R. B., Siaterli, E. A., Nixon, C. P. and King, L. A. (2007). Quantitative real-time PCR for rapid and accurate titration of recombinant baculovirus particles. *Biotechnology and bioengineering* 96(4), 810-814.

Hitchman, R. B., Possee, R. D., Crombie, A. T., Chambers, A., Ho, K., Siaterli, E., Lissina, O., Sternard, H., Novy, R. and Loomis, K. (2010a). Genetic modification of a baculovirus vector for increased expression in insect cells. *Cell biology and toxicology* 26(1), 57-68.

Hitchman, R. B., Possee, R. D., Siaterli, E., Richards, K. S., Clayton, A. J., Bird, L. E., Owens, R. J., Carpentier, D. C., King, F. L. and Danquah, J. O. (2010b). Improved expression of secreted

and membrane-targeted proteins in insect cells. *Biotechnology and applied biochemistry* 56(3), 85-93.

Hom, L. and Volkman, L. (2000). *Autographa californica* M nucleopolyhedrovirus *chiA* is required for processing of V-CATH. *Virology* 277(1), 178-183.

Hoover, K., Grove, M., Gardner, M., Hughes, D. P., Mcneil, J. and Slavicek, J. (2011). A gene for an extended phenotype. *Science* 333(6048), 1401-1401.

Hoppe, W. (1981). Three-dimensional electron microscopy. *Annual Review of Biophysics and Bioengineering* 10(1), 563-592.

Horton, H. M. and Burand, J. P. (1993). Saturable attachment sites for polyhedron-derived baculovirus on insect cells and evidence for entry via direct membrane fusion. *Journal of Virology* 67(4), 1860-1868.

Howard, S. C., Ayres, M. D. and Possee, R. D. (1986). Mapping the 5'and 3'ends of Autographa californica nuclear polyhedrosis virus polyhedrin mRNA. *Virus Research* 5(2-3), 109-119.

Hughes, K. M. (1950). A demonstration of the nature of polyhedra using alkaline solutions. *Journal of Bacteriology* 59(2), 189.

Hughes, L., Hawes, C., Monteith, S. and Vaughan, S. (2014). Serial block face scanning electron microscopy—the future of cell ultrastructure imaging. *Protoplasma* 251(2), 395-401.

Hunter-Fujita, F., Philip, F. E., Hugh, F. E. and Norman, E. C. (1998). *Insect Viruses and Pest Management,* Chichester, Wiley.

Jäggin, M. (2016). *General information baculovirus products* [Online]. Andermatt Biocontrol, [Accessed: 01 September 2016] Available: http://www.andermattbiocontrol.com/sites/products/bio-insecticides/baculovirus/baculovirus-products.html.

Jehle, J. A., Blissard, G. W., Bonning, B. C., Cory, J. S., Herniou, E. A., Rohrmann, G. F., Theilmann, D. A., Thiem, S. M. and Vlak, J. M. (2006). On the classification and nomenclature of baculoviruses: A proposal for revision. *Archives of Virology* 151(7), 1257-1266.

Kelly, B. J., King, L. A. and Possee, R. D. (2007). Introduction to Baculovirus Molecular Biology. In*:* Murhammer, D. W. (ed.) *Baculovirus and Insect Cell Expression Protocols.* Totowa, NJ: Humana Press. 25-53.

King, L. A. and Possee, R. D. (1992). *The Baculovirus System, A Laboratory Guide,* London, Chapman and Hall.

Kittelmann, M., Hawes, C. and Hughes, L. (2016). Serial block face scanning electron microscopy and the reconstruction of plant cell membrane systems. *Journal of Microscopy* 263(2), 200-211.

Kitts, P. A. and Possee, R. (1993). A method for producing recombinant baculovirus expression vectors at high frequency. *Biotechniques* 14(5), 810-817.

Knudson, D. and Harrap, K. (1976). Replication of a nuclear polyhedrosis virus in a continuous cell culture of *Spodoptera frugiperda*: Microscopy study of the sequence of events of the virus infection. *Journal of Virology* 17(1), 254-268.

Koivunen, M., Duke, S. O., Coats, J. R. and Beck, J. J. (2013). Pest management with natural products. Iowa: Entomology Publications. 1-4.

Kremer, J. R., Mastronarde, D. N. and Mcintosh, J. R. (1996). Computer visualization of three-dimensional image data using IMOD. *Journal of Structural Biology* 116(1), 71-76.

Kuzio, J., Rohel, D., Curry, C., Krebs, A., Carstens, E. and Faulkner, P. (1984). Nucleotide sequence of the *p10* polypeptide gene of *Autographa californica* nuclear polyhedrosis virus. *Virology* 139(2), 414-418.

Lacey, L. A., Grzywacz, D., Shapiro-Ilan, D. I., Frutos, R., Brownbridge, M. and Goettel, M. S. (2015). Insect pathogens as biological control agents: Back to the future. *Journal of Invertebrate Pathology* 132, 1-41.

Lee, S. Y., Poloumienko, A., Belfry, S., Qu, X., Chen, W., Macafee, N., Morin, B., Lucarotti, C. and Krause, M. (1996). A common pathway for *p10* and calyx proteins in progressive stages of polyhedron envelope assembly in AcMNPV-infected *Spodoptera frugiperda* larvae. *Archives of Virology* 141(7), 1247-1258.

References

Leighton, S. B. (1980). SEM images of block faces, cut by a miniature microtome within the SEM-a technical note. *Scanning electron microscopy* 2, 73-76.

Liu, A., Qin, J., Rankin, C., Hardin, S. E. and Weaver, R. F. (1986). Nucleotide sequence of a portion of the *Autographa californica* nuclear polyhedrosis virus genome containing the EcoRI site-rich region (hr5) and an open reading frame just 5' of the *p10* gene. *Journal of General Virology* 67(11), 2565-2570.

Livingstone, C. D. and Barton, G. J. (1993). Protein sequence alignments: a strategy for the hierarchical analysis of residue conservation. *Computer Applications in the Biosciences: CABIOS* 9(6), 745-756.

Long, G., Pan, X., Kormelink, R. and Vlak, J. M. (2006). Functional entry of baculovirus into insect and mammalian cells is dependent on clathrin-mediated endocytosis. *Journal of Virology* 80(17), 8830-8833.

Lu, A. and Miller, L. K. (1995). Differential requirements for baculovirus late expression factor genes in two cell lines. *Journal of Virology* 69(10), 6265-6272.

Lupas, A., Van Dyke, M. and Stock, J. (1991). Predicting coiled coils from protein sequences. *Science* 252(5009), 1162-1164.

Mackinnon, E. A., Henderson, J. F., Stoltz, D. B. and Faulkner, P. (1974). Morphogenesis of nuclear polyhedrosis virus under conditions of prolonged passage in vitro. *Journal of Ultrastructure Research* 49(3), 419-435.

Matsuura, Y., Possee, R. D., Overton, H. A. and Bishop, D. H. (1987). Baculovirus expression vectors: the requirements for high level expression of proteins, including glycoproteins. *Journal of General Virology* 68(5), 1233-1250.

Medema, M. H., Breitling, R., Bovenberg, R. and Takano, E. (2011). Exploiting plug-and-play synthetic biology for drug discovery and production in microorganisms. *Nature Reviews Microbiology* 9(2), 131-137.

Merzendorfer, H. and Zimoch, L. (2003). Chitin metabolism in insects: structure, function and regulation of chitin synthases and chitinases. *Journal of Experimental Biology* 206(24), 4393-4412.

Miele, S. A., Garavaglia, M. J., Belaich, M. N. and Ghiringhelli, P. D. (2011). Baculovirus: molecular insights on their diversity and conservation. *International Journal of Evolutionary Biology* 2011(22), 379-424.

Miller, D. W., Safer, P. and Miller, L. (1986). An insect baculovirus host-vector system for high-level expression of foreign genes. In*:* Setlow, J. K. and Hollaender, A. (eds.) *Genetic Engineering: Principles and Methods* New york: Plenum Press. 277-298.

Miller, L. K. (1997). *The baculoviruses,* New York, Plenum Press.

Minion, F., Coons, L. B. and Broome, J. (1979). Characterization of the polyhedral envelope of the nuclear polyhedrosis virus of *Heliothis virescens*. *Journal of Invertebrate Pathology* 34(3), 303-307.

Monsma, S. A., Oomens, A. G. and Blissard, G. W. (1996). The GP64 envelope fusion protein is an essential baculovirus protein required for cell-to-cell transmission of infection. *Journal of Virology* 70(7), 4607-4016.

Morris, T. and Miller, L. (1992). Promoter influence on baculovirus-mediated gene expression in permissive and nonpermissive insect cell lines. *Journal of Virology* 66(12), 7397-7405.

Mueller, J., Pfanzelter, J., Winkler, C., Narita, A., Le Clainche, C., Nemethova, M., Carlier, M.-F., Maeda, Y., Welch, M. D. and Ohkawa, T. (2014). Electron tomography and simulation of baculovirus actin comet tails support a tethered filament model of pathogen propulsion. *PLoS Biology* 12(1), 1-14.

Murphy, F. A., Fauquet, C. M., Bishop, D. H., Ghabrial, S. A., Jarvis, A. W., Martelli, G. P., Mayo, M. A. and Summers, M. D. (1995). *Virus taxonomy: classification and nomenclature of viruses. Sixth report of the International Committee on Taxonomy of Viruses,* New York, Springer Verlag.

Notredame, C., Higgins, D. G. and Heringa, J. (2000). T-Coffee: A novel method for fast and accurate multiple sequence alignment. *Journal of Molecular Biology* 302(1), 205-217.

References

Ohkawa, T., Volkman, L. E. and Welch, M. D. (2010). Actin-based motility drives baculovirus transit to the nucleus and cell surface. *Journal of Cell Biology* 190(2), 187-195.

Patmanidi, A. L., Possee, R. D. and King, L. A. (2003). Formation of P10 tubular structures during AcMNPV infection depends on the integrity of host-cell microtubules. *Virology* 317(2), 308-320.

Pearson, M. N., Russell, R. L., Rohrmann, G. F. and Beaudreau, G. S. (1988). *p39*, a major baculovirus structural protein: immunocytochemical characterization and genetic location. *Virology* 167(2), 407-413.

Pearson, W. R. (2013). An introduction to sequence similarity ("homology") searching. *Current Protocols Bioinformatics* Chapter 3.

Peng, K., Van Oers, M. M., Hu, Z., Van Lent, J. W. and Vlak, J. M. (2010). Baculovirus *per os* infectivity factors form a complex on the surface of occlusion-derived virus. *Journal of virology* 84(18), 9497-9504.

Pidre, M. L., Ferrelli, M. L., Haase, S. and Romanowski, V. (2013). Baculovirus Display: A Novel Tool for Vaccination. In*:* Romanowski, V. (ed.) *Current Issues in Molecular Virology-Viral Genetics and Biotechnological Applications.* National University of La Plata, Argentinia Institute of Molecular Biology and Biotechnology. 137-164.

Plonsky, I., Cho, M.-S., Oomens, A. G., Blissard, G. and Zimmerberg, J. (1999). An analysis of the role of the target membrane on the GP64-induced fusion pore. *Virology* 253(1), 65-76.

Possee, R. D. and Howard, S. C. (1987). Analysis of the polyhedrin gene promoter of the *Autographa californica* nuclear polyhedrosis virus. *Nucleic Acids Research* 15(24), 10233-10248.

Possee, R. D. (1997). Baculoviruses as expression vectors. *Current Opinion in Biotechnology* 8(5), 569-572.

Possee, R. D., Hitchman, R. B., Richards, K. S., Mann, S. G., Siaterli, E., Nixon, C. P., Irving, H., Assenberg, R., Alderton, D. and Owens, R. J. (2008). Generation of baculovirus vectors for the high-throughput production of proteins in insect cells. *Biotechnology and bioengineering* 101(6), 1115-1122.

Possee, R. D., Griffiths, C. M., Hitchman, R. B., Chambers, A., Murguia-Meca, F., Danquah, J., Jeshtadi, A. and King, L. A. (2010). Baculoviruses: Biology, Replication and Exploitation. In*:* Asgari, S. and Johnson, K. (eds.) *Insect virology.* Norfolk, UK: Caister Academic Press. 35-58.

Pritchett, D. W., Young, S. and Yearian, W. (1984). Some factors involved in the dissolution of *Autographa californica* nuclear polyhedrosis virus polyhedra by digestive fluids of *Trichoplusia ni* larvae. *Journal of Invertebrate Pathology* 43(2), 160-168.

Quant-Russell, R. L., Pearson, M. N., Rohrmann, G. F. and Beaudreau, G. S. (1987). Characterization of baculovirus *p10* synthesis using monoclonal antibodies. *Virology* 160(1), 9-19.

Rankin, C., Ladin, B. F. and Weaver, R. F. (1986). Physical mapping of temporally regulated, overlapping transcripts in the region of the 10K protein gene in *Autographa californica* nuclear polyhedrosis virus. *Journal of Virology* 57(1), 18-27.

Raza, F. (2013), *Analysis of baculovirus auxiliary proteins P10, cathepsin and chitinase,* Oxford Brookes University, PhD Thesis, Oxford.

Riegel, C. I. and Slavicek, J. M. (1997). Characterization of the replication cycle of the *Lymantria dispar* nuclear polyhedrosis virus. *Virus Research* 51(1), 9-17.

Rohel, D. Z., Cochran, M. A. and Faulkner, P. (1983). Characterization of two abundant mRNAs of *Autographa californica* nuclear polyhedrosis virus present late in infection. *Virology* 124(2), 357-365.

Rohel, D. Z. and Faulkner, P. (1984). Time course analysis and mapping of *Autographa californica* nuclear polyhedrosis virus transcripts. *Journal of Virology* 50(3), 739-747.

Rohrmann, G. F. (2011) Baculovirus molecular biology [online] 2nd ed [Accessed 20 September 2016] Available:www.ncbi.nlm.nih.gov/books/NBK49500.

References

Rohrmann, G. F. (2013) Introduction to the baculoviruses, their taxonomy, and evolution [online] *Baculovirus Molecular Biology.* 3rd ed [Accessed 01 Septemberr 2016] Available:http://www.ncbi.nlm.nih.gov/pubmed/24479205.

Russell, R. L. and Rohrmann, G. F. (1990). A baculovirus polyhedron envelope protein: immunogold localization in infected cells and mature polyhedra. *Virology* 174(1), 177-184.

Russell, R. L., Pearson, M. N. and Rohrmann, G. F. (1991). Immunoelectron microscopic examination of *Orgyia pseudotsugata* multicapsid nuclear polyhedrosis virus-infected *Lymantria dispar* cells: time course and localization of major polyhedron-associated proteins. *Journal of General Virology* 72(2), 275-283.

Saitou, N. and Nei, M. (1987). The neighbour-joining method: a new method for reconstructing phylogenetic trees. *Molecular Biology and Evolution* 4(4), 406-425.

Sambrook, J. and Russell, D. W. (2006). The Inoue Method for Preparation and Transformation of Competent *E. coli:*" Ultra Competent" Cells. *Cold Spring Harbour Protocols* (2), 3944.

Scheper, G. C., Vries, R. G., Broere, M., Usmany, M., Voorma, H. O., Vlak, J. M. and Thomas, A. A. (1997). Translational properties of the untranslated regions of the *p10* messenger RNA of *Autographa californica* multicapsid nucleopolyhedrovirus. *Journal of General Virology* 78 (3), 687-696.

Senger, T., Schädlich, L., Gissmann, L. and Müller, M. (2009). Enhanced papillomavirus-like particle production in insect cells. *Virology* 388(2), 344-353.

Shi, Y., Li, K., Tang, P., Li, Y., Zhou, Q., Yang, K. and Zhang, Q. (2015). Three-dimensional visualization of the *Autographa californica* multiple nucleopolyhedrovirus occlusion-derived virion envelopment process gives new clues as to its mechanism. *Virology* 476, 298-303.

Sjöstrand, F. (1958). Ultrastructure of retinal rod synapses of the guinea pig eye as revealed by three-dimensional reconstructions from serial sections. *Journal of Ultrastructure Research* 2(1), 122-170.

Slack, J. and Arif, B. M. (2006). The Baculoviruses Occlusion-Derived Virus: Virion Structure and Function. *Advances in Virus Research* 69, 99-165.

Slack, J. M., Kuzio, J. and Faulkner, P. (1995). Characterization of v-cath, a cathepsin L-like proteinase expressed by the baculovirus *Autographa californica* multiple nuclear polyhedrosis virus. *Journal of General Virology* 76(5), 1091-1098.

Smith, G. E., Vlak, J. M. and Summers, M. D. (1982). *In vitro* translation of *Autographa californica* nuclear polyhedrosis virus early and late mRNAs. *Journal of Virology* 44(1), 199-208.

Smith, G. E., Fraser, M. J. and Summers, M. D. (1983a). Molecular engineering of the *Autographa californica* nuclear polyhedrosis virus genome: deletion mutations within the Polyhedrin gene. *Journal of Virology* 46(2), 584-593.

Smith, G. E., Summers, M. D. and Fraser, M. J. (1983b). Production of human beta interferon in insect cells infected with a baculovirus expression vector. *Molecular Cell Biology* 3(12), 2156-2165.

Smith, G. E., Vlak, J. M. and Summers, M. D. (1983c). Physical analysis of *Autographa californica* nuclear polyhedrosis virus transcripts for Polyhedrin and 10,000-molecular-weight protein. *Journal of Virology* 45(1), 215-225.

Smyth, M. and Martin, J. (2000). X-ray crystallography. *Journal of Clinical Pathology* 53(1), 8.

Speidel, W., Fänger, H. and Naumann, C. (1996). The phylogeny of the Noctuidae (Lepidoptera). *Systematic Entomology* 21(3), 219-252.

Starborg, T., Kalson, N. S., Lu, Y., Mironov, A., Cootes, T. F., Holmes, D. F. and Kadler, K. E. (2013). Using transmission electron microscopy and 3View to determine collagen fibril size and three-dimensional organization. *Nature Protocols* 8(7), 1433-1448.

Steinhaus, E. A. (1949). Nomenclature and classification of insect viruses. *Bacteriological Review* 13(4), 203-223.

Summers, M. D. and Arnott, H. J. (1969). Ultrastructural studies on inclusion formation and virus occlusion in nuclear polyhedrosis and granulosis virus-infected cells of *Trichoplusia ni* (Hubner). *Journal of Ultrastructure Research* 28(5), 462-480.

Summers, M. D. and Smith, G. E. (1987). A manual of methods for baculovirus vectors and insect cell culture procedures. *Texas Agricultural Experiment Station* (1555).

Suzich, J. A., Ghim, S.-J., Palmer-Hill, F. J., White, W. I., Tamura, J. K., Bell, J. A., Newsome, J. A., Jenson, A. B. and Schlegel, R. (1995). Systemic immunization with papillomavirus L1 protein completely prevents the development of viral mucosal papillomas. *Proceedings of the National Academy of Sciences* 92(25), 11553-11557.

Thiem, S. M. and Miller, L. K. (1989). Identification, sequence, and transcriptional mapping of the major capsid protein gene of the baculovirus *Autographa californica* nuclear polyhedrosis virus. *Journal of Virology* 63(5), 2008-2018.

Thomas, C. J., Brown, H. L., Hawes, C. R., Lee, B. Y., Min, M.-K., King, L. A. and Possee, R. D. (1998). Localization of a baculovirus-induced chitinase in the insect cell endoplasmic reticulum. *Journal of Virology* 72(12), 10207-10212.

Van Der Wilk, F., Van Lent, J. W. and Vlak, J. M. (1987). Immunogold detection of polyhedrin, p10 and virion antigens in *Autographa californica* nuclear polyhedrosis virus-infected *Spodoptera frugiperda* cells. *Journal of General Virology* 68(10), 2615-2623.

Van Houte, S., Ros, V. I. and Van Oers, M. M. (2014a). Hyperactivity and tree-top disease induced by the baculovirus AcMNPV in *Spodoptera exigua* larvae are governed by independent mechanisms. *Naturwissenschaften* 101(4), 347-350.

Van Houte, S., Van Oers, M. M., Han, Y., Vlak, J. M. and Ros, V. I. (2014b). Baculovirus infection triggers a positive phototactic response in caterpillars to induce 'tree-top'disease. *Biology Letters* 10(12).

Van Lent, J., Groenen, J., Klinge-Roode, E., Rohrmann, G., Zuidema, D. and Vlak, J. (1990). Localization of the 34 kDa polyhedron envelope protein in *Spodoptera frugiperda* cells infected with *Autographa california* nuclear polyhedrosis virus. *Archives of Virology* 111(1), 103-114.

Van Oers, M. M., Flipsen, J. T., Reusken, C. B., Sliwinsky, E. L., Goldbach, R. W. and Vlak, J. M. (1993). Functional domains of the *p10* protein of *Autographa californica* nuclear polyhedrosis virus. *Journal of General Virology* 74(4), 563-574.

Van Oers, M. M., Flipsen, J. T., Reusken, C. B. and Vlak, J. M. (1994). Specificity of baculovirus *p10* functions. *Virology* 200(2), 513-523.

Van Oers, M. M. and Vlak, J. M. (1997). The baculovirus 10-kDa protein. *Journal of Invertebrate Pathology* 70(1), 1-17.

Van Oers, M. M., Hu, Z., Arif, B. M., Van Strien, E. A., Van Lent, J. W. and Vlak, J. M. (1998). The single-nucleocapsid nucleopolyhedrovirus of *Buzura suppressaria* encodes a P10 protein. *Journal of General Virology* 79(6), 1553-1562.

Van Oers, M. M., Pijlman, G. P. and Vlak, J. M. (2015). Thirty years of baculovirus-insect cell protein expression: from dark horse to mainstream technology. *Journal of General Virology* 96(1), 6-23.

Vanarsdall, A. L., Okano, K. and Rohrmann, G. (2004). Characterization of a baculovirus with a deletion of vlf-1. *Virology* 326(1), 191-201.

Vandeyar, M. A., Weiner, M. P., Hutton, C. J. and Batt, C. A. (1988). A simple and rapid method for the selection of oligodeoxynucleotide-directed mutants. *Gene* 65(1), 129-133.

Vaughn, J. L., Goodwin, R. H., Tompkins, G. J. and Mccawley, P. (1977). The establishment of two cell lines from the insect *Spodoptera frugiperda* (Lepidoptera; Noctuidae). *In Vitro* 13(4), 213-217.

Vlak, J. M., Klinkenberg, F. A., Zaal, K. J., Usmany, M., Klinge-Roode, E. C., Geervliet, J. B., Roosien, J. and Van Lent, J. W. (1988). Functional studies on the *p10* gene of *Autographa californica* nuclear polyhedrosis virus using a recombinant expressing a *p10*-beta-galactosidase fusion gene. *Journal of General Virology* 69(4), 765-76.

Vlak, J. M., Schouten, A., Usmany, M., Belsham, G. J., Klinge-Roode, E. C., Maule, A. J., Van Lent, J. W. and Zuidema, D. (1990). Expression of cauliflower mosaic virus gene I using a baculovirus vector based upon the *p10* gene and a novel selection method. *Virology* 179(1), 312-320.

References

Volkman, L., Summers, M. and Hsieh, C.-H. (1976). Occluded and nonoccluded nuclear polyhedrosis virus grown in *Trichoplusia ni*: comparative neutralization comparative infectivity, and *in vitro* growth studies. *Journal of Virology* 19(3), 820-832.

Volkman, L. E. and Goldsmith, P. A. (1985). Mechanism of neutralization of budded *Autographa californica* nuclear polyhedrosis virus by a monoclonal antibody: Inhibition of entry by adsorptive endocytosis. *Virology* 143(1), 185-195.

Volkman, L. E. and Zaal, K. J. (1990). *Autographa californica* M nuclear polyhedrosis virus: microtubules and replication. *Virology* 175(1), 292-302.

Wang, L., Salem, T. Z., Campbell, D. J., Turney, C. M., Kumar, C. S. and Cheng, X.-W. (2009). Characterization of a virion occlusion-defective *Autographa californica* multiple nucleopolyhedrovirus mutant lacking the *p26*, *p10* and *p74* genes. *Journal of General Virology* 90(7), 1641-1648.

Wang, P., Granados, R. R. and Shuler, M. L. (1992). Studies on serum-free culture of insect cells for virus propagation and recombinant protein production. *Journal of Invertebrate Pathology* 59(1), 46-53.

Wang, P., Hammer, D. A. and Granados, R. R. (1994). Interaction of *Trichoplusia ni* granulosis virus-encoded enhancin with the midgut epithelium and peritrophic membrane of four lepidopteran insects. *Journal of General Virology* 75(8), 1961-1967.

Wang, P. and Granados, R. R. (1997). An intestinal mucin is the target substrate for a baculovirus enhancin. *Proceedings of the National Academy of Sciences* 94(13), 6977-6982.

Wang, Q., Bosch, B. J., Vlak, J. M., Van Oers, M. M., Rottier, P. J. and Van Lent, J. W. (2016). Budded baculovirus particle structure revisited. *Journal of Invertebrate Pathology* 134, 15-22.

Ware, R. W. and Lopresti, V. (1975). Three-dimensional reconstruction from serial sections. *International Review of Cytology* 40, 325-440.

Westenberg, M., Veenman, F., Roode, E. C., Goldbach, R. W., Vlak, J. M. and Zuidema, D. (2004). Functional analysis of the putative fusion domain of the baculovirus envelope fusion protein F. *Journal of Virology* 78(13), 6946-6954.

Weyer, U. and Possee, R. D. (1988). Functional analysis of the *p10* gene 5' leader sequence of the *Autographa californica* nuclear polyhedrosis virus. *Nucleic Acids Research* 16(9), 3635-53.

Weyer, U. and Possee, R. D. (1989). Analysis of the promoter of the *Autographa californica* nuclear polyhedrosis virus *p10* gene. *Journal of General Virology* 70(1), 203-208.

Weyer, U., Knight, S. and Possee, R. D. (1990). Analysis of very late gene expression by *Autographa californica* nuclear polyhedrosis virus and the further development of multiple expression vectors. *Journal of General Virology* 71 (7), 1525-1534.

White, J. G., Southgate, E., Thomson, J. N. and Brenner, S. (1986). The structure of the nervous system of the nematode *Caenorhabditis elegans:* The mind of a worm. *Philosophical Transactions of the Royal of London. Series B, Biological Sciences* 314, 1-340.

Wickham, T., Davis, T., Granados, R., Shuler, M. and Wood, H. (1992). Screening of insect cell lines for the production of recombinant proteins and infectious virus in the baculovirus expression system. *Biotechnology Progress* 8(5), 391-396.

Wilke, S. A., Antonios, J. K., Bushong, E. A., Badkoobehi, A., Malek, E., Hwang, M., Terada, M., Ellisman, M. H. and Ghosh, A. (2013). Deconstructing complexity: serial block-face electron microscopic analysis of the hippocampal mossy fiber synapse. *The Journal of Neuroscience* 33(2), 507-522.

Williams, G. V., Rohel, D. Z., Kuzio, J. and Faulkner, P. (1989). A cytopathological investigation of *Autographa californica* nuclear polyhedrosis virus *p10* gene function using insertion/deletion mutants. *Journal of General Virology* 70(1), 187-202.

Wilson, J. A., Hill, J. E., Kuzio, J. and Faulkner, P. (1995). Characterization of the baculovirus *Choristoneura fumiferana* multicapsid nuclear polyhedrosis virus *p10* gene indicates that the polypeptide contains a coiled-coil domain. *Journal of General Virology* 76(12), 2923-2932.

References

Wong, T. K., Nielsen, L. K., Greenfield, P. F. and Reid, S. (1994). Relationship between oxygen uptake rate and time of infection of Sf9 insect cells infected with a recombinant baculovirus. *Cytotechnology* 15(1-3), 157-167.

Xeros, N. (1956). The virogenic stroma in nuclear and cytoplasmic polyhedroses. *Nature* 178, 412-413.

Young, J., Mackinnon, E. and Faulkner, P. (1993). The architecture of the virogenic stroma in isolated nuclei of *Spodoptera frugiperda* cells in vitro infected by *Autographa californica* nuclear polyhedrosis virus. *Journal of Structural Biology* 110(2), 141-153.

Zahiri, R., Kitching, I. J., Lafontaine, J. D., Mutanen, M., Kaila, L., Holloway, J. D. and Wahlberg, N. (2011). A new molecular phylogeny offers hope for a stable family level classification of the Noctuoidea (Lepidoptera). *Zoologica Scripta* 40(2), 158-173.

Zechmann, B. and Zellnig, G. (2009). Microwave-assisted rapid plant sample preparation for transmission electron microscopy. *Journal of Microscopy* 233(2), 258-268.